A COMPREHENSIVE INVESTIGATION OF PHOTOINDUCED ELECTRON TRANSFER AND CHARGE TRANSFER MECHANISMS IN PUSH-PULL DONOR-ACCEPTOR SYSTEMS: IMPLICATIONS FOR ENERGY HARVESTING APPLICATIONS

Ajyal Zaki Alsaleh

Dissertation Prepared for the Degree

DOCTOR OF PHILOSOPHY

UNIVERSITY OF NORTH TEXAS

December 2023

APPROVED:

Francis D'Souza, Major Professor
William E. Acree, Jr., Committee Member
Mohammad El Bouanani, Committee Member
Seare Berhe, Committee Member
Benjamin Sherman, Committee Member
Legrande Slaughter, Chair of the Department of Chemistry
John Quintanilla, Dean of the College of Science
Victor Prybutok, Dean of the Toulouse Graduate School

Alsaleh, Ajyal Zaki. *A Comprehensive Investigation of Photoinduced Electron Transfer and Charge Transfer Mechanisms in Push-Pull Donor-Acceptor Systems: Implications for Energy Harvesting Applications.* Doctor of Philosophy (Chemistry), December 2023, 215 pp., 11 tables, 100 figures, 7 schemata, numbered chapter references.

Donor-acceptor systems exhibit distinctive attributes rendering them highly promising for the emulation of natural photosynthesis and the efficient capture of solar energy. This dissertation is primarily devoted to the investigation of these unique features within diverse donor-acceptor system typologies, encompassing categories such as closely covalently linked, push-pull, supramolecular, and multi-modular donor- acceptor conjugates. The research encompasses an examination of photosynthetic analogs involving compounds such as chelated azadipyromethene (AzaBODIPY), N,N-dimethylaminophenyl (NND), phenothiazine (PTZ), triphenylamine (TPA), phenothiazine sulfone (PTZSO2), tetracyanobutadiene (TCBD), and expanded tetracyanobutadiene (exTCBD). The strategic configuration of the donor (D), acceptor (A), and spacer elements within these constructs serves to promote intramolecular charge transfer (ICT), which are crucial for efficient charge and electron transfer. The employment of cutting-edge analytical techniques, such as ultrafast transient absorption spectroscopy, is integral to the study. Furthermore, a comprehensive suite of analytical methodologies including steady-state UV-visible absorption spectroscopy, fluorescence and phosphorescence spectroscopies, electrochemical techniques (including cyclic voltammetry and differential pulse voltammetry), spectroelectrochemistry, and density functional theory calculation (DFT), collectively contribute to the comprehensive characterization of push-pull donor-acceptor systems, with a particular emphasis on their potential as highly effective solar energy harvesting application.

ACKNOWLEDGEMENTS

First and foremost, I wish to express my profound appreciation to my esteemed research advisor, Professor Francis D'Souza, for his unwavering support, guidance, and expertise, whom without his support I cannot accomplished this. In addition, this dissertation work benefited a lot from successful collaboration with Professor Rajneesh Misra, whom I would like to express my warmest appreciation. I would also like to extend my deep gratitude to the members of my research committee for their expertise and guidance, and my laboratory colleagues, both past and present, for their enduring support and collegiality. Furthermore, I sincerely appreciate the Department of Chemistry at the University of North Texas (UNT) for granting me admission to their esteemed program and providing me with the opportunity to accomplish my Ph. D work.

I am eternally grateful to my beloved parents, siblings, and extended family, without their unwavering support, unshakeable belief in me, and unconditional love, this journey would not have been possible. Despite the physical separation we endured for eight long years as I pursued my academic dreams, their continued love and support bridged the distance of space and time. In addition, I am profoundly grateful to my dear friends, for the laughter, support, and camaraderie that has kept me grounded and motivated.

Last but not least, I am grateful to the Saudi Arabia government and Imam Abdulrahman bin Faisal University for bestowing upon me the exceptional honor of a full scholarship to pursue my education. Their support and investment in my education have not only eased the financial burden but have also empowered achieve my academic journey with focus and determination, and to say this remarkable opportunity has been a driving force behind my accomplishments is an understatement. Additionally, I would like to extend my thanks to the National Science Foundation (NSF) for funding my research.

TABLE OF CONTENTS

Page

LIST OF TABLES

Page

LIST OF FIGURES

Page

LIST OF SCHEMATA

Page

CHAPTER 1

INTRODUCTION

1.1 The Evolution of Energy Utilization: From Historical Landmarks to Sustainable Adaptation in a Rapidly Changing World

Over 140 years ago, researchers began developing an innovative concept that would have a significant influence on how we utilize energy in houses and workplaces. This concept found its culmination in two pivotal moments in human history: the drilling of the first oil and gas well in Pennsylvania in 1859 and the invention of the light bulb by Thomas Edison in 1879. These landmark events marked the onset of a technological and industrial revolution that reshaped the trajectory of human society. Since those transformative discoveries, the continuing advancement of technology and industry has become inseparable from our daily lives, driving societal development, and rendering it indispensable. In this context, energy establishes a central role in controlling and adapting to our environment, enabling progress, and meeting the ever-growing needs of a rapidly evolving world. The convergence of the bright idea pursued by inventors and the subsequent innovations in lighting and energy extraction set in motion a cascade of developments that have propelled humanity into an era where energy serves as the backbone of modern civilization.[1, 2]

Energy is a fundamental concept that is core to numerous scientific disciplines and plays a crucial role in various aspects of our daily lives. It is a measurable quantity that enables the performance of work, the transfer of heat, and the generation of power. It takes on various manifestations, including thermal energy, potential energy, kinetic energy, chemical energy, and electrical energy (associated with the motion of charged particles). The understanding and harnessing of energy has been a driving force behind human progress, leading to advancements in technology, industry, and the overall development of societies.[3]

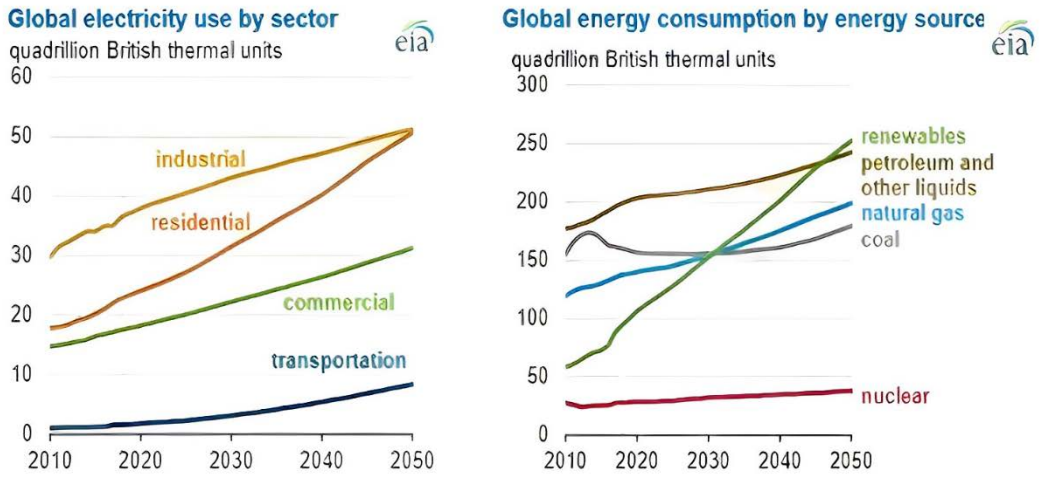

Figure 1.1: Global energy use by sector (left) and by energy source (right). Adapted from reference 4.

In recent years, the demand for energy has been on the rise across various sectors, leading to concerns about the sustainability of our energy resources. A recent report by the United States Energy Information Administration (EIA) (Fig. 1.1) indicates a significant surge in energy usage in the construction sector, encompassing residential and commercial buildings, with an anticipated growth of 65% between 2020 and 2050.[4] Additionally, the global industrial sector is expected to experience a more than 30% increase in energy consumption during this period. This escalating demand can be attributed to several factors, including growth in global population, rising income levels, urbanization, and increased access to electricity. As a result, it is crucial to address the increasing energy demand and explore sustainable alternatives, such as hydro, wind, and solar radiation, to ensure a more sustainable future.[4]

1.2 Transitioning Towards Renewable Energy for a Sustainable and Secure Future

The concept of energy is closely intertwined with environmental concerns and sustainability. As both industrialization and the global population grow exponentially, so has the demand for energy resources. Nonrenewable sources, such as petroleum, natural gas, and coal,

often referred to as fossil fuels, have historically served as the predominant sources of energy. Fossil fuels are generated from organic material such as algae and plants buried in sediments and in shallow oceans for millions of years. Over millions of years of tremendous pressure and temperature, the remnants of these animals changed into the fossil fuels we know today.[5] However, the finite nature of fossil fuels and their negative environmental impacts, including pollution, habitat destruction, and greenhouse gase (GHG) emissions, which include nitrous oxide (N_2O), carbon dioxide (CO_2), methane (CH_4), and fluorinated gases, have raised concerns about their long-term viability. In contrast, renewable energy sources such as solar electricity, wind, and hydroelectric power is expected remarkable growth from 2020 to 2050, surpassing petroleum and other liquid fuels to become the dominant energy source.[4] According to Figure 1.1, global consumption of renewable energy is projected to grow annually by 3.1%, while petroleum and other liquids, coal, and natural gas are expected to have growth rates of 0.6%, 0.4%, and 1.1%, respectively.[4] Prioritizing the harnessing of renewable energy sources like solar, wind, and hydroelectricity can contribute to the development of a sustainable and cleaner energy system that mitigates environmental degradation and maintains ecological balance.

1.3 The Importance of Emphasizing Renewable Energy Sources

Renewable energy sources, including hydro, wind, and solar radiation, have become crucial in the modern energy sector, playing a significant role in generating electrical energy. Currently, these sources meet more than 22% of the global electricity demand, offering sustainable alternatives to conventional fossil fuel-based systems. Their increasing prominence stems from their ability to mitigate the environmental impact of energy production and contribute to a more sustainable future. By harnessing the power of wind, water, and sunlight, these renewable

technologies are reshaping the energy landscape and facilitating the transition to a more diverse and environmentally conscious energy system.[6]

Wind power (onshore and offshore) utilizes wind turbines to both harness and transform the kinetic energy of the wind into electricity. It is a renewable and environmentally friendly resource that operates without producing greenhouse gas emissions. With its abundance and widespread availability, wind power serves as a viable option for electricity generation in various regions. In the United States, as depicted in Figure 1.2, wind energy accounted for approximately 9% of the total electricity generation in 2022, and it is projected to reach 14% by 2025.[7] However, the variability of wind availability is a challenge as it is reliant on weather conditions, necessitating significant investments in infrastructure and careful selection of suitable wind farm locations. Moreover, the integration of wind turbines into the power grid may require additional measures to ensure stability, and concerns about their visual and noise impacts need to be addressed.[6]

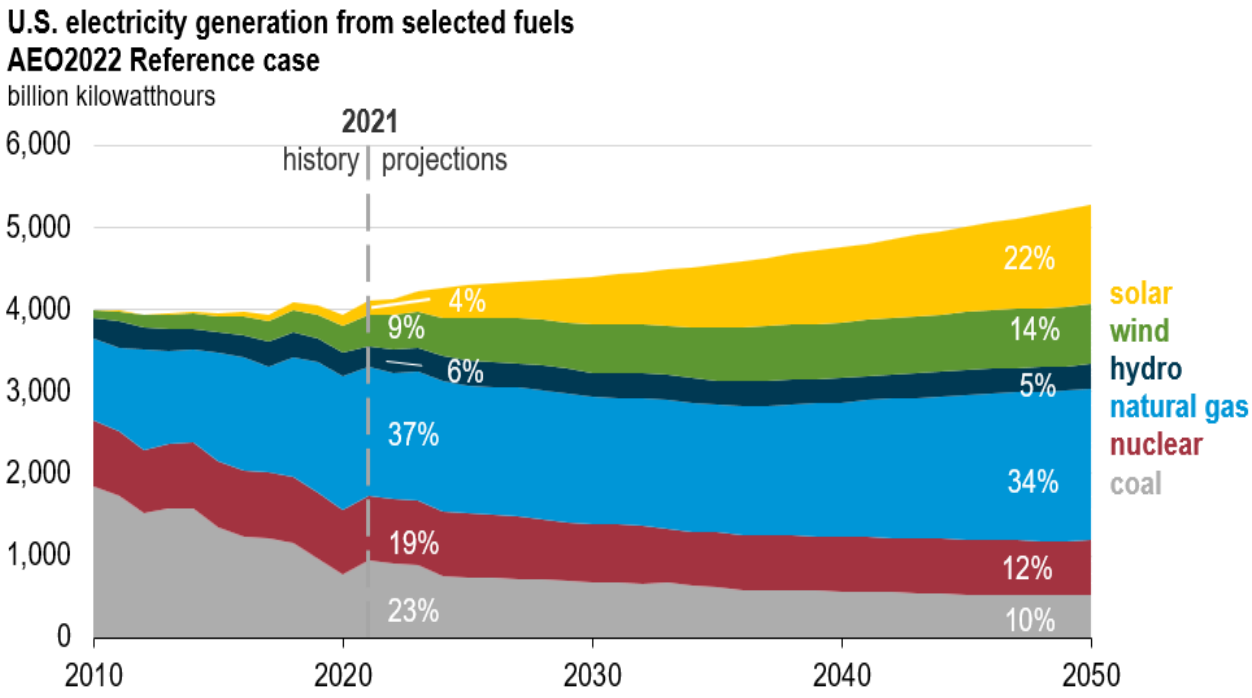

Figure 1.2: Electricity energy generation in U.S. 2022 by selected fuels. Adapted from reference 7.

Hydropower, a well-established technology, harnesses the potential energy of water derived from rivers, lakes, or dams to generate electricity. It offers a range of positive aspects, including the reliable provision of power that can be dispatched as needed, the ability to store energy through reservoirs, and its valuable contribution to controlling floods and managing water. Large-scale hydropower plants hold a significant role in the overall electricity production, accounting for 6% of global output 2022, in which the U.S. contributed approximately 101,000 megawatts.[7] However, despite its benefits, the construction and operation of such plants present significant environmental and social challenges, including changes to vegetation, the migration of local communities, alterations to ecosystems, and the high cost involved, rendering it unfeasible for implementation in many countries grappling with their socioeconomic situations. Concerns regarding the limited availability of suitable dam locations and the potential implications of climate change on water availability further underscore the need to question the long-term sustainability of hydropower.[8]

Ultimately, solar energy stands as a highly promising option among the available renewable energy sources to address the increasing global energy demand and ensure a secure energy supply. With its environmentally friendly, safe, abundant, and adaptable qualities, solar power emerges as a compelling substitute for traditional fossil fuels. According EIA, solar energy has the potential to meet around 22% of the electrical demand in the United States by 2025[7], emphasizing its substantial role in shaping the future energy scenario.

1.4 Solar Energy: The Future of Our Energy Needs

Solar power is an abundant, viable, clean, and naturally available source of energy. A substantial amount of solar radiation reaches the earth annually, estimated to be around 120,000 TW (terawatts). Despite the atmosphere absorbing some of this energy, approximately 36,000 TW

still reaches the earth's surface.[9] To put this into perspective, current levels of global energy consumption is roughly 13 TW, and it is projected to increase to 30 TW by 2050. However, by utilizing solar cells with just 10% efficiency that cover 0.16% of the earth's landmass, it becomes viable to generate an annual energy output of 60 TW. This level of energy production would be more than enough to fulfill the global societal energy needs.[10, 11]

Solar energy is commonly regarded as a clean source of energy as it does not generate GHGs and this makes it environmentally neutral. Therefore, solar energy is a viable solution to help combat climate change, avoid raising the sea level, and preserve the delicate balance of plant and wildlife.[12] Overall, solar energy stands as a promising renewable energy source, capable of meeting our future energy demands, while simultaneously reducing human impact on the environment and promoting a sustainable way of life, thus playing a pivotal role in shaping our energy future with advancements in technology.

1.5 Techniques of Capturing the Solar Radiant for Energy Production

The capture of solar energy is an essential mechanism that enables the conversion of the sun's radiant energy into usable power. Solar energy has garnered substantial interest as a renewable source because of its vast magnitude and global availability. In nature, solar energy is naturally harnessed through photosynthesis, transforming it into chemical energy, the form of carbon-carbon bonds, which is essential for all aerobic life on earth.[13] Throughout human history, innovative approaches have been developed to harness solar energy, with recent technological advancements driving significant cost reductions of more than 70% in solar power generation.[14] Various techniques are employed to effectively capture solar energy, with two primary categories of technological advice, active and passive techniques, playing a pivotal role. Passive systems utilize architectural and design strategies to maximize solar energy utilization without relying on

mechanical or electrical components. This involves maximizing building orientation, using materials with beneficial thermal qualities, and creating areas that encourage natural air circulation. On the other hand, active photovoltaic systems harness sun's radiation in a direct manner to produce either usable or storable energy. This involves mechanisms such as the interaction of photons with semiconducting materials in solar heating and cooling systems (SHC), concentrating solar power (CSP), and photovoltaic systems (PV).15 Active solar technologies play a crucial role in harnessing solar energy efficiently and offer versatile applications, reducing dependence on conventional energy sources.

1.5.1 Natural Photosynthesis

Photosynthesis is an essential biological process which consists of a number of photochemical and enzymatic reactions. Chlorophyll, found within the chloroplasts of plant leaves, is responsible for capturing light energy. This energy is subsequently used to promote the transformation of water, carbon dioxide (CO_2), and minerals into oxygen and energy-rich organic molecules such as glucose. The process of photosynthesis can be divided into two main stages: the light reactions, called non-cyclic photophosphorylation, and the dark reactions, named Calvin cycle. During the light reactions, electron (e^-) and proton (H^+) transfer occur, while the dark reactions involve the synthesis of carbohydrates from carbon dioxide.[16, 17] As seen in Figure 1.3, there are two reaction centers (RC), photosystem I (PSI), which holds a reduction catalyst, and photosystem II (PSII), an oxidation catalyst. The initial step of photosynthesis involves absorption of solar energy by the antenna systems. In Photosystem II, water splitting results in the release of electrons and generation of hydrogen ions (H^+) and oxygen atoms.[18] Molecular oxygen (O_2) is formed when oxygen atoms combine and are released into the environment. Additional hydrogen ions are pumped into the lumen by electron acceptor molecules.

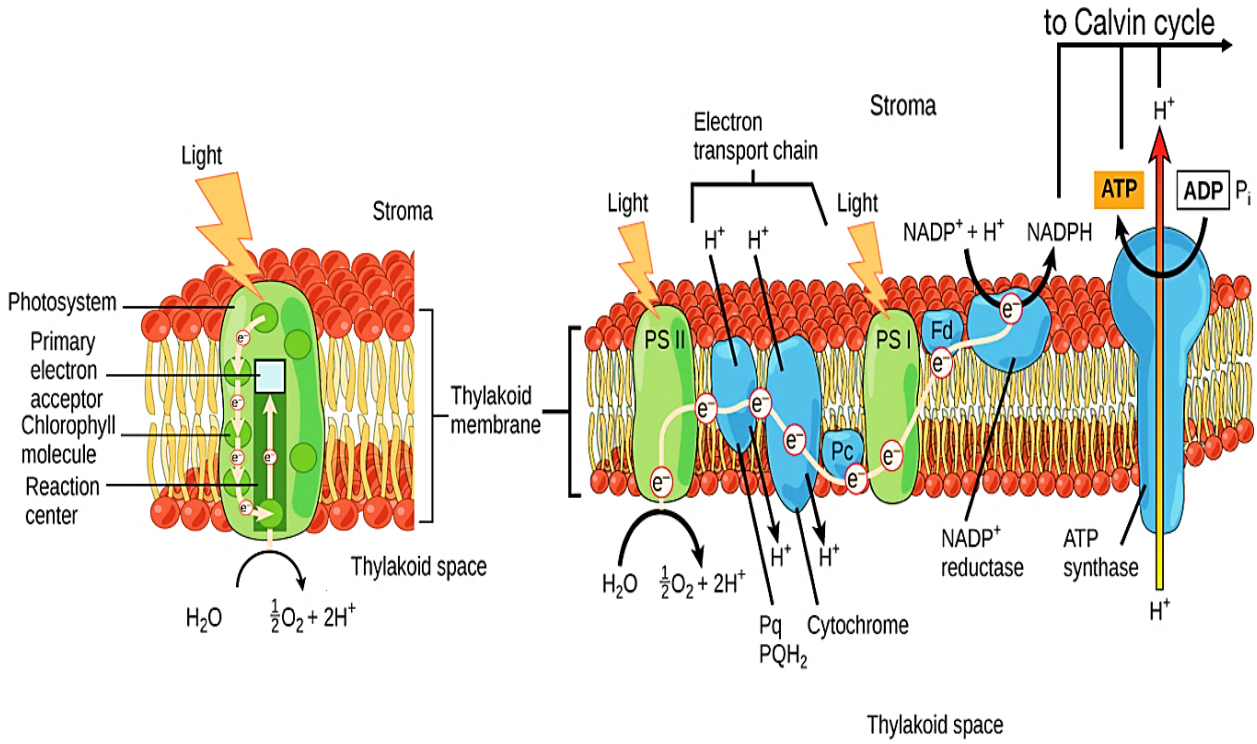

Figure 1.3: Schematic mechanism of photosynthesis in the thylakoid membrane: light reactions in oxygenic photosynthesis. Adapted from reference 18.

This results in a high hydrogen ion concentration within the lumen. The adenosine triphosphate (ATP), is a molecule that carries energy within cells, is produced by harnessing energy from hydrogen ions (H^+) moving back across the photosynthetic membrane. The enzyme nicotine adenine dinucleotide phosphate (NADPH) is generated through the capture of high-energy electrons during PSI upon absorption of light. The electron transport chain provides new electrons to Photosystem I. Subsequently, the Calvin cycle, or photosynthetic dark reaction, is powered by ATP for energy and NADPH for the supply of hydrogen atoms.[19, 20] In summary, these critical biochemical processes are represented as follows:

$$6\,CO_2 + 12\,H_2O + \text{light energy} \rightarrow C_6H_{12}O_6 + 6\,O_2 \qquad \text{Eq. 1.1}$$

Eq. 1.1 consists of two stages. The first process, known as the "light reaction," involves the splitting of water molecules. This reaction can be demonstrated as:

$$12\ H_2O + \text{light energy} \rightarrow 6\ CO_2 + 24\ H^+ + 24\ e^- \quad \text{Eq. 1.2}$$

A reduction process that converts NADPH from its oxidized form ($NADP^+$) to its reduced form (NADPH) is linked to the oxidation of water during the light reaction. The reduction reaction is illustrated as follows:[13]

$$NADP^+ + H_2O \rightarrow NADPH + H^+ + O \quad \text{Eq. 1.3}$$

1.5.2 Artificial Photosynthesis: Bridging the Gap between Nature and Solar Fuel Production

In recent years, inspiration has been drawn from nature, specifically the miraculous process of photosynthesis, giving rise to an entirely novel field of research known as artificial photosynthesis, which holds the potential to bridge the gap between the effectiveness and environmental sustainability of natural photosynthesis and the commercialization of solar fuels, thereby making it necessary to harness sunlight's energy and convert carbon dioxide into valuable products, mitigating climate change, enabling sustainable energy production, and reducing dependence on fossil fuels. The goal is to create artificial systems that are both innovative and extraordinarily efficient, and to do so requires a careful replication of the complex mechanics and basic principles of natural photosynthesis. These structures are designed to collect photons, the fundamental particles of light energy, and transform them into electrons and holes. Photovoltaic cells, commonly referred to as solar cells, are semiconductor devices crafted to convert sunlight into electrical power. The specific semiconductor material used in the construction of PV cells influences their characteristics, as illustrated in Table 1.1.[21] Presently, the dominant choice for PV systems in residential and commercial settings is crystalline silicon solar panels, specifically the monocrystalline (c-Si) and multicrystalline (mc-Si) types. In fact, over 90% of all PV installations consist of crystalline-silicon solar cells, which have a maximum power conversion efficiency (PCE) of approximately 30%.[22, 23] Nevertheless, the shortage of crucial materials such as high-

quality silicon crystalline wafers, contributes to the costly nature of the process. Extensive efforts are underway to create advanced solar cells that can efficiently convert larger amounts of sunlight into electricity while minimizing expenses. Although the research focus is moving away from monocrystalline technology, the prices of alternative technologies need to decrease significantly before they can be widely adopted.[24]

Table 1.1: The advantages and drawbacks of different types of photovoltaic devices. Adapted from reference 21.

Types of solar cells	Highest conversion efficiency (%)	Advantages	Disadvantages
Monocrystalline silicon	24.7 ± 0.5	High efficiency and mature technology	High cost
Polysilicon	20.3 ± 0.5	High conversion efficiency and mature technology	High cost
Amorphous silicon film	14.5 ± 0.7	Simple process and low cost	Poor stability
Polysilicon film	16.6 ± 0.4	Low cost, good stability, and high conversion efficiency	The production process needs to be optimized.
Copper indium gallium selenide (CIGS) thin films	19.5 ± 0.6	Good stability, high conversion efficiency, simple process flow	Indium and selenium are relatively rare and there is a lack of material sources
Cadmium sulphide (CdS), cadmium telluride (CdTe) cells	16.5 ± 0.5	Low cost, easy mass production, high efficiency	Cadmium is highly toxic and can cause pollution

There is a high level of anticipation concerning OPV cells in the manufacturing of cost-effective solar systems. According to the National Renewable Energy Laboratory (NREL), OPV cells have shown remarkable promise in both cost-effectiveness and power conversion efficiency (PCE) improvement. In just three years, from 2017 to 2020, the PCE of OPV cells increased significantly from 11.5% to 18.2%.[25] Although OPVs currently have lower efficiency compared to silicon-based devices, they offer certain advantages and have the potential to address some of the limitations associated with inorganic photovoltaic devices (IPVs). Organic systems have the

capability to utilize solar power in an environmentally sustainable fashion at a reduced cost, as well as being lighter in weight. Additionally, organic systems offer greater flexibility compared to inorganic systems as they can be manufactured using roll-to-roll techniques, allowing for efficient large-scale production.[26]

Simple OPV cells (Fig. 1.4[27]) generate electric power through the interface between donor and acceptor materials. The process involves the separation of photo-generated excitons (electron-hole pairs) at the donor-acceptor interface. When photons are absorbed, electrons are excited from the donor's highest occupied molecular orbital (HOMO) to the acceptor's lowest unoccupied orbital (LUMO), forming charge transfer (CT) states. By lowering overlap and Coulombic electric charge interaction, this pair may dissociate into free charges or move to charge-separated (CS) state. While the hole migrates to the anode (positive electrode) via the donor material, the separated electron migrates through the acceptor layer in the direction of the cathode (negative electrode).[28] Electricity is produced as a result of the movement of charges, which creates a difference in electrical potential. However, sometimes the electrons and holes can recombine before reaching the electrodes, which reduces the efficiency of electricity generation. This is known as charge recombination (CR), which is clearly demonstrated in Figure 1.5. OPVs endeavor to elevate electron transfer efficiency through the augmentation of charge separation while concurrently mitigating instances of charge recombination. Additionally, energy losses denote the dissipation of energy, diverting it away from productive electricity generation into the realms of heat or inefficiencies within the energy conversion progression. These energy losses manifest at multiple junctures during the device's operational cycle, spanning photon absorption, exciton dissociation, charge transport, and charge collection processes. Enhanced efficiency within OPVs stems from the astute selection of materials boasting attributes conducive to proficient photon absorption and

charge generation. By judiciously engineering materials and interfaces, the dual objectives of refining charge separation and ameliorating energy losses are realized. These ways, OPVs can generate electricity more effectively compared to traditional silicon solar panels.[26, 28, 29]

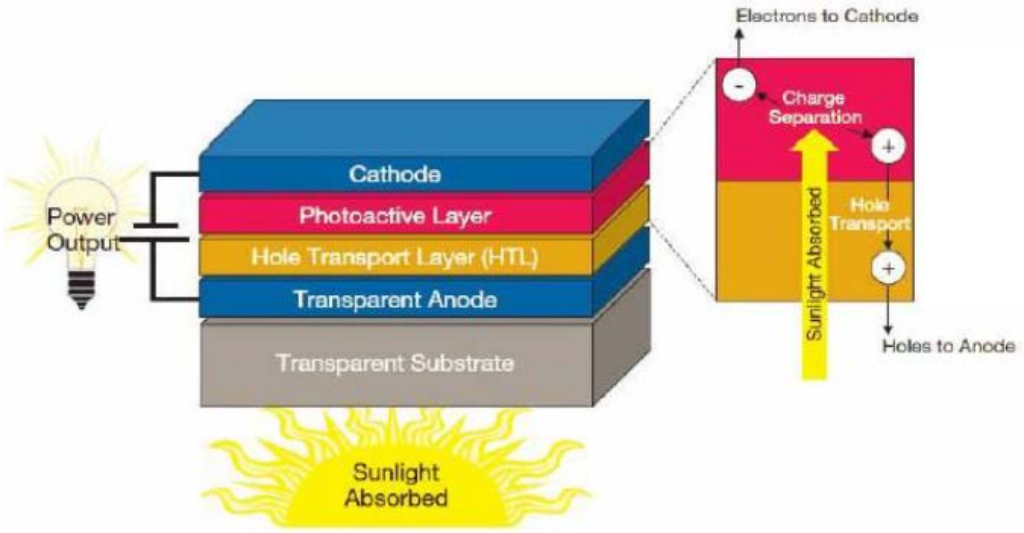

Figure 1.4: Design of an organic photovoltaic cell displaying photoactive layer. Adapted from reference 27.

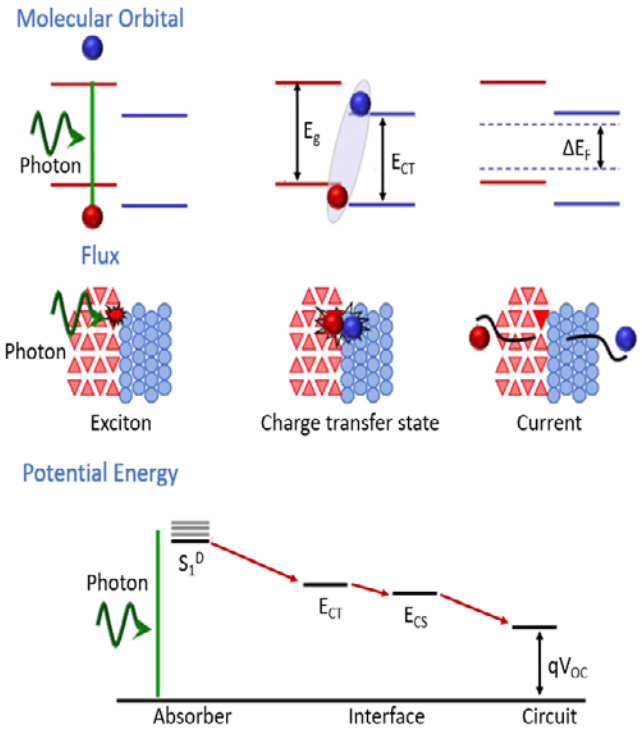

Figure 1.5: Photocurrent generation stages at an organic photovoltaic. The formation of charge begins with photon absorption and the activation of a bound exciton state (left). To create free

charges, this bound exciton must overcome coulombic attraction. With the addition of a donor-acceptor interface, the electron and hole pair may be separated through a charge-transfer state (center). This is qV_{oc} in the device at an open circuit (i.e., when the charge recombination balances the photo generation of free charge). The difference in energy between the charge-separated state (E_{CS}) and qV_{oc} in the bottom panel is due to charge recombination. In the diagram, E_g is the band-gap energy, E_{CT} is the energy of the charge-transfer state, ΔE_F is the splitting of the quasi-Fermi levels, $S_1{}^D$ is the donor's singlet energy, E_{CT} is the energy of the charge-transfer state, and E_{CS} is the energy of the charge-separated state. Adapted from reference 29.

In conclusion, the study and development of OPVs have shown significant promise in increasing the efficiency of energy transfer, electron transfer, and charge separation mechanisms for light-harvesting applications. By focusing on enhancing charge separation, reducing charge recombination, and minimizing energy waste, the performance of OPVs pave the way for more efficient and sustainable solar energy solutions. Throughout this dissertation, efforts have been dedicated to exploring and understanding the intricacies of ultrafast electron transfer and charge separation in donor-acceptor systems. These systems serve as the foundation for OPVs, which harness the power of sunlight to generate electricity. While challenges and opportunities remain in the development of ultrafast electron transfer and charge separation mechanisms in donor-acceptor systems, this desire represents a significant step forward in the quest for high-performance light-harvesting technologies. As the understanding of organic materials and nanoscale engineering continues to advance, even greater strides are anticipated in improving the efficiency and scalability of light-harvesting applications, ultimately contributing to a more environmentally friendly and sustainable energy landscape.[30]

1.6 The Jablonski Diagram: A Tool for Exploring Molecular Electronic Energy Levels

The conversion of solar energy into chemical energy is a remarkable process in both natural and artificial photosynthesis. To maximize the efficiency of this conversion and minimize energy waste, efficient energy transfer is essential as mentioned previously. Photoinduced Energy Transfer (PEnT) plays a crucial role in achieving this goal. PEnT involves the transfer of excitation

energy between two chromophores, which are light-sensitive molecules acting as the donor and acceptor. By utilizing PEnT, the system can optimize energy conversion and enhance quantum efficiency.[31]

In the antenna system in natural photosynthesis, energy transfer pathways are crucial for guiding the captured light energy towards the reaction center. Chromophores within the antenna system absorb photons, leading to their electronic excitation. When the excited chromophore returns to its ground state, the absorbed photon is released. The Jablonski diagram provides the most comprehensive depiction of the processes of photon absorption and emission in chromophores. It illustrates the energy levels and transitions involved, offering a clear understanding of the mechanisms underlying these phenomena.[32]

The Jablonski diagram is named after Alexander Jablonski, a Polish physicist who made significant contributions to the understanding of molecular spectroscopy. Figure 1.6[33] is a schematical representation of the electronic energy levels and transitions within a molecule. It provides a simplified depiction of the electronic structure and energy states of a molecule. In a typical Jablonski diagram, the ground state (S_0) of the system is shown at the bottom, and the excited states such as the first singlet excited state (S_1), the second singlet excited state (S_2), and the first triplet excited state (T_1) are represented by stacked horizontal lines above the ground state. Thicker lines indicate electronic energy levels, while thinner lines represent the vibrational states associated with each electronic energy level.[34, 35]

When a molecule is exposed to light, it absorbs energy and moves from its lowest energy state to a higher energy state. This is known as absorption and happens quickly, usually within femtoseconds. The molecule possesses the ability to become excited in two distinct states: the S_1 state, where unpaired electrons have opposite spins, and the T_1 state, where unpaired electrons

have the same spin. While in the excited state, the molecule can undergo different vibrational transitions, corresponding to various vibrational excited states, represented by 1, 2, 3, 4, and 5.[36, 37]

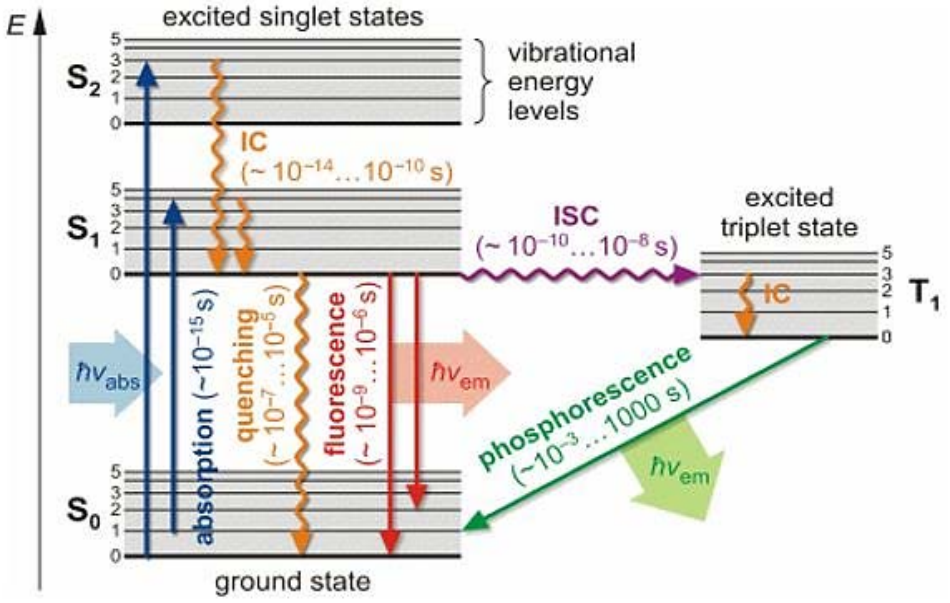

Figure 1.6: Jablonski energy diagram illustrating the electronic and vibrational energy levels and the possible radiative and non-radiative transitions of an excited molecule. Adapted from reference 33.

In the relaxation journey from an excited state to the ground state, there are different pathways and processes involved. One pathway involves photoluminescence, specifically fluorescence or phosphorescence. Fluorescence is a radiative decay process where the excited state returns to the S_0 by emitting light occurring at rates between 10^6 to 10^9 s^{-1}. On the other hand, phosphorescence is a radiative process involving the emission of photons, but it is not efficient at room temperature and is typically observed at lower temperatures due to reduced thermal energy, diminished non-radiative relaxation, and longer excited-state lifetimes. This fascinating phenomenon occurs when the T_1 relaxes back to the S_0 by emitting phosphorescence at a notably slower rate, approximately on the order of 10^{-3}-10^3 s^{-1}. Another pathway is known as vibrational

relaxation or internal conversion (IC). Here, the molecule relaxes from a higher vibrational level in the excited state to a lower vibrational level within the same electronic state. This internal conversion process happens at rates typically between 10^{10}-10^{14} s^{-1}. Another nonradiative process, called intersystem crossing (ISC), provides an alternative route for the S_1 to return to the ground state by populating T_1 state. In intersystem crossing, the S_1 state converts to the T_1. This process usually occurs at rates around 10^{8} -10^{10} s^{-1}.

Besides the deactivation pathways previously mentioned, there are additional routes for an excited system to return to its ground state, involving interactions with other molecular systems. These crucial pathways include electron transfer, where the excited system donates an electron to another molecular system or intramolecularly, resulting in changes to their electronic states and energy levels. The details of electron transfer will be explained further in the subsequent section, providing a more comprehensive understanding of this phenomenon. The second pathway is energy transfer, where energy from the excited state is transferred to neighboring molecules, leading to alterations in their energy levels. These processes play significant roles in natural phenomena like photosynthesis. Understanding and replicating electron transfer and energy transfer pathways are vital in designing synthetic systems that mimic photosynthesis, enabling efficient solar energy conversion for sustainable energy production and storage. Furthermore, these intricate pathways and processes contribute to the understanding of how excited states transition to the ground state, shedding light on the complex dynamics of molecular spectroscopy.[34, 38, 39]

1.7 Thermodynamic and Kinetic Aspects of Photoinduced Electron Transfer

Inter-and intramolecular PET is a fundamental chemical process characterized by the transfer of an electron from a donor molecule to an acceptor molecule. This electron transfer generates charge separation, a crucial phenomenon utilized in natural photosynthesis to convert

solar energy into chemical energy. The initiation of electron transfer occurs upon the absorption of photons, or light energy, leading to the excitation of electrons within the donor molecule. Subsequently, the excited electron is transferred to the acceptor molecule. The occurrence of PET enables the efficient conversion of solar energy into chemical energy, which is vital for organisms to sustain themselves through the synthesis of complex organic compounds. A comprehensive understanding of the thermodynamic and kinetic features of these processes is needed to reproduce the charge separation mechanisms shown in natural photosynthesis.[40] This understanding will allow us to optimize favorable processes that lead to the formation of long-lasting charge-separated states while minimizing unfavorable processes, such as rapid charge recombination, which result in energy loss. To effectively utilize the energy of a charge-separated state, the rate of the forward reaction (CS) must exceed that of the backward reaction (CR), providing sufficient time for subsequent processes to harness that energy. For electron transfer to take place, as shown in Figure 1.7, it is essential for the system to absorb ultraviolet-visible (UV-Vis) light to promote an electron from ground state to excited state. While this is happening, light should drive the transfer of an electron from the LUMO of the donor molecule to the LUMO of the acceptor molecule (Fig 1.7b), or from the HOMO of the donor to the singly occupied molecular orbital (SOMO) of the acceptor through an alternative electron transfer mechanism, also called hole transfer (Fig. 1.7a). As a result, the acceptor molecule is reduced to $A^{\bullet -}$ while the donor molecule is oxidized to $D^{\bullet +}$.[41] The alignment of the HOMO and LUMO orbitals, in the donor and acceptor molecules plays a crucial role in governing the charge transfer process. The careful selection of appropriate donor-acceptor systems is essential to facilitate efficient photoinduced electron transport. A number of groups studied various types of donor-acceptor architectures and have reported important insights into the dynamics and kinetics of the PET processes.

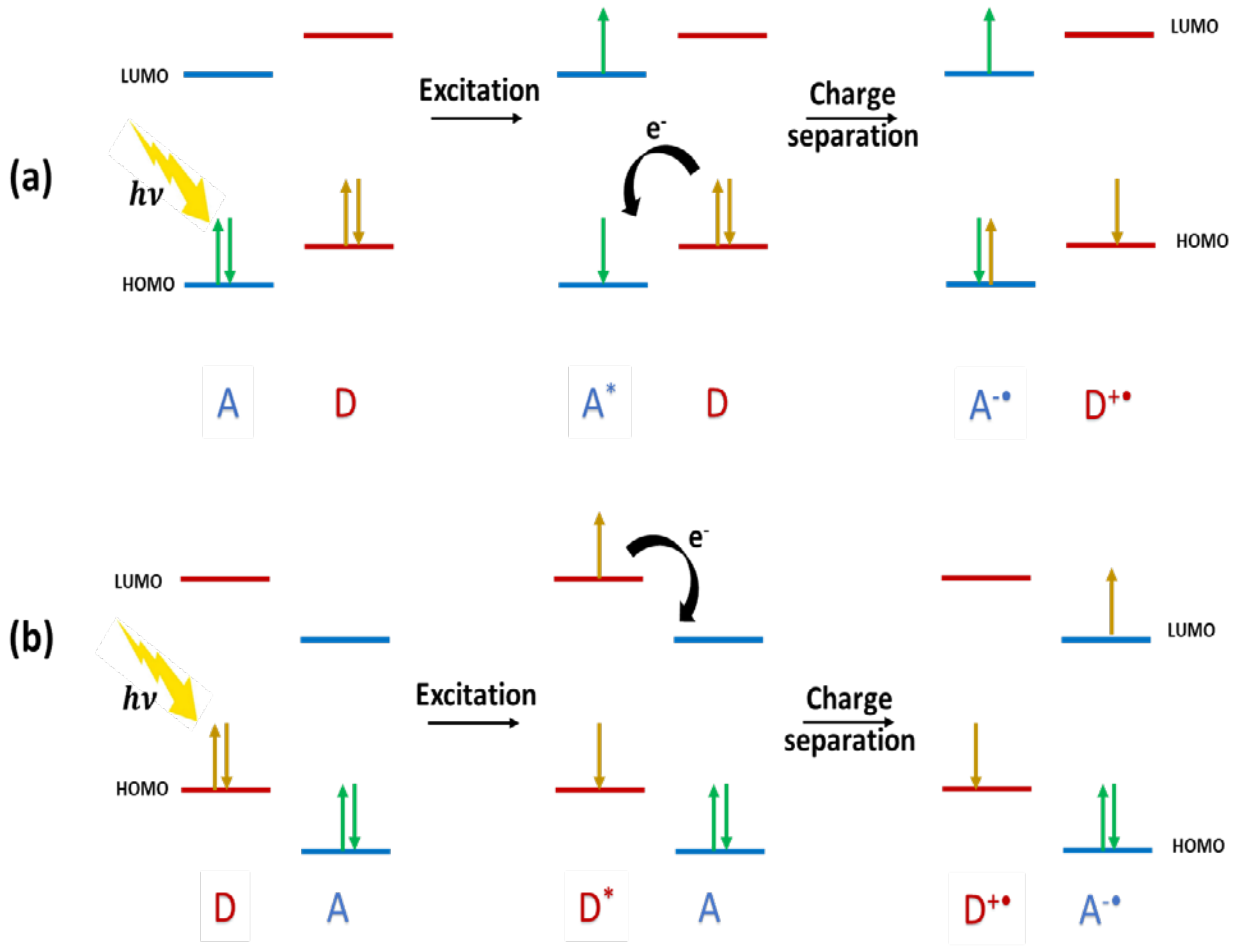

Figure 1.7: The description of photoinduced electron transfer events at a typical donor-acceptor interface (a) from D to A*and (b) D* to A molecules, as modified from references 40 and 41.

Since 1960s, researchers, including Weller and colleagues,[42] focused on understanding the driving force behind charge separation. The Rehm-Weller equation (Eq. 1.4) enables the determination of the thermodynamic driving force for electron transfer between a photoexcited donor and acceptor in a solution during PET. By quantifying the free energy requirements of the redox processes resulting from PET, this equation aids in assessing the feasibility of the process. Evaluating the free energies of charge-separated states (ΔG_{CS}) and charge recombination (ΔG_{CR}) using the lowest excitation energy and the redox potentials of both donor and acceptor molecules allows the feasibility of PET to be determined.[43, 44]

$$-\Delta G_{CS} = \Delta E_{0-0} - (-\Delta G_{CR}) \quad \text{Eq. 1.4}$$

$$-\Delta G_{CR} = (E_{ox} - E_{rd}) + \Delta G_s \quad \text{Eq. 1.5}$$

In the given equations, the symbol $\Delta E_{0\text{-}0}$ represents the energy of the lowest excited singlet state, while E_{ox} and E_{rd} denote the first half-oxidation and reduction potentials of the electron donor and acceptor, respectively. On the other hand, the term ΔG_S refers to the static energy or stability energy, which can be determined using the dielectric continuum model, called implicit solvation, and is expressed in equation form.[45] The dielectric continuum model aids in evaluating the stability and static energy associated with the system under consideration.

$$-\Delta G_S = -\frac{e^2}{4\pi\varepsilon_0}\left[\left(\frac{1}{2R_+} + \frac{1}{2R_-} - \frac{1}{R_{D-A}}\right)\right]\frac{1}{\varepsilon_s} - \left(\frac{1}{2R_+} + \frac{1}{2R_-}\right)\frac{1}{\varepsilon_R} \quad \text{Eq. 1.6}$$

Within the parameters of this equation, ($R_{D\text{-}A}$) represents the center-to-center distance between the electron donor and electron acceptor. The symbol (e) denotes the elementary charge, while (ε_0) refers to the permittivity of vacuum. (R_+ and R_-) represent the radii of the radical cation and anion, respectively. Additionally, (ε_S and ε_R) represent the dielectric constants of the solvents employed for photophysical investigations and redox potential measurements, respectively. These variables are essential for determining the physical and electrochemical features of the investigated system.

The Marcus Theory is frequently utilized to elucidate the mechanism of electron transfer (ET). To establish a deeper understanding of the relationship between reaction kinetics and thermodynamics, Marcus conducted further research focusing on parameters such as reorganization energy (λ) and the free energy of activation ($\Delta G^{\ddagger}$). By comparing the energy distributions of the donor and acceptor, Marcus made several noteworthy observations. It was observed that the rate of electron transfer (k_{ET}) increases as the driving force for the reaction (ΔG^0) increases. As depicted in Figure 1.7, $\Delta G^{\ddagger}$ the electron transport barrier decreases with increasing

exothermicity of the process, reaching a point in Figure 1.8(3) where there is no barrier for the reaction to proceed. This occurs when the potential energy curve of the product intersects with the minimum of the reactant curve. Subsequently, the reaction barrier increases as the exothermicity of the reaction continues to rise. Marcus categorized the regions along the curve where the rate of electron transfer either rises or drops with increasing driving force as the "normal region" and the "inverted region," respectively (Fig. 1.7(a)).[45]

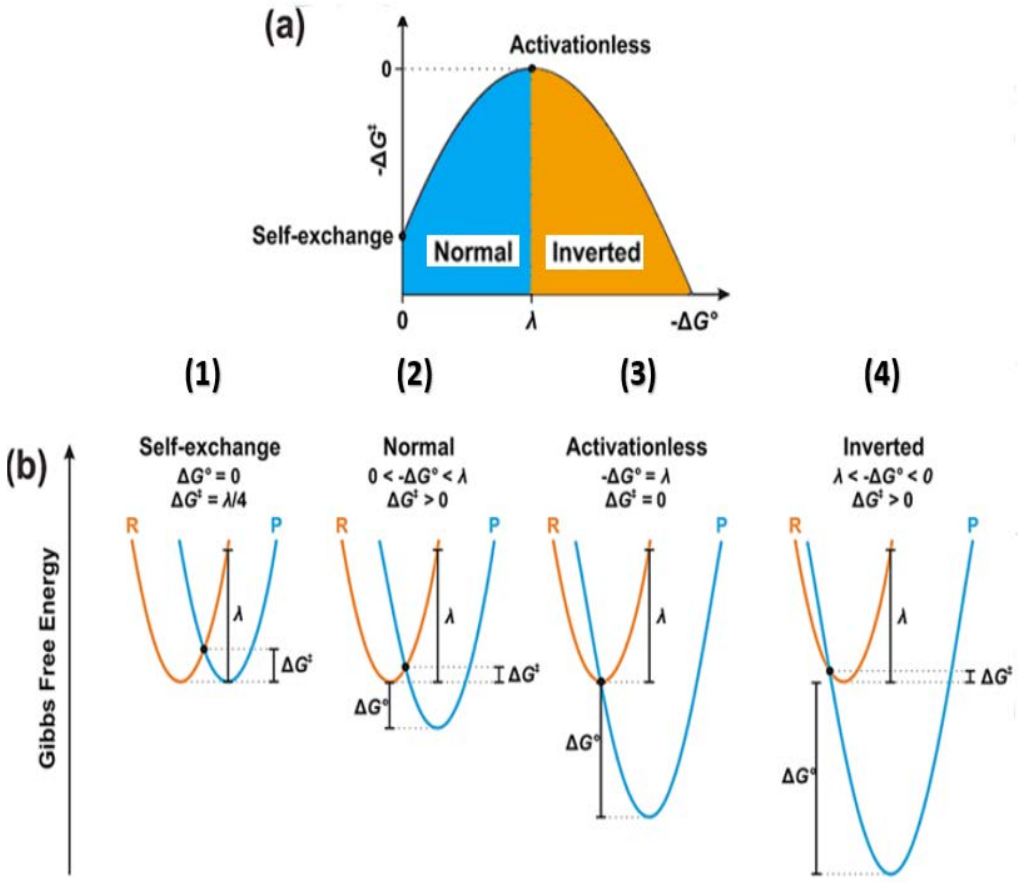

Figure 1.8: **The Marcus curves depicting the normal and inverted regions in electron transfer (top). The curves highlight the relationship between Gibbs free energy change and reorganization energy, enabling differentiation between the two regions in Marcus's theory of electron transfer (bottom). Modified from reference 45.**

Through the analysis of the geometric properties of parabolic curves representing the energies of the reactant and product, Marcus derived Eq. 1.7. This equation establishes a relationship between $\Delta G^{\ddagger}$ and the λ. It provides insights into how the thermodynamics of electron transfer is linked to electron transport in the outer sphere, where the λ accounts for the combined contributions of solvation energy (λ_i) and vibrational energy (λ_0) in the electron transfer process, represented as $\lambda = \lambda_i + \lambda_0$. In the case of an isoenergetic process (where $\Delta G^0 = 0$), the formula yields $\Delta G^{\ddagger} = \frac{\lambda}{4}$. This equation is a useful tool for determining the reorganization energy (λ).

$$\Delta G^{\ddagger} = \frac{\lambda}{4} \left(1 + \frac{\Delta G^0}{\lambda}\right)^2 \qquad \text{Eq. 1.7}$$

Marcus employed the Arrhenius principle to establish a connection between the k_{ET} and the $\Delta G^{\ddagger}$ in Eq. 1.8. The frequency factor (A_{ET}) represents the activation-less rate constant when $\Delta G^{\ddagger}$ approaches zero (or T approaches zero), signifying the frequency of effective associations at an infinitely high temperature. This frequency, $A_{ET}(r)$, can be related to the unit of collision frequency (Z) and the transmission coefficient κ(r), which represents the probability of electron transfer occurring once the reactant association complex reaches the transition state. This relationship is given by the equation $A_{ET}(r) = Z\kappa(r)$, where $\kappa(r) = \kappa_o e^{-\beta r}$, with κ_o being the transmission coefficient at r = 0 and β representing a constant related to the reorganization energy and temperature.

$$k_{ET} = A_{ET} e^{-\Delta G\ddagger/RT} \qquad \text{Eq. 1.8}$$

Eq. 1.9 derived from transition state theory, after substituting the values for the frequency factor (A), is as follows:[46]

$$k_{ET} = \frac{k_B T}{h} e^{-\frac{-(\Delta G^0 + \lambda_i)^2}{4\lambda_i k_B T}} \qquad \text{Eq. 1.9}$$

In this equation, k represents the rate constant, k_B is the Boltzmann constant (approximately 1.38 x 10^{-23} $J \cdot K^{-1}$), T is the temperature in Kelvin, and h is Planck's constant (approximately 6.626 x 10^{-34} $J \cdot s$). By plugging in the known values for these variables and solving for the rate constant, valuable insights into kinetics and temperature dependence of the electron transfer process can be acquired. This equation allows researchers to understand how the rate of the process changes with temperature and the efficiency of electron transfer.

In summary, the alignment of HOMO and LUMO orbitals and the application of theoretical frameworks like the Rehm-Weller method and the Marcus theory are instrumental in understanding and optimizing photoinduced electron transport processes. These approaches offer valuable tools for designing and evaluating donor-acceptor systems with the potential for efficient charge transfer, which is essential for various applications in chemistry, physics, and materials science.[46, 47]

1.8 Unraveling the Mechanisms of Charge Transfer in Donor-Acceptor Systems: A Focus on the differences Between Intermolecular and Intramolecular Processes

The investigation of intermolecular and intramolecular charge transfer processes has been a central focus in the fields of chemistry and biochemistry. Intermolecular charge transfer involves the interaction between an excited molecule and a neighboring molecule, where one molecule serves as the electron donor and the other as the electron acceptor. This phenomenon occurs when the donor and acceptor molecules are significantly separated in their ground state, leading to the migration of excitons (electron-hole pairs) towards the interface, where the charge transfer event takes place. The modulation of charge transfer rates in donor-acceptor systems is governed by a complex interplay of various factors. One of the key considerations is the alignment of energy levels between the donor and acceptor molecules. For charge transfer to occur efficiently, there needs to be a suitable energy level match between HOMO and LUMO. Additionally, the polarity

of the solvent in which these molecules are immersed can significantly impact the rate of charge transfer. Solvent polarity influences the environment around the molecules and can either facilitate or hinder the process. Another critical aspect to consider is the electronic architecture of the donor molecule itself. The arrangement of electrons within the donor molecule and its electronic structure play a pivotal role in determining how readily it can donate electrons to the acceptor molecule. Beyond these factors, the intricacies of charge transfer at the interface are further influenced by electrostatic interactions and electronic coupling between the donor and acceptor molecules. These interactions can either promote or hinder charge transfer, depending on their strength and orientation.

Intramolecular charge transfer (ICT) is observed when the donor and acceptor moieties are linked covalently, as seen in various small molecules. This linkage induces a significant redistribution of charge within the excited molecule, resulting in a substantial excited state dipole moment. Additionally, ICT is evident in conjugated systems, including oligomers or polymers, distinguished by alternating single and multiple bonds, where π-orbital bonding plays a crucial role in their electronic structure. Further elaboration on the concept of intramolecular charge transfer in (D-π-A) systems, which stand for Donor-π-Bridge-Acceptor system, will be provided in subsequent sections of this dissertation. In these (D-π-A) systems, charge delocalization occurs over the participating π-bonds, leading to a decrease in the molecule's energy and an increase in overall stability.

The efficiency of ICT is influenced by various factors, including the nature of the donor and acceptor moieties. Parameters such as energy band alignment and twisting angles between moieties significantly shape the charge transfer process. Additionally, solvent properties, such as polarity, viscosity, and hydrogen bonding capability, impact the efficiency of ICT. Furthermore,

the extent of the π-system, which determines the distance of charge transfer, also plays a critical role in the overall charge transfer efficiency in these systems. [48, 49]

A crucial aspect in understanding and optimizing intramolecular charge transfer is to decipher the mechanism of charge hopping or transfer through π-conjugated spacers within donor-bridge-acceptor (D-π-A) molecular assemblies. This area of investigation remains a subject of active debate in the scientific community, as it holds the key to unlocking the full potential of ICT-based applications in various fields of chemistry and biochemistry. [50, 51]

1.9 Design and Engineering of Current Photosynthetic Supramolecular Systems

In the pursuit of sustainable and renewable energy sources, artificial photosynthetic systems have gained significant attention as promising platforms for converting solar energy into usable forms. These intricate systems rely on the strategic integration of photo and redox active chromophores, which are responsible for light-harvesting and reaction center functionalities, inspired by the remarkable efficiency of natural photosynthesis. By mimicking the functions of their natural counterparts, these commonly used chromophores form the foundation for designing photosystems engineered to efficiently capture and convert solar energy. Among various photoinduced energy and electron transfer processes, certain families of chromophores as shown in Figure 1.9, including chelated Boron dipyrromethene (BODIPY), chelated azadipyromethene (AzaBODIPY), naphthalocyanines, porphyrins, phenothiazine, phthalocyanines, and triphenlamine (TPA),[52] have emerged as key players, excelling as light-harvesting and primary electron donor units. Complementing their roles, electron acceptors like fullerene, 1,2,4,5-tetracyanobenzene (TCNB), tetracyanoethylene (TCNE), and Tetracyanoquinodimethane (TCNQ)[53] exhibit exceptional capabilities in capturing and facilitating electron transport within the system, culminating in the successful completion of photoinduced energy and electron transfer

processes. In the subsequent sections, this dissertation undertakes a literature review of artificial photosynthetic systems, with a particular focus on those closely related to the systems studied herein.[54, 55]

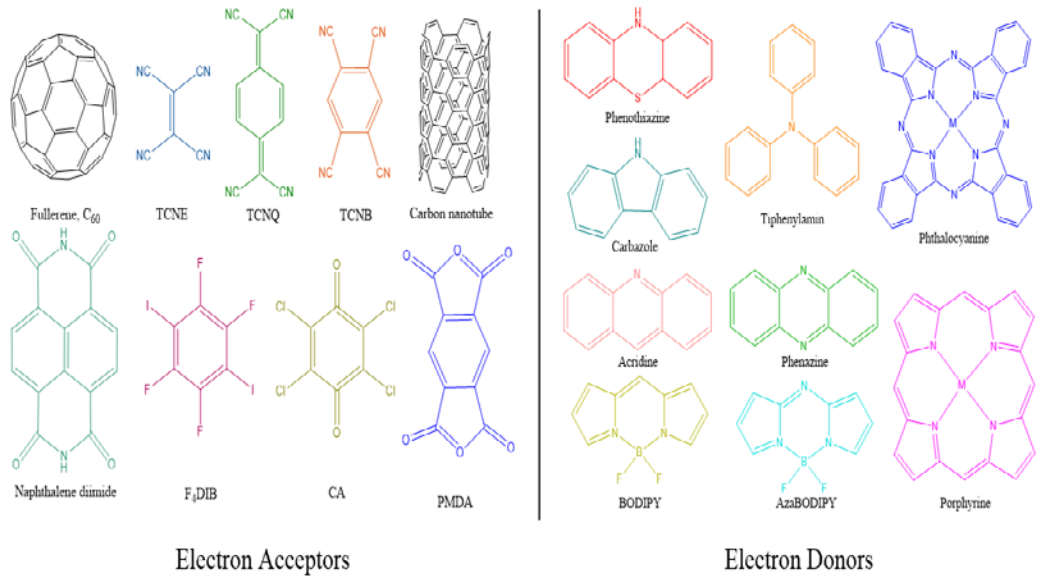

Figure 1.9: The most common electron donor and acceptor units used in organic electronic materials.

1.9.1 AzaBODIPY -based Push-Pull Derivatives

Aza-BODIPY derivatives, also known as ADP, have garnered significant attention in the scientific community due to their remarkable light absorption capabilities and versatility as chromophores, stemming from their unique molecular architecture. The nomenclature is derived from the substitution of the meso methene moiety in BOron DI-PYromethene with a nitrogen atom at eight positions (Fig. 1.10). Although the original synthesis of these derivatives was documented in 1993,[56] precursor versions without the BF_2 unit were already known as early as 1944.[57] However, it was the introduction of the BF_2-chelated tetraarylazadipyrromethene version by O'Shea et al. in 2002 that reignited interest in Aza-BODIPY dyes, primarily attributed to their enhanced fluorescence properties and potential applications in photodynamic therapy.[58]

These dyes exhibit a remarkable absorption range from visible to near-infrared with high

extinction coefficients ($7-8 \times 10^5\ M^{-1}\ cm^{-1}$), indicating their efficient light absorption capabilities. Additionally, Aza-BODIPY derivatives demonstrate noteworthy fluorescence quantum yields (> 0.42), making them highly effective at emitting light upon excitation. The narrow HOMO−LUMO gaps further facilitate facile light absorption and electronic transitions. Moreover, their exceptional solubility in various organic solvents, minimal sensitivity to solvent polarity, and negligible blue shift (6-9 nm) in absorption spectra during the transition from nonpolar to polar solvents significantly enhance their adaptability for diverse applications.[59-61]

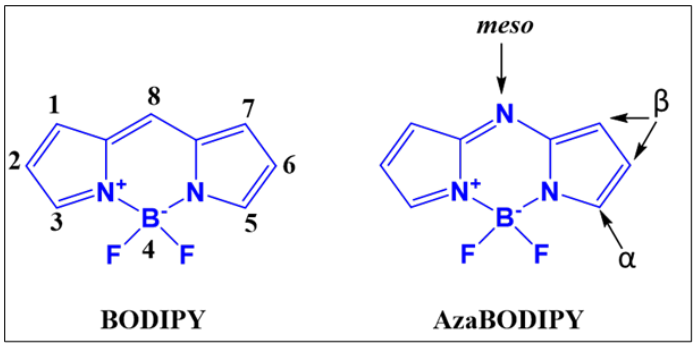

Figure 1.10: The structures of basic BODIPY and aza-BODIPY with their respective IUPAC numbering and typical notations.

Aza-BODIPY derivatives have become a focal point in chromophore research due to their photochemical and photophysical properties. This has led to the development of various synthetic approaches to create both symmetrical and unsymmetrical molecular configurations of these derivatives. Their versatility has opened up numerous scientific and technological possibilities, significantly advancing chromophore research. The dissertation primarily concentrates on exploring photosynthetic donor-acceptor systems utilizing ADP as acceptor. The main aim is to comprehend their crucial role in facilitating rapid photoinduced energy and electron transfer processes. To support this investigation, a thorough review of literature on donor-acceptor systems involving ADP is presented in the following section, providing valuable insights and establishing a strong foundation for the application of these compounds in state-of-the-art research concerning

electron transfer phenomena.

D'Souza and his colleagues aimed to replicate the energy and electron transfer mechanisms observed in natural photosynthesis. To achieve this, they employed a supramolecular triad, comprising three distinct molecules as illustrated in Figure 1.11. The triad consisted of an azaBODIPY unit, which acted as a fluorescent dye, a zinc porphyrin (ZnP) entity that functioned as a light-absorbing molecule, and fullerenes (C_{60}) as three-dimensional electron acceptors capable of receiving electrons. To enhance the interaction between the zinc porphyrin and fullerenes, the C_{60} molecules were chemically modified with two pyridine moieties, allowing them to coordinate with both zinc porphyrins in the host system. An effective energy transfer process from the singlet excited state of the zinc porphyrin ($^1ZnP^*$) to the singlet excited state of ADP was observed. This was evident from the spectral overlap between the emission of zinc porphyrin at wavelengths of 610 and 660 nm and the absorption of ADP at 680 nm.

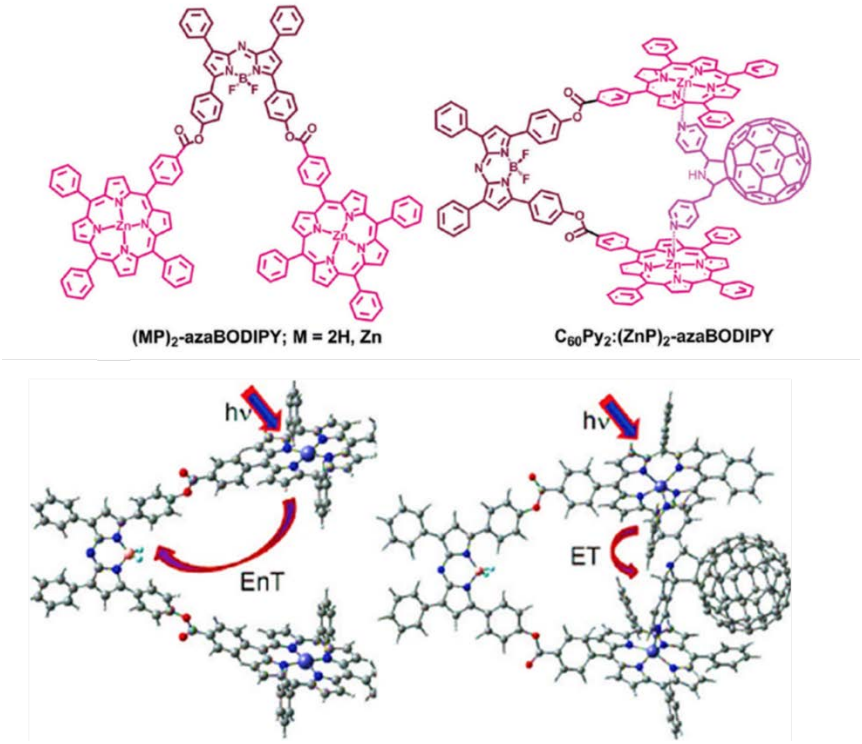

Figure 1.11: **Structure of triads and supramolecular tetrad. Adapted from reference 62.**

During the titration process of $(MP)_2$-azaBODIPY conducted in o-dichlorobenzene (DCB), a study aimed to investigate the formation of a supramolecular tetrad, with specific attention given to the complex $(ZnP)_2$-ADP:$C_{60}Py_2$ by adding $C_{60}Py_2$. The primary objective was to examine the absorption spectra of ZnP during the absorption titration. The results indicated a red shift and decreased intensity in the absorption spectra of ZnP, suggesting the presence of axial coordination. Axial coordination refers to interactions or bonding that occur parallel to the molecular axis, leading to changes in the electronic properties of ZnP, resulting in the spectral red shift and reduced intensity. On the other hand, the absorption band at 667 nm corresponding to ADP remained unchanged throughout the titration, indicating that ADP was not involved in the metal-ligand axial coordination. Therefore, ADP did not contribute to the observed spectral changes in ZnP or participate in the formation of the supramolecular tetrad complex $(ZnP)_2$-ADP:$C_{60}Py_2$. Furthermore, fluorescence experiments revealed that the addition of $C_{60}Py_2$ resulted in a reduction in ZnP fluorescence, consistent with the occurrence of excited state events originating from a single ZnP^*.

Femtosecond transient absorption spectroscopy was employed in toluene to investigate the fluorescence quenching mechanism. Selective excitation of the ZnP moiety in ZnP_2-ADP:$C_{60}Py_2$ at 420 nm resulted in the immediate generation of a ZnP^* with a distinct peak at 458 nm. The subsequent disappearance of this peak was succeeded by the appearance of two distinct peaks at 620 nm and 1000 nm, corresponding to the one-electron oxidized and reduced forms of ($ZnP^{\bullet+}$) and ($C_{60}^{\bullet-}$), respectively. These results offered further evidence for a photoinduced electron transfer pathway in the supramolecular system. By monitoring the time profiles of $ZnP^{\bullet+}$ or $C_{60}^{\bullet-}$ radicals, the kinetics of electron transfer were analyzed, revealing a sluggish charge recombination rate (k_{CR} = $1.8x10^8$ s^{-1}) compared to the rapid charge separation rate (k_{CS} = $6.2x10^{10}$ s^{-1}). The final charge-

separated state, denoted as $C_{60}Py_2^{\bullet-}$:$ZnP_2^{\bullet+}$-ADP, exhibited a lifetime of approximately 5.5 nanoseconds.[62] Subsequently, Energy transfer from the excited ZnP to the azaBODIPY unit was witnessed, and, under specific conditions, electron transfer from photoexcited zinc porphyrin to C_{60} was also observed. With an incident photon-to-current conversion efficiency of up to 17% achieved by the tetrad modified electrode, valuable insights into the energy and electron transfer mechanisms within these supramolecular polyads and their potential applications in converting light energy are provided by this study.

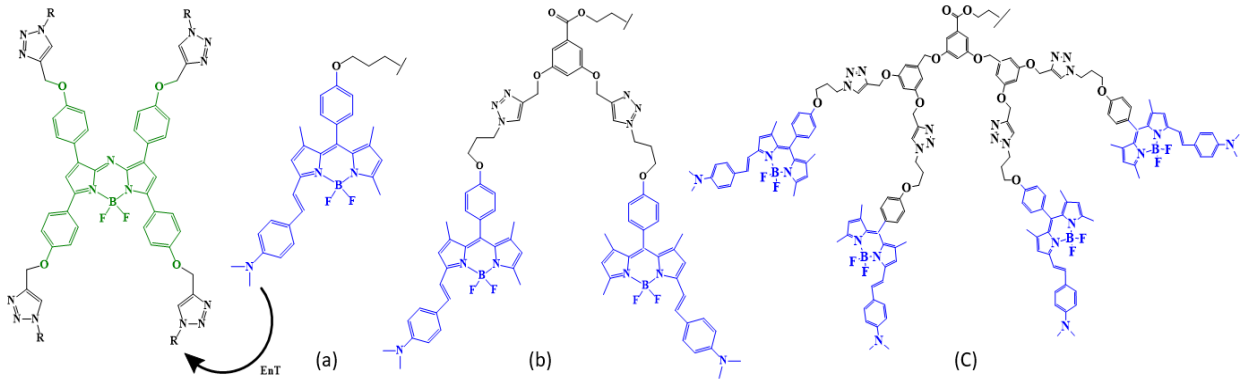

Figure 1.12: **Structure of dendritic azaBODIPY base systems. Adapted from reference 63.**

In another study, Li et al. conducted a study where they designed and synthesized a series of dendritic systems (a-c) comprising peripheral monostyryl BODIPY units that are connected to a central azaBODIPY core (Fig. 1.12). The objective was to investigate the transfer of absorbed energy from the peripheral monostyryl BODIPY units to the azaBODIPY core within these compounds. The light-harvesting efficiency of these dendritic systems was remarkably high, exceeding 90%. Furthermore, they observed that this efficiency increased as the number of monostyryl BODIPY units in the system increased. This implies that the more peripheral monostyryl BODIPY units there were, the better the energy transfer performance of the system. The excellent energy transfer efficiency was predominantly attributed to a significant spectral overlap between the fluorescence emission of the monostyryl BODIPY moieties and the Q-band

absorption of the azaBODIPY unit. This favorable spectral match facilitated efficient energy transfer from the periphery to the core, resulting in the observed high light-harvesting efficiency of the dendritic systems.[63]

In summary, Li et al. successfully designed and characterized a series of dendritic systems that exhibit high light-harvesting efficiency. The efficient energy transfer within these dendritic structures is primarily attributed to the favorable spectral overlap between the peripheral monostyryl BODIPY units and the azaBODIPY core, enabling effective funneling of energy towards the central core. This research holds significant potential for various applications that rely on efficient light-harvesting systems, such as solar energy conversion and photochemical processes.

1.9.2 Triphenylamine -based Push-Pull Derivatives

Triphenylamines, commonly referred to as TPAs, are tertiary amines characterized by the replacement of all three hydrogen atoms in ammonia with aryl groups. These organic nitrogen compounds and their derivatives play a crucial role in the production of a diverse range of fluorescent and optoelectronic materials. The formation of stable aminium radical cations is the primary reason for their practical utility.[64] TPAs exhibit favorable charge transport properties in different spectroscopic, electrochemical, and photophysical applications, owing to their high drift mobility. TPA moieties possess unique nonplanar propeller-like structures and structural flexibility, which make them ideal for producing fluorescent compounds that can be easily modified for emission and mechanofluorochromic properties. These modifications involve C-N vibrations and phenyl torsions. Moreover, TPAs are well-regarded for their high electron-donating capacity, excellent thermal stability, and remarkable processability. As a result, they are highly suitable for various applications, such as organic light-emitting diodes (OLEDs), dye-sensitized

solar cells (DSSCs), organic field-effect transistors, and other electrochromic systems.[65]

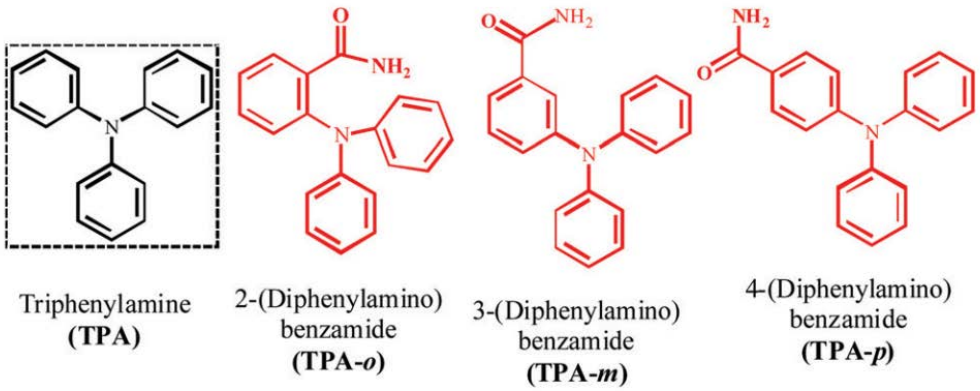

Figure 1.13: Structural variants of triphenylamine (TPA) cores and derivatives with amido-substitution at ortho-, meta-, or para-positions on one phenyl arm. Adapted from reference 65.

Over the years, various methods have been developed since 1903 for synthesizing triphenylamine-type molecules, resulting in economically viable forms of TPAs. Particularly intriguing are the oligomeric and dendrimeric structures of TPAs, resembling stars, as potential photo- and electro-active materials. By substituting the cores of TPA molecules with different electron acceptor groups, bioimaging agents, solvatochromic probes, interesting aggregation-induced emission (AIE) luminogens, and fluorescent chemosensors can be produced in certain conditions.[66] Researchers Yang and Ma conducted an investigation into the photophysical behavior of donor-acceptor substituted molecules using triphenylamine (TPA) as the electron donor. Through their studies, they revealed that these molecules could possess initial excited states in the form of locally excited states (LE), charge transfer states (CT), or hybridized local and charge transfer states (HLCT). In a separate study, Mandare et al. comprehensively explored fluorescence labeling applications involving TPAs, with a specific focus on the para-substituted derivatives known as TPA-p. TPA-p has garnered considerable attention as the preferred choice among various positionally substituted variants due to its distinct advantage in efficiently emitting light. This superior fluorescence quantum yield exhibited by TPA-p, when compared to other

derivatives, makes it highly desirable for fluorescence-based labeling techniques. As a result, TPA-p emerges as a promising candidate for achieving enhanced fluorescence performance and sensitivity in a diverse range of labeling applications, contributing significantly to its prominent position within the field of fluorescence research and technology.[65-68]

The given statement underscores the significant potential of triphenylamine and its derivatives as promising candidates for technological and scientific advancements in optoelectronics, photonics, and organic photovoltaics. Julio et al. developed two distinct sets of electron donors and acceptors, shown in Figure 1.14. The electron acceptor employed was [5,6]-pyrrolidine-I_h-$Sc_3N@C_{80}$, while the electron donor utilized was TPA. Moreover, analogous versions of these donors and acceptors based on C_{60} were synthesized to facilitate comparative analysis.

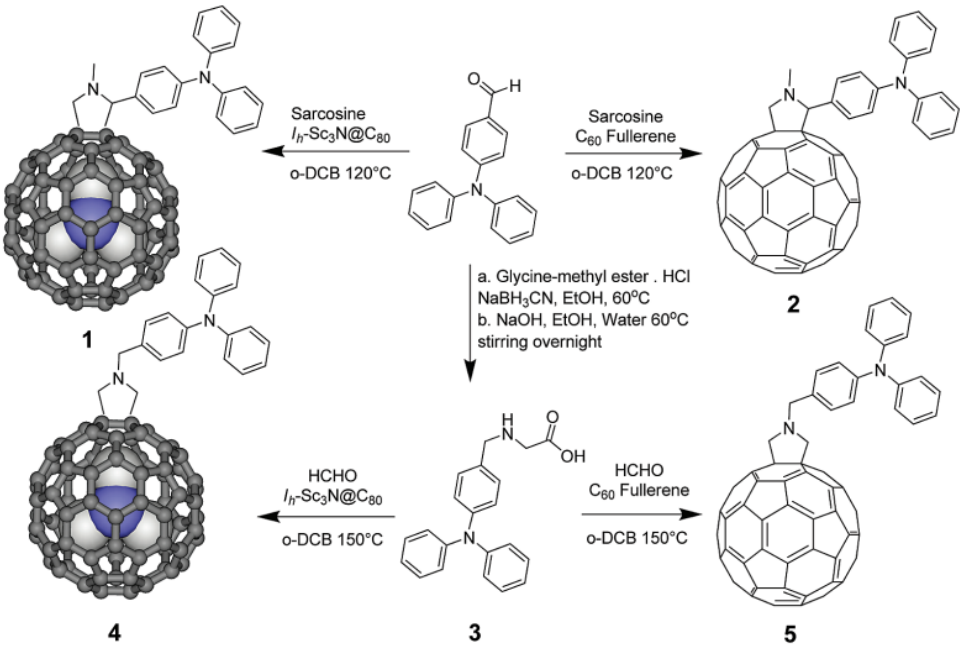

Figure 1.14: **Synthesis of triphenylaminofulleropyrrolidine system. Adapted from reference 69.**

The primary objectives of this research encompassed the examination of the influence of the donor's linkage position (N-substituted versus 2-substituted pyrrolidine) on the photoinduced

charge-separated states generation, the assessment of the thermal stability of the conjugates under elevated temperatures with respect to the retro-cycloaddition reaction, and the investigation of the consequences resulting from the replacement of C_{60} with I_h-$Sc_3N@C_{80}$ as the electron acceptor. The findings of the study demonstrated that when the donor was attached to the pyrrolidine nitrogen atom, the resulting dyad exhibited significantly enhanced stability of radical pairs in comparison to the corresponding 2-substituted isomer. This effect was consistently observed regardless of whether the electron acceptor used was C_{60} or I_h-$Sc_3N@C_{80}$. Moreover, the N-substituted TPA-I_h-$Sc_3N@C_{80}$ dyad displayed notably superior thermal stability at elevated temperatures compared to its 2-substituted counterpart. Furthermore, the dyads involving I_h-$Sc_3N@C_{80}$ as the acceptor exhibited substantially prolonged lifetimes of charge-separated states and lower first reduction potentials when compared to their C_{60} counterparts. These findings provide compelling evidence supporting the suitability of I_h-$Sc_3N@C_{80}$ as an effective acceptor for the construction of donor-acceptor conjugates.

The implications of these results are highly significant for the prospective utilization of I_h-$Sc_3N@C_{80}$ dyads as potential materials in the fabrication of plastic organic solar cells. The successful realization of these donor-acceptor conjugates and the comprehensive comprehension of their intrinsic attributes open up novel avenues to enhance their efficacy in various electronic and photonic applications. Particularly noteworthy is the enhanced thermal stability and augmented charge separation efficiency observed in the N-substituted TPA-I_h-$Sc_3N@C_{80}$ pair, which indicates the conceivable enhancement of stability and efficiency in organic solar cell technology. Furthermore, the comparative superiority of I_h-$Sc_3N@C_{80}$ over C_{60} as an electron acceptor imparts invaluable insights into the judicious design of fullerene-based donor-acceptor systems, thus facilitating the advancement of more proficient and enduring solar devices.[69]

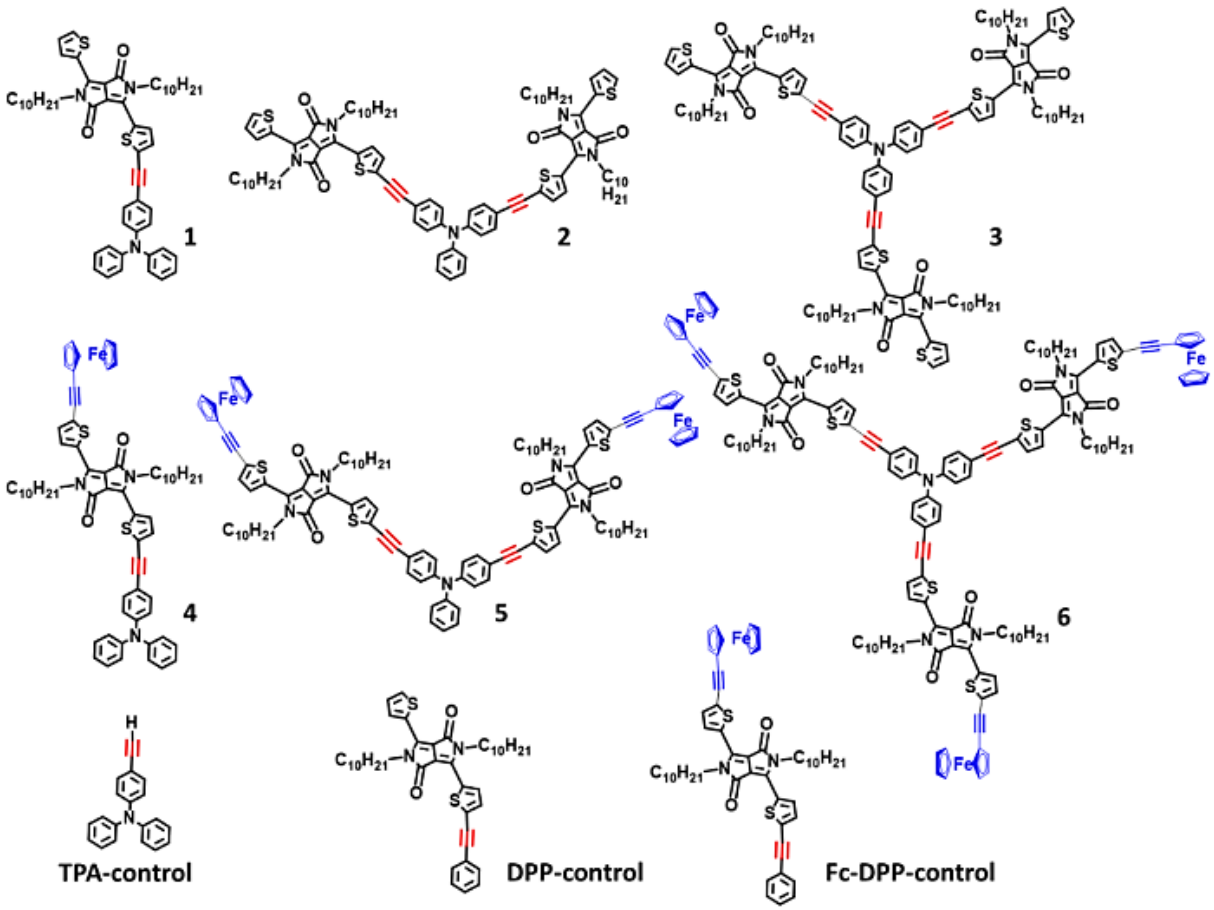

Figure 1.15: Structural representation of all the push–pull triphenylamine dyes. Modified from reference 70.

In another study, D'Souza et.al investigated star-shaped molecular systems comprising multiple donor-acceptor entities surrounding a central electron donor, triphenylamine (TPA), specifically TPA-DPP-Fc, TPA-(DPP-Fc)$_2$, and TPA-(DPP-Fc)$_3$. To synthesize these systems, the researchers employed Pd-catalyzed Sonogashira cross-coupling reactions, resulting in symmetric and asymmetric donor-acceptor conjugates with up to three ferrocenyl (Fc)-diketopyrrolopyrrole (DPP) entities linked to the central TPA electron donor. TPA was chosen for its ability to facilitate intramolecular interactions, leading to distinguishable rate constants of charge separation and recombination, and an extension of the π-conjugation, resulting in red-shifted optical properties. Additionally, the inclusion of thiophene-DPP, which forms covalent bonds with small organic

molecules, allowed for effective light absorption in the visible spectrum. The donor-acceptor complexes substituted with 1,1,4,4-tetracyanobuta-1,3-diene (TCBD, an electron acceptor) displayed broad absorption and strong intramolecular charge transfer (ICT) transitions, making them appealing for optoelectronic applications. Comparative analysis showed red-shifted absorbance in the DPP and Fc-DPP conjugates when compared to their respective control compounds, suggesting the presence of ground-state interactions.

The quantitative reduction of DPP fluorescence in 1–3 were ranged from 60% to 73%, indicating the presence of a small number of excited state events. Electrochemical studies were conducted on Fc-DPP-TPA-based systems (4-6) with additional ferrocene units, resulting in a decrease in oxidation potential. Interestingly, the charge-separated state $Fc^{\bullet+}$-$DPP^{\bullet-}$-TPA exhibited prolonged stability with an increased number of Fc-DPP entities in regions 4-6 compared to both the Fc-DPP-control and simple DPP-derived donor-acceptor systems mentioned in the literature. These states were found to exhibit an energy hierarchy, with TPA-DPP-Fc > TPA-$(DPP\text{-}Fc)_2$ > TPA-$(DPP\text{-}Fc)_3$. Moreover, the study observed that the charge recombination process in the star shaped TPA derivatives was slightly slower than anticipated. These significant findings shed light on the intriguing behavior and stability of charge-separated states within the investigated TPA donor-acceptor conjugates.[70]

1.9.3 Phenothiazines and their Sulfone based Push-Pull Derivatives

In 1883, the chemical compound phenothiazine (PTZ) was first synthesized by Bernthsen through a reaction between diphenylamine and sulfur. Since its discovery, PTZ has been extensively studied in the field of dye chemistry.[71] However, in the last two decades, its applications have extended to various other fields, leading to increased research on PTZ and its derivatives. Scientists have developed diverse synthetic methodologies to synthesize cost-effective

phenothiazine (PTZ) functionalized materials using inexpensive precursors. PTZ exhibits a distinctive butterfly or bent-type non-planar conformation, which is pivotal for its optoelectronic application. This feature impedes the formation of ground state aggregates and excimers, i.e., molecular arrangements in their lowest energy state and excited-state dimers, respectively. In DSSCs and similar devices, the non-planar structure of PTZ mitigates charge recombination, resulting in heightened device efficiency and more effective photovoltaic conversion of light into electrical energy.[72-74]

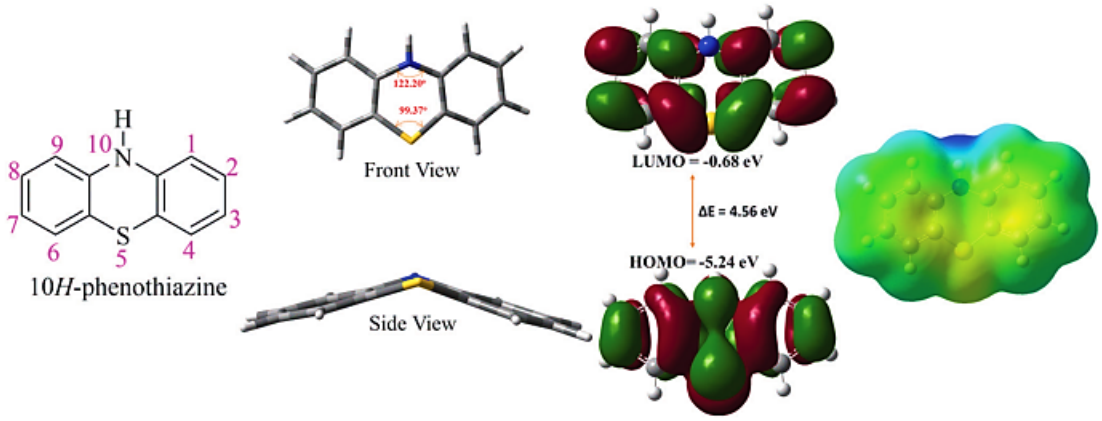

Figure 1.16: Chemical structure, DFT optimized views, energy levels, and ESP map of phenothiazine (PTZ). Adapted from reference 77.

The symmetrical nonplanar structure of PDO (presumably phenothiazine dioxides) undergoes a transformation from a donor-acceptor-donor (D-A-D) to a donor-acceptor-acceptor (D-A-A) of PDO configuration by replacing the electron-donating sulfur atom with an electron-withdrawing sulfone group (PTZ to PDO).[75, 76] This substitution enhances the charge affinity of the core unit. The improved intrinsic charge carrier transport properties observed in the D-A-D structure can be rationalized by the reduction in energy of the HOMO, as proposed by the molecular orbital hybridization theory.[76] A comprehensive and systematic investigation has been carried out to explore the effects of the sulfone group and various N-substituent groups on the material characteristics and photovoltaic performance. The resulting PDO-based systems

demonstrate outstanding attributes, including high hole mobility, favorable conductivity, and appropriate HOMO and LUMO energy levels, establishing them as highly promising candidates for photovoltaic applications.[77]

Ding et al. investigated the impact of N-substitution and sulfur atom oxidation on two systems called PDO1 and PDO2, which is shown in Figure 1.17, focusing on their molecular configuration and photovoltaic performance. By introducing a sulfuryl group to the central building block, they were able to control the energy levels of the HOMO and the electron density in these systems. This modification led to significant improvements in the photovoltaic performance of PDO1 and PDO2 compared to the previously studied PTZ system.

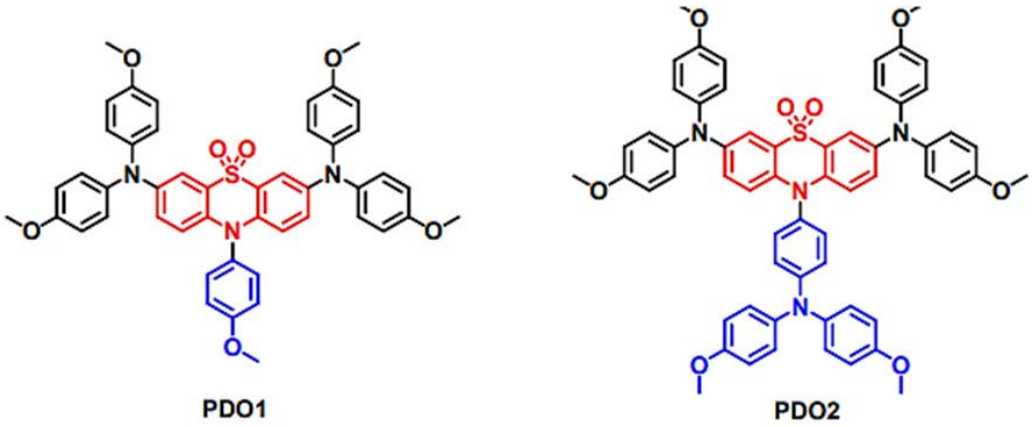

Figure 1.17: The synthesis of PDO1 and PDO2 systems. Adapted from reference 78.

The enhanced photovoltaic performance of PDO1 and PDO2 with the addition of the sulfuryl group can be attributed to several factors. Firstly, the optimal energy level alignment facilitated efficient charge transport and separation in the photovoltaic device. Secondly, these modified systems exhibited superior charge carrier mobility, enabling more efficient movement of electrons and holes within the material. Thirdly, the introduction of the sulfuryl group resulted in a lower bandgap, which allowed the material to absorb a broader range of photons from the solar spectrum, thereby increasing the overall light harvesting efficiency. The researchers also observed

that the molecular configuration of the PDO core unit became more planar, and the stacking behavior between molecules became significantly stronger. This improved molecular arrangement led to enhanced charge transport properties and reduced charge recombination, further contributing to the improved photovoltaic performance of PDO1 and PDO2.

As a result of these beneficial modifications, the power conversion efficiency (PCE) of the photoactive layer based on PDO2 reached an impressive 20.2%. This signifies that the photovoltaic devices employing PDO2 as the active material achieved a high level of energy conversion from light to electricity, making it a promising candidate for advanced photovoltaic applications.[78]

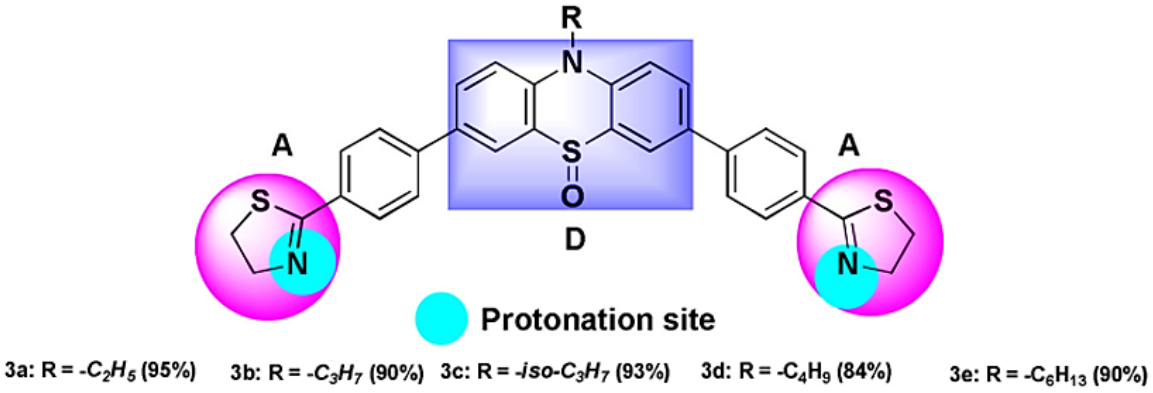

Figure 1.18: The synthesis of phenothiazine based thiazoline systems. Adapted from 79.

Chaudhary et al. focused on investigating the properties of certain D-π-A molecules containing pyridyl and benzothiazole nitrogen atoms. In the presence of an acid, these nitrogen atoms have a tendency to get protonated due to their possession of a lone pair of electrons. As a result, the protonation makes these molecules more electron-deficient, leading to the manifestation of strong ICT character. To address the challenges posed by this phenomenon, the researchers aimed to design and synthesize pH-sensitive fluorescent probes. These probes were constructed using phenothiazine-5-oxide as the donor unit and 2-arylthiazoline rings as the acceptor unit, forming an A-D-A type of push-pull molecule. The push-pull nature of these molecules refers to

the spatial arrangement of the donor and acceptor groups, which facilitates efficient charge transfer between them.

The compounds under study for their behavior as acidochromic sensors for volatile acids, specifically trifluoroacetic acid (TFA) and hydrogen chloride (HCl) in a solution state, contain a thiazoline unit attached to pendant phenyl rings. The presence of this thiazoline unit makes these compounds suitable for sensing the volatile acids mentioned. Acidochromic sensors are substances that undergo a color change in response to changes in acidity or pH levels. In this case, the compounds with the thiazoline unit are expected to exhibit a color change when exposed to volatile acids. This color change is likely to be observable and measurable, making these compounds potentially useful for detecting and monitoring the presence of volatile acids in a solution. The specific mechanism of the color change in these compounds is likely related to the interaction between the thiazoline unit and the acidic species. Acidic substances can potentially protonate the thiazoline ring, leading to changes in the electronic structure and, consequently, changes in the absorption or emission properties of the compounds, resulting in the observed color change. Among the compounds studied, compound 3c exhibited a minimum detection limit of 0.98 parts per million (ppm) for TFA, indicating its high sensitivity in detecting this acid. On the other hand, compound 3a showed a minimum detection limit of 13.1ppm for HCl, demonstrating its excellent sensitivity for detecting this acid at extremely low concentrations. To further understand the electronic properties of these compounds and their protonated forms, the researchers employed density functional theory (DFT) studies to calculate the HOMO-LUMO energy gap. This theoretical approach allowed them to gain insights into the molecular electronic structure and aid in explaining the experimental observations.

Understanding the behavior of these compounds as acidochromic sensors can have

practical applications in various fields, such as environmental monitoring, industrial safety, and chemical analysis, where the detection and quantification of volatile acids are essential. However, it's important to note that the effectiveness of these compounds as sensors will depend on their chemical properties and the specific experimental conditions in which they are used.[79]

1.10 Exploring the Vast Scope of this Study

In the current global scenario, addressing pressing environmental and energy challenges has prompted a growing focus on renewable sources, particularly solar energy. Artificial photosynthesis has emerged as a promising solution, with interdisciplinary scientists actively involved in developing molecular photosynthetic systems capable of efficiently converting solar energy into electricity or fuel. The urgency is driven by the energy crisis, compounded by population growth, depleting fossil fuel reserves, and inadequate renewable energy infrastructure, necessitating the transition to solar energy to meet global demands while minimizing environmental impact. To achieve this transition, researchers are dedicated to designing and synthesizing artificial photosynthetic analogues that can achieve high solar energy to electricity conversion rates. Central to this research is the investigation of artificial photosynthetic systems through the study of photochemical events in donor-acceptor systems that mimic natural photosynthesis.

This current research is mainly involved in the design and characterization of donor-acceptor photosystems that emulate the light-harvesting and charge separation functions observed in natural photosynthesis. Novel donor-acceptor photosynthetic systems, including donor-azaBODIPY push-pull systems, triphenylamine/phenothiazine-based push-pull derivatives, and phenothiazine sulfone-derived donor–acceptor systems were actively constructing. The primary objective of this research is to explore molecular structures that facilitate ultrafast electron and

charge transfer, which play a critical role in optimizing primary events for light energy conversion and advancing optoelectronics. These endeavors hold significant promise in contributing to a cleaner and more sustainable energy by effectively harnessing abundant and renewable solar energy.

Chapter 1 provides a comprehensive overview of artificial photosynthesis in comparison to natural photosynthesis, focusing on the mechanisms of light-energy harvesting and energy conversion through redox reactions in phototrophic organisms. It explores how artificial systems aim to imitate natural photosynthesis to convert light energy into electricity or fuel. This chapter covers principles related to the interaction of molecular species with light, including photophysical and photochemical reactions, and discusses quantitative formulation and measurement techniques. Proposing solar energy harvesting as a solution to the global energy crisis, it explains the complex photochemistry involved and highlights the importance of replicating these processes in laboratory settings. The basics of photochemistry, emphasizing energy pathways within a photochemical system, are also presented. Additionally, physical-analytical chemistry principles are discussed to optimize solar energy harvesting, specifically mentioning the utilization of the Marcus theory for elucidating electron transfer mechanisms and the Rehm-Weller equation for determining thermodynamic driving force during photoinduced electron transfer in a solution. The chapter concludes by comparing intra- and inter-molecular charge transfer processes and gives examples of such artificial photosynthetic systems, shedding light on their differences and advantages in the pursuit of efficient solar energy conversion.

Chapter 2 offers a comprehensive overview of the analytical techniques used to explore the photophysical and photochemical processes in the studied systems. These techniques encompass steady-state and time-resolved spectroscopy, electrochemistry, and photochemistry methods. The

chapter also provides a detailed discussion of the materials used in the research, as well as a list of crucial instruments employed to study the photophysical properties of donor and acceptor systems. Each instrument's significance in the investigation process is highlighted. The chapter concludes by delving into electronic coupling calculations through computational studies, which combine photochemical and physical concepts to enhance the understanding of the compounds being studied. This in-depth analysis equips the reader with a comprehensive understanding of the methodologies and tools used to investigate the intricate processes involved in the photophysical and photochemical aspects of the donor-acceptor systems.

Chapter 3 delves into the realm of electron transfer phenomena within donor-acceptor push-pull systems, incorporating the far-red absorbing sensitizer azaBODIPY along with various nitrogenous electron donors through an acetylene linker. Advanced physical techniques, including spectroscopic, electrochemical, spectroelectrochemical, and DFT computational methods are employed to investigate the structural integrity and excited state properties of these systems. The main focus is on understanding the role of nitrogenous donor, such as phenothiazine (PTZ), N, N-dimethylaniline (NND), and triphenylamine (TPA), in governing far-red excited state CT and CS, particularly in different solvent environments. Spectroelectrochemistry Results revealed diagnostic azaBODIPY anion radical peaks (azaBODIPY$^{\bullet-}$) in both visible and near-IR regions, indicating charge separation in polar solvents, including benzonitrile, but also partial charge transfer in nonpolar solvents, including toluene. The developed push-pull systems, linking high-energy CT species TPA-TCBD to a near-IR sensitizer, demonstrate panchromatic light absorption, and electron exchange between TPA-TCBD entities extending the lifetime of charge-separated states.

Chapter 4 of this study focuses on investigating a novel mechanism designed to enhance

the stability of CS states. The main idea revolves around facilitating the exchange of electrons among different acceptor components within multimodular donor-acceptor conjugates. The primary objective of this research is to create and characterize star-shaped conjugates featuring a core triphenylamine (TPA) derived dimethylamine-tetracyanobutadiene (NND-TCBD) moiety. In this study of these complexes, a fascinating phenomenon was observed, where electrons are exchanged in the compounds that contain multiple electron acceptors. To better comprehend this phenomenon, ultrafast spectroscopy was employed, enabling the effective demonstration of the occurrence of charge separation in excited states. Furthermore, the influence of electron exchange on prolonging the duration of charge-separated states in conjugates containing multiple acceptors was investigated. Through the study of this process, insights can be gained into how this novel mechanism could contribute to enhancing the stability of charge-separated states, thus potentially improving the overall efficiency of donor-acceptor conjugates in various applications.

The second part of this chapter involves understanding the process of CT in multi-modular push-pull systems, with a particular focus on its implications for technological advancements in light energy conversion and optoelectronic device development. A series of symmetrical and unsymmetrical push-pull systems (labeled as 1-4) was synthesized through Pd-catalyzed Sonogashira cross-coupling and [2+2] cycloaddition-retroelectrocyclization Sonogashira cross-coupling reactions. The systems consist of a centrally located core of (TPA), an end-capping unit of phenothiazine (PTZ) acting as a donor (labeled as D'), and a central electron acceptor of tetracyanobutadiene (TCBD) (labeled as A). The work also includes the synthesis of control compounds (labeled as C1-C4) to evaluate the role of terminal PTZ in charge transfer events. The analysis of photophysical and electrochemical properties, along with frontier orbital visualization and femtosecond transient absorption spectral studies, aims to shed light on the excited charge

transfer behavior and understand the significance of terminal PTZ in stabilizing the charge transfer state. The findings from this study could potentially contribute to the design and optimization of novel materials for more efficient light energy conversion and enhanced performance of optoelectronic devices.

Chapter 5 addresses the critical challenge of extending the lifetime of charge-separated states (CS) in artificial photosynthetic donor-acceptor (D-A) constructs, particularly in situations where the (D-A) systems are closely spaced and strongly interacting. The fundamental objective is to establish a future class of light energy harvesting technology. To achieve this, the study focuses on utilizing the triplet excited state of the electron donor and excitation wavelength selectivity. Novel push-pull systems (PTS2–PTS6) are synthesized and developed, utilizing phenothiazine sulfone as the π-conjugated framework. These systems are designed to incorporate highly efficient electron acceptors, namely 1,1,4,4-tetracyanobutadiene (TCBD) and cyclohexa-2,5-diene-1,4-diylidene-expanded TCBD (exTCBD), with the aim of manipulating the spectral and photophysical characteristics of the constituent components. The PTS2, in particular, exhibits solvatochromism, aggregation-induced emission, and mechanochromic behaviors. Through energy calculations and pump-probe spectroscopic studies, the work demonstrated that excitation wavelength-dependent charge stabilization can effectively prolong the lifetime of CS in highly interacting push-pull systems when excited at LE peak positions, as opposed to wavelengths corresponding to the CT transitions.

Chapter 6 provides a comprehensive conclusion of the work done on ultrafast charge and electron transfer systems, summarizing the results from Chapters 3 to 5, and outlining potential future research directions in the field of photosynthesis and energy conversion.

1.11 List of References

1. American Chemical Society National Historic Chemical Landmarks. Development of the Pennsylvania Oil Industry., http://www.acs.org/content/acs/en/education/whatischemistry/landmarks/pennsylvaniaoilindustry.html . 2009).

2. The History of the Light Bulb, https://www.energy.gov/articles/history-light-bulb).

3. I. Newton, A. Motte and N. W. Chittenden, *Newton's Principia. The mathematical principles of natural philosophy,*, New-York, D. Adee, 1848., 1848.

4. *Journal*, 2019.

5. A. Turgeon and E. Morse, Petroleum, or crude oil, is a fossil fuel and nonrenewable source of energy., https://education.nationalgeographic.org/resource/petroleum/).

6. A. Chaudhuri, R. Datta, M. P. Kumar, J. P. Davim and S. Pramanik, *Materials (Basel)*, 2022, **15**.

7. *Journal*, 2022.

8. R. Berera, R. van Grondelle and J. T. M. Kennis, *Photosynthesis Research*, 2009, **101**, 105-118.

9. L. Fara, *Advanced solar cell materials, technology, modeling, and simulation*, IGI Global, 2012.

10. B. Viswanathan and J. S. Lee, *Materials and processes for solar fuel production*, Springer, 2014.

11. N. S. Lewis, G. Crabtree, A. J. Nozik, M. R. Wasielewski, P. Alivisatos, H. Kung, J. Tsao, E. Chandler, W. Walukiewicz and M. Spitler, *Basic research needs for solar energy utilization. report of the basic energy sciences workshop on solar energy utilization, april 18-21, 2005*, DOESC (USDOE Office of Science (SC)), 2005.

12. C. Oertel, J. Matschullat, K. Zurba, F. Zimmermann and S. Erasmi, *Geochemistry*, 2016, **76**, 327-352.

13. S. C. Bhatia, in *Advanced Renewable Energy Systems*, ed. S. C. Bhatia, Woodhead Publishing India, 2014, DOI: https://doi.org/10.1016/B978-1-78242-269-3.50020-6, pp. 509-522.

14. M. Soroush and Y. Hajimolana, *Computers & Chemical Engineering*, 2023, **170**, 108103.

15. D. A. Kumar, *Int. J. Eng. Res. Technol*, 2014, **3**.

16. J. A. a. L. Bassham, . Hans, photosynthesis summary, https://www.britannica.com/science/photosynthesis).

17. F. K. Fong, *Light reaction path of photosynthesis*, Springer, 1982.

18. C. Molnar and J. Gair, in *Concepts of biology*, BCcampus, Biology, life sciences, 2015, pp. 197-200.

19. H. Hashimoto, Y. Sugai, C. Uragami, A. T. Gardiner and R. J. Cogdell, *Journal of Photochemistry and Photobiology C: Photochemistry Reviews*, 2015, **25**, 46-70.

20. G. Renger, S. K. Sopory, G. S. Singhal, K. D. Irrgang and Govindjee, in *Concepts in Photobiology: Photosynthesis and Photomorphogenesis*, eds. G. S. Singhal, G. Renger, S. K. Sopory, K. D. Irrgang and Govindjee, Springer Netherlands, Dordrecht, 1999, DOI: 10.1007/978-94-011-4832-0_1, pp. 1-7.

21. D. Lin, Z. Liu, X. Li, Z. Cao and R. Xiong, *Clean Energy*, 2023, **7**, 532-546.

22. M. A. Fusella, Y. L. Lin and B. P. Rand, in *Handbook of Organic Materials for Electronic and Photonic Devices (Second Edition)*, ed. O. Ostroverkhova, Woodhead Publishing, 2019, DOI: https://doi.org/10.1016/B978-0-08-102284-9.00020-6, pp. 665-693.

23. W. Shockley and H. J. Queisser, *Journal of Applied Physics*, 2004, **32**, 510-519.

24. A. Luque and S. Hegedus, *Handbook of Photovoltaic Science and Engineering*, John Wiley & Sons, Incorporated, New York, UNITED KINGDOM, 2011.

25. G. Bernardo, T. Lopes, D. G. Lidzey and A. Mendes, *Advanced Energy Materials*, 2021, **11**, 2100342.

26. J. Yu, Y. Zheng and J. Huang, *Polymers*, 2014, **6**, 2473-2509.

27. Preparing the Plexcore® PV 1000 Ink System, https://www.sigmaaldrich.com/US/en/technical-documents/protocol/materials-science-and-engineering/organic-electronics/preparing-the-plexcore).

28. G. Chidichimo and L. Filippelli, *International Journal of Photoenergy*, 2010, **2010**, 123534.

29. M. Azzouzi, T. Kirchartz and J. Nelson, *Trends in Chemistry*, 2019, **1**, 49-62.

30. X. Liu, B. P. Rand and S. R. Forrest, *Trends in Chemistry*, 2019, **1**, 815-829.

31. J. Pawley, in *Handbook of biological confocal microscopy*, Springer Science & Business Media, 2006, vol. 236, p. 184.

32. J. R. Lakowicz, *Principles of fluorescence spectroscopy*, Springer, 2006.

33. S. Gregersen Echers, Ph.D Doctoral Thesis, University of Copenhagen, 2014.

34. K. L. Williamson and K. M. Masters, in *Macroscale and microscale organic experiments*, Cengage Learning, 2016, pp. 758-760.

35. N. J. Turro, in *Molecular photochemistry*, New York, 1965, vol. 224, pp. 96-103.

36. J. C. Lindon, G. E. Tranter and D. Koppenaal, in *Encyclopedia of spectroscopy and spectrometry*, Academic Press, 2016, pp. 636-695.

37. K. Laqua, W. H. Melhuish and M. Zander, *Pure and Applied Chemistry*, 1988, **60**, 1449-1460.

38. S. Gregersen Echers, 2014.

39. G. L. Lim, Ph.D. Dissertation, University of North Texas Libraries, 2017.

40. M. R. Wasielewski, *Chemical Reviews*, 1992, **92**, 435-461.

41. Z. Pan, *University of Florida, USA*, 2015.

42. R. Williams, DOI: 10.13140/RG.2.2.16547.30244, 2007.

43. M. Reckenthäler and A. G. Griesbeck, *Advanced Synthesis & Catalysis*, 2013, **355**, 2727-2744.

44. D. Rehm and A. Weller, *Israel Journal of Chemistry*, 1970, **8**, 259-271.

45. A. V. Müller, W. M. Wierzba, M. N. Pastorelli and A. S. Polo, *Journal of the Brazilian Chemical Society*, 2021, **32**.

46. R. A. Marcus and N. Sutin, *Biochimica et Biophysica Acta (BBA) - Reviews on Bioenergetics*, 1985, **811**, 265-322.

47. M. Kuss-Petermann and O. S. Wenger, *Physical Chemistry Chemical Physics*, 2016, **18**, 18657-18664.

48. K. B. Eisenthal, *Laser Chemistry*, 1983, **3**, 128404.

49. P. K. Samanta and R. Misra, *Journal of Applied Physics*, 2023, **133**.

50. O. F. Mohammed, *The Journal of Physical Chemistry A*, 2010, **114**, 11576-11582.

51. S. Sumalekshmy and K. R. Gopidas, *Photochemical & Photobiological Sciences*, 2005, **4**, 539-546.

52. Y. Wang, W. Zhu, H. Dong, X. Zhang, R. Li and W. Hu, *Topics in Current Chemistry*, 2016, **374**.

53. F. Dias, T. Penfold and A. Monkman, *Methods and Applications in Fluorescence*, 2017, **5**, 012001.

54. D. Wróbel and A. Graja, *Coordination Chemistry Reviews*, 2011, **255**, 2555-2577.

55. C. B. Kc and F. D'Souza, *Coordination Chemistry Reviews*, 2016, **322**, 104-141.

56. G. Sathyamoorthi, M.-L. Soong, T. W. Ross and J. H. Boyer, *Heteroatom Chemistry*, 1993, **4**, 603-608.

57. E. B. Knott, *Journal of the Chemical Society (Resumed)*, 1947, DOI: 10.1039/JR9470001196, 1196-1201.

58. J. Killoran, L. Allen, J. F. Gallagher, W. M. Gallagher and D. F. O'Shea, *Chem Commun (Camb)*, 2002, DOI: 10.1039/b204317c, 1862-1863.

59. W. M. Gallagher, L. T. Allen, C. O'Shea, T. Kenna, M. Hall, A. Gorman, J. Killoran and D. F. O'Shea, *Br J Cancer*, 2005, **92**, 1702-1710.

60. S. Kumar, H. B. Gobeze, T. Chatterjee, F. D'Souza and M. Ravikanth, *J Phys Chem A*, 2015, **119**, 8338-8348.

61. A. N. Amin, M. E. El-Khouly, N. K. Subbaiyan, M. E. Zandler, M. Supur, S. Fukuzumi and F. D'Souza, *The Journal of Physical Chemistry A*, 2011, **115**, 9810-9819.

62. F. D'Souza, *Journal of the American Chemical Society*, 2012, **v. 134**, pp. 654-664-2012 v.2134 no.2011.

63. W. Shi, Doctor of Philosophy in Chemistry Ph.D Thesis Chinese University of Hong Kong, 2013.

64. J. M. Ganley, P. R. D. Murray and R. R. Knowles, *ACS Catalysis*, 2020, **10**, 11712-11738.

65. N. Mandare, P. Shanmugam, M. Sundararajan and S. Dutta Choudhury, *New Journal of Chemistry*, 2020, **44**, 19061-19075.

66. T. Manifar and S. Rohani, *Canadian Journal of Chemical Engineering*, 2008, **82**, 323-334.

67. W. Li, Y. Pan, L. Yao, H. Liu, S. Zhang, C. Wang, F. Shen, P. Lu, B. Yang and Y. Ma, *Advanced Optical Materials*, 2014, **2**, 892-901.

68. S. C. Creason, J. Wheeler and R. F. Nelson, *The Journal of Organic Chemistry*, 1972, **37**, 4440-4446.

69. J. R. Pinzón, D. C. Gasca, S. G. Sankaranarayanan, G. Bottari, T. Torres, D. M. Guldi and L. Echegoyen, *Journal of the American Chemical Society*, 2009, **131**, 7727-7734.

70. C. Popli, Y. Jang, Y. Patil, R. Misra and F. D'Souza, *Chemistry – A European Journal*, 2020, **26**, 15109-15115.

71. S. P. Massie, *Chemical Reviews*, 1954, **54**, 797-833.

72. E. A. Onoabedje, U. C. Okoro and D. W. Knight, *Journal of Heterocyclic Chemistry*, 2017, **54**, 206-214.

73. J. D. Bell, J. F. Blount, O. V. Briscoe and H. C. Freeman, *Chemical Communications (London)*, 1968, DOI: 10.1039/C19680001656, 1656-1657.

74. C.-L. Wang, J.-W. Shiu, Y.-N. Hsiao, P.-S. Chao, E. Wei-Guang Diau and C.-Y. Lin, *The Journal of Physical Chemistry C*, 2014, **118**, 27801-27807.

75. I. J. Al-Busaidi, A. Haque, N. K. Al Rasbi and M. S. Khan, *Synthetic Metals*, 2019, **257**, 116189.

76. S. Revoju, A. Matuhina, L. Canil, H. Salonen, A. Hiltunen, A. Abate and P. Vivo, *Journal of Materials Chemistry C*, 2020, **8**, 15486-15506.

77. P. S. Gangadhar, G. Reddy, S. Prasanthkumar and L. Giribabu, *Physical Chemistry Chemical Physics*, 2021, **23**, 14969-14996.

78. X. Ding, C. Chen, L. Sun, H. Li, H. Chen, J. Su, H. Li, H. Li, L. Xu and M. Cheng, *Journal of Materials Chemistry A*, 2019, **7**, 9510-9516.

79. S. Chaudhary, M. Mukherjee, T. K. Paul, S. Taraphder and M. D. Milton, *Journal of Photochemistry and Photobiology A: Chemistry*, 2020, **397**, 112509.

CHAPTER 2

MATERIALS AND ANALYTICAL METHODS

This chapter provides a comprehensive and in-depth analysis of the synthesis of diverse supramolecular and ultrafast charge and electron transfer systems. It offers detailed insights into the specific chemical reagents, solvents, and precursor materials used in the synthesis process. Furthermore, the chapter thoroughly explores the physical methodologies employed to characterize these systems, with a strong emphasis on the instruments utilized for this purpose. Notably, the extensive discussion of the synthesis of the examined photosystems in chapters 3 through 5, originating from the prestigious research laboratory of Professor Rajneesh Misra at the Indian Institute of Technology in Indore, India, contributes significantly to the advancement of research in this fascinating scientific discipline. The abundance of information presented in this chapter is vital for furthering knowledge and understanding in this field of study.

2.1 Materials

All the reagents and bulk solvents were purchased from commercial sources including Aldrich Chemicals (Milwaukee, WI) and Fischer Chemicals. The tetra-*n*-butylammonium perchlorate (TBA)ClO_4 used in electrochemical studies was from Fluka Chemicals or MilliporeSigma. All chemicals were used as received unless otherwise indicated. All oxygen or moisture-sensitive reactions were performed under an inert atmosphere such as a nitrogen/argon atmosphere using the standard Schlenk method.

2.2 Analytical Methods

In this section, a detailed account of the experimental techniques utilized to investigate and understand the photochemical and photophysical properties is provided, with specific emphasis on the phenomena of charge, electron, and hole transfer reactions. The methods employed enable a

detailed characterization of these processes, shedding light on the underlying mechanisms and contributing to a deeper comprehension of the studied systems.

2.2.1 Steady State UV-Vis Absorbance Spectroscopy

The fundamental photophysical phenomenon underlying artificial photosynthesis, encompassing its applications in both direct photon-to-electricity conversion (Photovoltaics) and fuel generation, revolves around the absorption of light by the antenna chromophores. This process initiates a sequence of photophysical and photochemical events, with the first step being the absorption of light and the consequent photoexcitation of the antenna chromophore or the donor molecule. This initial photoexcitation takes precedence over subsequent processes, such as excitation energy transfer and electron transfer. In practical scenarios, such as in the realm of photovoltaics, the excitation energy is harnessed from energy carrier photons originating from solar energy.

The assessment of absorption spectra is conventionally accomplished through spectrophotometric techniques, establishing research into the light-absorbing attributes of synthetic photosensitizers as highly critical. In this dissertation, the research endeavors involved employing a double-beam ultraviolet (UV) and visible (vis) spectrometer (Jasco V-670 and Shimadzu UV 3600) between 300 nm to 1600 nm, a sophisticated instrument capable of simultaneous reference and sample measurements, to systematically record the absorption spectra of a specific target molecule. In this study, an experiment was conducted using an optically identical quartz cuvette, which contained only the solvent, and served as a reference. The goal was to subtract the absorption of the solvent from the absorption of a sample of chromophore in solution, which had a known concentration (c). A xenon lamp was used as the excitation light source for the experiment. The resulting spectra displayed the absorbed photon's wavelength on

the x-axis and the absorption strength on the y-axis. The molecule's resonance frequency (ν) is a crucial determinant of permissible transitions within the molecular system, and these resonances, occurring during allowed transitions, significantly govern the molecule's absorption properties. As the energy difference between these transitions is quantized, only photons with specific energies (wavelengths) can be exchanged. Consequently, similar molecules may exhibit identical absorption properties, making the molecule's absorption a distinct characteristic of its electronic structure. To calculate the energy (E) in joules or the ($\tilde{\nu}$) wavenumber (cm^{-1}) associated with a particular transition, (Eq. 2.1)[1] can be employed where c is the light speed ($2.99X10^{10}$ cm. s^{-1}).

$$E = h\frac{c}{\lambda} \qquad \text{Eq. 2.1}$$

$$\tilde{\nu} = \frac{1}{\lambda} \qquad \text{Eq. 2.2}$$

In the context of photosynthetic chromophores, the absorption wavelength of a molecule, along with its molar absorptivity (ε) or molar absorption coefficient, plays a crucial role in understanding their spectral absorption properties in the UV-vis regions. The molar extinction coefficient quantifies the number of photons absorbed by the molecule in (*mole.* l^{-1} or M^{-1}) at a specific wavelength, serving as a fundamental measure for comparing molecules' capabilities to absorb electromagnetic radiation. The significance of a molecule's absorption in harnessing solar energy relies on its molar extinction coefficient; molecules with low coefficients may have limited impact. Consequently, when assessing the absorption properties of chromophores, both the absorption wavelength and the molar extinction coefficient are pertinent factors. The Beer-Lambert equation is utilized to calculate the molar extinction coefficient of a molecule in units of ($M^{-1}cm^{-1}$).[2]

$$A = \varepsilon bc \qquad \text{Eq. 2.3}$$

The variable A represents the absorbance at a specific wavelength, while the variable b

signifies the optical path length. By collecting absorbance values at different concentrations and plotting them as absorbance versus concentration, the resulting slope on the graph provides the molar extinction coefficient. This robust methodology facilitated a comprehensive analysis and assessment of the molecule's light absorption properties.

2.2.2 Fluorescence and Phosphorescence Emission Spectroscopy

Fluorescence and phosphorescence are distinct radiative decay pathways, both involving the emission of photons during the relaxation of a photoexcited molecule from its higher energy excited state back to its lower energy ground state. Specifically, fluorescence occurs when photons are emitted from the S_1 of the molecule, while phosphorescence involves photon emission from T_1. In Section 1.6, these two phenomena are discussed and differentiated based on their origins. The Jablonski energy level diagram provides a comprehensive visualization of the energy states and the transitions involved in fluorescence and phosphorescence processes, including IC and ISC. A spectrofluorometer, equipped with excitation and emission monochromators, a Xenon-arc lamp as the excitation light source, and a suitable emission detector, was utilized for measuring and studying the emission spectra of fluorescence and phosphorescence, capturing emissions within the desired wavelength range. These experimental tools and knowledge about radiative decay pathways contribute to a deeper understanding of the light-matter interactions in molecules and are essential for various applications, ranging from fluorescence spectroscopy in biological research to phosphorescent materials in optoelectronics and sensors.

In the field of artificial photosynthesis, the fluorescence exhibited by molecules plays a crucial role, as it is an essential prerequisite for their effective utilization in this process. However, not all light-absorbing molecules possess the ability to fluoresce. Thus, a careful selection of compounds based on their specific absorption characteristics and molar extinction coefficients is

essential as an initial step in this research pursuit. Subsequently, understanding the photon emission capability of the chosen compound becomes pivotal in comprehending its luminescent behavior. To quantitatively evaluate the efficiency of the photon emission process, a metric known as the quantum yield (Φ_F) is utilized by scientists. The quantum yield (Φ_F) is a quantitative measure used for assessing the yield of emitted photons and will be further discussed in the following section.

As mentioned earlier, spectrofluorometers are instruments used to measure fluorescence or phosphorescence. They resemble spectrophotometers in design and use monochromators to direct light from a source through a sample to a detector. The key difference between luminescence and absorption studies is the detector's position. In luminescence studies, the detector is placed at a right angle (90°) to the sample, while in absorption studies, the detector is opposite the excitation light source. This setup allows only emitted light, not incident light, to be observed. To excite the sample, an excitation monochromator selects a specific wavelength of light based on the sample's absorption spectrum. After excitation, the sample emits photons in different directions, which are captured by an emission monochromator and directed to the detector. The signals generated by the detector are interpreted as a spectrum, enabling researchers to analyze and study the luminescence properties of the sample.

On the other hand, the phosphorescence phenomenon can be measured in a manner akin to fluorescence, but only if the material exhibits phosphorescence at cryogenic temperatures achieved by liquid nitrogen. To enhance phosphorescence, a heavy atom triplet sensitizer (e.g., iodine or bromine) is introduced to promote intersystem crossing, a process that facilitates phosphorescence. Achieving phosphorescence might necessitate cooling the sample to cryogenic temperatures with liquid nitrogen. After the sample is prepared, it is dissolved in a solution that has the property of

freezing into a transparent state. Once the sample is in this solution, it is then frozen inside a specialized quartz Nuclear Magnetic Resonance (NMR) tube. The NMR tube is designed to withstand low temperatures and is transparent to certain types of light, allowing for the analysis of the phosphorescent properties using standard fluorescence measurement techniques.

A photosynthetic analogue is distinguished by two important characteristics: its quantum yield and excited state lifetime. In the domain of synthetic chromophores employed for solar energy harvesting and organic photovoltaics, the fluorescence quantum yield (Φ_F) and fluorescence lifetime (τ) constitute two essential characteristics. The fluorescence quantum yield (Φ_F) represents the ratio of emitted photons to absorbed photons. Molecules exhibiting a higher intensity of fluorescence emission demonstrate an enhanced fluorescence quantum yield, making them particularly well-suited for implementation as photosensitizers in solar cell applications. The quantum yield can be quantitatively expressed:[3]

$$\Phi_F = \frac{\#\ of\ emitted\ photons}{\#\ of\ aborbed\ photons} = \frac{k_r}{k_r + k_{nr}} \qquad \text{Eq. 2.4}$$

The equation involves two crucial parameters: the rate of radiative decay ($_{kr}$) and the rate of non-radiative decay (k_{nr}). Notably, when the rate of non-radiative decay is reduced to zero, the quantum yield of the molecular system becomes 1, signifying a perfect conversion of absorbed photons into emitted photons. Minimizing non-radiative decay pathways through molecular design or environmental optimization can significantly increase the quantum yield, making it relevant for optoelectronic materials, where high quantum yields are sought-after for applications like light-emitting devices and solar cells, as they ensure efficient energy conversion and minimize energy losses.

$$\Phi_s = \Phi_r \left(\frac{I_s/A_s}{I_r/A_r}\right)\left(\frac{\eta_s}{\eta_r}\right) \qquad \text{Eq. 2.5}$$

An innovative approach for quantifying the fluorescence quantum yield (Φ_F) of a

molecule. Instead of employing direct quantum yield measurements, the proposed method adopts a comparative strategy. This entails comparing the fluorescence intensity (I_s) of the molecule under investigation with that of a well-established reference standard (I_r), which could be free base porphyrin, azaBODIBY, TPA, or similar compounds. The specific formula for this comparison, provided in the text (Eq. 2.5), employs the relative quantum yield calculation method to determine the Φ_F of the molecules discussed in the dissertation. The formula involves variables such as Φ_s (quantum yield of the sample), Φ_r (quantum yield of the reference standard), A_s and A_r (intensity of the absorption peaks of the sample and reference, respectively), and η_s (solvent refractive index of the sample) and η_r (solvent refractive index of the reference). By utilizing this approach, researchers can assess the fluorescence efficiency of diverse molecules without requiring absolute quantum yield measurements.[3]

Steady-state luminescence spectra were obtained using either a Varian (Cary Eclipse) Spectrofluorometer, a Shimadzu UV-1700 PharmaSpec, or a Horiba Jobin Yvon Nanolog spectrofluorometer, all of which were outfitted with PMT detectors for UV-visible light and InGaAs photodiode for near-IR light. Additionally, an FTIR spectrometer (Equinox 55 from Bruker Optics) equipped with a single reflection diamond ATR attachment (Dura- Samp1IR II by SensIR Technologies) was utilized to acquire mid-IR spectra in the range of 550–4000 cm^{-1}.

2.2.3 Time-Resolved Fluorescence Emission Spectroscopy

The fluorescence lifetime (τ) is a critical parameter that characterizes the time taken by a fluorophore to transition from (S_1) to (S_0). This temporal duration plays a vital role in advancing artificial photosynthetic molecular systems. Understanding the fluorescence lifetime data is essential for optimizing the performance and efficiency of these systems in light-harvesting and energy conversion applications. Eq. 2.6 can be adapted and utilized to estimate the (τ) in a specific

format, providing valuable insights into the dynamics of the excited states. Additionally, it empowers researchers to fine-tune the design and functionality of artificial photosynthetic materials, thus facilitating further progress in the field.[4]

$$\tau = \frac{1}{k_r + k_{nr}} \quad \text{Eq. 2.6}$$

The fluorescence lifetimes of the chromophores were investigated employing the time-correlated single photon counting (TCSPC) method, in which nano-LED (Light Emitting Diode) excitation sources were utilized through a Horiba Jobin Yvon Nanolog spectrofluorometer. The specific excitation wavelength of the nanoLED was carefully selected based on the absorbance spectrum of the chromophores. For both steady-state fluorescence and time-resolved emission measurements, a right-angle detection method was applied, and prior to measurements, all solutions were purged with Argon gas. The fluorescence lifetime plot was represented as a decay curve, displaying counts versus time. Subsequently, the obtained data was subjected to analysis and fitted using computer software. This facilitated the determination of the chromophore's lifetime as a monoexponential, biexponential, etc., with a CHISQ value less than 1.2, indicating a good fit to the experimental data. This comprehensive experimental approach and data analysis method contribute to a deeper understanding of the fluorescence behavior of the chromophores, providing valuable insights into their photophysical properties and potential applications in various fields, including optoelectronics and light harvesting.

2.2.4 Cyclic Voltammetry and Differential Pulse Voltammetry

In the construction of a photosynthetic system, numerous factors, encompassing thermodynamics and kinetics, are pivotal in determining electron transfer efficacy. Primarily, thermodynamics ascertains the feasibility of electron transfer. Secondly, kinetics governs the electron transfer rate vis-à-vis competing processes. Thirdly, the efficiency of charge separation,

as characterized by the excitation energy assimilated by the charge-separated state, is paramount for subsequent catalytic functions like proton reduction and carbon dioxide fixation. Moreover, the quantum yield of the charge-separated state holds significant importance. The redox potentials of the donor and acceptor are fundamental in achieving these objectives. The Rehm-Weller approach and Marcus' electron transfer theory facilitate the comprehension of these aspects, especially when the optical and redox properties of the building blocks are well-defined. Computational methods also aid in predicting essential properties before commencing synthesis. Hence, it is crucial to investigate the first oxidation and reduction potentials of the donor and acceptor chromophores using an electrochemical setup.

To attain the research objectives comprehensively, two distinct electrochemical techniques were employed, namely cyclic voltammetry (CV) and differential pulse voltammetry (DPV). In the CV experiments, the potential was cyclically varied between two predefined values, thereby facilitating the elucidation of the redox behavior and identification of the oxidation and reduction peaks. In direct contrast, differential pulse voltammetry methodically applies the potential in a step-wise, unidirectional manner, offering unparalleled precision in determining the oxidation and reduction potentials as compared to CV. The primary focal point of this study centers on the precise elucidation of redox potentials of the chromophores employing the DPV approach, while CV is employed to diligently monitor the reversibility of the detected peaks.[5, 6]

This research employs a three-electrode electrochemical configuration to investigate the redox potentials of chromophores. The experimental setup comprises an Ag/AgCl reference electrode (RE), serving as a stable reference potential, a platinum button working electrode (WE) that facilitates the redox reactions of the chromophores, and a platinum wire counter electrode (CE) to ensure the continuity of the electrical circuit. The voltammograms obtained through this

procedure offer detailed understanding of the current-potential (I-V) characteristics, thus revealing essential electrochemical properties of the system. To acquire a cyclic voltammogram, the potentiostat is employed to apply either positive (for oxidation) or negative (for reduction) potential, initiating from a zero potential (typically) and reaching a vertex potential, after which it returns to the initial potential, completing a full cycle.[7] In the dissertation, all the electrochemical data presented were collected using three different instruments: an EG&G 263A Electrochemical Analyzer, an AMETEK VersaSTAT 4 Potentiostat/Galvanostat Analyzer, and an AMETEK PARSTAT 4000A Potentiostat/Galvanostat/EIS Analyzer.

2.2.5 Spectroelctrochemical Technique

Spectroelectrochemistry is a scientific approach that combines the principles of spectrophotometry and electrochemical techniques. In this method, the sample under investigation is repetitively analyzed using a spectrophotometer while redox potentials are applied. Key components necessary for this methodology include the spectroelectrochemical cuvette, a mesh-type working electrode, a standard reference electrode (RE), and a counter electrode (CE). The spectroelectrochemical cuvette features a Y-shaped internal configuration, enabling simultaneous measurements of optical and electrochemical properties of the sample. It accommodates three electrodes (working, reference, and counter) and a 1 mm light path for spectroscopic analysis. The working electrode, such as Pt mash type, facilitates the electrochemical reaction, while the reference electrode, including an Ag/AgCl reference electrode, maintains a stable potential for precise measurements. The counter electrode, like a Pt, balances the electrical flow. Researchers can observe optical changes in the sample while applying redox potentials to the working electrode. The Y-shaped design minimizes the volume of the solution, enabling efficient measurements of fast reactions.[8-10]

In the context of photoinduced electron transfer reactions, the transfer of electrons from the photoexcited donor to the acceptor leads to the formation of charged intermediate species, which act as the reaction products. The cation radical ($D^{\cdot+}$) and the anion radical ($A^{\cdot-}$) exhibit distinct absorption spectra in the solution due to subtle differences in their electronic structures compared to the neutral species. The application of a specific oxidizing potential, determined from the first oxidation potential of the donor chromophore in the D-A complex through CV, induces the formation of a cation radical in the cuvette placed in the Spectrophotometer beam path (section 2.2.1). During the spectroelectrochemical experiment lasting approximately 15 minutes, significant changes occur in the absorption spectra of the complex. Firstly, a prominent absorption peak corresponding to the charged cation radical species emerges, signifying their accumulation in the solution. Concurrently, there is a reduction in the absorption peaks of the neutral species, indicating a conversion of some neutral species into the cation radical. The presence of a common absorption point shared by the growing cation radical peak and the decreasing neutral species peak, referred to as the isosbestic point, implies that a single equilibrium process governs the observed transformations. In a similar manner to determining the absorption of the cation radical, the absorption of the anion radical can be assessed by applying a reduction potential that corresponds to the reduction potential of the acceptor moiety. This reduction potential can be obtained through cyclic voltammetry. These two absorption characteristics of radical ions (the cation and anion radicals) become highly significant in later transient absorption studies.

2.2.6 Transient Absorption Spectroscopy

Transient absorption spectroscopy, renowned as ultrafast spectroscopy due to its exceptionally brief optical event durations measured in femtoseconds (10^{-15}) or picoseconds (10^{-12}), is an extensively utilized and potent method for studying photochemical events in intricate

chemical systems, encompassing donor-acceptor systems. Its advantages over other spectroscopic methods are particularly evident when studying rapid and transient processes. The method employs short-duration, intense pulses of light to selectively excite specific states or transitions in the sample, with pulse durations much shorter than the time scales of the photochemical events being studied. The experimental setup consists of two laser beams: the pump beam triggers the photochemical event of interest, while the probe beam, with a controllable time delay, allows for the observation of transient changes in the sample (Fig. 2.1)[11]. By varying the time delay, transient absorption spectroscopy captures the real-time evolution of the sample's electronic and vibrational states during the photochemical event, providing insights into processes such as energy transfer, electron transfer, absorption, and emission. The short pump pulse duration prevents interference with the subsequent probe pulse, ensuring clear and accurate information about the sample's transient states. Another key advantage is the technique's capability to detect transient species, including short-lived intermediates and excited states, which are typically challenging to observe using other steady-state spectroscopic techniques.

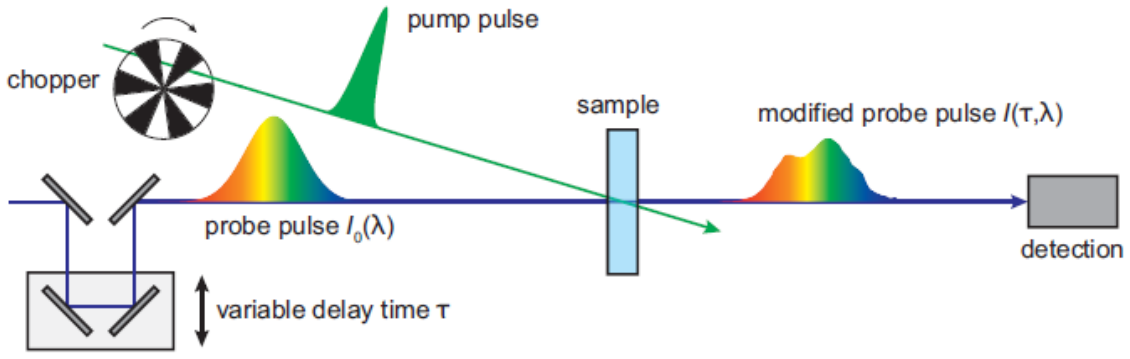

Figure 2.1: Schematic of employing a pump pulse principle in femtosecond transient absorption spectroscopy.

In the studies presented in this dissertation, the ultrafast transient absorption spectroscopy with femtosecond (fs) and nanosecond (ns) time scales was employed to investigate electron

transfer and energy transfer processes in photosystems. The fs laser excitation source operates with a pulse duration spanning 100 - 150 fs, while the ns excitation laser has a pulse duration of approximately 7 ns. The instrument comprises essential components, including a fundamental laser generator producing an intense 800 nm laser beam with a 100-femtosecond pulse duration. This beam is split into two parts: 95% is directed through an Optical Parametric Amplifier (OPA) to create beams of different wavelengths, while the remaining 5% is sent to a white light generating crystal to obtain a broad-band white light continuum for further analysis as shown in Figure 2.2.[12]

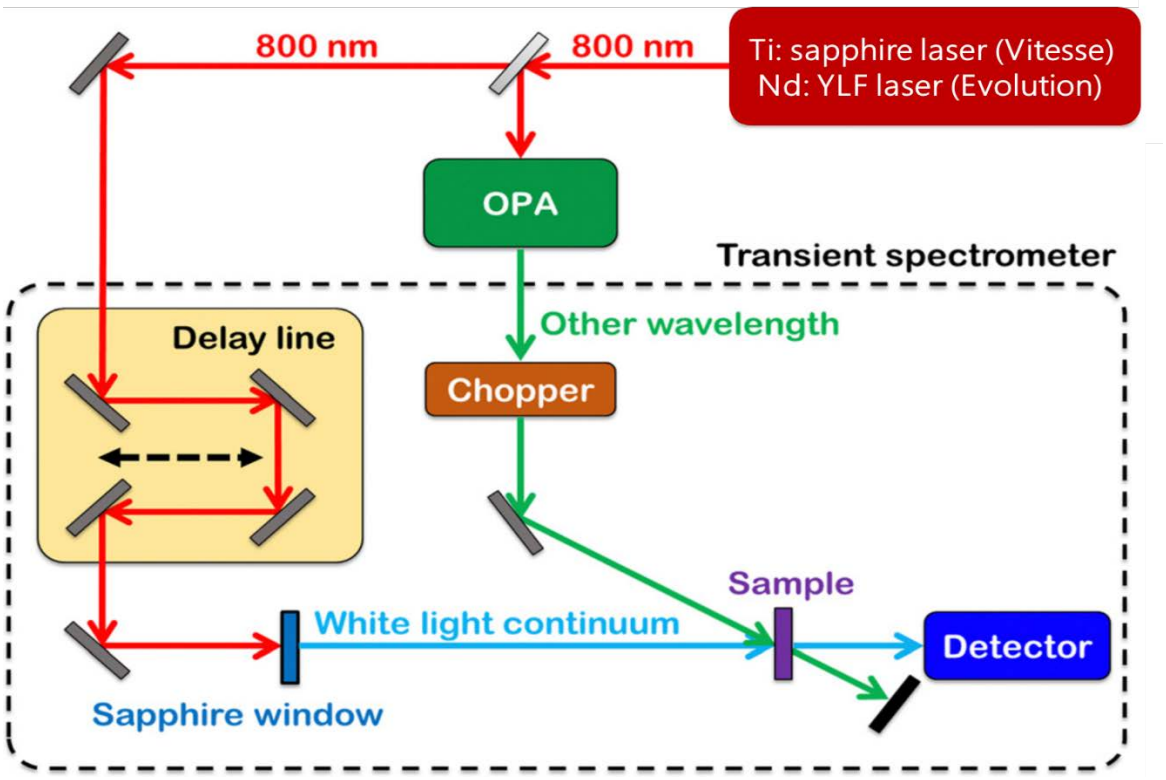

Figure 2.2: **A schematic of the working principal femtosecond transient absorption spectroscopy (fs-TAS).**

The probe beam, obtained through the delay line, is temporally delayed compared to the pump beam and used to observe spectral changes in the sample during the ultrafast process. The pump beam excites the sample, while the probe beam allows for observing the sample's behavior over time. The Femtosecond transient absorption is equipped with an Ultrafast Femtosecond Laser

Source (Libra) by Coherent, incorporating a diode-pumped, mode-locked Ti:sapphire laser (Vitesse) and a diode-pumped intracavity doubled Nd:YLF laser (Evolution) to generate a compressed laser output of 1.45 W. For a broader range of excitation wavelengths, a TOPAS-Prime optical parametric amplifier (OPA) system by Light Conversion with a tuning range of 290-2600 nm was used. A portion of the laser output was used for white light continuum generation, and kinetic traces at specific wavelengths were obtained from time-resolved spectral data for analysis. The combination of different laser sources and optical parametric amplifiers enabled a comprehensive investigation of photochemical processes in the studied systems.[12]

As previously discussed, the experimental configuration involves the utilization of two laser pulses, namely a "pump" pulse intended to stimulate molecules within a confined sample region and a "probe" pulse composed of white light to gauge the absorption behavior of species in the same spatial domain. The pump pulse is adept at exciting a subset of molecules, inducing them to transition into an excited state. To prevent interference with the probe measurement, the energy from the pump pulse is intentionally not detected by the apparatus. Subsequently, the probe pulse captures two distinct types of absorption phenomena: Excited State Absorption (ESA), stemming from molecules elevated to higher energy levels by the pump pulse, and Ground State Bleaching (GSB), which arises from molecules in their ground state being depleted due to the influence of the pump pulse. In order to distinguish between these absorptions, the spectral data are presented as changes in absorption (ΔA), derived by subtracting the signal obtained from the unpumped sample from that of the pumped sample.[11]

$$\Delta A(\lambda) = -\log\left(\frac{I(\lambda)_{pumped}}{I(\lambda)_{unpumped}}\right) \qquad \text{Eq. 2.7}$$

Upon excitation of the molecular sample, a series of intricate optical phenomena ensues, each contributing distinct signals. Ground-state bleaching is characterized by a decline in the

absorbance of the S_0 due to the partial depopulation of its energy levels. This event induces a negative change in absorbance ($\Delta A < 0$) at specific positions in the spectrum where steady-state absorption bands are observable. Stimulated emission (SE) manifests when the probe pulse engages with an excited molecule, stimulating the return of the molecule to the ground state through the process of photon emission. This process leads to a reduction in the signal (ΔA) within the probe range corresponding to the molecule's emission, resulting in a negative ΔA. Excited-state absorption (ESA) takes place as the probe pulse further elevates an already excited molecule to higher-lying excited states, resulting in a reduction of the probe pulse intensity. This occurrence induces a positive change in absorbance ($\Delta A > 0$). In instances where excitation yields a photoproduct, the newly formed molecule interacts with the probe pulse, and the absorption of this photoproduct (PA) generates a positive signal in the transient data.[11]

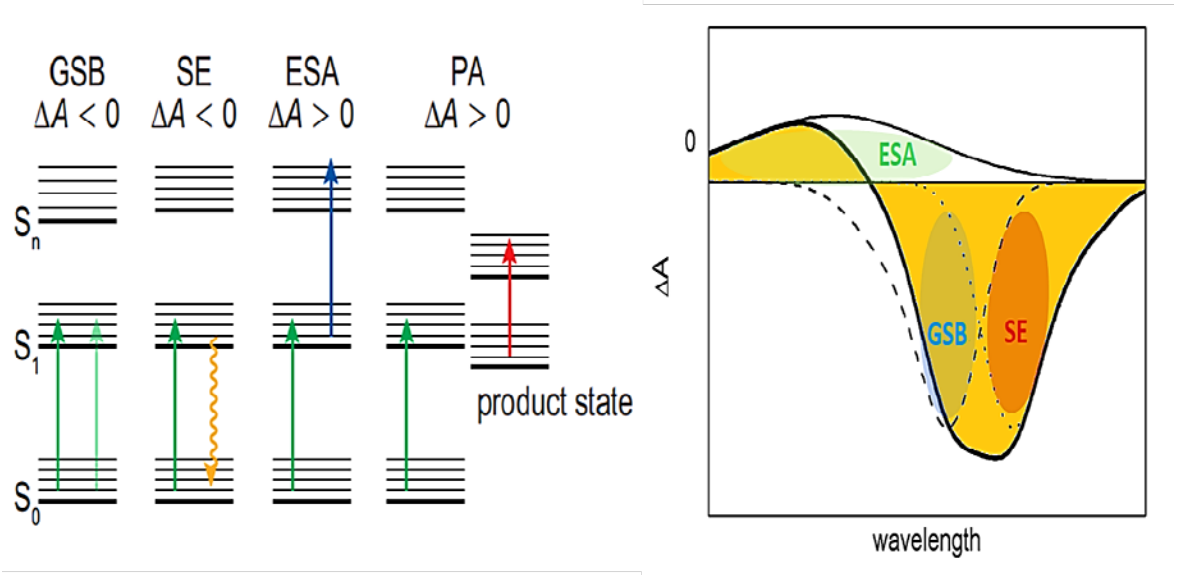

Figure 2.3: Signal contributions in pump-probe femtosecond transient absorption spectroscopy (left) and the Fs-TA spectrum displays GSB (dashed line), SE (dotted line), ESA (solid line), and the sum of all contributions (gray line). Adapted from reference 11,13.

Pump-probe femtosecond transient absorption spectroscopy yields a three-dimensional (3D) spectrum (Fig. 2.3)[11, 13], $\Delta A\ (\lambda, \tau)$, representing changes in absorption intensity (ΔA) as a

function of wavelength (λ) and time delay (τ). The method involves exciting the sample with a pump pulse, creating transient species, and inducing changes in its electronic or vibrational states. A delayed probe pulse then interacts with the modified sample, and its intensity is measured after passing through the sample, capturing changes in absorbance at different wavelengths and time delays. The resulting 3D spectrum displays distinct features (Fig. 2.3),[11] including Ground State Bleach (GSB) indicating depletion of the ground-state population, Excited State Absorption (ESA) showing increased absorbance due to excited states or transient species, and Stimulated Emission (SE) revealing emission of photons as the sample relaxes to lower energy states.[11, 13]

The experimental data shows combinations of all states and is difficult to determine each state at a specific time range. To define each state and time profile, analytical softwares (surface Xplorer and GloTarAn) are used. Surface Xplorer focuses on conducting global analysis, providing a comprehensive overview of the various photo-induced states present within the sample. In contrast, GloTarAn offers an added advantage by enabling both global and target analysis, empowering researchers to identify and examine specific states of interest within the dataset. Global analysis involves subjecting the data to a multiexponential fit, where each exponent corresponds to distinct photo-induced states, such as singlet excited state, triplet excited state, charge-separated state, and others. However, it is essential to acknowledge that the fitting process may not perfectly align with the actual number of states in the system due to complexities and approximations inherent in the underlying mathematical framework employed during the analysis.

Global analysis assumes that each state in a system occurs independently and simultaneously. This means that the decay or behavior of one state is not influenced by other states in the system. When global analysis is applied to experimental data obtained using a femtosecond technique, it produces a decay-associated spectrum (DAS), as shown in Figure 2.4(c).[14] This

spectrum gives a representation of the data where different states are deconvoluted, i.e., separated from each other. However, the global analysis approach can lead to overestimation of the number of states in the system because it assumes complete independence between them. One drawback of global analysis is that it may show negative peaks in the spectra. These negative peaks occur because the different species (states) are represented as a linear combination of each other, and this can result in certain parts of the spectrum appearing to have negative values. Additionally, global analysis cannot accurately determine the concentrations or populations of individual states in the system. Its underlying assumption is that each state starts with 100% population and decays independently over time. However, this assumption may not hold true when states interact with each other.

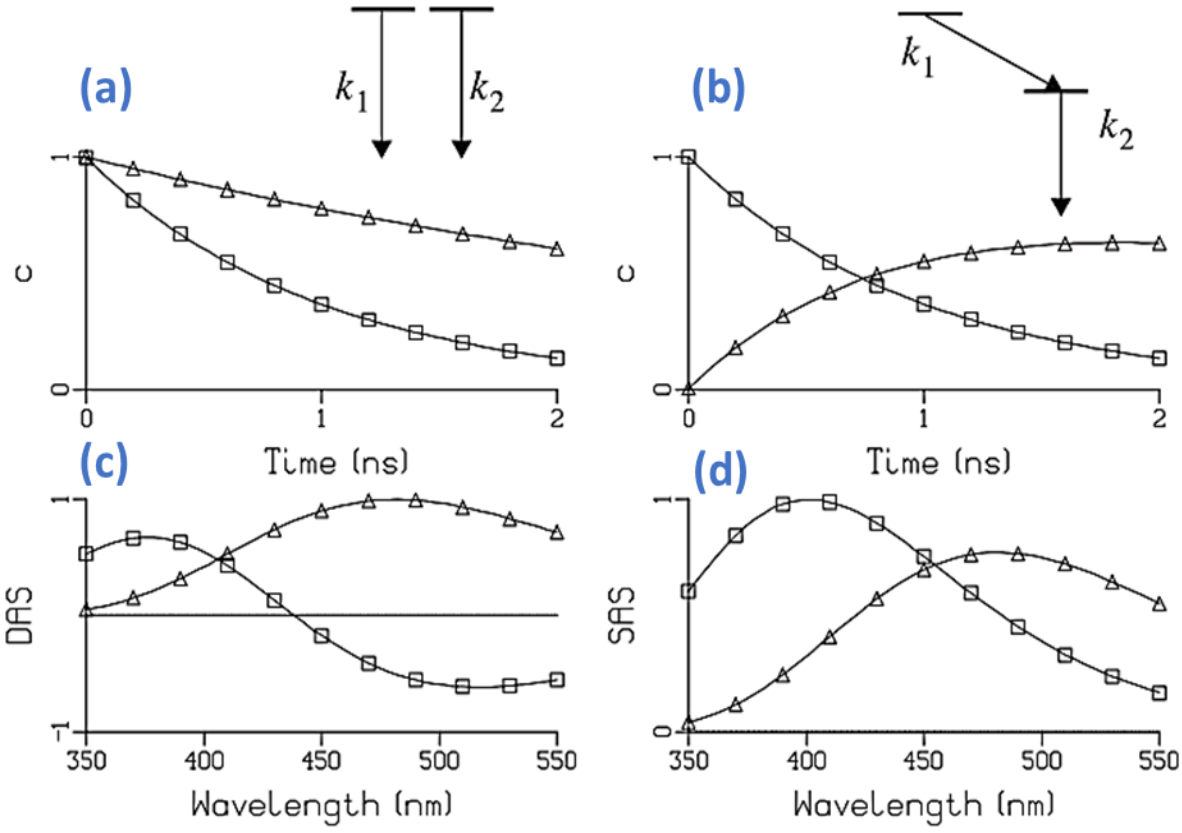

Figure 2.4: A Schematic of global (a, c) and target analysis (b, d). Adapted from reference 14.

Target analysis, on the other hand, utilizes kinetic data provided by the user and performs a multiexponential fit. Unlike global analysis, target analysis assumes that the states in the system do interact with each other. This means that the behavior of one state can be influenced by other states. With this assumption, target analysis can estimate the population of each state over time. The results of target analysis are typically shown in a population versus time plot, as depicted in Figure 2.4(b).[14] This plot displays the relative percentage of each state within the system as a function of time. Moreover, the spectra of the individual states provided by target analysis are termed species-associated spectra (SAS). Each component of the SAS shows the spectral features of a specific state (or species) within the data, as illustrated in Figure 2.4(d).[14] In summary, global analysis assumes independence between states and may overestimate the number of states and produce decay-associated spectra, while target analysis considers interactions between states, estimates their populations, and presents species-associated spectra showing the spectral features of each state.

2.3 List of References

1. J. Brooks, 2009.
2. T. G. Mayerhöfer, S. Pahlow and J. Popp, *ChemPhysChem*, 2020, **21**, 2029-2046.
3. J. R. Lakowicz, *Principles of fluorescence spectroscopy*, Springer, 2006.
4. G. Hungerford, A. Allison, D. McLoskey, M. K. Kuimova, G. Yahioglu and K. Suhling, *The Journal of Physical Chemistry B*, 2009, **113**, 12067-12074.
5. S. Mendoza, E. Bustos, J. Manríquez and L. Godínez, 2015, DOI: 10.1002/9781118684030.ch2, pp. 21-48.
6. N. Elgrishi, K. J. Rountree, B. D. McCarthy, E. S. Rountree, T. T. Eisenhart and J. L. Dempsey, *Journal of Chemical Education*, 2018, **95**, 197-206.
7. C. Sandford, M. A. Edwards, K. J. Klunder, D. P. Hickey, M. Li, K. Barman, M. S. Sigman, H. S. White and S. D. Minteer, *Chemical Science*, 2019, **10**, 6404-6422.
8. C. G. Zoski, *Journal*, 2007.

9. K. Karoń, M. Łapkowski and J. C. Dobrowolski, *Spectrochimica Acta Part A: Molecular and Biomolecular Spectroscopy*, 2021, **250**, 119349.

10. W. Kaim and J. Fiedler, *Chemical Society Reviews*, 2009, **38**, 3373-3382.

11. F. Kanal, 2015.

12. J. Zhang, B. Zhu, L. Zhang and J. Yu, *Chemical Communications*, 2023, **59**, 688-699.

13. R. Berera, R. van Grondelle and J. T. M. Kennis, *Photosynthesis Research*, 2009, **101**, 105-118.

14. I. H. M. van Stokkum, D. S. Larsen and R. van Grondelle, *Biochimica et Biophysica Acta (BBA) - Bioenergetics*, 2004, **1657**, 82-104.

CHAPTER 3

EXPLORING FAR-RED EXCITATION-INDUCED ELECTRON TRANSFER AND NITROGENOUS DONORS' ROLE IN CHARGE SEPARATION: BRIDGING HIGH-ENERGY STATES TO NEAR-IR SENSITIZERS FOR EFFICIENT ELECTRON TRANSFER

3.1 Far-Red Excitation Induced Electron Transfer in Bis Donor-AzaBODIPY Push-Pull Systems; Role of Nitrogenous Donors in Promoting Charge Separation*

3.1.1 Introduction

The study of multi-modular donor-acceptor constructs[1–8] has played a prominent role in a range of applications in energy harvesting, organic electronics, and photonics.[9–17] In this scenario, the use of a π-bridge to covalently connect the donor and acceptor entities is recognized as a means to enhance ICT in the excited state and finely adjust the optical and excited-state properties. Furthermore, when employed in polar solvents, these ICT states have the potential to transition into a fully separated state with complete charge transfer.[18–20] The persistence of charge separated state however depends on the low-lying triplet states of either the donor or acceptor. In such instances, the CR could occur rapidly thus lowering their overall lifetime. In synthetic artificial photosynthetic systems, long-lived charge-separated states (CSS) are often achieved by optimal positioning of the donor and acceptor systems and following a multi-step sequential electron transfer mechanism.[21–26] In a few instances, heavy atom-bearing high-energy triplet sensitizers have also been used to build donor-acceptor constructs to achieve long-lived CSS.[27,28]

Among the electron donor or acceptor photosensitizers, BF_2-chelated azadipyrromethene (abbreviated azaBODIPY),[29] a structural analog of BF_2-chelated dipyrromethene (BODIPY®),[30,31]

* Section 3.1 is reproduced from Alsaleh, Ajyal Z., Dilip Pinjari, Rajneesh Misra, and Francis D'Souza. "Far-Red Excitation Induced Electron Transfer in Bis Donor-Azabodipy Push-Pull Systems; Role of Nitrogenous Donors in Promoting Charge Separation." Chemistry – A European Journal 29, no. 53 (2023): e202301659, doi.org/10.1002/chem.202301659, with permission from John Wiley and Sons.

has recently gained much attention for its novel photochemical properties, applicable in energy harvesting, sensing and imaging applications.[29,30] Depending upon the peripheral substituents, azaBODIPYs absorb in the 300–850 nm region with very high molar absorptivity and desirable emission in the red to the near-IR region (660–900 nm) with quantum yields exceeding 40%.[31] One of the most interesting properties of azaBODIPYs is in their facile reduction making them rarely encountered electron acceptor far-red capturing photosensitizer molecules.[32] In addition, azaBODIPYs are now being explored for applications involving near-IR absorbing dyes for biological applications,[33] photocatalysts,[34] and triplet photosensitizers.[35]

In recent years, we have been involved in exploring novel features of azaBODIPY in photoinduced charge separation and stabilization, useful for light energy conversion and optoelectronic materials. To summarize our key findings, when azaBODIPY was connected to ferrocene, efficient photoinduced reductive electron transfer from ferrocene to ^{1}azaBODIPY* to yield Fc^{+}-azaBODIPY$^{\bullet-}$ was witnessed.[36] Alternatively, when ferrocene was replaced by fullerene, C_{60}, oxidative electron transfer leading to the formation of azaBODIPY$^{\bullet+}$-$C_{60}^{\bullet-}$ was observed.[37] Excitation transfer was observed when either chlorophyll derivatives or BODIPY was covalently linked to azaBODIPY.[38] Interestingly, when two porphyrins were covalently linked to azaBODIPY, the resulting ‘molecular clip’ supramolecularly bound to C_{60} via metal-ligand coordination. In this molecular system, energy and electron transfer events were possible to regulate.[39] Furthermore, by a combination of zinc porphyrin, BODIPY, and azaBODIPY, a novel broad-band capturing and emitting supramolecular push-pull system capable of wide-band emission was recently reported.[40] Supramolecular donor-acceptor hybrids of zinc phthalocyanine (ZnPc)-azaBODIPY and zinc naphthalocyanine (ZnNc)-azaBODIPY, that is, near-infrared absorbing entities, were constructed and photoinduced electron transfer by near-IR excitation was

witnessed,[41] wherein $ZnPc^{\bullet+}$- $azaBODIPY^{\bullet-}$ and $ZnNc^{\bullet+}$- $azaBODIPY^{\bullet-}$ were the reaction products. Directly connected azaBODIPY-donor systems exhibiting intramolecular charge transfer were also reported.[42] More recently, azaBODIPY was covalently linked to powerful electron acceptors, tetracyanobutadiene (TCBD) and extended-TCBD, and the occurrence of excited state charge transfer was successfully demonstrated.[43] These are in addition to studies reported by other groups.[44–55]

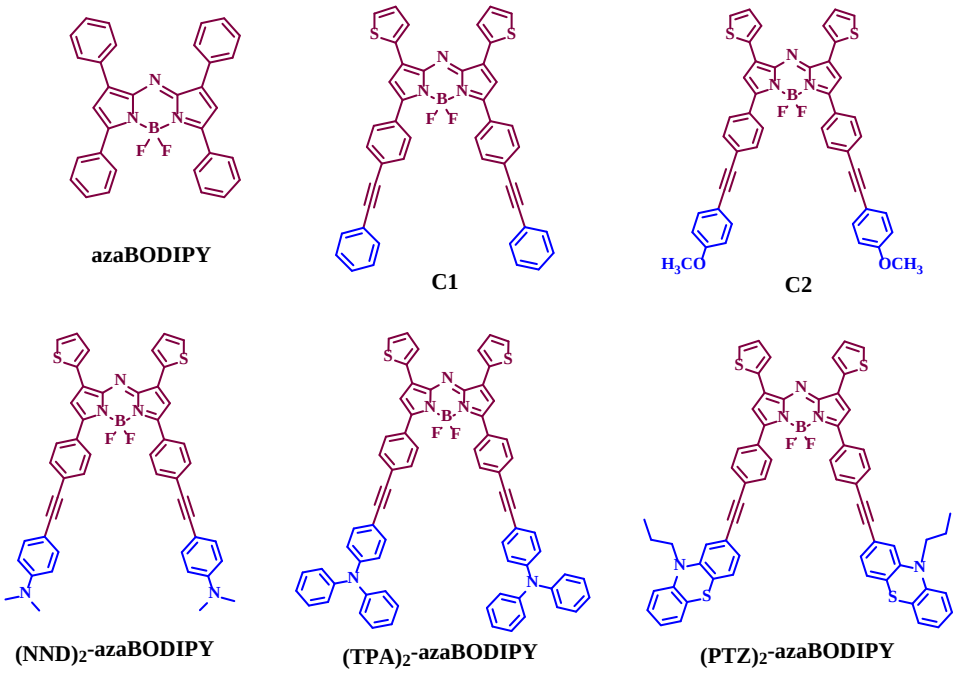

Figure 3.1: Structures and abbreviations of pristine azaBODIPY, control azaBODIPYs carrying ethynyl linkers, and nitrogenous amine donors carrying azaBODIPY push-pull systems studied in the present investigation.

In the present study, we report a new series of bisdonor-acceptor push-pull systems featuring nitrogenous electron donors, viz., *N*,*N*-dimethylaniline (NND), triphenylamine (TPA), and phenothiazine (PTZ) with the help of acetylene linkers (see Fig. 3.1 for structures along with those of the control compounds). Here, the azaBODIPY core is different from the traditionally used azaBODIPY in which two β-pyrrole-phenyl rings have been replaced with thiophene units and the α-phenyl groups have acetenyl-phenyl entities. The immediate consequence of this small

structural change is in extending the absorption envelope by 40 nm to the red making them far-red absorbers. The significance of the nitrogenous donors in governing far-red excited state charge transfer/separation as a function of solvent polarity is presented. Our studies demonstrate that in nonpolar toluene, the push-pull systems undergo partial charge transfer while in polar, benzonitrile, they undergo full charge separation. The persistence of the charge-separated state (CSS) with respect to the nature of the donor, as revealed by transient pump-probe spectroscopic studies is presented.

3.1.2 Results and Discussion

Synthesis of different donor substituted aza-BODIPY derivatives namely $(NND)_2$-azaBODIPY, $(TPA)_2$-azaBODIPY, $(PTZ)_2$-azaBODIPY along with control azaBODIPYs (C1, C2) is shown in Scheme 3.1. Dibromo-aza-BODIPY 1 was reacted with various ethynyl substituted aryl derivatives (phenyl, anisole, N,N-dimethylamine, triphenylamine and phenothiazine) under Pd-catalyzed Sonogashira coupling reaction to obtain C1, C2, $(NND)_2$-azaBODIPY, $(TPA)_2$-azaBODIPY, $(PTZ)_2$-azaBODIPY with 85%, 80%, 75%, 82%, and 77% yield, respectively. This reaction was carried out in a THF/TEA mixture (v/v,1:1) with Pd-catalyst at 60 ^oC for 12 hrs under an argon atmosphere. The synthesis of triphenylamine based aza-BODIPY $(TPA)_2$-azaBODIPY was recently reported by us.[43] The precursor dibromo-aza-BODIPY 1 was synthesized using a reported procedure by reacting thiophene-2-carbaldehyde with 4-bromo-acetophenone.[56] All the aryl substituted azaBODIPY derivatives (C1, C2, $(NND)_2$-azaBODIPY, $(TPA)_2$-azaBODIPY, $(PTZ)_2$-azaBODIPY) were purified by using neutral activated alumina.

The absorption and fluorescence spectra of the investigated compounds in benzonitrile, DCB, and toluene are depicted in Figure 3.2 while the optical data are summarized in Table 3.1. In benzonitrile, the pristine azaBODIPY peak located at 671 nm was shifted to 724 and 731 nm in

C1 and C2, respectively. That is, a 43–49 nm red shift as a consequence of the peripheral substitution of thiophene and phenyl-acetenyl entities was witnessed. Appending electron donors further shifted the peak maxima to another 20–30 nm depending on the type of donor entities. These observations suggest electronic interactions between the azaBODIPY and donor entities via the acetenyl linkers. Such a trend was also observed in DCB and toluene. For example, in toluene, a 46–51 nm red-shift between azaBODIPY and C1/C2 and a further 20–30 nm after appending the electron donor entities.

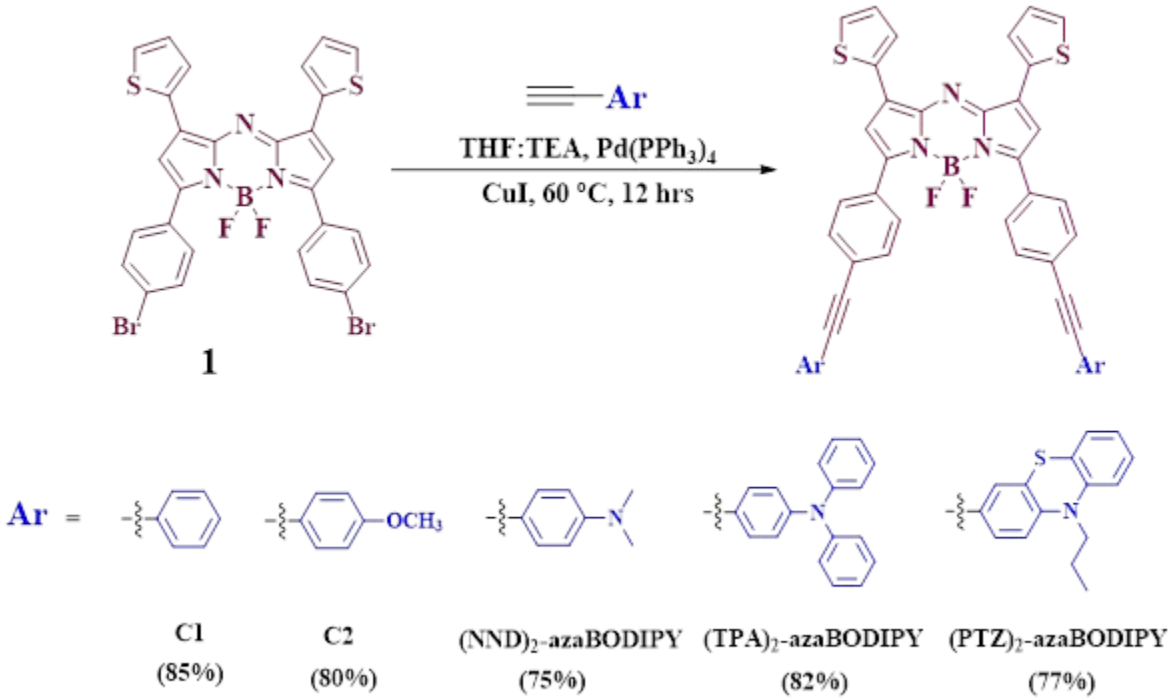

Scheme 3.1: Synthetic route for various aryl functionalized azaBODIPY donor-acceptor constucts.

Table 3.1: **Optical absorption and emission data for the investigated compounds in solvents of varying polarity.**

Compound	Solvent	λ_{abs}, nm	λ_{em}, nm	$E_{0,0}$	Φ_f
azaBODIPY	PhCN	326, 511, 671	702	1.80	0.23[a]
C1		358, 551, 724	751	1.68	0.028
C2		320, 552, 732	762	1.66	0.016
$(NND)_2$-azaBODIPY		359, 609, 758	--	--	--
$(TPA)_2$-azaBODIPY		367, 590, 745	--	--	--

Compound	Solvent	λ_{abs}, nm	λ_{em}, nm	$E_{0,0}$	Φ_f
$(PTZ)_2$-azaBODIPY		365, 584, 744	--	--	--
azaBODIPY	DCB	315, 503, 670	700	1.80	0.23[a]
C1		356, 542,727	752	1.68	0.030
C2		350, 521, 737	763	1.65	0.025
$(NND)_2$-azaBODIPY		359, 615, 761	828	1.56	0.010
$(TPA)_2$-azaBODIPY		371, 594, 751	--	--	--
$(PTZ)_2$-azaBODIPY		369, 570, 745	--	--	--
azaBODIPY	Toluene	300, 506, 663	686	1.83	0.23[a]
C1		354, 463, 535	751	1.69	0.033
C2		319, 492, 536	759	1.67	0.027
$(NND)_2$-azaBODIPY		351, 600, 750	813	1.59	0.019
$(TPA)_2$-azaBODIPY		366, 591, 742	777	1.63	0.018
$(PTZ)_2$-azaBODIPY		363, 575, 740	773	1.64	0.0007

a -from Refences 30.

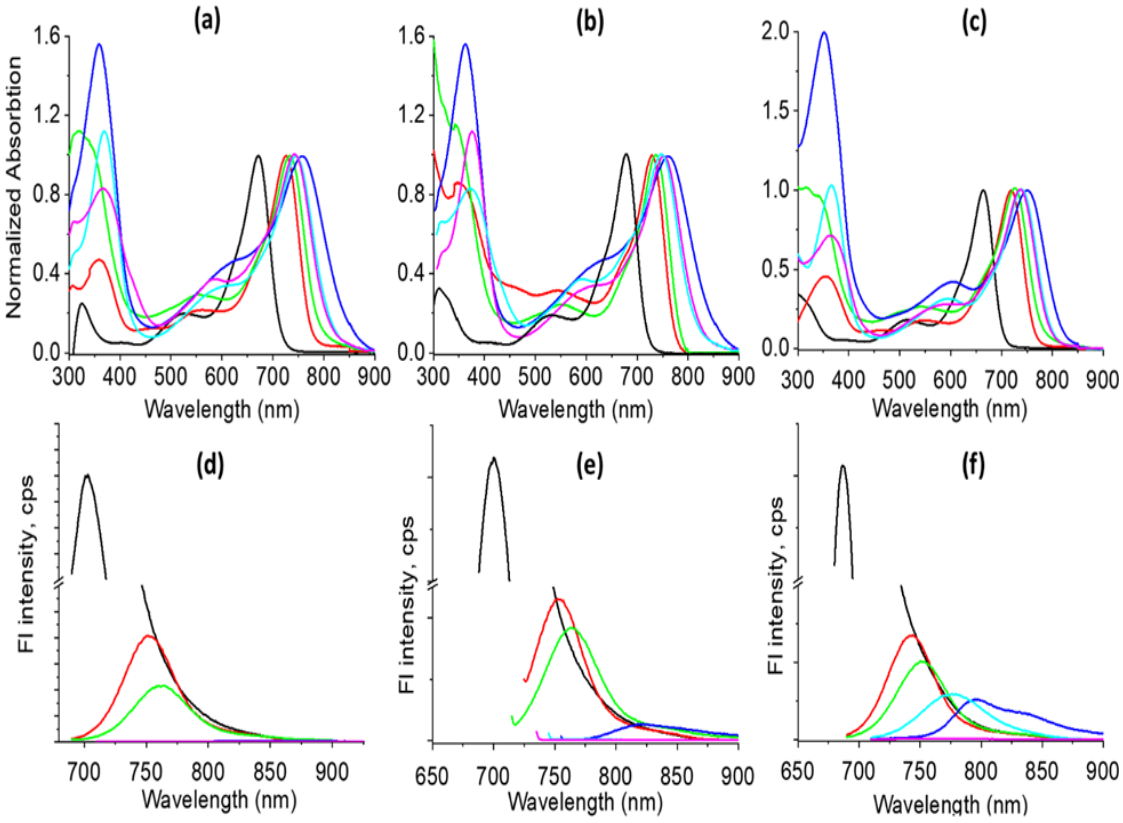

Figure 3.2: Absorption (a, b and c) fluorescence (d, e and f) spectrum of azaBODIPY (black), C1 (red), C2 (green), $(NND)_2$-azaBODIPY (blue), $(TPA)_2$-azaBODIPY (light blue), and $(PTZ)_2$-azaBODIPY (magenta) in benzonitrile (a and d), DCB (b and e), and toluene (c and f). Samples were excited at the far-red peak listed in Table 3.1.

Considerable red-shift in the fluorescence emission was also witnessed. At the excitation of azaBODIPY absorption peak maxima, the fluorescence emission of azaBODIPY in benzonitrile, located at 702 nm, was red shifted to 751 and 762 nm in C1 and C2. However, in the push-pull systems, the emission was quantitatively quenched. Interestingly, in DCB and toluene, although such a trend with respect to substitution was observed, the quenching was only nearly 50% in the case of $(NND)_2$-azaBODIPY and $(TPA)_2$-azaBODIPY push-pull systems (slightly more in DCB), however, it was over 96% for $(PTZ)_2$-azaBODIPY. These results indicate the significance of the nature of donors and solvents in governing the fluorescence properties of the investigated push-pull systems. The measured Φ_f are also listed in Table 3.1. Substantially lower Φ_f for C1 and C2 compared to azaBODIPY, and almost zero for the push-pull systems in benzonitrile were noted. The singlet excited energy was calculated from the average energy of the low energy absorption and fluorescence peak and was found to be ~1.67 eV which was about 0.13 eV lower than that of pristine azaBODIPY, being 1.80 eV. The triplet energy of azaBODIPY reported earlier is about 0.92 eV.[32,36] The fluorescence lifetime determined from the time-correlated single photon counting technique resulted in a lifetime of ~4 ns for azaBODIPY that was substantially lower in C1 and C2 ranging between 0.7–1.5 ns depending upon the solvent. For the push-pull systems, due to low emissions, no reliable data could be secured.

Fluorescence studies were also performed by exciting the samples corresponding to the absorption peak maxima of the nitrogenous donors. As shown in Figure 3.3, in benzonitrile, pristine TPA and PTZ revealed absorption peak maxima at 330 and 370 nm, respectively. In the push-pull systems, they revealed minor changes due to linkage and overlap of azaBODIPY absorption in this region. Fluorescence peak maxima of TPA and PTZ were located at 405 and 488 nm, respectively. Interestingly, in the push-pull systems, these emissions were quenched over 95%

with no new peaks in the region of azaBODIPY emission suggesting that the quenching is likely not due to energy transfer. Such a trend was also observed in toluene; however, the quenching was ~80%. The solvent polarity dependent quenching suggests it is due to charge transfer type interactions.[8]

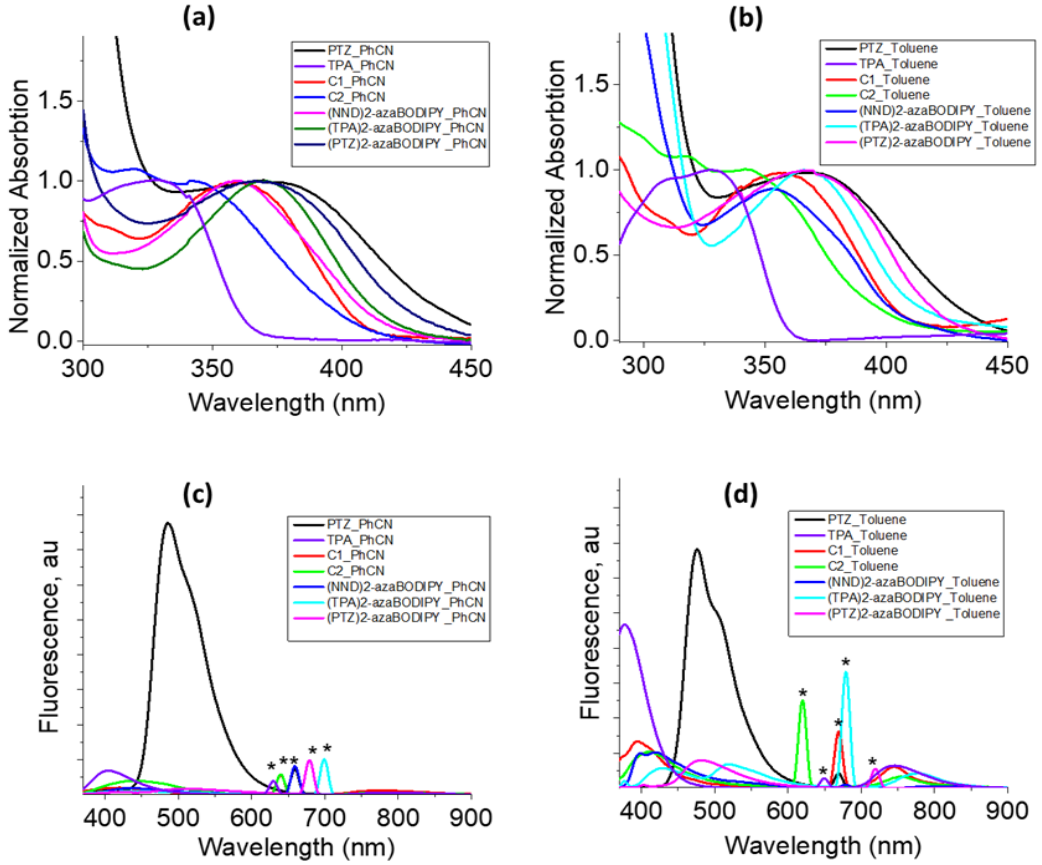

Figure 3.3: Absorption (a, and b) fluorescence (c and d) spectrum of indicated compounds in benzonitrile (a and c), and toluene (c and f). Samples were excited corresponding to the terminal electron donor entities. The asterisks indicate grating scattered peaks, and in (d), the peak at 750 nm of TPA is due to the second harmonic and not real fluorescence.

As the redox potentials of the donor and acceptor take up a key role in governing the free-energy changes for electron transfer reactions, electrochemical studies using both differential pulse voltammetry (DPV) and cyclic voltammetry (CV) were performed in benzonitrile. Figure 3.4 shows the DPVs of the compounds, while Table 3.2 lists redox potential along with the calculated free-energy values for charge separation and recombination.

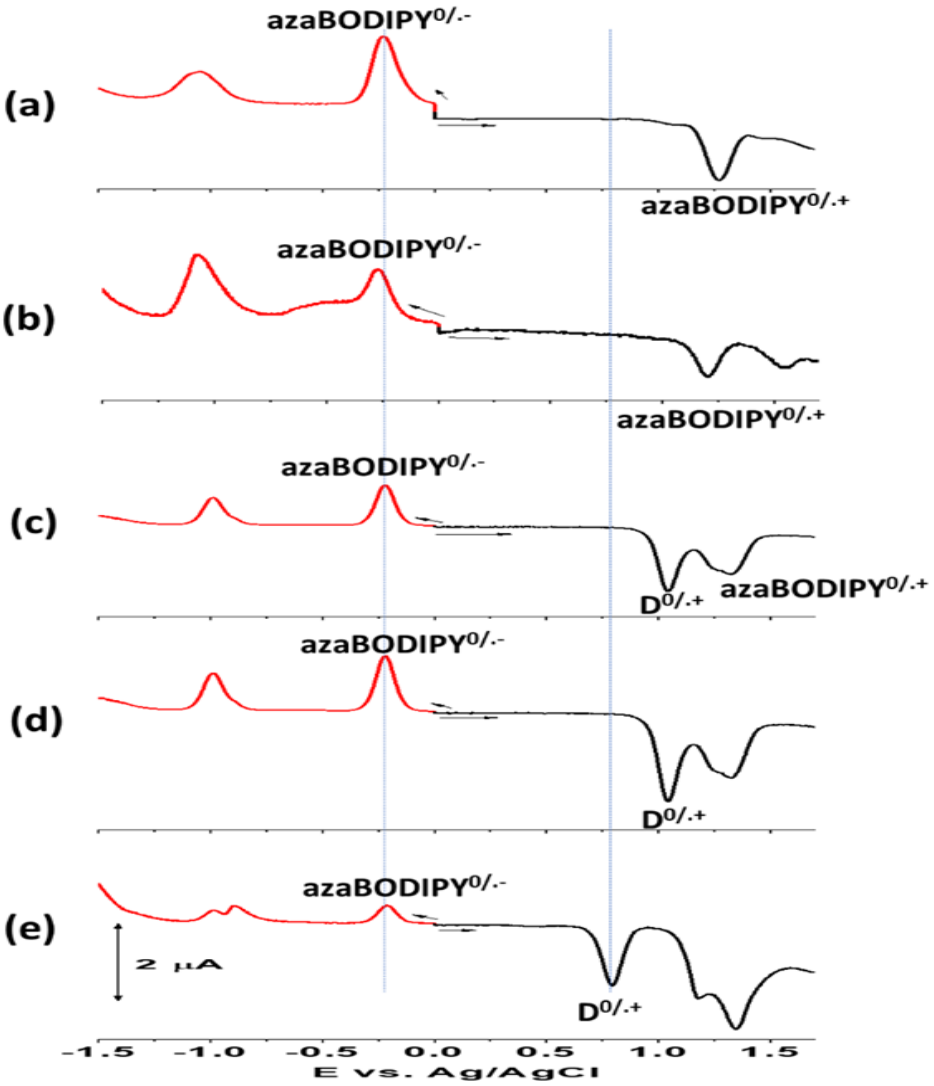

Figure 3.4: Differential pulse voltammograms of (a) C1, (b) C2 (c) $(NND)_2$-azaBODIPY (d) $(TPA)_2$-azaBODIPY, and (e) $(PTZ)_2$-azaBODIPY in benzonitrile containing 0.1 M $(TBA)ClO_4$.

Table 3.2: **Electrochemical redox potentials and free-energy changes associated with light-induced electron transfer of the push-pull systems.[b]**

Compound	Reduction, V vs. Ag/AgCl	Oxidation, V vs. Ag/AgCl	ΔG_s, eV	ΔG_{CS}, eV	ΔG_{CR}, eV
C1	-1.06, -0.22	1.27	--	--	--
C2	-1.06, -0.27	1.20	--	--	--
$(NND)_2$-azaBODIPY	-1.02, -0.25	0.85,[a] 1.10	-0.094	-0.26	-1.36
$(TPA)_2$-azaBODIPY	-0.99, -0.21	1.05,[a] 1.25	-0.086	-0.24	-1.37
$(PTZ)_2$-azaBODIPY	-0.89, -0.21	0.78,[a] 1,19	-0.086	-0.32	-1.31

a - Oxidation corresponding to the Donor entity. b - Estimated error in values = +5%

The first reduction and first oxidation of C1 were located at -0.22 and 1.27 V vs. Ag/AgCl while that of C2 these values were at -0.27 and 1.20 V resulting in an electrochemical redox gap of 1.47 to 1.49 V which was about 0.20 V smaller than that calculated from optical data (see $E_{0,0}$ values in Table 3.1). Importantly, the facile reduction of azaBODIPY in C1 and C2 was borne out. The presence of donor entities in the push-pull systems revealed additional oxidation waves and they appeared prior to the oxidation process of the azaBODIPY entity. Owing to the presence of two donor entities in each push-pull system, the peak currents were roughly twice as much of the first reduction of the azaBODIPY entity of a given push-pull system. Oxidation of NND, TPA, and PTZ entities of the push-pull systems appeared at 0.85, 1.05 and 0.78 V, facile oxidation of PTZ compared to the other two donors was clear from this study. Unlike the reversible azaBODIPY first reduction, the oxidation process of the donor entities in the push-pull systems was quasi-reversible.

Frontier orbitals of the investigated compounds on B3LYP/6-31G(d, p) optimized structures[57] are shown in Figure 3.5. For C1 and C2 having no donor entities, the HOMO was distributed all over the molecule including the phenyl-acetylene linkers (see Fig. 3.5 for C2), however, the HOMO-1 was more on the phenyl-acetylene linkers. The LUMO was mainly on the azaBODIPY part with considerable coefficients on the thiophene entities while the LUMO+1 were distributed on the entire molecule without appreciable coefficients on the thiophene entities. Having two donor entities on the azaBODIPY revealed notable changes (Fig. 3.5 b to d). In all three push-pull systems, the HOMO was distributed on the entire molecule including the donor entities but without contributions to the thiophene entities. Interestingly, the HOMO-1 was localized symmetrically on the acetylene-donor part of the push-pull systems. The LUMO of the push-pull systems was on the azaBODIPY entity with contributions on the thiophene units while

LUMO+1 were on the azaBODIPY-acetylene part of the molecules. A charge transfer from HOMO → LUMO or HOMO-1 → LUMO could be envisioned from the location of the frontier orbitals.

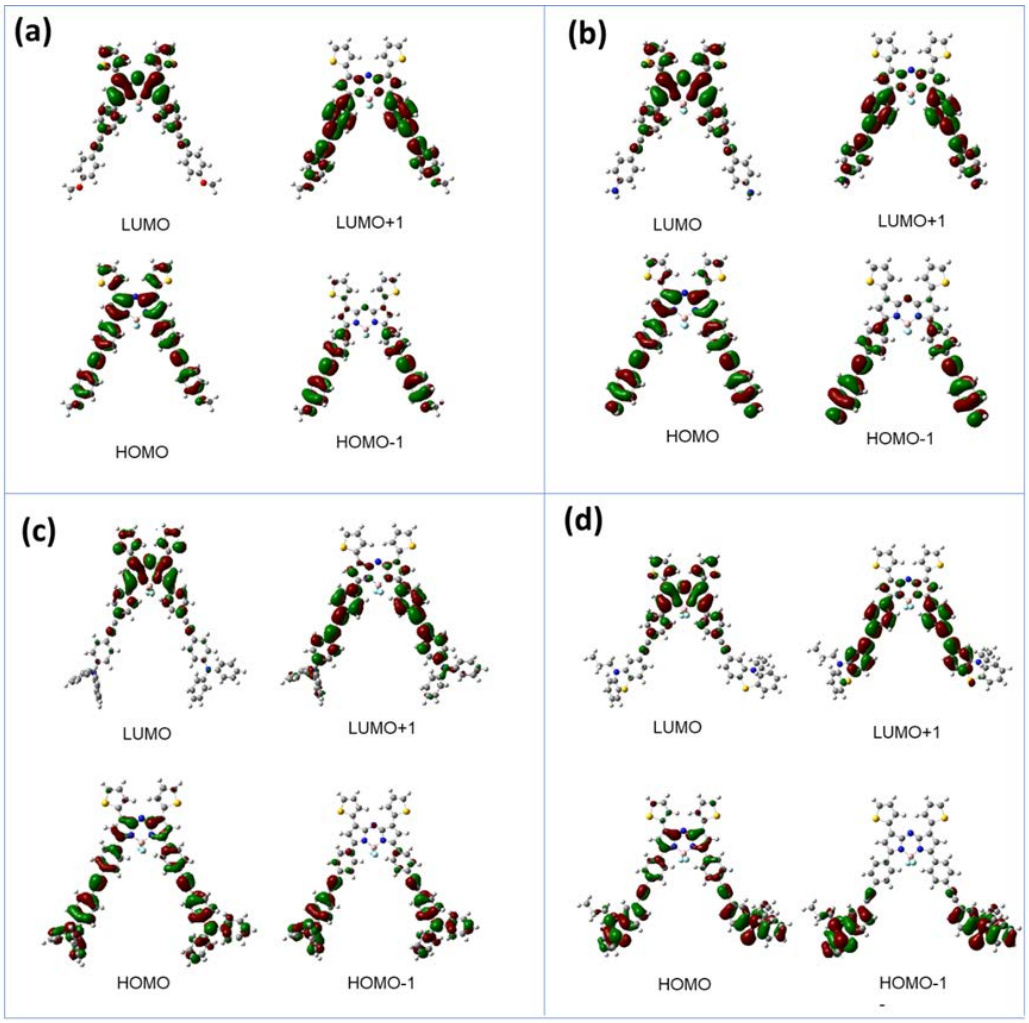

Figure 3.5: Frontier orbitals on B3LYP/6-31G (d, p) optimized structures of (a) C2 (b) $(NND)_2$-azaBODIPY, (c) $(TPA)_2$-azaBODIPY, and (d) $(PTZ)_2$-azaBODIPY.

The redox potentials are used in combination with optical data to estimate the energies of the radical ion pair states (E_{CS}) and free energy change for the charge separation (ΔG_{CS}) by using the following equations:[58]

$$E_{CS} = e[E_{1/2}(D^{+\cdot}/D) - E_{1/2}(A/A^{-\cdot})] + G_S \quad \text{(Eq. 3.1)}$$

$$\Delta G_{CS} = E_{CS} - E_{0-0} \quad \text{(Eq. 3.2)}$$

where $E_{1/2}(D^{\bullet+}/D)$ is the first oxidation potential of the donor, $E_{1/2}(A/A^{\bullet-})$ is the first reduction potential of the acceptor and G_S is the ion-pair stabilization energy,

$$G_S = \frac{-e^2}{4\pi\varepsilon_0\varepsilon_S R_{D-A}} \quad \text{(Eq. 3.3)}$$

where $R_{D\text{-}A}$ is the centre-to-centre distance between the donor and acceptor, ε_S is the dielectric constant of the solvent used for the optical and redox studies, in this case benzonitrile. The lowest excited singlet state energy ($E_{0\text{-}0}$) is estimated from the crossing point of absorption and fluorescence spectra as listed in Table 3.1.

The estimated free-energy values listed in Table 3.2 reveal that reductive electron transfer (excited molecule accepting an electron) is indeed possible in these push-pull systems from one of the donor entities to the single excited azaBODIPY. Energy level diagrams were subsequently established using the information discussed in the above paragraphs and such diagrams are shown in Figure 3.6. For C1 and C2, a simple scheme could be envisioned, that is, excitation of azaBODIPY corresponding to its singlet state (low energy absorption peak maxima in Table 3.1) would produce ^{1}azaBODIPY*. The ^{1}azaBODIPY* thus produced could emit from the singlet excited state (radiative fluorescence) or undergo nonradiative energy loss (thermal), or in part undergo ISC to populate the triplet state. The ^{3}azaBODIPY* would eventually return to the ground state via the process of phosphorescence (Fig. 3.6a).

Interestingly, in the case of the push-pull systems where efficient fluorescence quenching was observed, deactivation of ^{1}azaBODIPY* *via* radiative emission is going to a minor process, and as charge separation is thermodynamically feasible, ^{1}azaBODIPY* could undergo reductive electron transfer by abstracting an electron from one of the donor entities to the half-filled HOMO (or HOMO-1) orbital, resulting in $D^{\bullet+}$-azaBODIPY$^{\bullet-}$ (D = NND, TPA, or PTZ) charge separated states. As the entities in the push-pull system are coupled, an intermediate charge transfer state,

$D^{\delta+}$-azaBODIPY$^{\delta-}$, prior to the solvated charge-separated state could also be envisioned. The charge-separated state could return to the ground state directly by the process of charge recombination either radiatively via the process of charge recombination emission or nonradiatively. Alternatively, this state could populate the low-lying ^{3}azaBODIPY* (E_T ~ 1.0 eV). The newly formed ^{3}azaBODIPY* would return to the ground state via phosphorescence or by nonradiative mechanism. As no charge recombination emission was observed in benzonitrile for the investigated push-pull systems, the latter mechanism of populating the ^{3}azaBODIPY* could be considered a more likely path (Fig. 3.6b). In nonpolar toluene, a complete charge separation is not expected due to high solvation energy demand, however, a partial charge transfer could occur as is supported by fluorescence quenching observed for these push-pull systems in toluene.

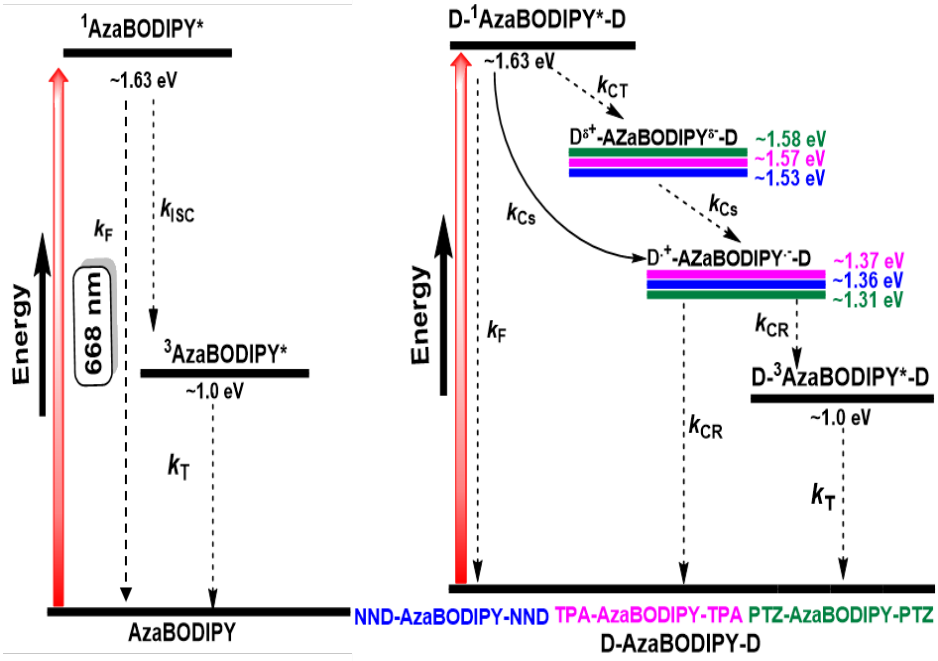

Figure 3.6: Jablonski-type energy level diagram for the (a) control azaBODIPY and (b) push-pull systems in benzonitrile. Solid line – most likely process, dashed line-less likely process.

Spectroelectrochemical studies were subsequently performed to characterize the one-electron reduced and one-electron oxidized products of the investigated compounds, as shown in Figure 3.7. For each process a potential 100 mV past the peak potential was applied and the spectra

were recorded until no additional changes were observed. During the process of first reduction of control azaBODIPY (C2), intensity decrease of the original peaks was associated with new peaks 456, 524, and 918 nm. Isosbestic points at 388 and 783 nm were also observed. Conversely, during the first oxidation process, a decrease in intensity of the original peaks did not result in new peaks, only an increase in intensity in the 300–320 nm range was observed. For the push-pull systems, the spectral trends were almost similar but with slightly red-shifted peaks. For example, for $(TPA)_2$-azaBODIPY, new peaks of one-electron reduced product were located at 491, 533 and 924 nm, however, no new peaks were observed during the process of one-electron oxidation except for a blue-shift of 10 nm in the case of $(TPA)_2$-azaBODIPY for the high-energy UV-band corresponding to the TPA donor entities was observed. It is important to note that although the oxidation is mainly donor-centered, the reduction in azaBODIPY peaks suggest strong electronic coupling between them, as suggested by the distribution of the HOMO orbitals.

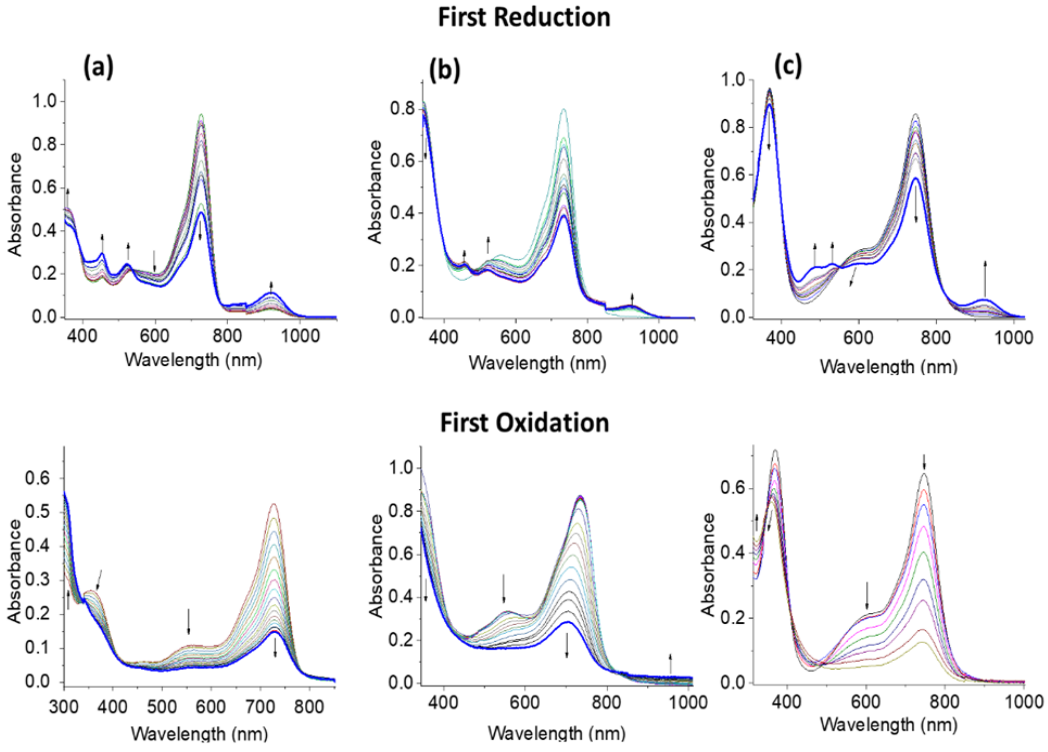

Figure 3.7: Spectral changes during first reduction (top) and first oxidation (bottom) of (a) C1, (b) $(NND)_2$-azaBODIPY and $(TPA)_2$-azaBODIPY in benzonitrile containing 0.2 M $(TBA)ClO_4$.

Finally, pump-probe studies were performed to probe photodynamics and secure evidence of charge separation in the push-pull systems. Figure 3.8a shows the femtosecond transient absorption (fs-TA) spectra at the indicated delay times of control azaBODIPY, C2 in benzonitrile. The instantaneously formed ^{1}azaBODIPY* revealed excited state absorption bands at 438, 580, and 1080 nm. In addition, negative peaks at 535, 663 and 738 nm were observed. By comparison with the absorption and fluorescence, the first two peaks are attributed to the ground state bleaching (GSB) and the latter to stimulated emission (SE). Decay of the positive peaks and recovery of the negative peaks started slowly developing new peaks around 625, 678 and 830 nm that could be attributed to ^{3}azaBODIPY* although such a process was not complete within the delay time window of 3 ns.

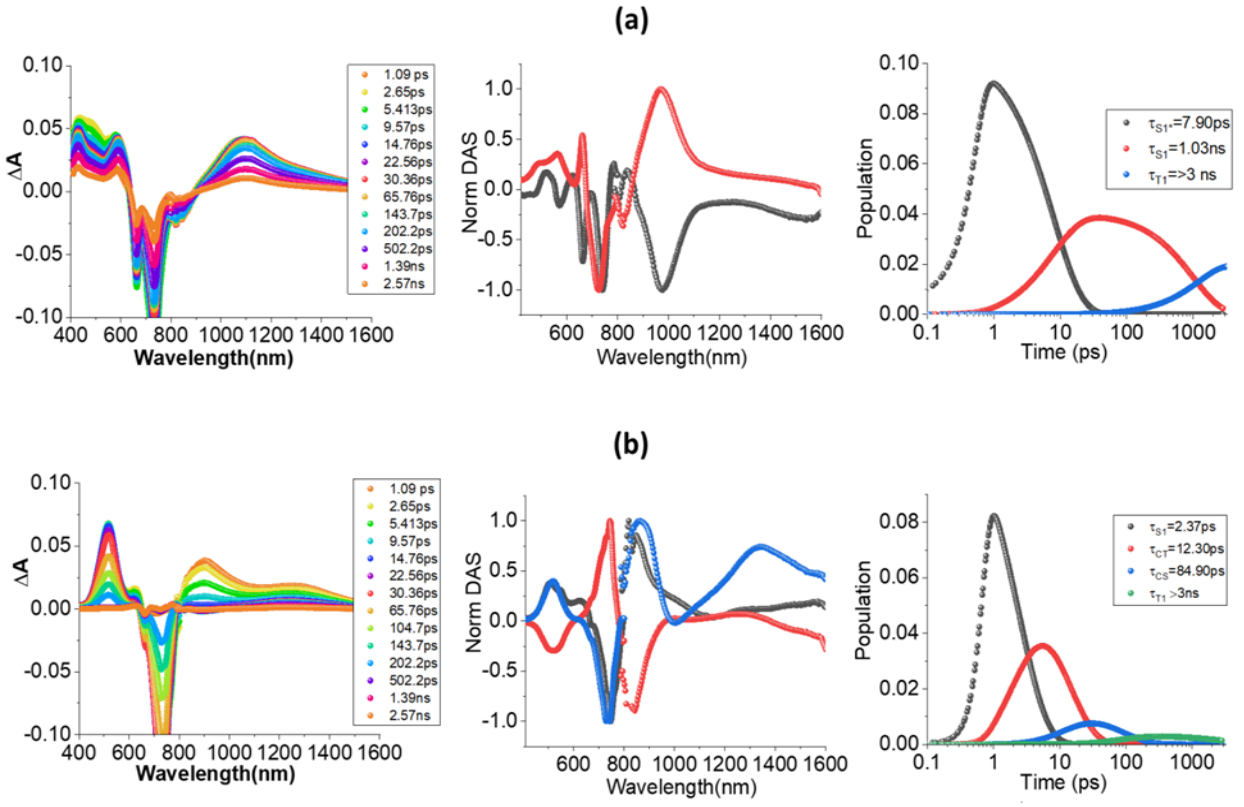

Figure 3.8: Fs-TA spectra at the indicated delay times of (a) C2 and (b) $(PTZ)_2$-azaBODIPY in benzonitrile at the excitation wavelength of 668 nm. The decay-associated spectra and population time profiles from GloTarAn analysis are shown in the middle and right-hand panels, respectively. The DAS of T_1 state is not shown for clarity.

The data was further analyzed using Global Target Analysis (Glotaran) program.[59] A three-component fit, representing $S_0 \rightarrow S_1 \rightarrow T_1$ was adopted. The decay associated spectra (DAS) are shown in Figure 3.8a middle panel were good complementarity between the two singlet states was apparent. Time constants of 7.9 ps for $S_0 \rightarrow S_1$ population and 1.03 ns for the S_1 state were obtained (Fig. 3.8a, right-hand panel). The S_1 lifetime agreed well with the earlier discussed lifetime from the TCSPC technique. A third component with a lifetime > 3 ns was also observed. Nanosecond transient absorption (ns-TA) spectral studies resulted in weak/noisy spectra from where the time constant for the triplet state was difficult to arrive.

Figure 3.8b shows the fs-TA spectra at the indicated delay times $(PTZ)_2$-azaBODIPY in benzonitrile. At the earliest delay time of 1–2 ps, peaks corresponding to both S_1 and CT state were visible. ESA peaks at 500, 900 and 1317 nm were observed. In addition, negative peaks at 663 and 744 nm, corresponding to GSB and SE were observed. During the next 30 ps, the positive ESA peaks experienced a small spectral shift, that is, the 900 nm peak shifted to 890 nm and the 1317 nm peak moved to 1346 nm, likely to the transformation of CT $\rightarrow$ CS was observed. In the next 30–100 ps range, new peaks started emerging at 626, 678 and 826 nm, attributable to the CS state populating the triplet state. Glotaran analysis of the data by fitting $S_1 \rightarrow$ CT $\rightarrow$ CS $\rightarrow T_1$ state is shown in Figure 3.8b, middle panel. Good complementarity for the conversion of CT $\rightarrow$ CS (inverse of the peaks between the two states) was observed. The derived time constants were found to be 12.3 ps for the CT state and 84.9 ps for CS (Fig. 3.8b, right-hand panel).

As shown in Figure 3.9, fs-TA spectral features of the push-pull systems $(NND)_2$-azaBODIPY and $(TPA)_2$-azaBODIPY closely resembled that of $(PTZ)_2$-azaBODIPY. These results conclusively prove charge separation in the push-pull systems. Time constants for the different processes from Glotaran analysis are summarized in Table 3.3. In all, the CS state lasted

between 50–200 ps depending on the nature of the Donor entity suggesting charge stabilization to some extent in these push-pull systems in benzonitrile.

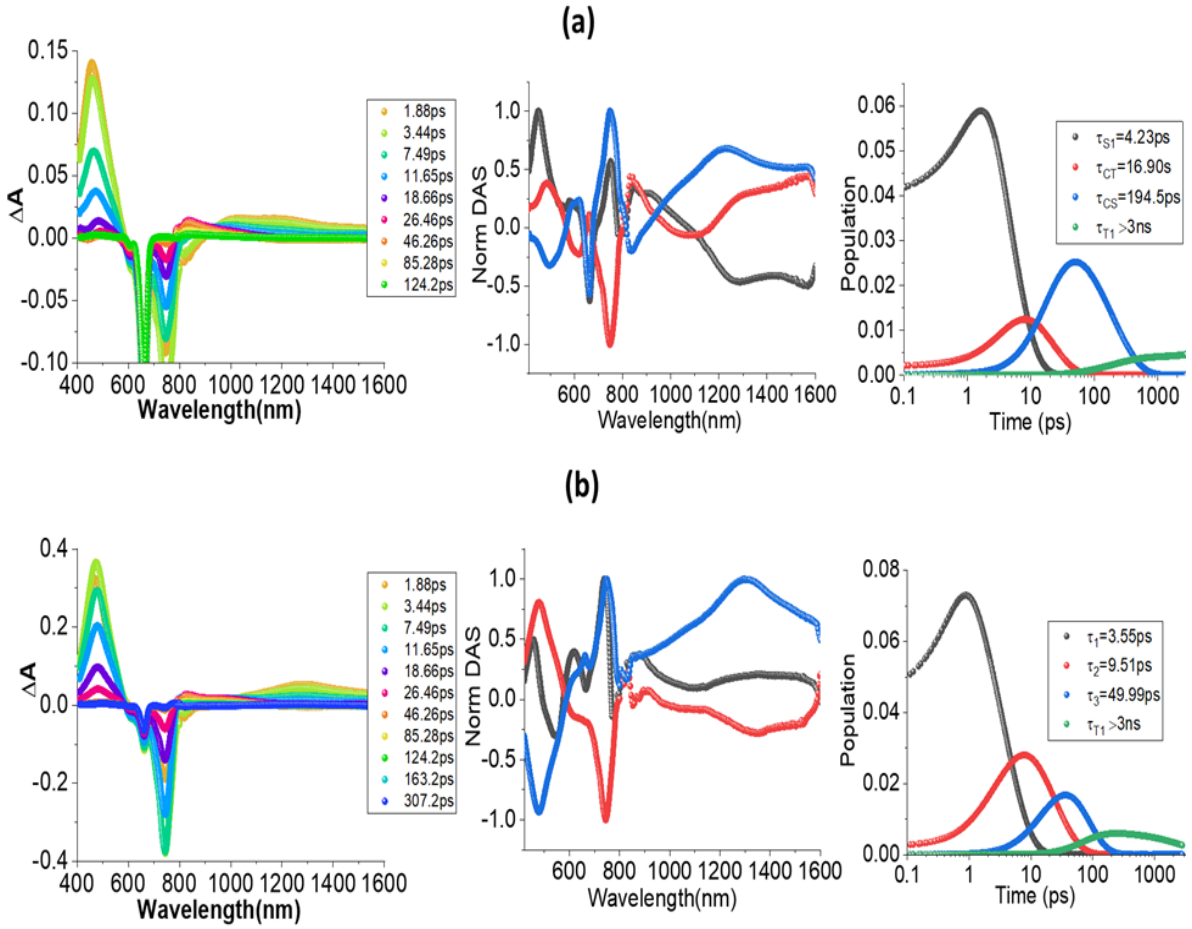

Figure 3.9: Fs-TA spectra at the indicated delay times of (a) $(NND)_2$-azaBODIPY and (b) $(TPA)_2$-azaBODIPY in benzonitrile at the excitation wavelength of 668 nm. The decay-associated spectra and population time profiles from GloTarAn analysis is shown in the middle and right-hand panels, respectively. The DAS of T_1 state is not shown for clarity.

Table 3.3: **Kinetic values for different photo events of the studies systems.**[a]

Compound	Solvent	τ_{rise}, ps	τ_{S1}, ps	τ_{CT}, ps	τ_{CS}, ps
C1	PhCN	7.90	1000	--	--
C2		6.33	998	--	--
$(NND)_2$-azaBODIPY		--	4.23	16.99	194.5
$(TPA)_2$-azaBODIPY		--	3.55	9.51	49.99
$(PTZ)_2$-azaBODIPY		--	2.37	12.30	84.90
C1	Toluene	7.72	1060	--	--

Compound	Solvent	τ_{rise}, ps	τ_{S1}, ps	τ_{CT}, ps	τ_{CS}, ps
C2		6.53	1100	--	--
$(NND)_2$-azaBODIPY		--	5.97	265.4	--
$(TPA)_2$-azaBODIPY		--	3.74	30.3	--
$(PTZ)_2$-azaBODIPY		--	3.10	90.3	--

a -estimated error = $\pm$10%

The photophysical properties were also monitored in toluene as charge transfer was predicted for the push-pull systems due to substantial lowering of their fluorescence quantum yields (Table 3.1). Figure 3.10a shows the fs-TA spectra at the indicated delay times for control C2. Overall, the spectral features were similar to that observed in benzonitrile. Time constants for the different events were evaluated by Glotaran analysis of the data by fitting $S_0 \rightarrow S_1 \rightarrow T_1 \rightarrow$ GS model (Fig. 3.10b, middle panel and right-hand panel) and the results are given in Table 3.3. The time constants for S_1 state agreed well with lifetimes determined from the TCSPC technique.

Fs-TA results obtained for $(PTZ)_2$-azaBODIPY are shown in Figure 3.10b. Immediately after excitation, the spectrum recorded at a delay time of 1 ps revealed ESA peaks at 502, 898, and 1323 nm. In addition, GSB peaks at 660 nm and SE peaks at 744 nm were observed. The ESA peaks at 502 and 898 nm had features of $PTZ^{\bullet+}$-$azaBODIPY^{\bullet-}$ charge transfer state suggesting its ultrafast occurrence from the initially formed ^{1}azaBODIPY*. Decay and recovery of the positive and negative peaks revealed another set of new peaks at 683 and 827 nm expected for ^{3}azaBODIPY*. The data was further subjected to Glotaran analysis by providing two kinetic paths, viz: $S_o \rightarrow S_1 \rightarrow$ CT $\rightarrow$ CS $\rightarrow$ GS and $S_o \rightarrow S_1 \rightarrow$ CT $\rightarrow$ GS. The last one is without the charge separated state. As shown in Figure 3.10(b) middle panel, the best fit was the latter model. This is reasonable since formation of fully charge separated state, $PTZ^{\bullet+}$-$azaBODIPY^{\bullet-}$, in the nonpolar solvent is unlikely due to the high solvation energy requirement. The time constant for the CT state

was about 90 ps (see Fig. 3.10b, right-hand panel).

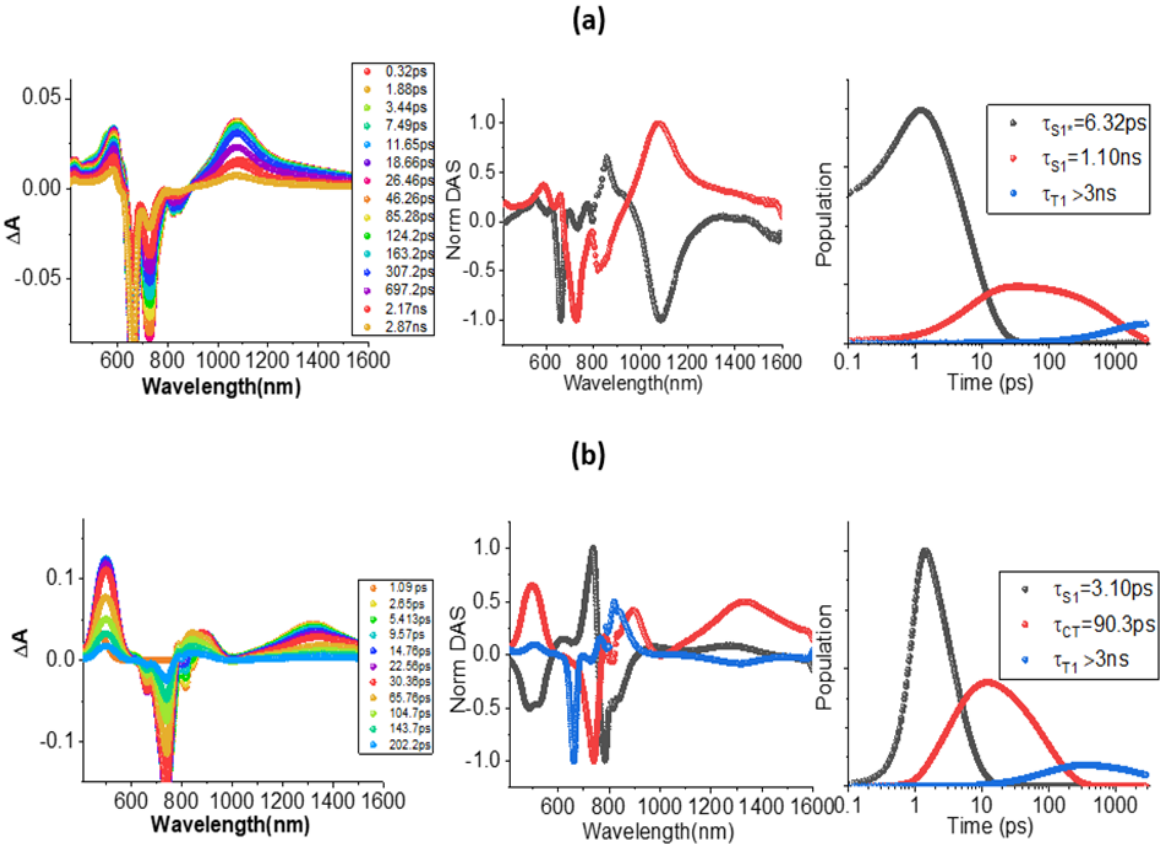

Figure 3.10: Fs-TA spectra at the indicated delay times of (a) C2 and (b) $(PTZ)_2$-azaBODIPY in toluene at the excitation wavelength of 668 nm. The decay-associated spectra and population time profiles from GloTarAn analysis is shown in the middle and right-hand panels, respectively. The DAS of T_1 state is not shown for clarity.

For the next two push-pull systems, $(NND)_2$-azaBODIPY and $(TPA)_2$-azaBODIPY, transient spectral features revealed features of charge transfer, however, not as well developed as that of $(PTZ)_2$-azaBODIPY (Fig. 3.11). In these cases, although the 500 nm peak corresponding to the charge transfer state was present, the 900 nm peak appeared as only a shoulder peak. Glotaran analysis was subsequently performed by fitting the data to the $S_o \rightarrow S_1 \rightarrow CT \rightarrow GS$ model and the time constants are listed in Table 3.3. The CT states persisted more in the case of $(NND)_2$-azaBODIPY compared to $(TPA)_2$-azaBODIPY.

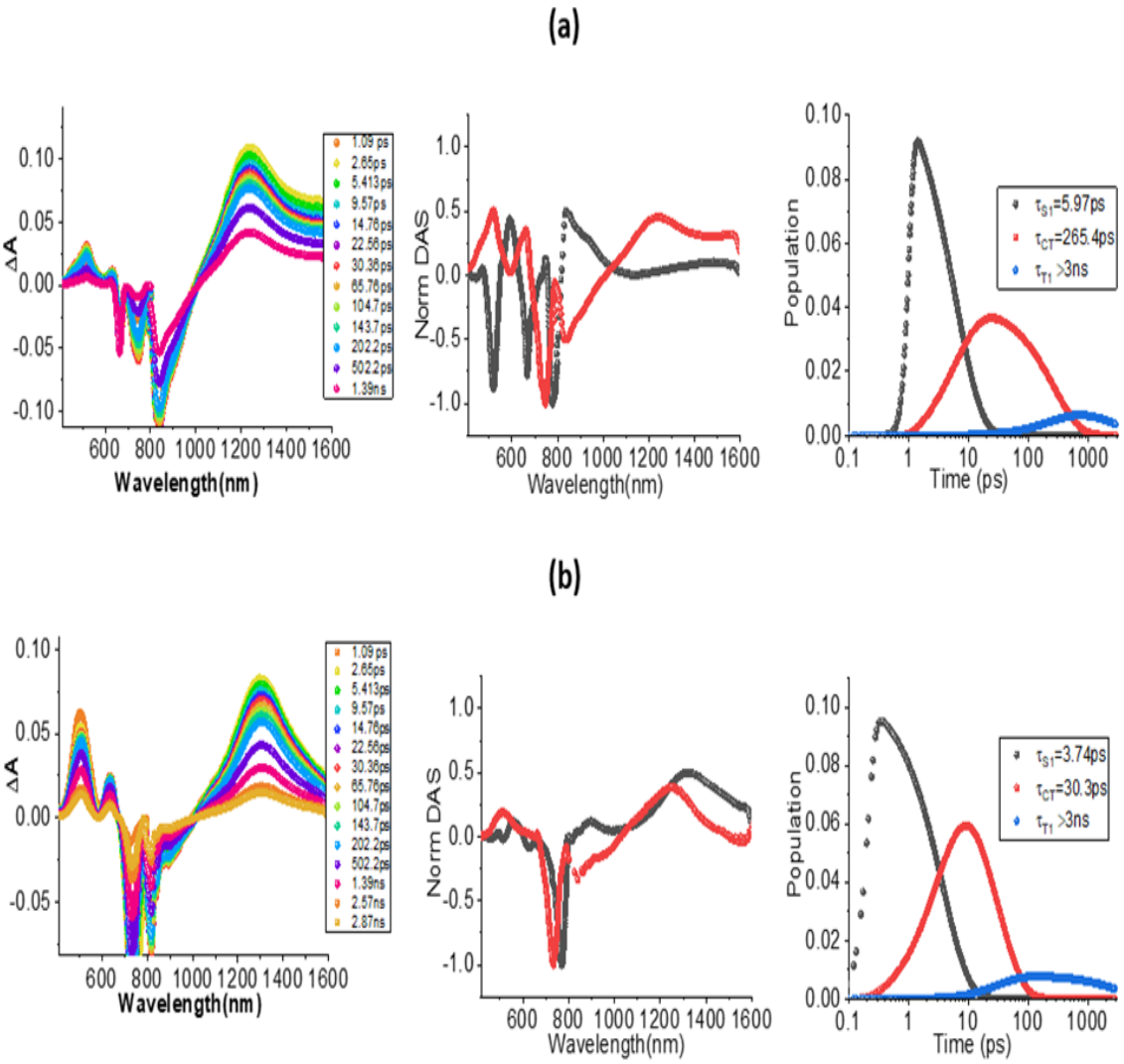

Figure 3.11: Fs-TA spectra at the indicated delay times of (a) $(NND)_2$-azaBODIPY and (b) $(TPA)_2$-azaBODIPY in toluene at the excitation wavelength of 668 nm. The decay-associated spectra and population time profiles from GloTarAn analysis are shown in the middle and right-hand panels, respectively. The DAS of T_1 state is not shown for clarity.

3.1.3 Conclusions

The newly synthesized donor-acceptor push-pull systems featuring far-red absorbing sensitizer azaBODIPY as a photosensitizer-electron acceptor along with nitrogenous electron donors *N*,*N*-dimethylaniline, triphenylamine, and phenothiazine revealed several interesting features with regard to their excited state electron transfer properties. Using a range of physico-

chemical techniques, it was possible to arrive at the structure of these push-pull systems. The measured redox potentials revealed facile reduction of azaBODIPY and facile oxidation of nitrogenous donors and the performed spectroelectrochemical studies revealed diagnostic peaks of azaBODIPY$^{\bullet-}$ in the visible and near-IR regions. Further, free-energy calculations indicated charge separation from one of the donor entities to the ^{1}azaBODIPY* to yield charge-separated states in a polar solvent but only partial charge transfer in toluene. The fluorescence emission of ^{1}azaBODIPY* and calculated quantum yields revealed a different level of quenching depending upon the nature of the solvent and donor entities. Fs-TA studies confirmed the occurrence of charge separation in benzonitrile, and kinetic analysis performed by GloTarAn analysis revealed the charge-separated states to last about 50–200 ps depending on the nature of the donor. Finally, the charge transfer states in toluene and charge-separated states in benzonitrile populated the low-lying ^{3}azaBODIPY* prior to returning the push-pull system to the ground state.

3.1.4 References

1. M. R. Wasielewski, *Acc. Chem. Res.* 2009, **42**, 1910–1921.
2. S. D. Straight, G. Kodis, Y. Terazono, M. Hambourger, T. A. Moore, A. L. Moore, D. Gust, *Nat. Nanotechnol.* 2008, **3**, 280–283.
3. G. Bottari, G. de la Torre, D. M. Guldi, T. Torres, *Chem. Rev.* 2010, **110**, 6768–6816.
4. D. M. Guldi, V. Sgobba, *Chem. Commun.* 2011, **47**, 606–610.
5. F. D'Souza, O. Ito, *Chem. Soc. Rev.* 2012, **41**, 86–96.
6. F. D'Souza, O. Ito, *Ed Kim Pan Stanf. Publ. Singap.* 2012, **8**, 389–437.
7. H. Imahori, T. Umeyama, S. Ito, *Acc. Chem. Res.* 2009, **42**, 1809–1818.
8. C. B. Kc, F. D'Souza, *Coord. Chem. Rev.* 2016, **322**, 104–141.
9. J. Zhang, W. Xu, P. Sheng, G. Zhao, D. Zhu, *Acc. Chem. Res.* 2017, **50**, 1654–1662.
10. M. Sommer, S. Huettner, M. Thelakkat, *J. Mater. Chem.* 2010, **20**, 10788–10797.

11. C. Deibel, T. Strobel, V. Dyakonov, *Adv. Mater.* 2010, **22**, 4097–4111.

12. V. Balzani, A. Credi, M. Venturi, *ChemSusChem* 2008, **1**, 26–58.

13. N. Armaroli, V. Balzani, *Angew. Chem. Int. Ed.* 2007, **46**, 52–66.

14. P. M. Beaujuge, J. M. J. Fréchet, *J. Am. Chem. Soc.* 2011, **133**, 20009–20029.

15. L. Hammarström, *Acc. Chem. Res.* 2015, **48**, 840–850.

16. T. Torres, G. Bottari, *Organic Nanomaterials: Synthesis, Characterization, and Device Applications*, John Wiley & Sons, 2013.

17. Y. Wu, W. Zhu, *Chem. Soc. Rev.* 2013, **42**, 2039–2058.

18. R. Misra, S. P. Bhattacharyya, *Intramolecular Charge Transfer: Theory and Applications*, John Wiley & Sons, 2018.

19. V. May, O. Kühn, *Charge and Energy Transfer Dynamics in Molecular Systems*, Wiley-VCH-Verlag, Weinheim, 2011.

20. S. Fukuzumi, K. Ohkubo, T. Suenobu, *Acc. Chem. Res.* 2014, **47**, 1455–1464.

21. M. Barrejón, L. M. Arellano, F. D'Souza, F. Langa, *Nanoscale* 2019, **11**, 14978–14992.

22. J. Yang, D. Kim, *Philos. Trans. R. Soc. Math. Phys. Eng. Sci.* 2012, **370**, 3802–3818.

23. T. Higashino, T. Yamada, M. Yamamoto, A. Furube, N. V. Tkachenko, T. Miura, Y. Kobori, R. Jono, K. Yamashita, H. Imahori, *Angew. Chem.* 2016, **128**, 639–643.

24. N. Zarrabi, S. Seetharaman, S. Chaudhuri, N. Holzer, V. S. Batista, A. Van Der Est, F. D'Souza, P. K. Poddutoori, *J. Am. Chem. Soc.* 2020, **142**, 10008–10024.

25. R. Canton-Vitoria, H. B. Gobeze, V. M. Blas-Ferrando, J. Ortiz, Y. Jang, F. Fernández-Lázaro, Á. Sastre-Santos, Y. Nakanishi, H. Shinohara, F. D'Souza, *Angew. Chem.* 2019, **131**, 5768–5773.

26. S. I. van Dijk, C. P. Groen, F. Hartl, A. M. Brouwer, J. W. Verhoeven, *J. Am. Chem. Soc.* 1996, **118**, 8425–8432.

27. C. O. Obondi, G. N. Lim, B. Churchill, P. K. Poddutoori, A. van der Est, F. D'Souza, *Nanoscale* 2016, ***8***, 8333–8344.

28. M. Kivala, C. Boudon, J.-P. Gisselbrecht, P. Seiler, M. Gross, F. Diederich, *Angew. Chem. Int. Ed.* 2007, **46**, 6357–6360.

29. Y. Ge, D. F. O'Shea, *Chem. Soc. Rev.* 2016, **45**, 3846–3864.

30. A. Loudet, K. Burgess, *Chem. Rev.* 2007, **107**, 4891–4932.

31. G. Ulrich, R. Ziessel, A. Harriman, *Angew. Chem. Int. Ed.* 2008, **47**, 1184–1201.

32. M. E. El-Khouly, S. Fukuzumi, F. D'Souza, *ChemPhysChem* 2014, **15**, 30–47.

33. Z. Shi, X. Han, W. Hu, H. Bai, B. Peng, L. Ji, Q. Fan, L. Li, W. Huang, *Chem. Soc. Rev.* 2020, **49**, 7533–7567.

34. P. Rana, N. Singh, P. Majumdar, S. Prakash Singh, *Coord. Chem. Rev.* 2022, **470**, 214698.

35. K. Chen, Y. Dong, X. Zhao, M. Imran, G. Tang, J. Zhao, Q. Liu, *Front. Chem.* 2019, **7**.

36. A. N. Amin, M. E. El-Khouly, N. K. Subbaiyan, M. E. Zandler, M. Supur, S. Fukuzumi, F. D'Souza, *J. Phys. Chem. A* 2011, **115**, 9810–9819.

37. A. N. Amin, M. E. El-Khouly, N. K. Subbaiyan, M. E. Zandler, S. Fukuzumi, F. D'Souza, *Chem. Commun.* 2011, **48**, 206–208.

38. M. E. El-Khouly, A. N. Amin, M. E. Zandler, S. Fukuzumi, F. D'Souza, *Chem. Eur. J.* 2012, **18**, 5239–5247.

39. F. D'Souza, A. N. Amin, M. E. El-Khouly, N. K. Subbaiyan, M. E. Zandler, S. Fukuzumi, *J. Am. Chem. Soc.* 2012, **134**, 654–664.

40. V. Bandi, K. Ohkubo, S. Fukuzumi, F. D'Souza, *Chem. Commun.* 2013, **49**, 2867–2869.

41. S. K. Meher, G. R. Rao, *J. Phys. Chem. C* 2013, **117**, 4888–4900.

42. M. A. Collini, M. B. Thomas, V. Bandi, P. A. Karr, F. D'Souza, *Chem. – Eur. J.* 2017, **23**, 4450–4461.

43. D. Pinjari, A. Z. Alsaleh, Y. Patil, R. Misra, F. D'Souza, *Angew. Chem. Int. Ed.* 2020, **59**, 23697–23705.

44. S. Guo, L. Ma, J. Zhao, B. Küçüköz, A. Karatay, M. Hayvali, H. Gul Yaglioglu, A. Elmali, *Chem. Sci.* 2014, **5**, 489–500.

45. S. Kumar, K. G. Thorat, M. Ravikanth, *J. Org. Chem.* 2017, **82**, 6568–6577.

46. A. Koch, M. Ravikanth, *J. Org. Chem.* 2019, **84**, 10775–10784.

47. Q. Bellier, S. Pégaz, C. Aronica, B. L. Guennic, C. Andraud, O. Maury, *Org. Lett.* 2011, **13**, 22–25.

48. N. Balsukuri, S. Mori, I. Gupta, *J. Porphyr. Phthalocyanines* 2016, **20**, 719–729.

49. A. Koch, M. Ravikanth, *Eur. J. Org. Chem.* 2018, **2018**, 228–234.

50. N. Balsukuri, N. Jyoti Boruah, P. E. Kesavan, I. Gupta, *New J. Chem.* 2018, **42**, 5875–5888.

51. N. Balsukuri, M. Y. Lone, P. C. Jha, S. Mori, I. Gupta, *Chem. - Asian J.* 2016, **11**, 1572–1587.

52. Y. Gawale, N. Adarsh, S. K. Kalva, J. Joseph, M. Pramanik, D. Ramaiah, N. Sekar, *Chem. - Eur. J.* 2017, **23**, 6570–6578.

53. Ł. Łapok, I. Cieślar, T. Pędziński, K. M. Stadnicka, M. Nowakowska, *ChemPhysChem* 2020, **21**, 725–740.

54. B. Anjaiah, M. Naga Rajesh, L. Giribabu, R. Chitta, *Chem. – Asian J.* 2023, e202300050.

55. G. Rotas, M. B. Thomas, R. Canton-Vitoria, F. D'Souza, N. Tagmatarchis, *Chem. – Eur. J.* 2020, **26**, 6652–6661.

56. N. Balsukuri, N. Manav, M. Y. Lone, S. Mori, A. Das, P. Sen, I. Gupta, *Dyes Pigments* 2020, **176**, 108249.

57. *Gaussian 16*, Revision C.A03, M. J. Frisch, G. W. Trucks, H. B. Schlegel, G. E. Scuseria, M. A. Robb, J. R. Cheeseman, G. Scalmani, V. Barone, B. Mennucci, G. A. Petersson, H. Nakatsuji, M. Caricato, X. Li, H. P. Hratchian, A. F. Izmaylov, J. Bloino, G. Zheng, J. L. Sonnenberg, M. Hada, M. Ehara, K. Toyota, R. Fukuda, J. Hasegawa, M. Ishida, T. Nakajima, Y. Honda, O. Kitao, H. Nakai, T. Vreven, J. A. , Jr. , Montgomery, J. E. Peralta, F. Ogliaro, M. Bearpark, J. J. Heyd, E. Brothers, K. N. Kudin, V. N. Staroverov, R. Kobayashi, J. Normand, K. Raghavachari, A. Rendell, J. C. Burant, S. S. Iyengar, J. Tomasi, M. Cossi, N. Rega, J. M. Millam, M. Klene, J. E. Knox, J. B. Cross, V. Bakken, C. Adamo, J. Jaramillo, R. Gomperts, R. E. Stratmann, O. Yazyev, A. J. Austin, R. Cammi, C. Pomelli, J. W. Ochterski, R. L. Martin, K. Morokuma, V. G. Zakrzewski, G. A. Voth, P. Salvador, J. J. Dannenberg, S. Dapprich, A. D. Daniels, Ö. Farkas, J. B. Foresman, J. V. Ortiz, J. Cioslowski, D. J. Fox, Gaussian, Inc., Wallingford, CT, USA, 2016.

58. D. Rehm, A. Weller, *Isr. J. Chem.* 1970, **8**, 259–271.

59. J. J. Snellenburg, S. Laptenok, R. Seger, K. M. Mullen, I. H. M. van Stokkum, *J. Stat. Softw.* 2012, **49**, 1–22.

3.2 Interfacing High-Energy Charge Transfer States to a Near-IR Sensitizer for Efficient Electron Transfer upon Near-IR Irradiation*

3.2.1 Introduction

Near-IR absorbing molecular systems have been widely used in light energy harvesting,

* Section 3.2 is reproduced from Pinjari, Dilip, Ajyal Z. Alsaleh, Yuvraj Patil, Rajneesh Misra, and Francis D'Souza. "Interfacing High-Energy Charge-Transfer States to a near-Ir Sensitizer for Efficient Electron Transfer Upon near-Ir Irradiation." Angewandte Chemie International Edition 59, no. 52 (2020): 23697-705, doi.org/10.1002/anie.202013036, with permission from John Wiley and Sons.

sensing and biosensing, and biomedical applications.[1] In the area of light energy harvesting, the near-IR sensitizers offer maximum utilization of the useful sunlight in energy harvesting schemes,[2] while in the area of sensors and biosensors, due to its spectral isolation, near-IR excitation provides excitation selectivity from absorption interference of molecular/biomolecular species present in the sensing environment.[3] In biomedical applications, near-IR probes are known for their deep tissue penetration properties in imaging applications.[4]

Push–pull chromophores, derived from closely linked, highly interacting, electron rich and electron deficient entities have been studied for variety of technological applications including multi–photon absorption and organic photovoltaics, and optoelectronics in general.[5] Under the conditions of strong intramolecular interactions, the push-pull systems are known to result in new type of optical transition called ICT that is different from the regular π–π^* type transitions of individual chromophores (also called locally excited, LE transitions).[6] Due to their different origin, spectral properties of ICT and LE transitions differ making this class of compounds as one of the widely studied ones for various light induced applications.[7]

An elegant approach of building ICT molecular systems, developed by Diederich, involves incorporation of a strong electron acceptor such as tetracyanoethylene (TCNE) in a highly facile, catalyst-free [2+2] cycloaddition-retroelectrocyclization reaction with ethynyl functionalized strong electron donor molecules.[8] Based on this concept, few groups have been successful in building push-pull conjugates.[9-11] Research teams of Bottari, Torres, and Guldi have also reported phthalocyanine-TCBD and subphthalocyanine-TCBD D-A systems.[10] Our groups have reported a few TCBD functionalized chromophores, and established excited state charge separation useful for optoelectronic applications.[11]

An elegant approach of building ICT molecular systems, developed by Diederich, involves

incorporation of a strong electron acceptor such as tetracyanoethylene (TCNE) in a highly facile, catalyst-free [2+2] cycloaddition-retroelectrocyclization reaction with ethynyl functionalized strong electron donor molecules.[8] Based on this concept, few groups have been successful in building push-pull conjugates.[9-11] Research teams of Bottari, Torres, and Guldi have also reported phthalocyanine-TCBD and subphthalocyanine-TCBD D-A systems.[10] Our groups have reported a few TCBD functionalized chromophores, and established excited state charge separation useful for optoelectronic applications.[11]

In general, in polar solvents, ICT transitions of push-pull systems occur at the low-energy side of the spectrum while that of LE transitions occur at the high-energy side of the spectrum.[6] This trend could be reversed if a high-energy ICT exhibiting species can be connected to a near-IR sensitizer.[10a] If this condition is met, due to different spectral origin, one could observe a reverse trend in optical transitions, *viz*., low-energy LE and high-energy ICT transitions while extending their spectral coverage. Such compounds due to varying optical properties can offer new class of push-pull systems for light-induced applications. In the present study, an electron deficient near-IR probe, azaBODIPY[12] has been covalently linked to one or two $TPA^{\delta+}$-$TCBD^{\delta-}$, charge transfer (CT) entities[8] , as shown in Figure 3.12. The azaBODIPY used here absorbs in the near-IR region of 740 nm region and emits in the 770 nm region, and is highly electron deficient. [12d] This is unlike the electron rich zinc phthalocyanine near-IR probe employed in a previous study.[10a] Importantly, due to structural arrangement of placing the electron acceptor, TCBD between the electron donor TPA and azaBODIPY, CT is mainly confined to the TPA-TCBD segment and not so much on the TCBD-azaBODIPY segment as both TCBD and azaBODIPY are good electron acceptors (Fig. 3.12). Consequently, the original ICT from TPA-TCBD occurring in the high-energy side of the spectrum is largely unperturbed while the low-energy LE transitions of the near-IR probe,

azaBODIPY minimally affected. Further, to seek potential of this class of compounds for light energy harvesting applications, excited state electron transfer upon near-IR and ICT excitations has been investigated in both polar and nonpolar solvents using transient spectroscopy, and meaningful structure-property relationships have been derived.

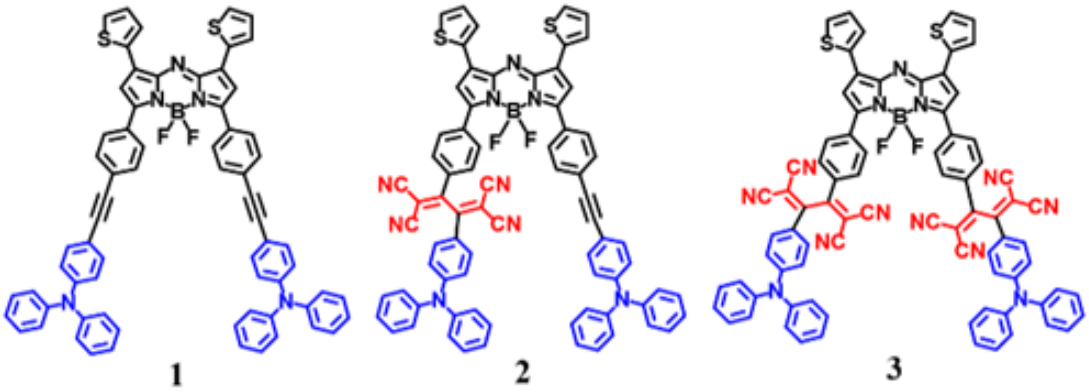

Figure 3.12: **Structure of the high-energy charge transfer, TPA$^{\delta+}$-TCBD$^{\delta-}$, connected to near-IR, azaBODIPY sensitizer, push-pull systems investigated in the present study.**

3.2.2 Synthesis

Synthesis of azaBODIPY derived push-pull systems is shown in Scheme 3.2 while details are given in the supporting information. Briefly, the di-bromo-aza-dipyrromethene 1a was synthesized as per reported procedure. [13a] The TPA based aza-dipyrromethene 1b was synthesized by the Sonogashira cross-coupling reaction of di-bromo aza-dipyrromethene 1a with 4- ethynyl-*N*,*N*-diphenylaniline in a THF/TEA mixture (v/v,1:1) at 60 ^{o}C for overnight under argon atmosphere in 10% yield. Further the triphenylamine based azaBODIPY 1 was synthesized by chelating BF_2 with aza-dipyrromethene 1b in presence of diisopropylethylamine at room temperature (Scheme 3.2). The [2+2] cycloaddition-retroelectrocyclization reactions of TPA based aza-dipyrromethene 1b with one and two equivalents of TCNE in dichloromethane at room temperature for 4 hours resulted in mono-TCBD substituted aza-dipyrromethene 2a and di-TCBD substituted aza-dipyrromethene 3a in 65% and 85% yield respectively. The TPA based

azaBODIPYs, 2 and 3 were obtained by the complexation reaction of aza-dipyrromethenes 2a and 3a with boron trifluoride etherate ($BF_3.OEt_2$) in dichloromethane solvent and diisopropylethylamine for 4 hours in 80% and 85% yield respectively. The newly synthesized compounds 1-3 were purified by column chromatography using neutral activated alumina.

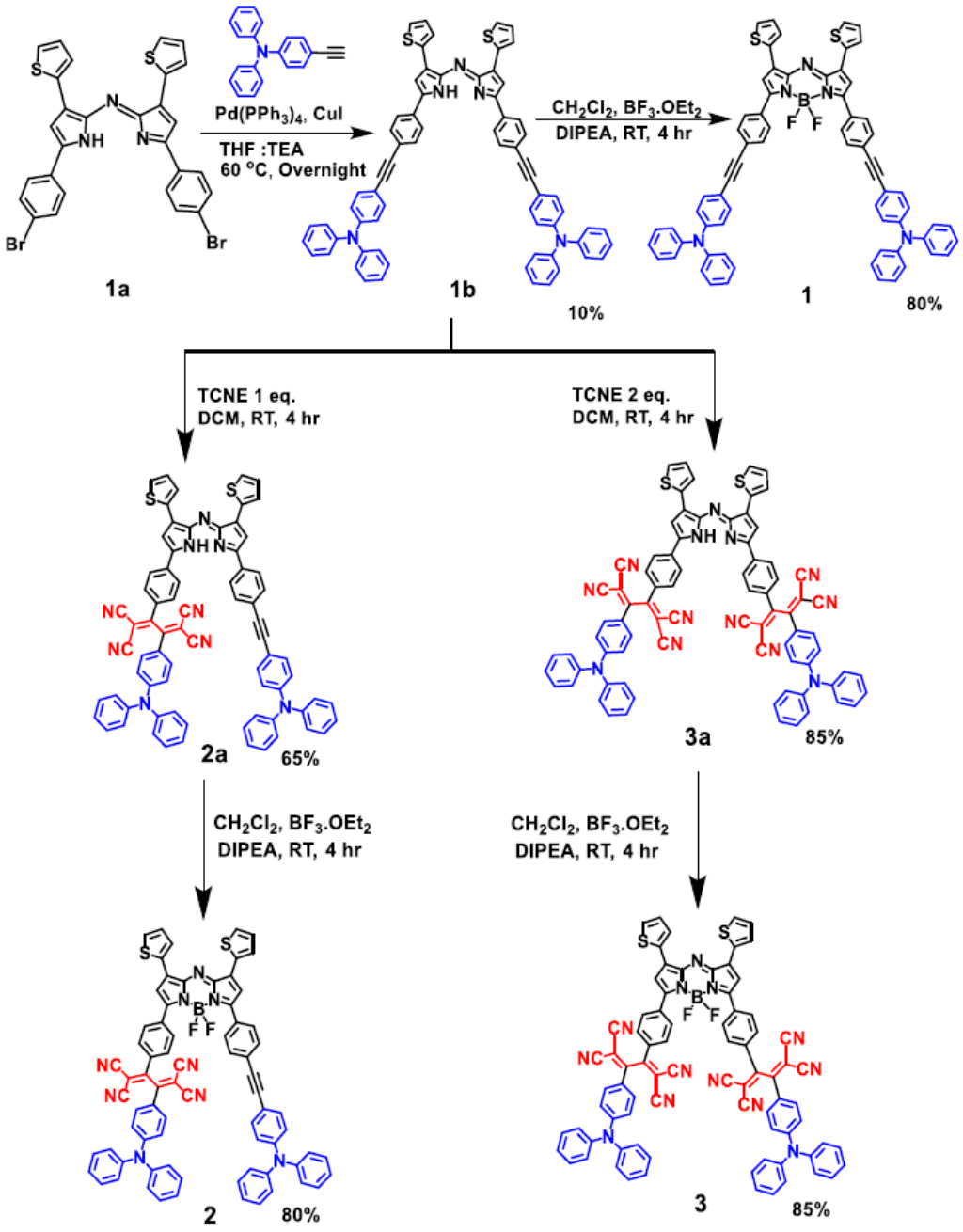

Scheme 3.2: **Synthetic methodology for TPA-TCBD connected to azaBODIPY push-pull systems.**

3.2.3 Results and Discussion

Figure 3.13a shows the absorption spectrum of the investigated compounds in benzonitrile. Compound 1 lacking TCBD entities between the TPA and azaBODIPY revealed two majors peaks at 370 and 744 nm. The 744 nm peak was due to the Q-band transition of azaBODIPY while the 370 nm peak had contributions from both TPA and Soret band of azaBODIPY. Introducing TCBD between TPA and azaBODIPY in 2, resulted in diminished intensity with a small red-shift of 6 nm of the 370 nm peak with the appearance of a new peak at 491 nm. The origin of the new peak stems from CT interactions between TPA-TCBD ($TPA^{\delta+}$-$TCBD^{\delta-}$) from our earlier study,[11a] and a control experiment involving structurally similar N,N-dimethylaminophenyl-TCBD compound whose CT peak was located at 478 nm (see Fig. 3.15). Introducing a second TCBD into the second arm resulted in compound 3 exhibiting peaks at 380, 484 and 748 nm. The diminished intensity of 380 nm Soret band of azaBODIPY (without TPA contributions) and doubling the intensity of 484 nm peak due to the presence of two $TPA^{\delta+}$-$TCBD^{\delta-}$ CT entities was witnessed. Importantly, no significant changes either in azaBODIPY Q-band position in the near-IR region or CT band position from TPA-TCBD interactions in the visible region was observed suggesting that azaBODIPY and TPA-TCBD entities are minimally involved in ground state charge transfer type interactions in 2 and 3. Since ICT is solvent polarity sensitive, the optical studies were also performed in nonpolar toluene. The absorption spectral trends were almost similar to that observed in benzonitrile (see Fig. 3.15a for absorption spectra). Contrary to the expectations, due to their positioning, location of the $TPA^{\delta+}$-$TCBD^{\delta-}$ charge transfer peak in 2 and 3 revealed only a small red-shift (<3 nm) in toluene. Generally, a large red shift is expected in polar solvents for CT absorption bands.[6]

Fluorescence of these compounds was also investigated. In benzonitrile, only compound 1

was found to be weakly fluorescent with peak maxima around 856 nm. However, in toluene a relatively more intense peak with a peak maximum at 780 nm was observed (see Fig. 3.13a). Measured fluorescence quantum yields, Φ_f, were found to be 0.04 in toluene and <0.003 in benzonitrile with respect to pristine azaBODIPY (Φ_f = 0.23[13b]). Red shift of fluorescence in polar media but not in absorption suggests stabilization of excited state dipoles and not the ground state dipoles of 1. An optical gap of 1.55 eV in benzonitrile and 1.63 eV in toluene for 1 was possible to arrive from these data (HOMO-LUMO gap, midpoint energy of 0,0 transitions of absorption and fluorescence peaks). Lifetime of 1 in toluene measured using time correlated single photon counting method (629 nm pulsed nanoLED excitation) was found to be 1.56 ns (see Fig. 3.15b for decay profile). The lack of emission in 2 and 3 indicate occurrence of excited state events, such as electron or energy transfer in 2 and 3 in both polar and nonpolar solvents.[14] For compound 1, having electron rich TPA and electron deficient azaBODIPY, excited state CT appears to be occurring, more so, in polar benzonitrile.

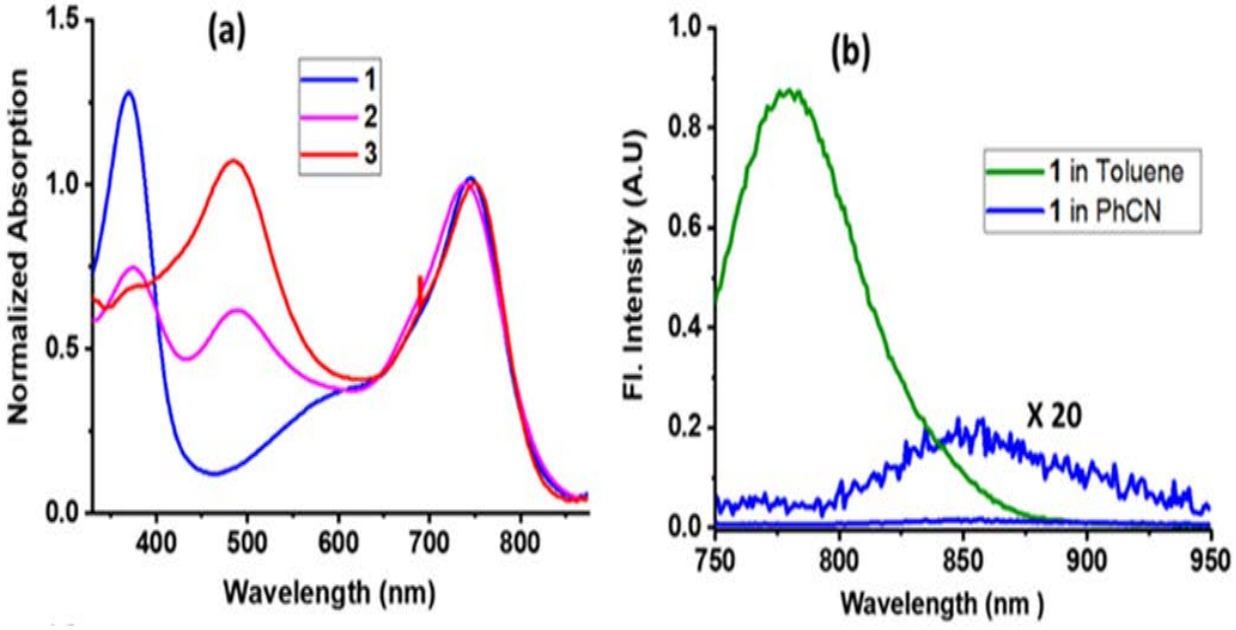

Figure 3.13: Optical absorption in benzonitrile, and fluorescence in benzonitrile and toluene of indicated compounds. Samples were excited at near-IR peak maxima.

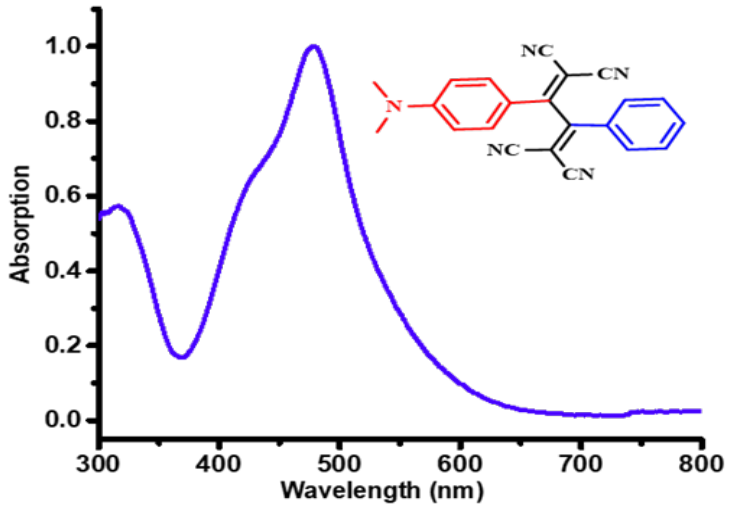

Figure 3.14: Absorption spectrum on control N,N-dimethylaminophenyl-TCBD compound in benzonitrile.

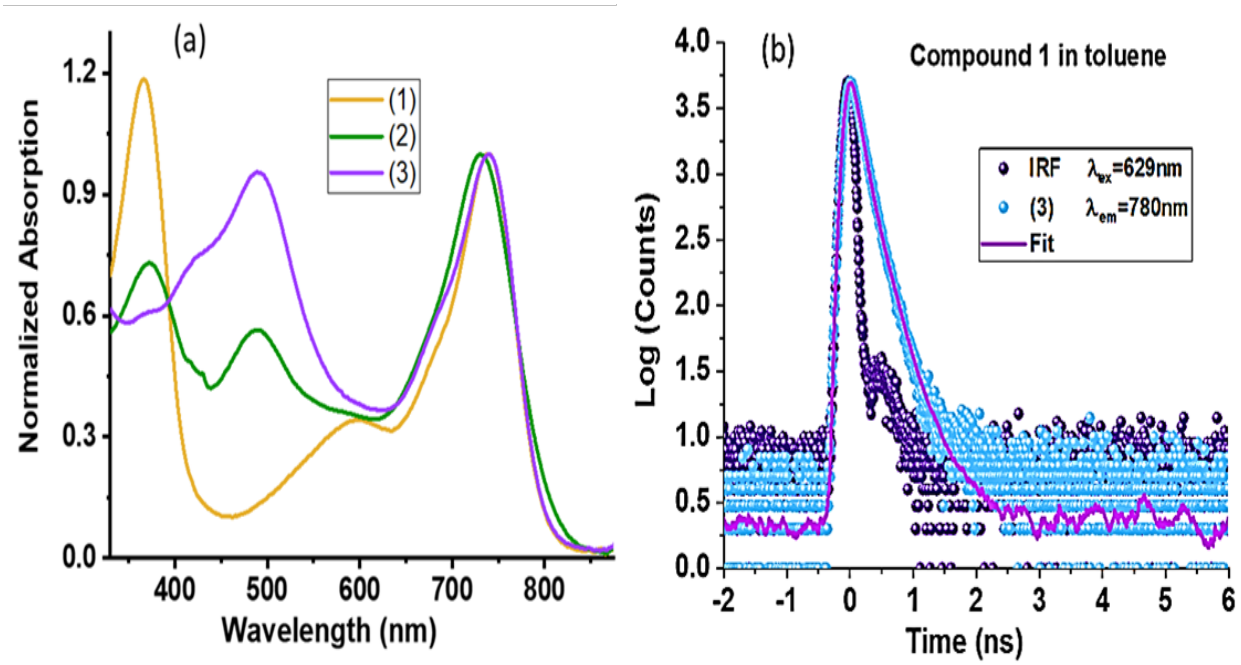

Figure 3.15: Absorption spectra of the indicated compounds in toluene, and (b) fluorescence decay profile of 1 in toluene.

Systematic electrochemical studies using differential pulse voltammetry (DPV), cyclic voltammetry (CV), and spectroelectrochemical studies in an optically transparent thin-layer cell-assembly were carried out. The electrochemical redox potentials of multi-modular systems are key

in accessing energetics of electron and energy transfer between the components while spectroelectrochemical data is vital in securing spectral evidence of electron transfer products. DPVs of the investigated compounds is shown in Figure 3.16 (a-b) in benzonitrile containing 0.1 M $(TBA)ClO_4$. Reversibility of reach redox wave was assessed with the help of CV (see Fig. 3.17 for CVs). The first reversible reduction of 1 was located at -0.23 V vs. Ag/AgCl and was attributed to reduction of azaBODIPY as TPA had no reduction in this potential range. The first quasi-reversible oxidation was located at 1.10 V, and from earlier studies,[11a] this was assigned to the TPA oxidation while the subsequent oxidation located at 1.28 V was due to azaBODIPY oxidation. The determined electrochemical HOMO-LUMO gap (potential difference between azaBODIPY centered oxidation and reduction) was 1.51 eV that agreed well with the optical bandgap value of 1.55 eV discussed earlier. The TCBD entity in compound 2 revealed reversible reductions at -0.33 and -0.72 V while reduction of azaBODIPY was slightly facile and appeared at -0.09 V due to the electronic influence of neighbouring TCBD. Assignment of TCBD reductions was based on a control compound carrying a TCBD entity without the azaBODIPY (see Fig. 3.18 for the structure, CV and DPV curves). The TPA and azaBODIPY oxidations revealed a slight 10-20 mV positive shift. In the case of compound 3, where two TPA-TCBD entities are positioned on azaBODIPY arms, the first reversible reduction of TCBD was found to be split and appeared at -0.25 and -0.38 V, that is, about 130 mV separation suggesting the TCBD entities interact through the azaBODIPY π-system or could be due to different structural arrangement of the appended TCBD-TPA entities as shown in Figure 3.19a(iii) and b(iii). The second TCBD reduction was located at -0.70 and had the expected current of two one-electron reductions (from integrating the area under the curve). Interestingly, the reversible azaBODIPY reduction appeared at +0.05 V, more positive than that in 1 or 2 owing to the presence of two neighbouring TCBD entities. A slight anodic shift of

oxidation potentials was also witnessed, however, the TPA and azaBODIPY oxidations were overlapped. Importantly, both CT excitation at 490 nm (2.52 eV) or LE excitation (1.63 eV in toluene and 1.55 eV in benzonitrile) are higher in energy compared to the energy gap (HOMO-LUMO gap) between the donor-acceptor (TPA-azaBODIPY) confirming possibility of excited state electron transfer in these systems.

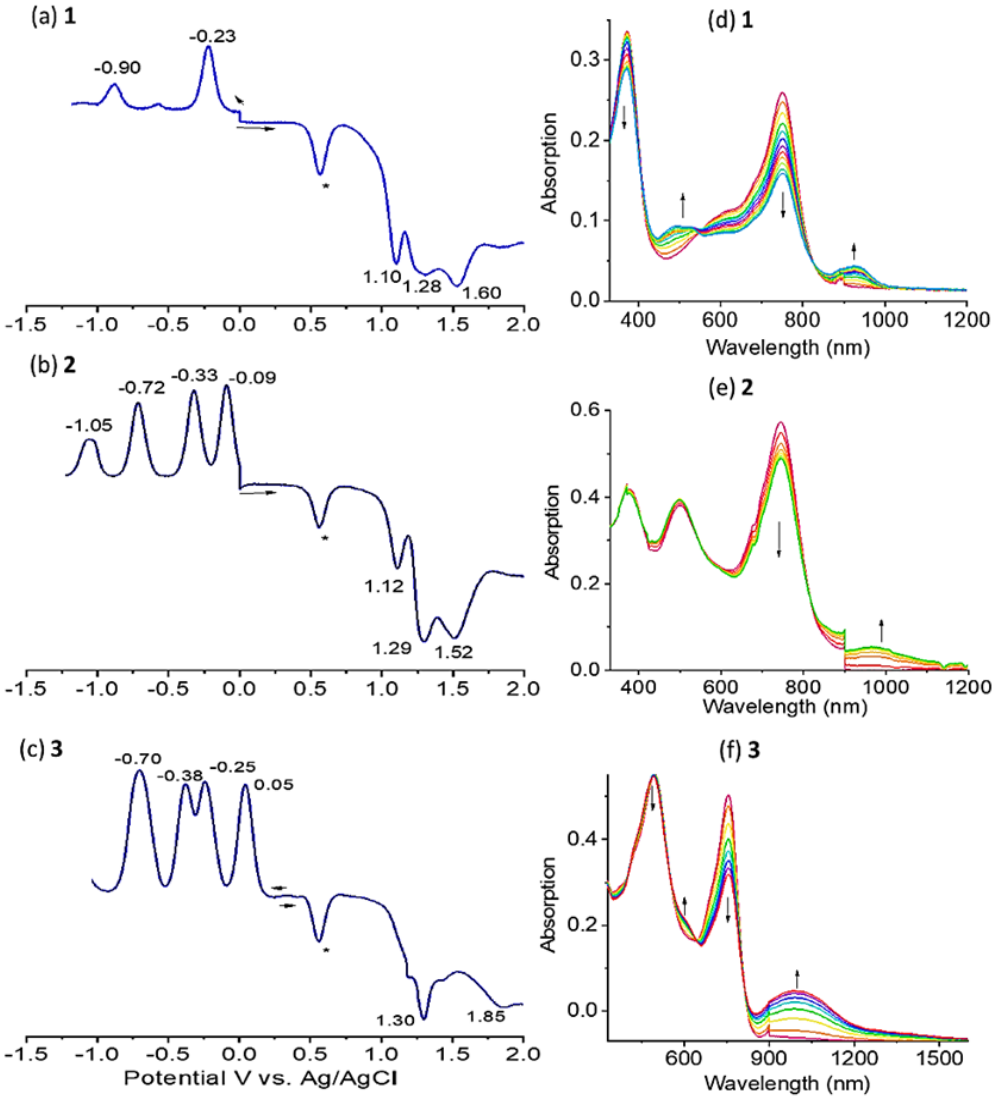

Figure 3.16: (a-c) DPVs of 1-3 in benzonitrile containing 0.1 M (TBA)ClO_4. The "*" indicates oxidation of ferrocene used as internal reference (E_{ox} = 0.55 V). (d-f) Spectral change was observed during first reduction of 1-3 in benzonitrile, 0.2 M (TBA)ClO_4. Potentials past 80 mV of the first reduction potential was applied in each case and spectra were recorded until no additional spectral changes were observed. The spike in the spectra at 900 nm is due to change of visible to near-IR detectors.

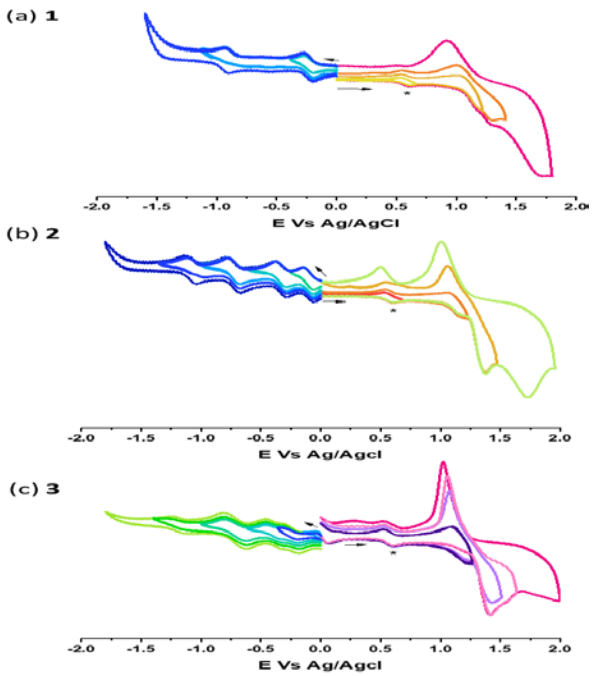

Figure 3.17: Cyclic voltammograms of 1-3 in benzonitrile containing 0.1 M (TBA)ClO_4. The "*" indicates oxidation of ferrocene used as an internal reference. The reversibility of each redox process was verified by changing the direction of the scan immediately after each redox process. The sharp peak in the anodic side seen after scanning the potential beyond 1.5 V is due to surface adsorption of oxidized TPA product.

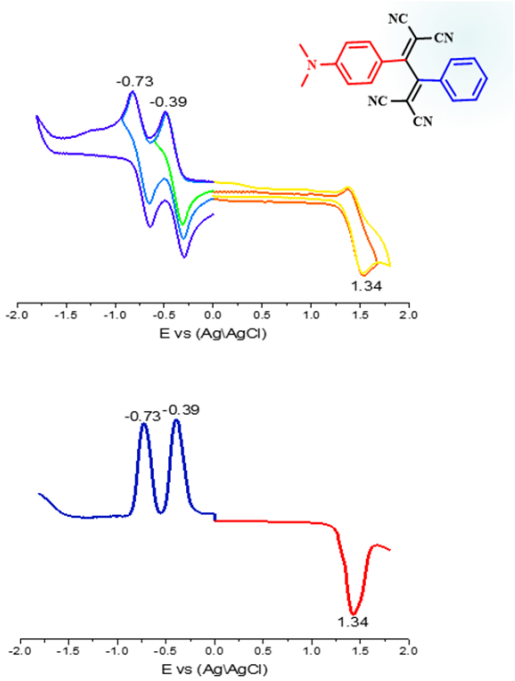

Figure 3.18: CV and DPV of control N,N-dimethylaminophenyl-TCBD compound in benzonitrile containing 0.1 M (TBA)ClO_4.

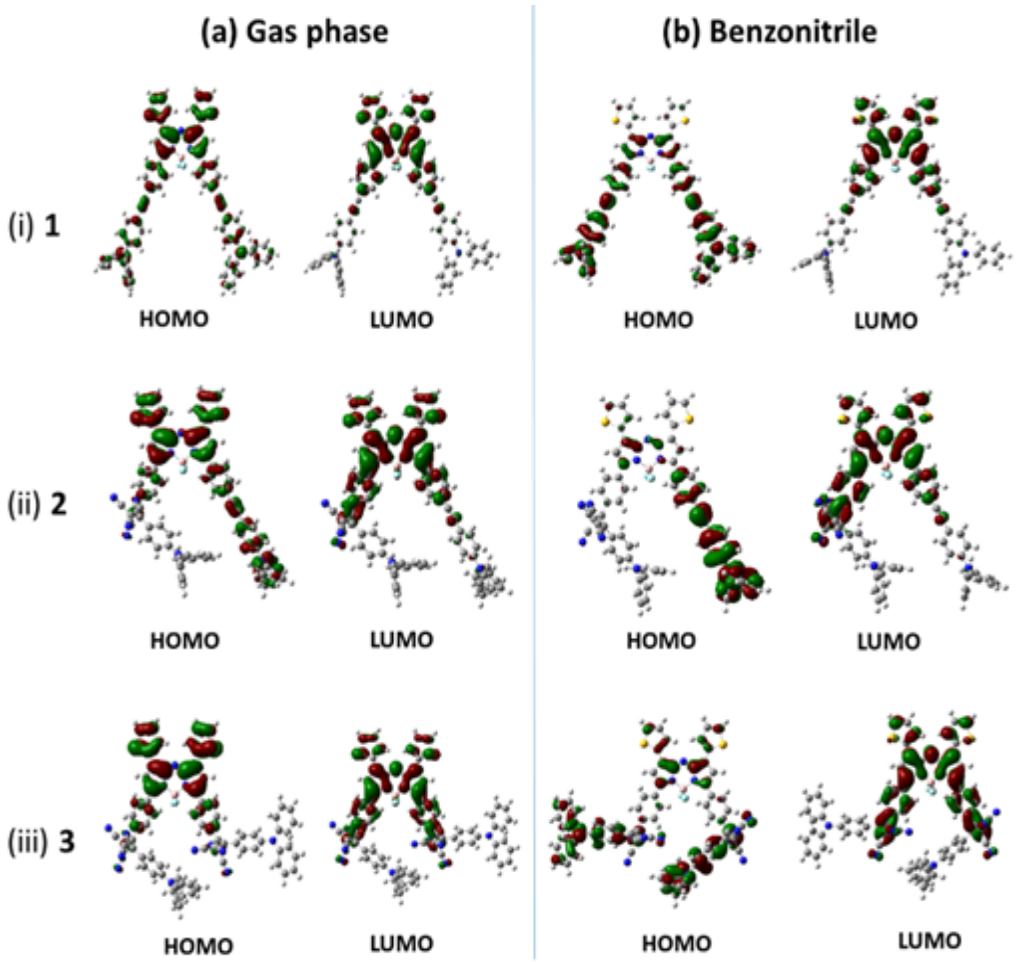

Figure 3.19: Frontier orbitals of compounds 1-3 generated on B3LYP/6-31G(d, p) optimized geometries in (a) gas phase and (b) polar benzonitrile.

Next, spectroelectrochemical studies were performed to spectrally characterize the one-electron oxidation and one-electron reduction products of compounds 1-3. For all three investigated compounds no drastic spectral changes involving generation of new peaks during first oxidation were witnessed (see Fig. 3.20), as this process was TPA centered. Only a small reduction of peak intensities was observed, especially for the TPA absorption bands. Interestingly, during first reduction which is azaBODIPY centered, decreased intensity of the azaBODIPY centered peaks was accompanied by new peaks (see Fig. 3.16 d-f). Peaks of 1 were located at 495 and 930 nm while for 2, a single peak at 972 nm and for 3, signature peaks at 605 (shoulder type) and 992 nm was observed. One or more isosbestic points were observed in all three cases.

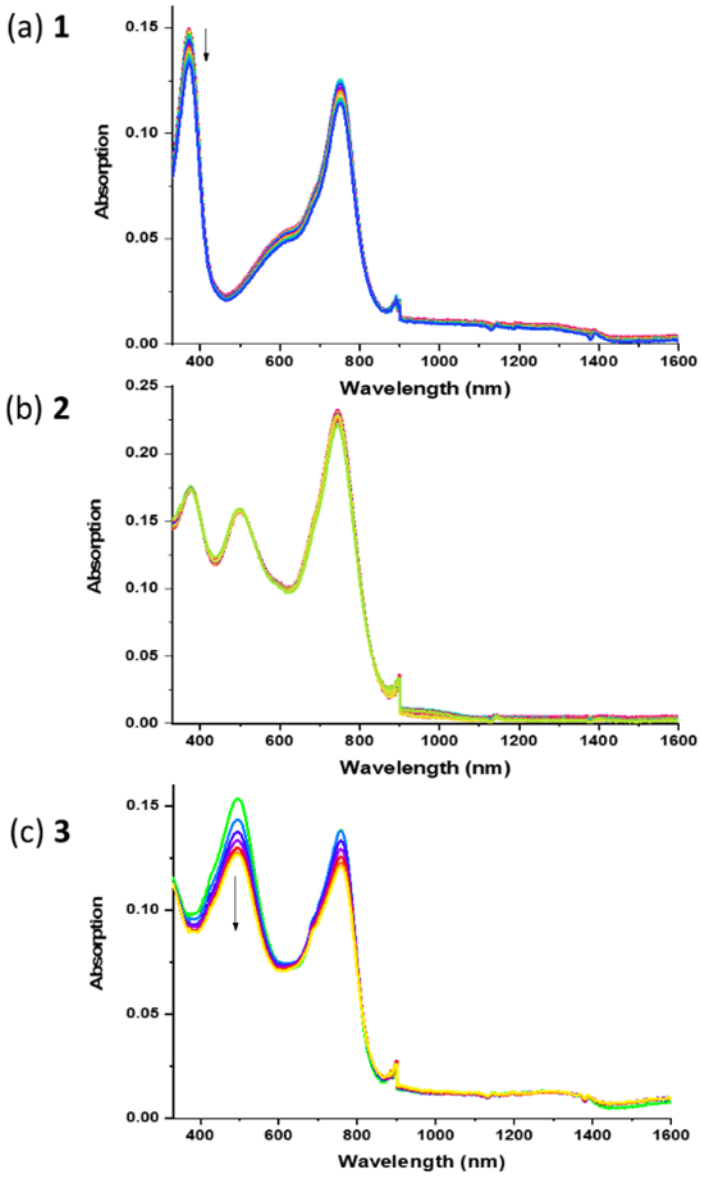

Figure 3.20: Spectral change observed during first oxidation of 1-3 in benzonitrile, 0.2 M (TBA)ClO_4. Potentials past 80 mV from the first oxidation potential was applied in each case. The spike in the spectra at 900 nm is due to change of visible to near-IR detectors.

The systematic bathochromic shift of the azaBODIPY near-IR peak on increasing the number of TCBD entities suggests greater delocalization of the radical anion across the TCBD moieties. Further, the final spectrum of the radical anion and radical cation of a given compound was averaged and subtracted from the neutral compound, as shown in (see Fig. 3.21). This spectrum would resemble the differential absorption spectrum of charge separation product from transient

absorption studies. Main observations involved two negative peaks in the visible and far-red region due to loss of original intensity of the neutral compound, and a broad positive peak in the near-IR region covering 850-1200 nm region, corresponding to the radical anion absorption in this region.

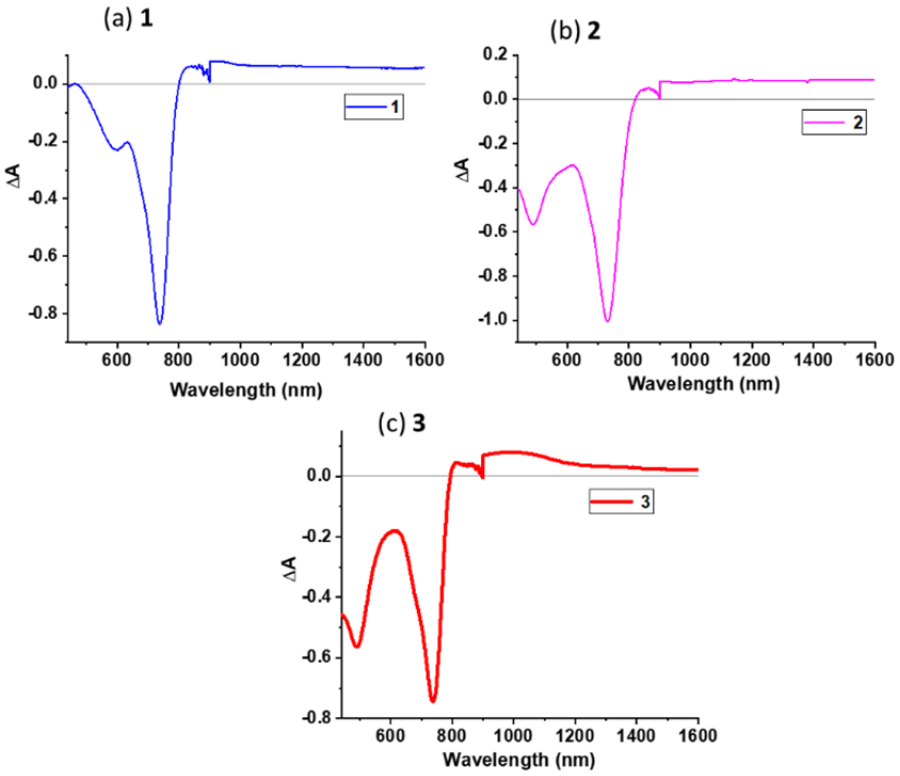

Figure 3.21: Differential spectrum of indicated compounds deduced for charge separated species from spectroelectrochemical data (see text for details).

The electronic structures were computationally investigated to gain additional support on the extent of orbital delocalization among different entities of a given push-pull system and orbitals involved in charge transfer process. For this, the geometries were fully optimized on a Born-Oppenheimer potential energy surface using B3LYP/6-31G(d, p) model chemistry,[15] and the frontier orbitals, generated both in gas phase and polar benzonitrile, as shown in Figure 3.19. In the case of gas phase 1, the HOMO was delocalized over the TPA-azaBODIPY while the LUMO was solely on the azaBODIPY. From the location of these orbitals a CT state, $TPA^{\delta+}$-$azaBODIPY^{\delta-}$, could be arrived in the gas phase. In polar benzonitrile, however, the CT state could undergo

complete charge separation to yield $TPA^{\delta+}$-$azaBODIPY^{\delta-}$ charge separated state upon photoexcitation. This is supported by the frontier HOMO and LUMO where majority of the HOMO on TPA arm (donor) and LUMO solely on azaBODIPY (acceptor) of 1 was observed (see Fig. 3.19b(i)).

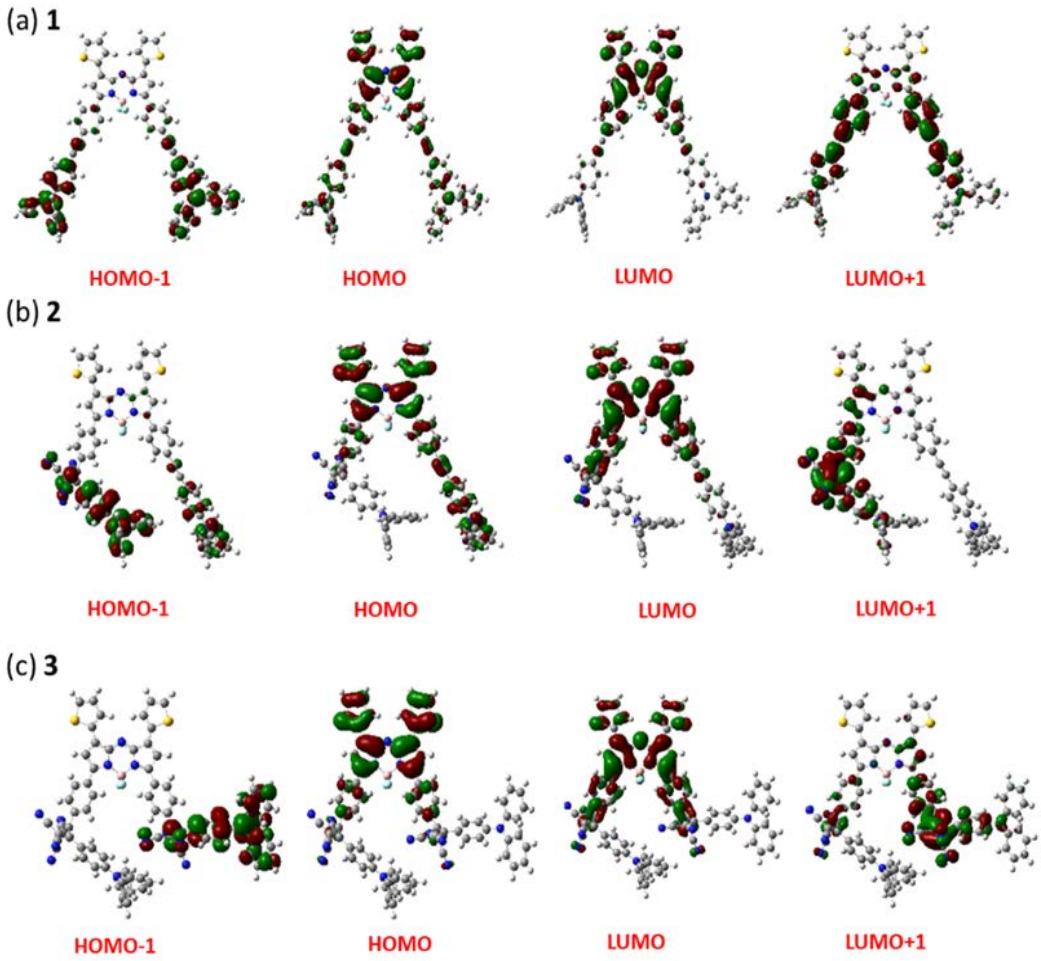

Figure 3.22: Gas phase frontier orbitals for the investigated compounds on B3LYP/6-31G(d, p) optimized geometries.

In the case of gas phase 2, HOMO on the TPA-azaBODIPY arm and LUMO on TCBD-azaBODIPY and LUMO+1 on the TCBD (see Fig. 3.22 for HOMO-1 and LUMO+1 in gas phase) was observed. From the orbital location, a $TPA^{\delta+}$-$(azaBODIPY\text{-}TCBD)^{\delta-}$-TPA CT state could be envisioned. Interestingly, in benzonitrile, HOMO mainly on the free TPA arm without TCBD, and

LUMO on TCBD-azaBODIPY was observed. This suggests formation of $TPA^{\delta+}$- (azaBODIPY-TCBD)$^{\delta-}$-TPA electron transfer product in polar solvent. In the case of gas phase 3, HOMO-1 on TCBD-TPA (Fig. 3.22), HOMO on azaBODIPY, LUMO on azaBODIPY-TCBD, and LUMO+1 on TCBD-TPA was observed. Symmetric distribution of LUMO on TCBD-azaBODIPY-TCBD suggests formation of initial $TPA^{\delta+}$-(TCBD-azaBODIPY-TCBD)$^{\delta-}$-TPA CT state. Interestingly, in benzonitrile, majority HOMO on TPA-TCBD (more on TPA) and LUMO on TCBD-azaBODIPY was observed. This suggests the CT state could undergo complete charge separation to yield $TPA^{\delta+}$-(TCBD-azaBODIPY-TCBD)$^{\delta-}$-TPA in polar media. These results suggest formation of CT states in nonpolar solvent toluene, and charge separated state in polar solvent, benzonitrile in compounds 1-3. The gas phase HOMO-LUMO were found to be 1.04, 1.06 eV and 1.08 eV that compared with the electrochemical gap of 1.33, 1.21 and 1.25 eV, respectively, for 1, 2 and 3.

Having envisioned the different possibilities of CT and CS in these high-energy CT-near-IR sensitizer conjugates, energy level diagrams were built to verify thermodynamic feasibilities of the envisioned photo-events. Here, $E_{0,0}$ stands for excitation energy of ^{1}azaBODIPY* (= 1.67 eV) and E_{CT} stands for excitation energy of the CT state, $TPA^{\delta+}$-$TCBD^{\delta-}$ state (= 2.52 eV for 2 and 2.56 eV for 3) were calculated from the optical data. Please note that the E_{CT} is higher by nearly 0.89 eV compared to $E_{0,0}$. The free-energy for charge separation, $-\Delta G_{CS}$ and charge recombination, $-\Delta G_{CR}$ were estimated according to Rehm-Weller approach[16] using following equations.

$$-\Delta G_{CR} = E_{ox} - E_{red} + \Delta G_S \quad \text{(Eq. 3.4)}$$

$$-\Delta G_{CS} = \Delta E_{0\text{-}0}\text{-}(-\Delta G_{CR}) \quad \text{(Eq. 3.5)}$$

where $\Delta E_{0\text{-}0}$ corresponds to the excited energy $E_{0\text{-}0}$ of ^{1}azaBODIPY* and E_{CT} is that of $TPA^{\delta+}$-$TCBD^{\delta-}$ state (calculated from CT peak maxima). The term ΔG_S refers to electrostatic energy calculated according to dielectric continuum model (see Eq. 3.6). The E_{ox} and E_{red} represent the

first oxidation potential and the first reduction potential, respectively, of the donor (TPA) and acceptor (azaBODIPY or TCBD) moieties of the conjugates.

$$\Delta G_S = e^2/4\,\pi\varepsilon_o\,[\,-\,1/R_{cc}\,\varepsilon_R] \qquad \text{(Eq. 3.6)}$$

The symbols ε_0 and ε_R represent vacuum permittivity and dielectric constant of benzonitrile used for photochemical and electrochemical studies (= 26.0). R_{CC} are the center-to-center distance between donor and acceptor entities from the computed structures.

Figure 3.23a shows the energy diagram for compound 1 having donor TPA and acceptor azaBODIPY entities. In polar benzonitrile, CS from ^{1}azaBODIPY* to yield TPA$^{\bullet+}$-azaBODIPY$^{\bullet-}$ is thermodynamically possible with an energy of charge separated state of 1.31 eV (=ΔG_{CR}). Formation of charge separation could also involve an intermediate CT state, as shown in Figure 3.23a. The energy of the CS state in this case is about 0.3 eV higher than that of ^{3}azaBODIPY* (E_T ~ 1.0 eV),[17] and under such conditions, the CS state could undergo CR to populate the low-lying ^{3}azaBODIPY* state. The ^{3}azaBODIPY* could relax back to the ground state slowly via the spin-forbidden triplet (phosphoresce) emission.

In the case of compound 2 (TPA-azaBODIPY-TCBD$^{\delta-}$-TPA$^{\delta+}$), exciting the sample at 490 nm corresponding to the CT state would produce excited TPA-azaBODIPY-^{1}[(TCBD$^{\delta-}$-TPA$^{\delta+}$)]* state (Fig. 3.23b). Being higher in energy, this state could readily populate the ^{1}azaBODIPY* state that could also be produced by direct excitation of 2 at 700 nm (LE excitation). Supported by the earlier discussed spectral and computational studies, ^{1}azaBODIPY* could yield TPA$^{\delta+}$-(azaBODIPY-TCBD)$^{\delta-}$-TPA CT state, and in polar solvent would yield TPA$^{\bullet+}$-(azaBODIPY-TCBD)$^{\bullet-}$-TPA CS product. Alternatively, the CT and CS states could be formed directly from the excited TPA-azaBODIPY-^{1}[TCBD$^{\delta-}$-TPA$^{\delta+}$)]* in competition with populating the ^{1}azaBODIPY* (see Fig. 3.23b). In nonpolar solvent, where the energy of CS state is higher than the CT state (lack

of solvent stabilization), the CT state could relax directly to the low-lying ^{3}azaBODIPY* and then return to the ground state (see Fig. 3.24 for energy diagram in toluene).

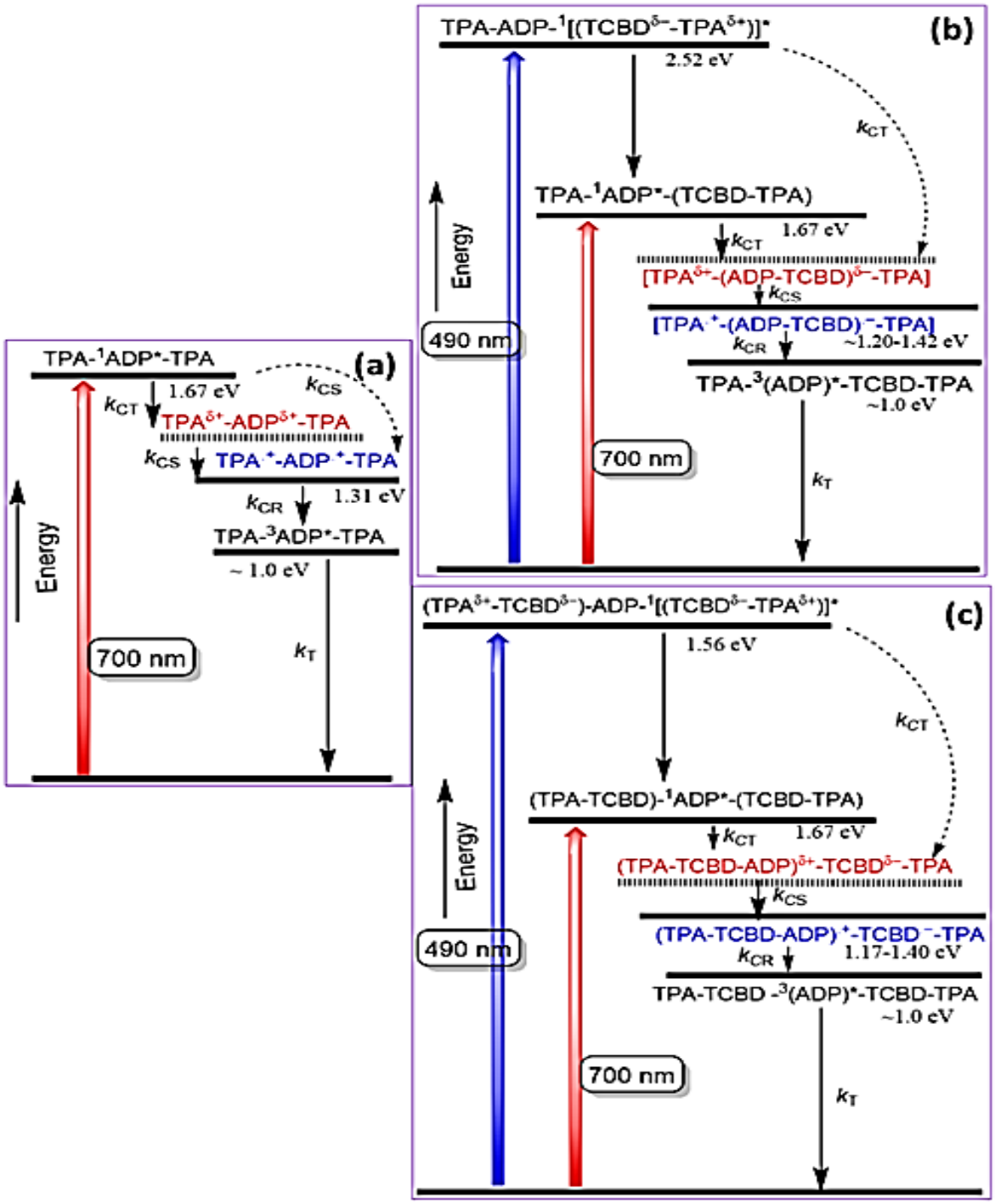

Figure 3.23: (a-c) Energy level diagram depicting different CT and CS processes in compounds 1-3, respectively, upon photoexcitation of either the CT or LE states in benzonitrile. Abbreviations: ADP = azaBODIPY and T_1 = triplet emission. Solid arrow: most likely process, dashed arrow: less likely process.

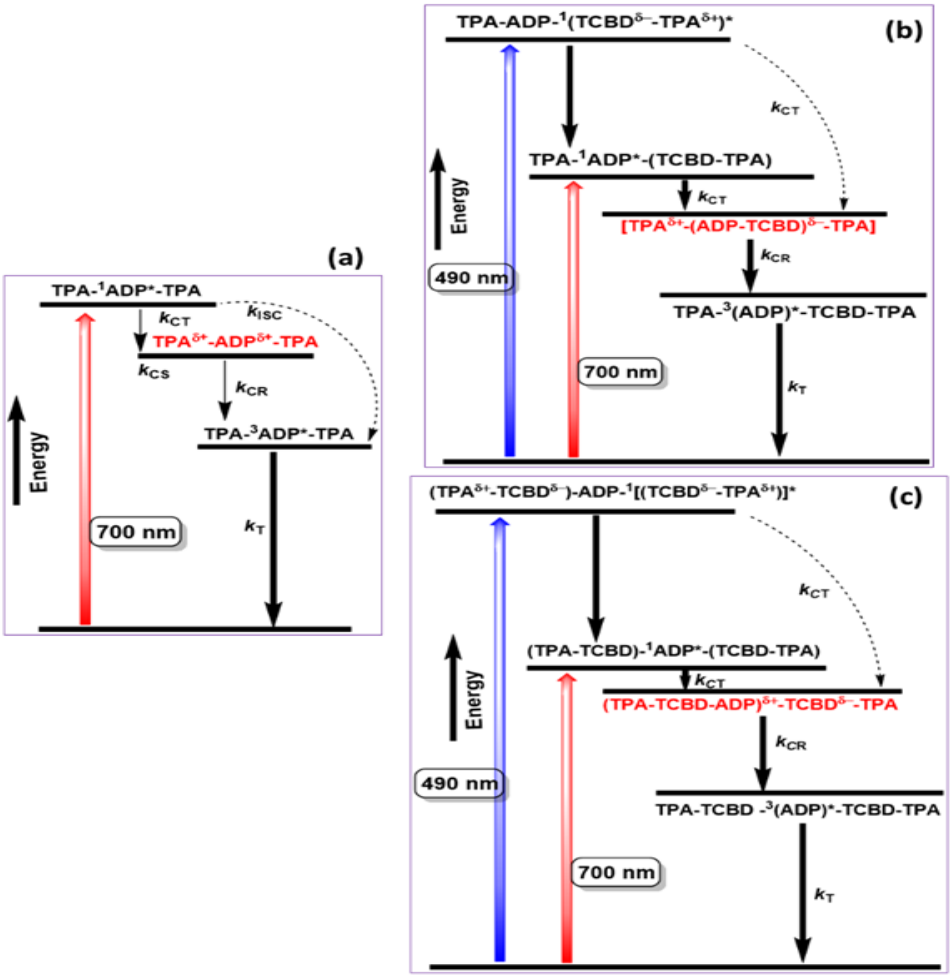

Figure 3.24: **Energy level diagram depicting different CT processes in compound 1-3 upon photoexcitation of either the CT or LE states in toluene. Note: CT states are lower in energy compared to CS states, therefore, CS state is not shown. Abbreviations: ADP = azaBODIPY and T = triplet emission. Solid arrow: most likely process, dashed arrow: less likely process.**

Likewise, in the case of compound **3**, ($TPA^{\delta+}$-$TCBD^{\delta-}$-azaBODIPY-$TCBD^{\delta-}$-$TPA^{\delta+}$), excitation of CT peak at 490 nm would produce the ($TPA^{\delta+}$-$TCBD^{\delta-}$)-azaBODIPY-^{1}[($TCBD^{\delta-}$-$TPA^{\delta+}$)]* state that would populate the low-lying ^{1}azaBODIPY* state or directly involve in producing the $TPA^{\delta+}$-(TCBD-azaBODIPY-TCBD)$^{\delta-}$-TPA CT state, supported by earlier discussions (see Fig. 3.23c). In polar benzonitrile, the CT state could produce the $TPA^{\bullet+}$-(TCBD-azaBODIPY-TCBD)$^{\bullet-}$-TPA CS state. This state, being higher in energy would populate the ^{3}azaBODIPY* state prior returning to the ground state. Similar to that anticipated for 2, in toluene,

the $TPA^{\delta+}$-(TCBD-azaBODIPY-TCBD)$^{\delta-}$-TPA CT state could directly relax to the ^{3}azaBODIPY* without yielding a charge separated state (see Fig. 3.24 for energy diagram in toluene). In summary, these energy level diagrams have helped to unravel different photo-events, and successfully figure out structure-photofunctionality of these high-energy charge transfer-near-IR sensitizer systems.

Finally, in order to verify whether near-IR excitation of azaBODIPY and direct excitation of the CT band of $TPA^{\delta+}$-$TCBD^{\delta-}$ in these push-pull systems would promote charge transfer and charge separation, femtosecond transient absorption (fs-TA) spectral studies were performed. Figure 3.25 (a-c) show fs-TA spectra at the indicated delay times of 1-3 in benzonitrile at the excitation wavelength of 700 nm exciting mainly the azaBODIPY entity. The corresponding spectra in toluene are shown in Figure 3.26. From earlier discussed spectral data, a charge separation process was anticipated in the case of 1 in polar benzonitrile and may not be in nonpolar toluene. Figure 3.23a shows fs-TA spectra at the indicated delay times of 1 in benzonitrile upon azaBODIPY excitation. The ^{1}azaBODIPY* revealed positive peaks at 466 and 1206 nm due to ESA and a negative peak at 750 nm due to GSB (see Fig. 3.27 for fs-TA of pristine azaBODIPY revealing ~1100 nm near-IR singlet-singlet transition). Within the next 2-3 ps, peaks expected for the charge separated state were evolved, especially $1^{\cdot-}$ peak expected in the 935 nm range. The near-IR peak in the 1300 nm range is due to excited TPA (perhaps due to simultaneous excitation, see Fig. S29 for fs-TA of a TPA control compound revealing ~1350 nm ^{1}TPA* excitation, see Fig. 3.28 for fs-TA of a TPA control compound revealing ~1350 nm ^{1}TPA* transition). However, as shown in Figure 3.26a, spectra recorded for 1 in toluene revealed no strong spectral features characteristic of the charge separated state from the initial CT state. Instead, weak features of ^{3}azaBODIPY* started emerging (see Fig. 3.29 for nanosecond transient spectra of

^{3}azaBODIPY*),[17] suggesting CT state directly relaxing to the ^{3}azaBODIPY* instead of generating charge separated species.

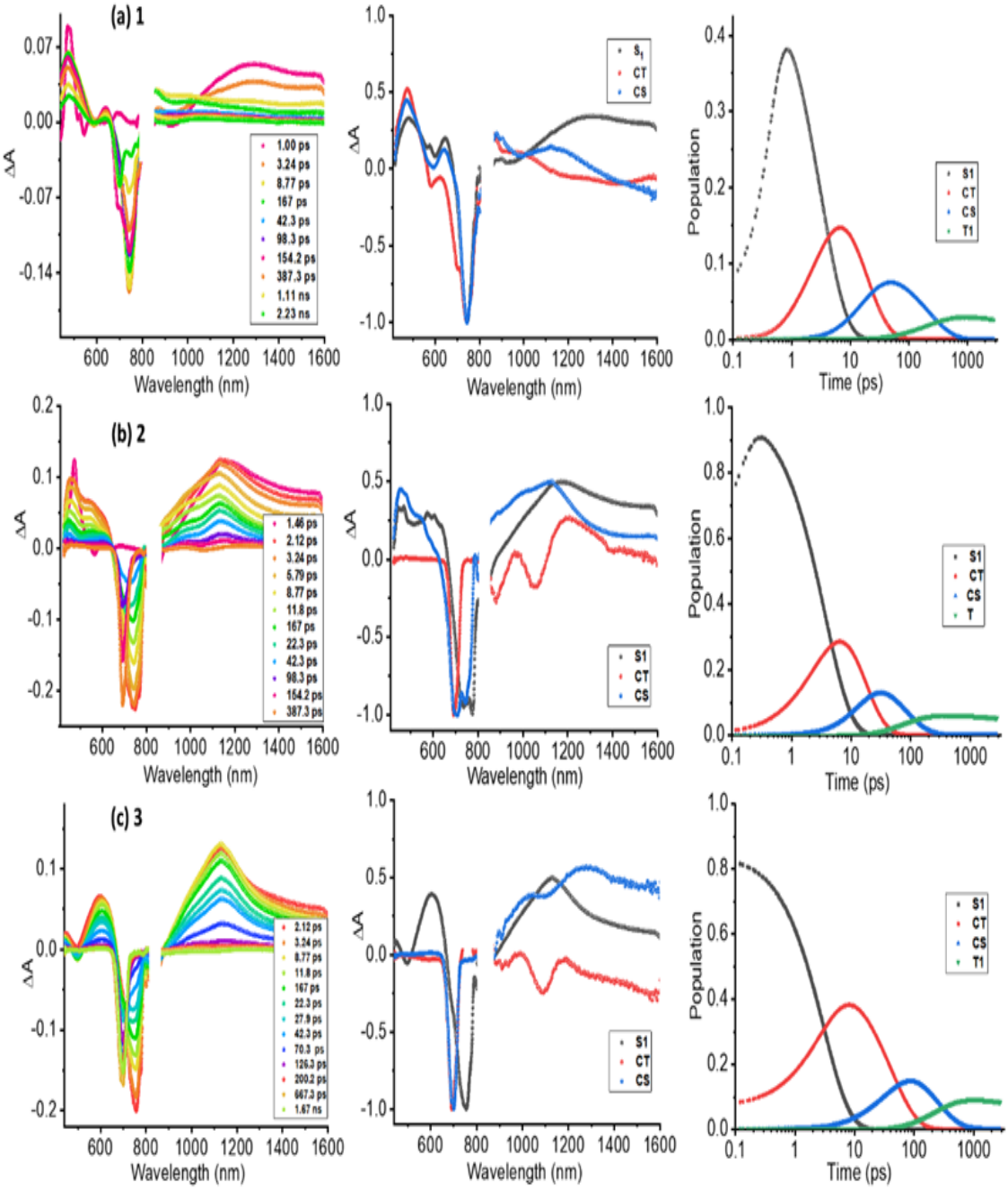

Figure 3.25: (a-b) Fs-TA spectra of indicated compounds in benzonitrile at the excitation wavelength of 490 nm corresponding to CT excitation. The species associated spectra and population kinetics from global target analysis are shown on the middle and right-hand side panels for the corresponding compound. SAS of T_1 state is not shown for simplicity, only the major species are shown. The sharp peak at 490 nm both in fs-TA and SAS is due to excitation pulses. The spectra are blocked in the 800 nm region from the noises generated at the extreme end of the detectors.

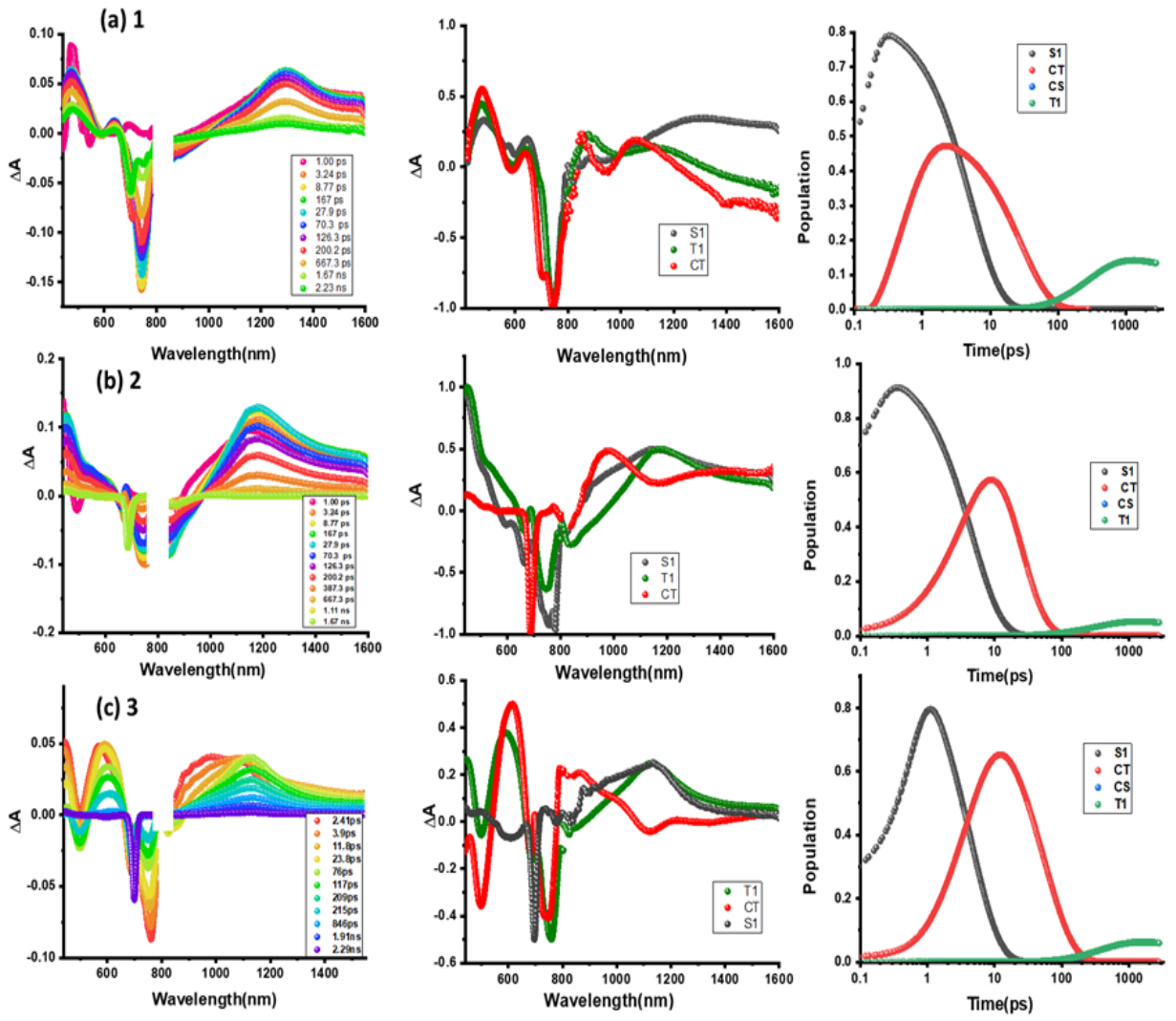

Figure 3.26: (a-c) Fs-TA spectra of indicated compounds in toluene at the excitation wavelength of 700 nm corresponding to azaBODIPY excitation. The species associated spectra from global target analysis are shown on the right hand side panels for the corresponding compound. The sharp peak at 700 nm both in fs-TA and SAS is due to excitation pulses. The spectra are blocked in the 800 nm region from the noises generated at the extreme end of the detectors (detector change was at 800 nm).

The fs-TA transient spectra of 2 and 3 in benzonitrile proved formation of charge separation upon near-IR excitation of azaBODIPY, as shown in Figures 3.25 (b and c). For both compounds, faster recovery of the GSB/ESA peaks resulted in the expected $2^{\bullet-}$ peak in the 970 nm range and that of $3^{\bullet-}$ in the 990 nm range appeared as a shoulder peak to main peak at 1100 nm, providing spectral evidence of charge separation. Changing the solvent to toluene provided very weak spectral evidence for charge separation (Fig. 3.26).

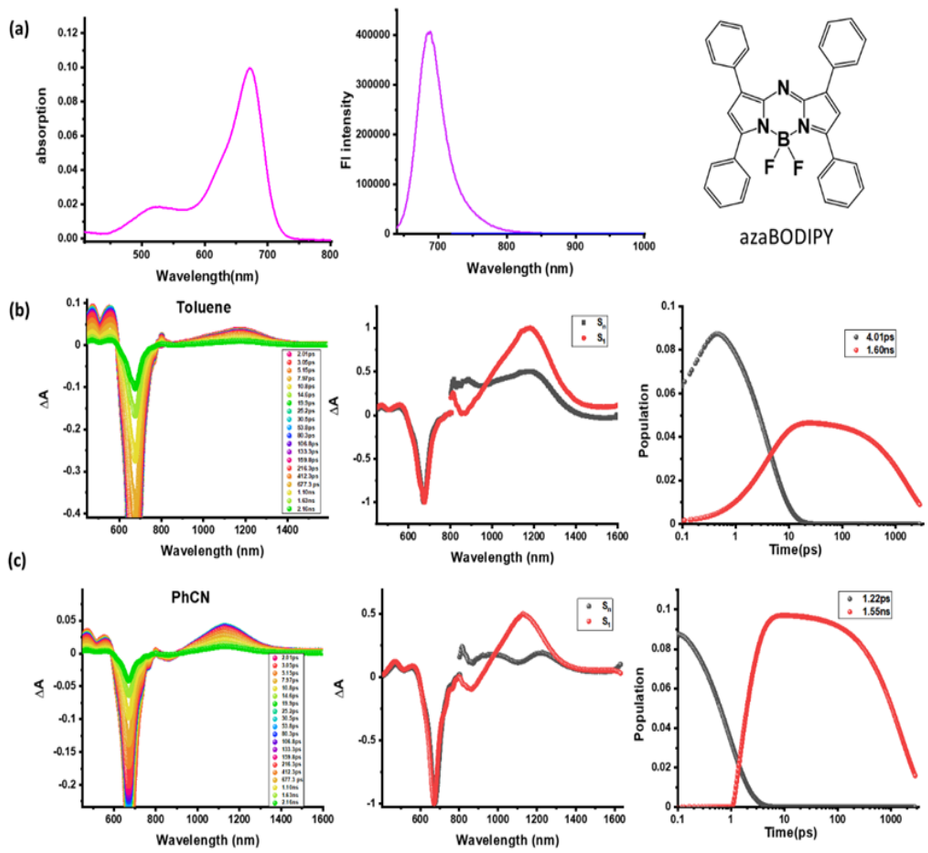

Figure 3.27: Fs-TA spectra and target analysis results on pristine azaBODIPY in toluene and benzonitrile. The compound was excited at visible peak maxima. The near-IR band is due to singlet-singlet transition.

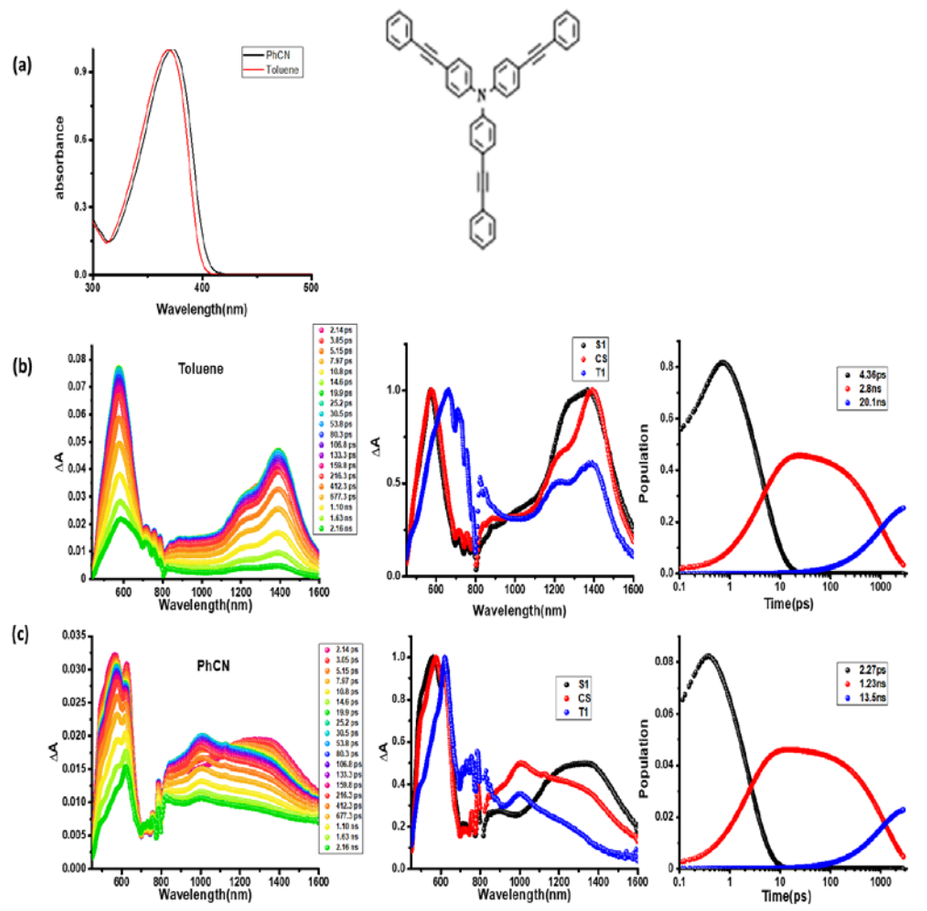

Figure 3.28: Fs-TA spectra and target analysis results on a control TPA compound in toluene and benzonitrile. The compound was excited at visible peak maxima. The near-IR band is due to singlet-singlet transition.

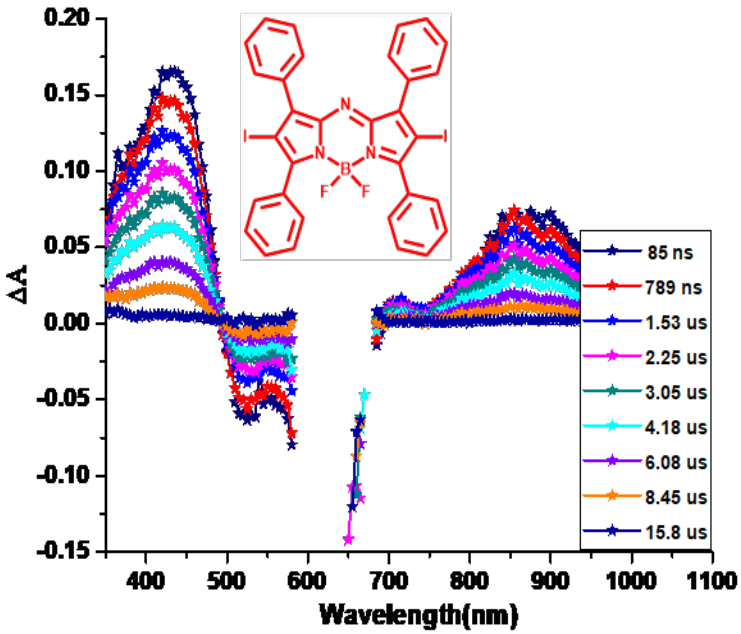

Figure 3.29: Nanosecond transient absorption spectra of β-iodo azaBODIPY in toluene (λ_{ex} = 650 nm).

The transient data was subjected to global target analysis,[17] and species associated spectra (SAS) and population kinetics of different species were generated for the best fit. These results are shown in Figure 3.25 middle and right-hand side columns for the corresponding system. In all the studied systems, the data could be satisfactorily fitted to four components. The first SAS appearing in 3-5 ps had peaks characteristic of ^{1}azaBODIPY* and the second SAS with features that could be attributed to the anticipated charge transfer state while the third SAS had features expected for the charge separated state from earlier discussed spectroelectrochemical results, thus confirming occurrence of charge separation upon near-IR excitation in these conjugates. Finally, the last SAS lasting over 3 ns had features of developing ^{3}azaBODIPY* suggesting that the CS state relaxes to the triplet state prior returning to the ground state (SAS not shown, see spectrum at latter delay times in fs-TA spectra). Time constants evaluated from population kinetics plots (right hand panel) are listed in Table 3.4.

Table 3.4: **Time constants for various photo-events from global target analysis of transient data of compounds 1-3 in benzonitrile and toluene.**

Compound	Solvent	λ_{ex}, nm	$\tau_{(CT)int,ps}$	τ_{S1}, ps	τ_{CT}, ps	τ_{CS}, ps	τ_{T1}, ns
1	PhCN	700	--	4.03	11.4	63.3	> 3
2			--	3.68	12.9	72.5	> 3
3			--	3.06	41.4	218.7	> 3
2		490	1.02	7.25	28.4	295.5	> 3
3			0.58	8.69	34.4	283.4	> 3
1	Tol	700	--	4.94	33.3	--	> 3
2			--	4.68	20.1	--	> 3
3			--	4.32	53.9	--	> 3
2		490	2.22	12.67	34.8	--	> 3
3			1.33	18.18	49.7	--	> 3

Having established successful excited state charge separation upon near-IR irradiation, next, compounds 2 and 3 having strong CT absorption in the visible region were excited at 490 nm corresponding to the high-energy CT state. Characteristic peaks of ^{1}azaBODIPY* started developing from the initial excited CT state within the first 1-2 ps, as predicted from the energy diagram in Figure 3.23 (b and c) (denoted as $\tau_{(CT)int}$ in Table 3.4). Following this, photo-events from ^{1}azaBODIPY* tracked largely that observed when azaBODIPY was directly excited, leading to the process of charge transfer, charge separation and population of ^{3}azaBODIPY*, as shown in Figure 3.30. Changing the solvent to nonpolar toluene revealed CT formation without much evidence for CS (see Fig. 3.31).

Glotaran analysis of these transient data needed up to five component fits resulting in five SASs, as shown in the middle panel of Figure 3.30. The first SAS with a time constant of 0.5-2.2 ps was attributed to excited charge transfer state (denoted as $\tau_{(CT)int}$ in Table 3.4), that relaxes to populate the ^{1}azaBODIPY* in about 8-20 ps (see Fig. 3.30 right hand panel for population kinetics). The time constant for this process was slightly longer than that observed for direct excitation of

azaBODIPY at 700 nm where a time constant of 3-5 ps was observed. The third SAS attributed to excited CT state (see Fig. 3.23 b and c, marked in red) had also had slightly large time constants in the order of 28-50 ps as against 11-54 ps when the sample was excited at 700 nm. The fourth SAS (blue) resembled to that expected for the charge separated state with higher time constants. Finally, the slowly developing fifth SAS was attributable to ^{3}azaBODIPY*.

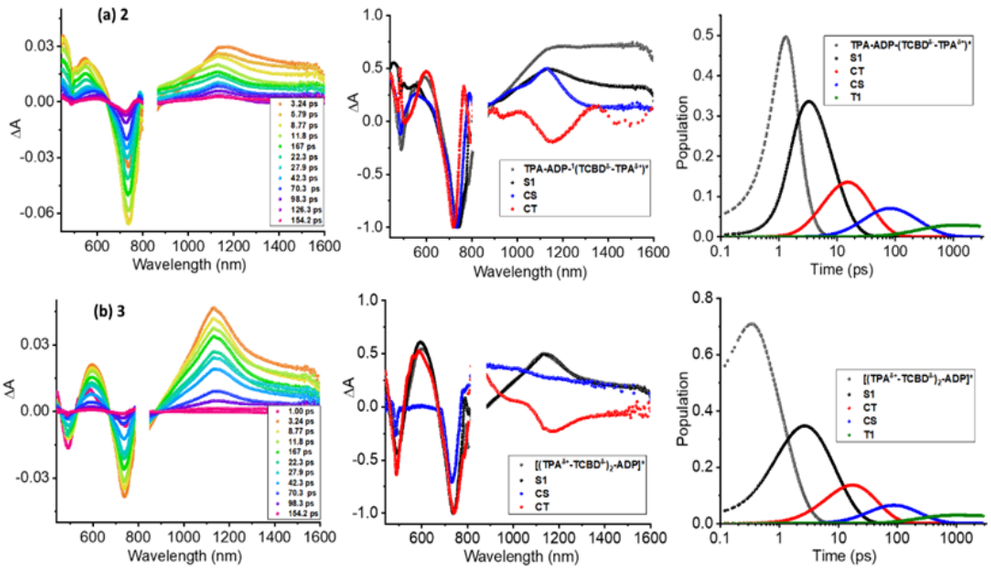

Figure 3.30: (a-b) Fs-TA spectra of indicated compounds in benzonitrile at the excitation wavelength of 490 nm corresponding to CT excitation. The species associated spectra and population kinetics from global target analysis are shown on the middle and right hand side panels for the corresponding compound. SAS of T_1 state is not shown for simplicity, only the major species are shown. The sharp peak at 490 nm both in fs-TA and SAS is due to excitation pulses. The spectra are blocked in the 800 nm region from the noises generated at the extreme end of the detectors.

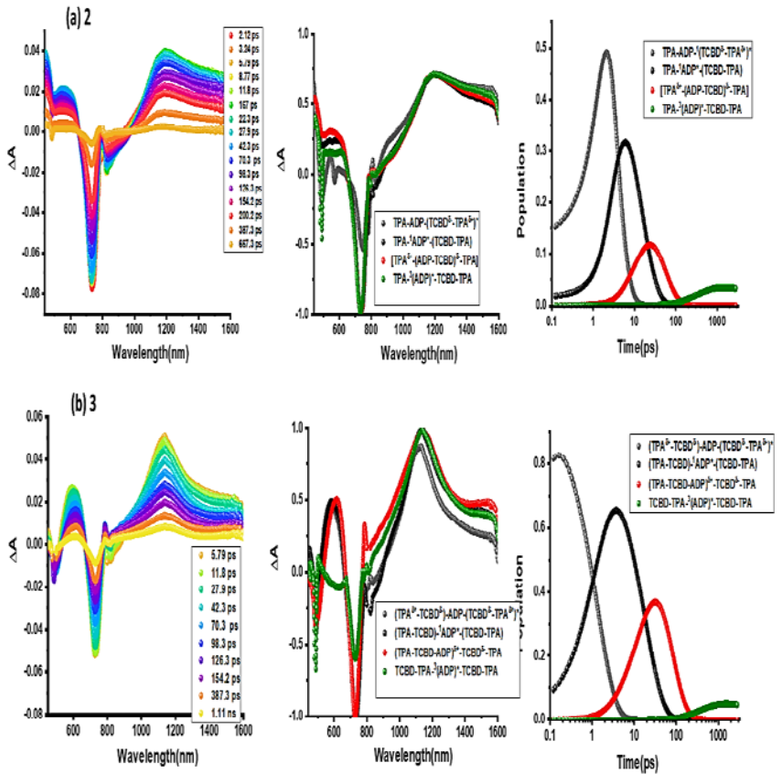

Figure 3.31: (a-b) Fs-TA spectra of indicated compounds in toluene at the excitation wavelength of 490 nm corresponding to CT excitation. The species associated spectra from global target analysis are shown on the right-hand side panels for the corresponding compound. The sharp peak at 490 nm both in fs-TA and SAS is due to excitation pulses.

Transient spectral results discussed above and the kinetic data secured from global target analysis as summarized in Table 3.4 revealed several unprecedented observations. First and foremost, the observation of near-IR excitation leading to charge separation in these novel 'high-energy CT coupled near-IR push-pull systems' opens up new design strategies for wide-band capturing, multi-modular push-pull systems for ultrafast charge separation. Second, presence of a second TCBD in 2, made both τ_{CT} and τ_{CS} last longer. It is likely that the electron exchange between the two TCBD entities upon electro-reduction as shown in Figure 3.16b prolongs lifetime of charge separated state, along with any structure variations, a property that was never been reported to-date. Third, as a consequence of closely positioned, strongly interacting push-pull nature of the present systems, changing the solvent from polar to nonpolar did not hinder the process of charge transfer, although no clear evidence for charge separated state could be established in toluene. Finally, exciting the samples corresponding to their high-energy CT states, almost instantaneously populated the low-lying ^{1}azaBODIPY* state (~2 ps) which in turn promoted the subsequent CT and CS processes in sequence in polar benzonitrile.

It may be pointed out here that in benzonitrile at the excitation wavelength of 700 nm corresponding to azaBODIPY, both τ_{CT} and τ_{CS} of 1 are shorter than those observed for 2 and 3 (Table 3.4). This suggests existence of strong excited state interactions between electron rich TPA and electron deficient azaBODIPY entities in 1.

3.2.4 Conclusions

In summary, this work reports on interfacing high-energy charge transfer states to near-IR sensitizer for wide-band capture and ultrafast charge separation. Interfacing the high-energy absorbing, one or two TPA$^{\delta+}$-TCBD$^{\delta-}$ charge transfer entities onto near-IR absorbing azaBODIPY caused marginal perturbation of their ground state optical properties, however, their combination

made them panchromatic light absorbing multi-modular systems. In compound 3, having two symmetrically attached TPA-TCBD entities, electron exchange between the TCBD entities upon electroreduction was observed, that is, electron exchange through the central azaBODIPY was possible to witness. Presence of TPA-TCBD entities caused quantitative quenching of azaBODIPY fluorescence indicating occurrence of excited state events. Electrochemical results coupled with computational studies, revealed presence of different charge transfer and charge separation states in 2 and 3. Further, spectroelectrochemical studies provided spectral proof in the form of new near-IR bands upon one-electron reduction, and from further analysis of such data, it was possible to deduce spectrum of the charge separated species. Finally, although fairly complex, it has been possible to dissect different photo-events and successfully figure out structure-photofunctionality in these high-energy charge transfer-near-IR sensitizer systems. That is, systematic studies performed using fs-TA coupled with global target analysis successfully demonstrated charge separation upon photoexcitation corresponding to either near-IR or CT excitation in benzonitrile. The CS states lasted longer in 3 likely due to an electron exchange mechanism, a result new to this class of compounds. The present strategy of building, broad-band capturing, push-pull systems for excited state charge separation is expected to open up a new direction in building novel multi-modular systems for different energy and optoelectronic applications. Further studies along this line are in progress in our laboratories.

3.2.5 References and Notes

1. a) Y. Cai, Z. Wei, C. Song, C. Tang, W. Han, X. Dong, *Chem. Soc. Rev.* 2019, **48**, 22; b) B. Li, M. Zhao, F. Zhang, *ACS Materials Lett.* 2020, 2, **8**, 905–917; c) J. K.-H. Wong, M. H. Todd, P. J. Rutledge, *Molecules* 2017, **22**, 200; d) Y. Patil, R. Misra, *J. Mater. Chem. C*, 2019, **7**, 13020-13031.

2. a) T. Liu, G. Xie, C. Zhong, S. Gong, C. Yang, *Adv. Funct. Mater.* 2018, **28**, 1706088; b) B. N. Giepmans, S. R. Adams, M. H. Ellisman, R. Y. Tsien, *Science* 2006, **312**, 217; c) E. L. Williams, J. Li, G. E. Jabbour, *Appl. Phys. Lett.* 2006, **89**, 3506; d) D. Y. Kim, D. W. Song,

N. Chopra, P. De Somer, F. So, *Adv. Mater*. 2010, **22**, 2260; e) B. Stender, S. F. Völker, C. Lambert, J. Pflaum, *Adv. Mater*. 2013, **25**, 2943; f) N. Tessler, V. Medvedev, M. Kazes, S. Kan, U. Banin, *Science* 2002, **295**, 1506; g) G. Chen, W. Shao, R. R. Valiev, T. Y. Ohulchanskyy, G. S. He, H. Argren, P. N. Prasad, Adv. Opt. Mater. 2016, **4**, 1760-1766; h) C. C. Chen, L. Dou, R. Zhu, C. H. Chung, T. B. Song, Y. B. Zhen, S. Hawks, G. Li, P. S. Weiss, Y. Yang, *ACS Nano*, 2012, **6**, 7185-7190.

3. a) A. K. East, M. Y. Lucero, J. Chan, *Chem. Sci*. 2020, in press; b) C. Farrera, A. Torres, F. N. Fernando, *ACS Nano*, 2017, **11**, 10637-10643; C) Y. Ni, J. Wu, *Org. Biomol. Chem*. 2014, **12**, 3774-3791.

4. a) S. V. Eliseeva, J. C. G. Bunzli, *Chem. Soc. Rev*. 2010, **39**, 189-227; b) E. I. Altinoglu, J. H. Adair, *Wiley Interdisc. Rev., Nanomed and Nanotech.* 2010, **2**, 461-477; c) X. He, K. Wang, Z. Cheng, *Wiley Interdisc. Rev., Nanomed and Nanotech*. 2010, **2**, 349-366; d) B. Saremi, V. Bandi, S. Kazemi, Y. Hong, F. D'Souza, B. Yuan, *Polymers*, 2020, **12**, 540 and references cited therein.

5. a) M. O. Senge, M. Fazekas, E. G. A. Notaras, W. J. Blau, M. Zawadezka, O. B. Locos, E. M. N. Mhuircheartaigh, *Adv. Mater*. 2007, **19**, 2737-2774; b) Y. Patil, R. Misra, *Chem. Asian J.* 2018, **13**, 220-229; c) M. Kivala, and F. Diederich, *Acc. Chem. Res*. 2009, **42**, 235-248; d) B. Patrizi, C. Concetta, A. Pietropaolo, P. Foggi, M. S. de Cumis, *Molecules*, 2020, **25**, 430; e) Y. Patil, R. Misra, *Chem. Rec.* 2019, **19**, 1–9.

6. a) M. R. Bryce, *Adv. Mater*. 1999, **11**, 11-23; b) J. W. Verhoeven, J. *Photochem. Photobiol C: Photochem. Rev*. 2006, **7**, 40-60.

7. a) Y. Li, T. Liu, H. Liu, M. Z. Tian, Y. Li, *Acc. Chem. Res*. 2014, **47**, 186-1198; b) M. Sauer, *Angew. Chem. Int. Ed*. 2003, **42**, 1790-1793; c) P. Gautam, R. Sharma, R. Misra, M. L. Keshtov, S. A. Kuklin, G. D. Sharma, *Chem. Sci.* 2017, **8**, 2017; d) Y. Patil, R. Misra, R. Singhal, G. D. Sharma, *J. Mater. Chem. A* 2017, **5**, 13625–13633.

8. a) T. Michinobu, J. C. May, J. H. Lim, C. Boudon, J. Gisselbrecht, P. Seiler, M. Gross, I. Biaggio and F. Diederich, *Chem. Commun*., 2005, 737–739; b) M. Kivala, C. Boudon, J.-P. Gisselbrecht, P. Seiler, M. Gross, F. Diederich, *Angew. Chem*. 2007, ***119***, 6473–6477; *Angew. Chem. Int. Ed*. 2007, **46**, 6357–6360.

9. a) A. Gopinath, N. Manivannan, S. Mandal, N. Mathivanan, A. S. Nasar, *J. Mater. Chem. B* 2019, **7**, 6010–6023; b) T. Michinobu, I. Boudon, J.-P. Gisselbrecht, P. Seiler, B. Frank, N. N. P. Moonen, M. Gross, F. Diederich, *Chem. Eur. J.* 2006, **12**, 1889–1905; c) T. Michinobu, *Chem. Soc. Rev.* 2011, **40**, 2306–2316; d) T. Shoji, S. Ito, K. Toyota, T. Iwamoto, M. Yasunami, N. Morita, *Eur. J. Org. Chem.* 2009, 4316–4324; e) H. Gotfredsen, T. Neumann, F. E. Strom, A. V. Munoz, M. Jevric, O. Hammerich, K. V. Mikkelsen, M. Freitag, G. Boschloo, M. B. Nielsen, *ChemPhotoChem*. 2018, **2**, 976. f) A. T. Bui, C. Philippe, M. Beau, N. Richy, M. Cordier, T. Roisnel, L. Lemiegre, O. Mongin, F. Paul, Y. Trolez, *Chem. Commun*. 2020, **56**, 3571-3574. g) M. Yamada, W. B. Schweizer, F. Schoenebeck, F. Diederich, *Chem. Commun*. 2010, **46**, 5334-5336. h) M. Yamada, P.

Rivera-Fuentes, W. B. Schweizer, F. Diederich, *Angew. Chem. Int. Ed*. 2010, **49**, 3532-3535.

10. a) M. Sekita, B. Ballesteros, F. Diederich, D. M. Guldi, G. Bottari, T. Torres, *Angew. Chem. Int. Ed.* 2016, **55**, 5560; b) K. A. Winterfeld, G. Lavarda, J. Guilleme, M. Sekita, D. M. Guldi, T. Torres, G. Bottari, *J. Am. Chem. Soc*. 2017, **139**, 5520; c) K. A. Winterfeld, G. Lavarda, J. Guilleme, D. M. Guldi, T. Torres, G. Bottari, *Chem. Sci*., 2019, **10**, 10997.

11. a) P. Gautam, R. Misra, M. B. Thomas, F. D'Souza, *Chem. Eur. J.* 2017, **23**, 9192; b) R. Sharma, M. B. Thomas, R. Misra, F. D'Souza, *Angew. Chem. Int. Ed.* 2019, **58**, 4350; c) Y. Rout, Y. Jang, H. B. Gobeze, R. Misra, F. D'Souza, *J. Phys. Chem. C* 2019, **123**, 23382; d) M. Poddar, Y. Jang, R. Misra, F. D'Souza, *Chem. Eur. J*. 2020, **26**, 6869–6879.

12. a) G. Ulrich, R. Ziessel, A. Harriman, *Angew. Chem. Int. Ed*. 2008, **47**, 1184; b) R. Ziessel, A. Harriman, *Chem. Commun*. 2011, **47**, 611; c) M. E. El-Khouly, S. Fukuzumi, F. D'Souza, *ChemPhysChem*, **2014**, *15*, 30; D) V. Bandi, H. B. Gobeze, F. D'Souza, *Chem. Eur. J.* 2015, **21**, 11483-11494.

13. a) S. Liu, Z. Shi, W. Xu, H. Yang, N. Xi, X. Liu, Q. Zhao, W. Huang, *Dyes and Pigments*, 2013**, 103**, 145-153. b) A. Loudet, K. Burgess, *Chem. Rev*. 2007, **107**, 4891-4932.

14. *Principles of Fluorescence Spectroscopy*, 3rd ed. (Ed.: J. R. Lakowicz), Springer, Singapore, 2006.

15. *Gaussian 09*, Revision C.01, Gaussian, Inc., Wallingford, CT, USA, 2009.

16. D. Rehm, A. Weller, *Isr. J. Chem*. 1970, **8**, 259–271.

17. S. Shao, H. B. Gobeze, V. Bandi, C. Funk, B. Heine, M. J. Duffy, V. Nesterov, P. A. Karr, and F. D'Souza, *ChemPhotoChem*, 2020, **4**, 68.

18. http://glotaran.org/

CHAPTER 4

ENHANCING CHARGE STABILIZATION IN SYMMETRIC TRIPHENYLAMINE-DERIVED CONJUGATES AND STAR-SHAPED PUSH-PULL SYSTEMS

4.1 Charge Stabilization via Electron Exchange: Excited Charge Separation in Symmetric, Central Triphenylamine Derived, Dimethylaminophenyl-Tetracyanobutadiene Donor-Acceptor Conjugates*

4.1.1 Introduction

Excited state charge transfer in donor-acceptor conjugates is one of the widely investigated topics in recent years due to their usage in building energy harvesting photonics devices.[1-19] Understanding the principles governing the kinetics of charge transfer and separation, securing high charge separation quantum yields, avoiding large energy losses, and prolonging the lifetime of the radical ion-pairs by molecular engineering of the conjugates have been the main focus of these studies.[1-12] In simple donor-acceptor conjugates, charge separation from the excited singlet state of the donor or acceptor can store the greatest amount of energy, however, since the process originates from the singlet excited state, the charge separated states are generally short-lived. In natural photosynthesis, lifetime of charge separation is prolonged by subsequent electron transfer to secondary acceptors.[20-22] This method of charge stabilization, optimizes the quantum yields but comes at the cost of lowering the overall efficiency due to the energy losses encountered during secondary electron transfer steps. Alternate approaches including electron/hole delocalization in conjugates having closely interacting multiple donor or acceptor entities,[23-24] and utilization of high energy triplet sensitizers to promote charge transfer from long-lived triplet excited states to

* Section 4.1 is reproduced from Yadav, Indresh S., Ajyal Z. Alsaleh, Rajneesh Misra, and Francis D'Souza. "Charge Stabilization Via Electron Exchange: Excited Charge Separation in Symmetric, Central Triphenylamine Derived, Dimethylaminophenyl–Tetracyanobutadiene Donor–Acceptor Conjugates," Chemical Science 12, no. 3 (2021): 1109-20. https://doi.org/10.1039/D0SC04648E. Originally published by Royal Society of Chemistry under CC-BY; authors retain copyright.

prolong lifetime of charge separated states[25-26] have also been proven to work.

In recent years, the design and synthesis of π-conjugated symmetrical and unsymmetrical donor-acceptor chromophores have been extensively investigated due to their potential applications in organic photovoltaics,[27-30] molecular electronics[31] and bioimaging.[32] The star-shaped π-conjugated molecular systems exhibit many advantages over linear conjugated molecular systems including excellent solubility and lesser aggregation.[33] Tuning of electronic and photonic properties of these systems can be achieved by modulating the design of donor or acceptor units and connecting π-spacer unit.[34-36] The small organic π-conjugated donor-acceptor systems exhibit low band gap, intense absorption, and strong intramolecular interactions.[37-38] In several of these studies, triphenylamine, a classical nonplanar propeller shaped optoelectronic molecule, has been extensively used; extending their applications for developing field effect transistors, sensors, and solid state fluorescent and smart fluorescent materials.[39-40]

Tetracyanoethylene (TCNE) is a strong electron acceptor due to presence of four cyano groups, undergoes [2+2] cycloaddition reaction with electron rich alkynes to form cyclobutene rings followed by retroelectrocyclization reaction to give 1,1,4,4-tetracyanobutadiene (TCBD) derivatives.[41] The donor-acceptor systems containing TCBD acceptor are potential candidates for organic photovoltaics and non-linear optics due to strong intramolecular charge transfer (ICT) and lower HOMO-LUMO gaps.[42-48] Photochemical behavior of few donor-TCBD derived systems have been reported in literature.[49-56] Although with high quantum yields, due to close proximity between the donor and acceptor entities, ultrafast charge separation and recombination was observed in these systems. That is, no charge stabilization could be accomplished. In this regard, developing higher analogs of donor-TDCB bearing systems that would exhibit novel photochemical properties including charge stabilization have been scarce due to the associated

synthetic challenges. A recent example involves C_3-symmetric central truxene-derived phenothiazine-TCBD and its expanded molecular systems.[54] Although elegant, the central truxene made exclusively of saturated carbons played no role in stabilizing the charge separated states.

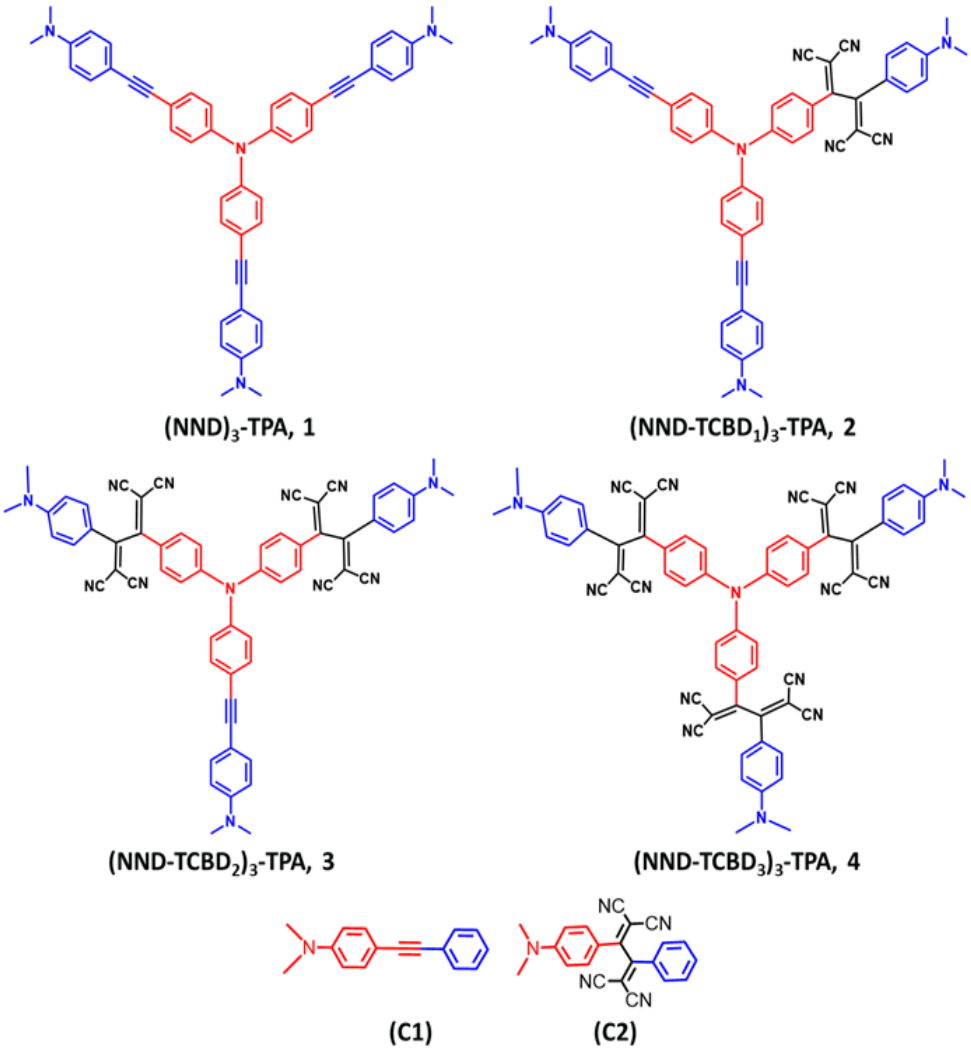

Figure 4.1: **Structure and abbreviation of star-shaped, central triphenylamine derived, dimethylamine-tetracyanobutadiene conjugates, 1-4 and the control compounds, C1-C2 newly designed, synthesized to demonstrate charge stabilization via electron exchange in the present study.**

In the present study, we hypothesize that by choosing a redox/photoactive central unit instead of truxene, we could modulate the properties that would lead to novel redox- and photochemical discoveries. With this in mind, we have newly designed and synthesized star-shaped symmetric compound $(NND)_3$-TPA, 1 and their TCBD functionalized symmetric and

unsymmetric derivatives (NND-TCBD$_{1-3}$)$_3$-TPA, 2–4 (see Fig. 4.1 for structures; NND = N,N-dimethylaminophenyl, TPA and TCBD = 1,1,4,4-tetracyanobutadiene). These novel systems show strong ICT with lowered HOMO-LUMO gaps. Further, upon electroreduction of NND-TCBD entities in compounds 3 and 4 containing two and three NND-TCBD entities, electron exchange among the NND-TCBD was witnessed. Femtosecond transient absorption studies revealed the occurrence of ultrafast charge transfer processes in these systems. Importantly, charge stabilization in 3 and 4 was witnessed as a consequence of electron exchange. These unpresented new findings provide a new mechanism of stabilizing the charge separated states via electron exchange in multi-modular donor-acceptor conjugates.

4.1.2 Synthesis

Scheme 4.1 shows the developed synthetic scheme for compounds 1-4 and their controls. Briefly, the symmetric (NND)$_3$-TPA, 1 was synthesized in 60% yield by the Pd-catalyzed Sonogashira cross coupling of tris-(4-iodo-phenyl)-amine and 4-ethynyl-*N*,*N*-dimethylaniline in degassed THF:TEA (1:1) under argon atmosphere, in the presence of Pd(PPh$_3$)$_4$ and CuI. Next, (NND-TCBD$_{1-3}$)$_3$-TPA, 2–4 were synthesized *via* [2+2] cycloaddition-retroelectrocyclization reaction with the strong electron acceptor TCNE. The reaction of 1 with one equivalent of TCNE in DCM at room temperature for 4 h resulted in an exclusive mono TCBD bearing (NND-TCBD$_1$)$_3$-TPA, 2 in 63% yield. Similarly, the reaction of 1 with two equivalent of TCNE in DCM solvent at 40 ^{o}C for 12 h resulted in (NND-TCBD$_2$)$_3$-TPA, 3 in 65% yield, whereas upon increasing the reaction temperature to 80 ^{o}C in DCE solvent for 24 h using four equivalent of TCNE with 1, resulted in symmetrical (NND-TCBD$_3$)$_3$-TPA, 4 in 70% yield. The control compound C1 was synthesized by the Pd-catalyzed Sonogashira cross-coupling reaction of 4-ethynyl-*N*,*N*-dimethylaniline and iodobenzene in 60% yield. The acetylene linked control compound C1 further

subjected to [2+2] cycloaddition-retro-electrocyclization reaction with one equivalent of TCNE at room temperature for 8 h, which resulted in TCBD substituted control compound C2 in 82% yield. The newly synthesized compounds were purified over silica gel (100-200 mesh) column chromatography using Hexane:DCM as solvent.

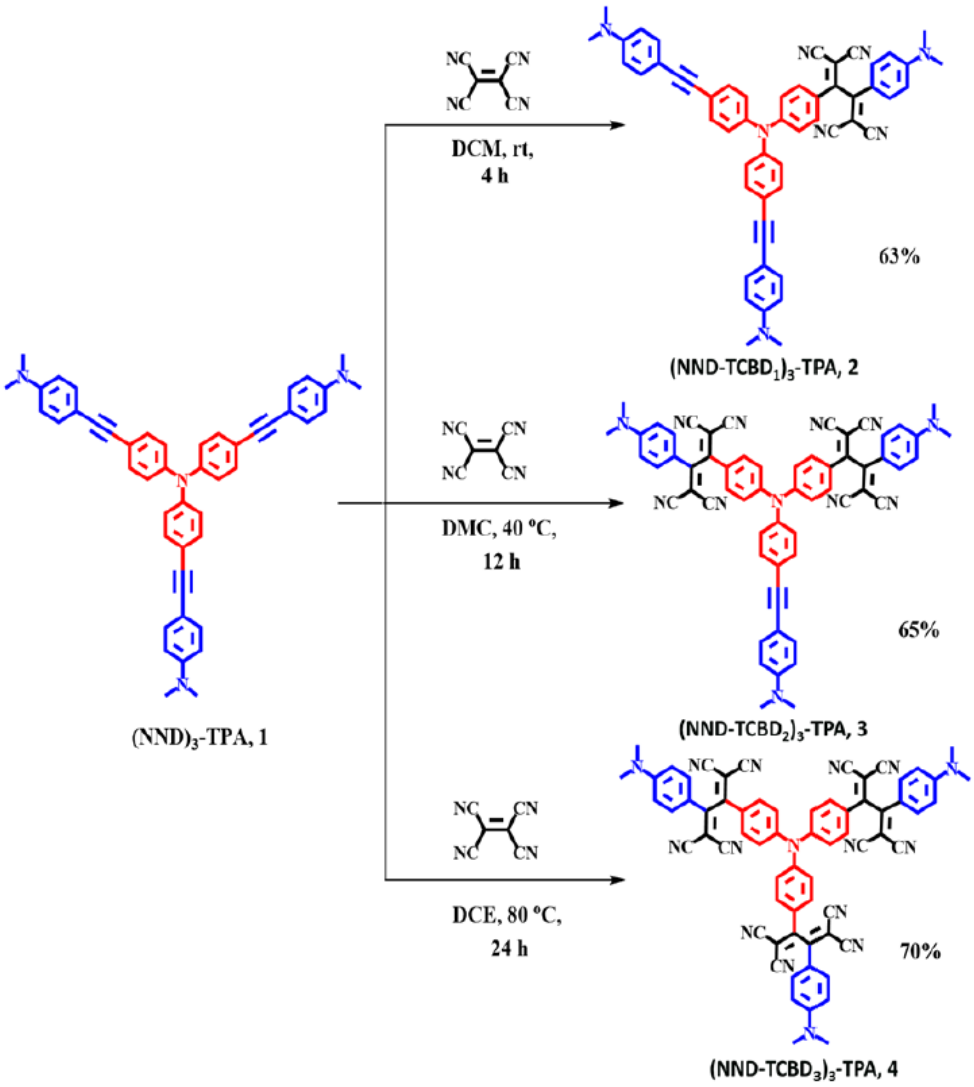

Scheme 4.1: Synthetic scheme of compounds $(NND)_3$-TPA, 1 and $(NND\text{-}TCBD_{1\text{-}3})_3$-TPA, 2–4.

4.1.3 Results and Discussion

Absorption spectrum of the investigated compounds is shown in Figure 4.2a. Control C1, having only a NND entity without either TPA or TCBD entities revealed an absorption band at

342 nm. In case of control C2, having an electron acceptor, TCBD next to the electron donor, NND entity, promoted charge transfer interactions between them. Consequently, two peaks, the first one at 315 and a second broad peak corresponding to charge transfer absorption at 478 nm, was observed. For compound 1, having a central TPA and three terminal NND entities revealed a single absorption peak at 386 nm. As predicted, no charge transfer type peak was present. However, in the case of compounds 2-4, having one, two and three TCBD entities between the NND and TPA entities, the expected charge transfer peak in the 478-484 nm region was possible to witness. In addition, a UV peak at 372 nm for 2, 350 nm for 3 and, <300 nm for 4, respectively, was also observed. Intensity of the charge transfer band increased with increasing the number of TCBD entities. Due to spectral similarities between C2 and compounds 2-4, and enhaneced absorption of the charge transfer band with increase in TDCB, it was possible to conclude that the origin of the charge transfer band is primarily due to interaction between NND and TCBD entities with lesser contributions from TPA interaction with TCBD. Optical data is summarized in Table 4.1.

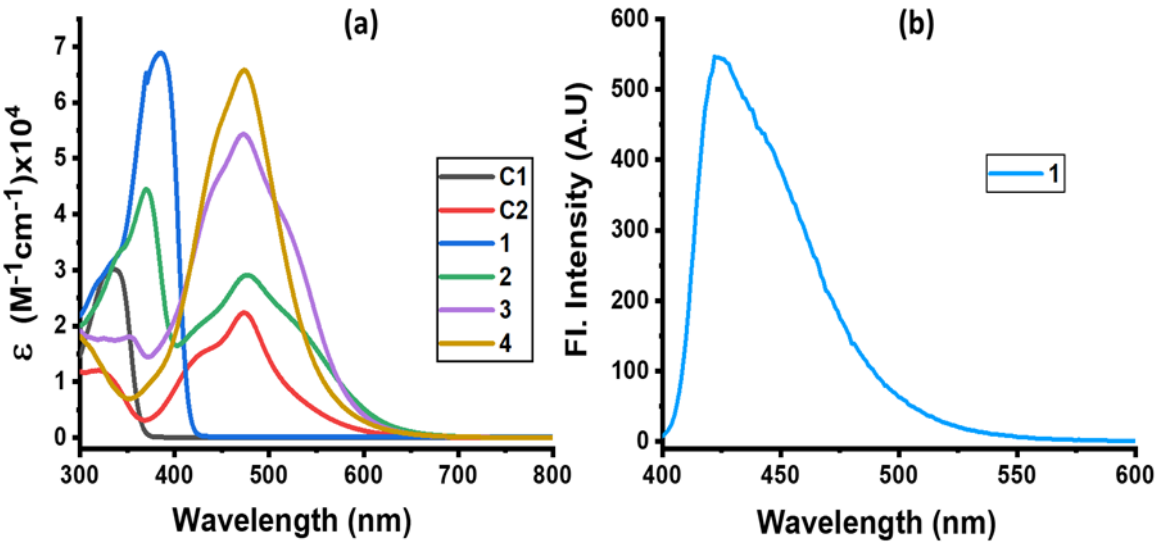

Figure 4.2: (a) Absorption and (b) fluorescence spectra of indicated compounds in DCB. Compound 1 was excited at 386 nm. No measurable emission was observed for compounds 2-4 upon exciting the samples either at the locally excited or charge transfer absorption peak positions.

Table 4.1: **Absorption and fluorescence, redox potentials (V vs. Ag/AgCl), and free-energy changes for charge recombination (CR), charge separation (CS), and charge transfer (CT) for the investigated central triphenylamine derived, dimethylamine-tetracyanobutadiene conjugates in DCB.**

System	λ_{max}, nm	E (10^5 M^{-1} cm^{-1})	λ_{em}, nm	Red-2 TCBD	Red-1 TCBD	Ox-1 TPA	Ox-2 NND	Ox-3 NND	$-\Delta G_{CR}$	$-\Delta G_{CS}$	$-\Delta G_{CT}$
C1	337	2.99		--	--	--	0.96	--	--	--	--
C2	327 473	1.16 2.23		-0.73	-0.39	--	1.43	--	--	--	--
1	384	6.89	420	--	--	0.80	1.15	--	--	--	--
2	372 477	4.40 2.91	419	-0.69	-0.43	0.88	1.30	1.45	1.11	1.85	2.56
3	354 472	1.80 5.43	418	-0.73	-0.33[a] -0.48	0.96	1.20	1.50	1.01	1.95	2.59
4	316 476	1.63 6.56	417	-0.70	-0.30[a] -0.40	1.35	1.63	--	1.35	1.61	2.59

Among the investigated compounds, only compound 1 revealed fluorescence emission as shown in Figure 4.2b. A broad peak with maxima at 420 nm and spectrum spanning the 400-575 nm range was observed (estimated quantum yield = 0.43). Lifetime from single photon counting technique revealed a monoexponential decay with a lifetime of 1.16 ns. For compounds 2-4, having 1-3 numbers of strong electron acceptor TCBD entities, no measurable emission, either at the locally excited or charge transfer band positions, was observed; perhaps such emission were too weak to detect. In any case, the strong quenching observed in the case of compounds 2-4 suggest occurrence of excited state events such as energy or electron transfer in the highly interacting push-pull conjugates.

Next, in order to seek possible intramolecular interactions among the NND-TCBD entities via central TPA in compounds 3 and 4, electrochemical studies using differential pulse (DPV) and cyclic voltammetry (CV) were performed in DCB containing 0.1 M (TBA)ClO_4. The site of electron transfer was arrived from control C1 and C2 and remainder of compounds, and is summarized in Table 4.1 and representative voltammograms are shown in Figure 4.3. Complete CVs are shown in Figure 4.4.

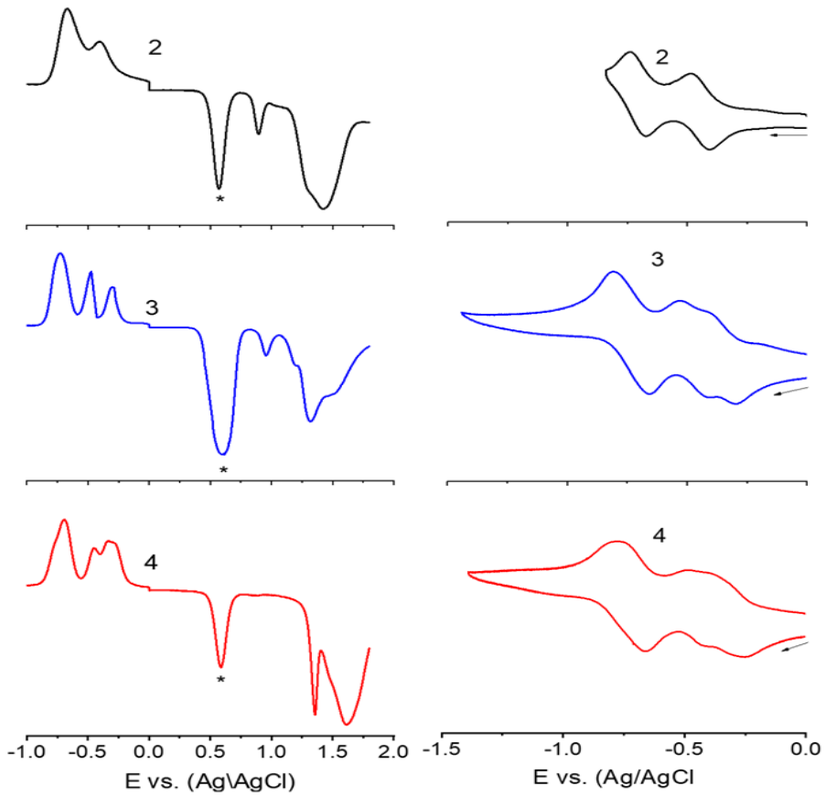

Figure 4.3: DPVs (left panel) and CVs (right panel) of indicated compounds in DCB containing 0.1 M (TBA)ClO_4. For DPV: scan rate = 5 mV/s, pulse width = 0.25 s, pulse height = 0.025 V. For CV: scan rate = 100 mV/s. The '*' in left panel represents oxidation peak of ferrocene used as internal standard. Note: the first reduction corresponding to TCBD in 3 and 4 is a split wave (see text for details).

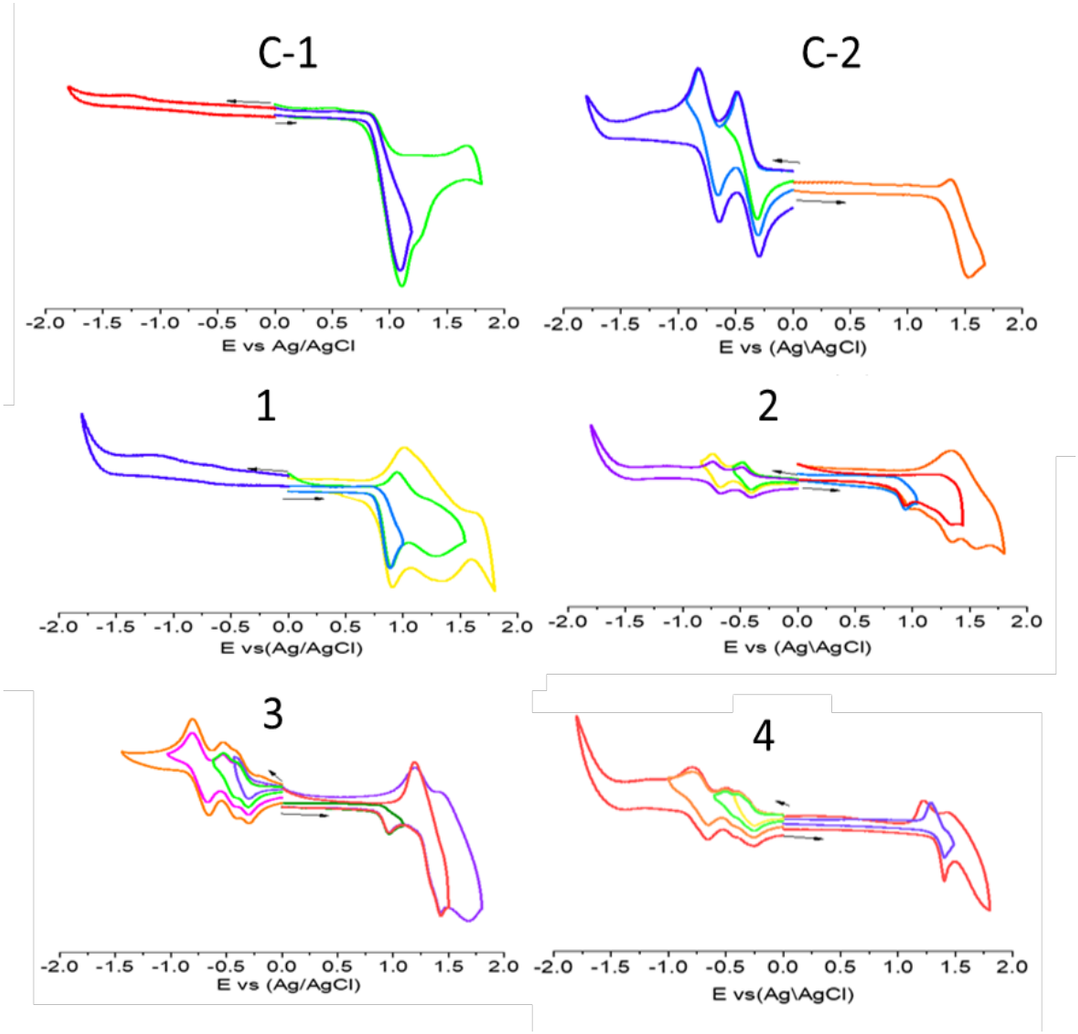

Figure 4.4: CVs of indicated compounds in DCB containing 0.1 M (TBA)ClO_4. Scan rate = 100 mV/s.

Key observations from electrochemical studies involved: (i) The first oxidation of C1 located at 0.96 V vs. Ag/AgCl was anodically shifted to 1.43 V in C2 due the presence of electron deficient TCBD. The TCBD reductions, all one-electron reversible, were located at -0.39 and -0.73 V. (ii) Compound 1 revealed two oxidations, the first one at 0.80 V and a second one at 1.15 V. From the peak currents and by comparison with oxidation potential of C1, the first oxidation to TPA and the second one to NND entities was possible to arrive. (iii) In the case of compound 2, having a single NND-TCBD entity, the TPA oxidation was shifted to 0.88 V while the NND oxidations were split and appeared at 1.30 and 1.45 V owing to the presence of two types of NNDs (one linked to TCBD and another without TCBD). The TCBD reductions were located at -0.43 and -0.69 V. (iv) Introduction of a second TCBD entity in 3 and a third one in 4 revealed additional interesting features. As predicted, oxidation peaks revealed further anodic shift especially for TPA oxidation. Interestingly, the first reduction of TCBD in both compounds 3 and 4 were found to be split waves. The split reduction peaks for 3 were located at -0.33 and -0.48 V, that is, a 140 mV potential difference while for 4, the split peaks were located at -0.30 and -0.40 V, that is, about 100 mV potential difference. The second reduction of TCBD in both 3 and 4 were one-electron reductions without noticeable splitting. The splitting of first reduction show electron exchange among the NND-TCBD entities in 3 and 4 via the central TPA entity.

The electron exchange between the NND-TCBD entities upon first electroreduction of compounds 3 and 4 motivated us to perform computational studies to probe their electronic structures. Compounds 1-4 were fully optimized on a Born-Oppenheimer potential energy surface at the B3LYP/6-31G* level calculations.[57] The generated frontier orbitals on the optimized structures are shown in Figure 4.5. The C_3 type symmetry originating from the central TPA entity was obvious in all these compounds. In the case of 1, the HOMO was distributed evenly on the

entire molecule while the LUMO coefficient was slightly more on one of the arms. In the case of 2, the HOMO was localized NND-TPA arms while the LUMOs were on the TCBD entity with some contributions extending into the NND and TPA entities.

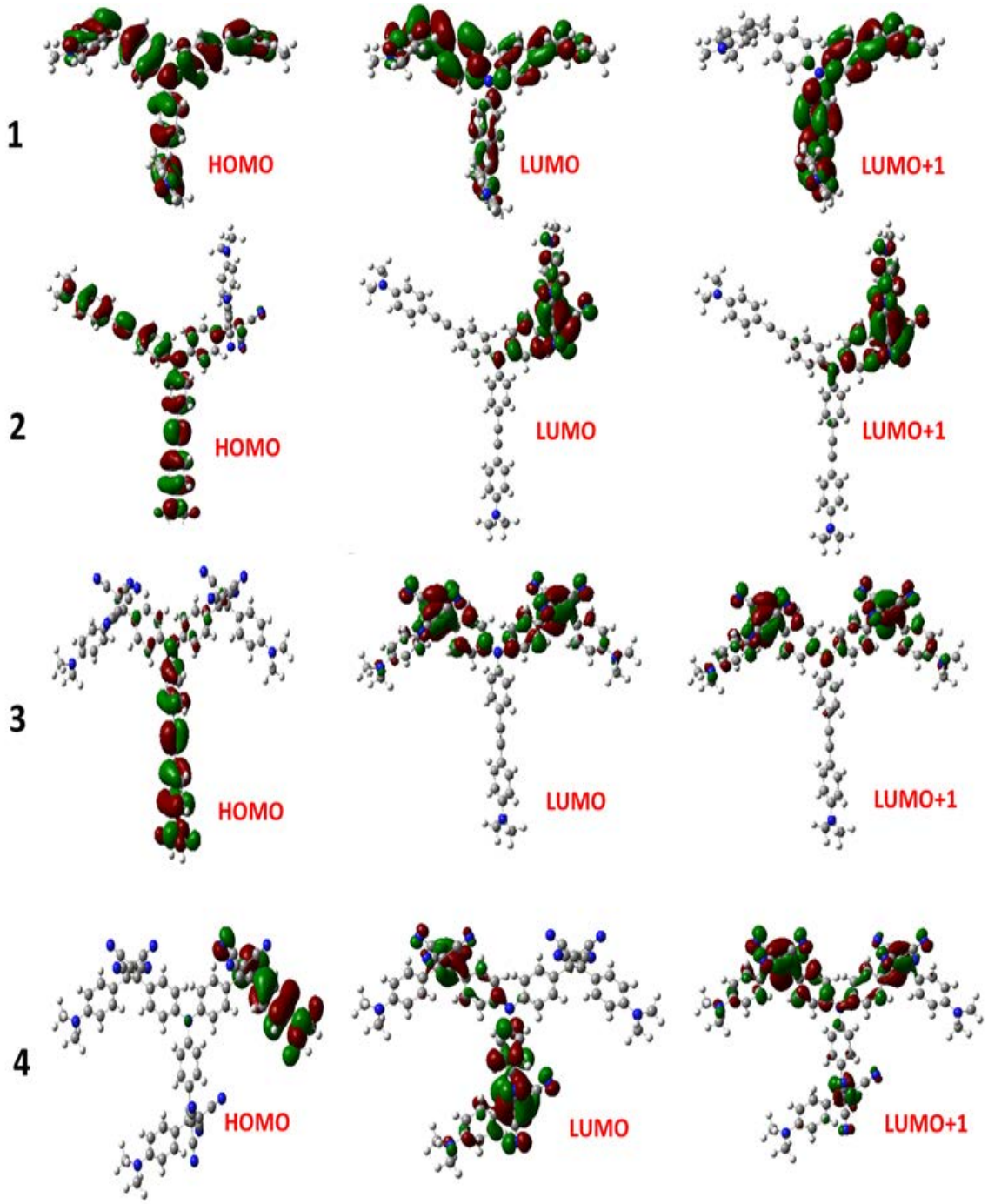

Figure 4.5: Frontier HOMO, LUMO and LUMO+1 of investigated compounds from the B3LYP/6-31G optimized structures (see SI for coordinates of computed structures).**

The energy difference between the two LUMOs was 0.0211 hartrees. In the case of compound 3, the HOMO occupied only the NND-TPA arm while the LUMOs occupied the two NND-TCBD with almost even distribution. The energy difference between the two LUMOs was 0.00527 hartrees. This situation was also true for compound 4, where the LUMO was distributed over two NND-TCBD entities while the LUMO+1 had contribution on all three NND-TDBD entities. The energy difference between the LUMOs was 0.0047 hartrees. Splitting of the first reduction peak due to electron exchange in the case of compounds 3 and 4 can now be attributed to energetically closely spaced LUMOs.

One of the approaches to visualize the spectrum of charge separation products is by performing spectroelectrochemical studies followed by spectral interpretation. Here, by applying appropriate potentials corresponding to oxidation or reduction, spectrum of the radical cation and radical anion can be generated. Subsequently, the average of the radical cation and radical anion spectrum will be digitally generated and subtracted from the spectrum of the neutral compound. This represents the differential absorption spectrum of the charge separation product. Positive peaks represent transitions associated with the electron transfer product while negative peaks represent depletion of the absorption of the neutral compound.[54] We have used this approach in the present study as shown in Figure 4.6 (a-c). Spectral changes associated during first oxidation of 3 is shown in Figure 4.6a. A new peak during the process of oxidation was observed at 662 nm. The spectral changes were minimal in the visible region as the main 478 nm peak was due to NND-TDCB charge transfer transition whereas the oxidation was on the TPA entity (*vide supra*), ascertaining the earlier discussed site of electron transfer. On the contrary, the spectral changes during first reduction (Fig. 4.6b) revealed drastic decrease in intensity of the charge transfer band with broad positive spectral features in the 600-800 nm range. It may be mentioned here that during

both oxidation and reduction, now new peaks beyond 800 nm was observed. The spectrum generated for the charge transfer product using the above-described procedure is shown in Figure 4.6c. Such spectrum revealed a positive peak at 670 nm and depleted peak at 478 nm. Witnessing such a spectrum in transient absorption spectral studies would provide direct proof of charge transfer in these donor-acceptor conjugates. Similar spectra were derived for compounds 2 and 4 (see Fig. 4.7).

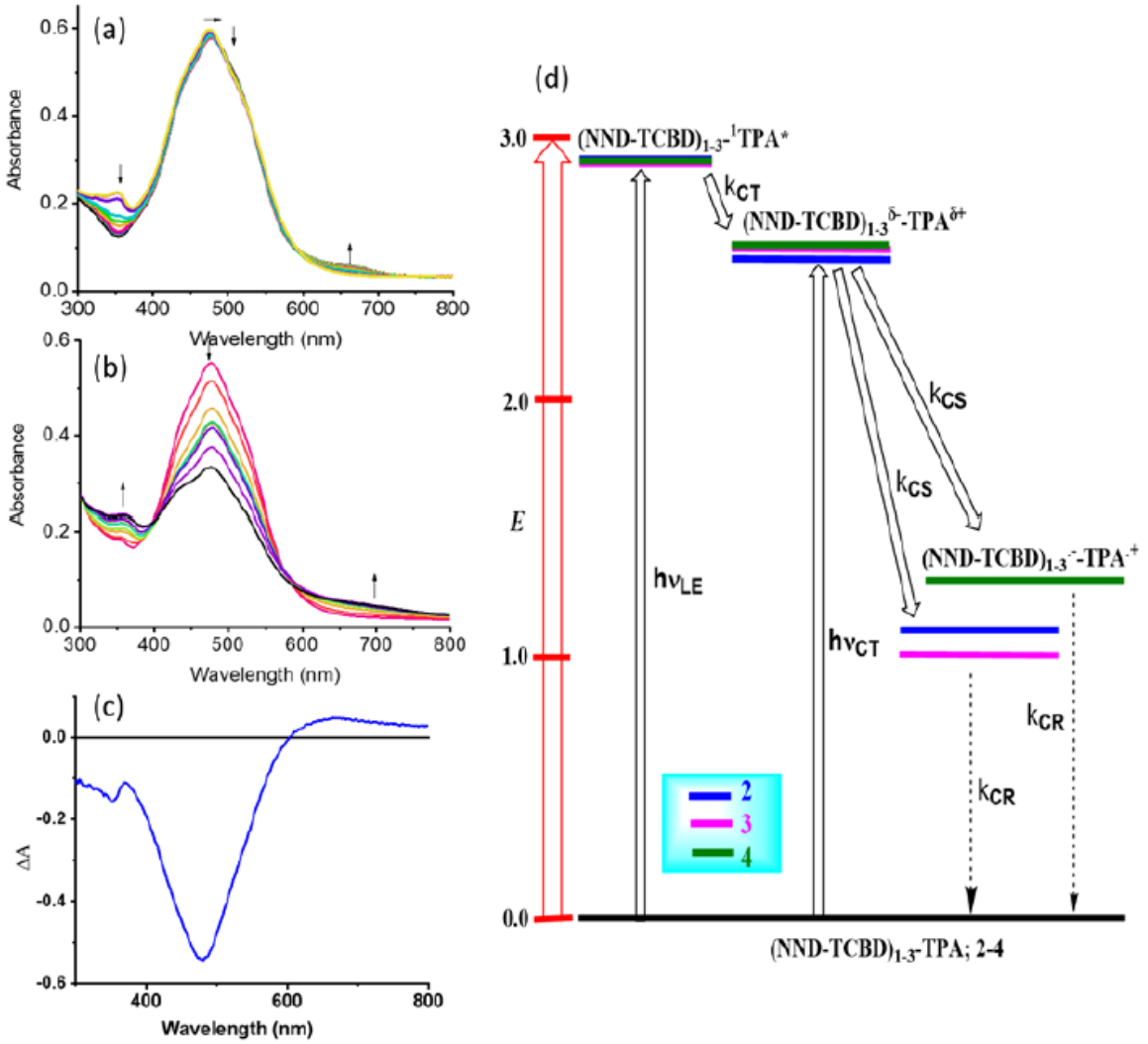

Figure 4.6: Spectral changes observed during (a) first oxidation and (b) first reduction of 3 in DCB containing 0.2 M (TBA)ClO_4. (c) Spectrum deduced for the charge separation state using spectroelectrochemical data (see text for details, and Fig. 4.7 in SI for complete results). (d) Energy level diagram showing possible charge transfer and charge separation events upon photoexcitation of the compounds 2-4. NND without linked TCBD in 2-3 is not shown in the abbreviated formula for simplicity.

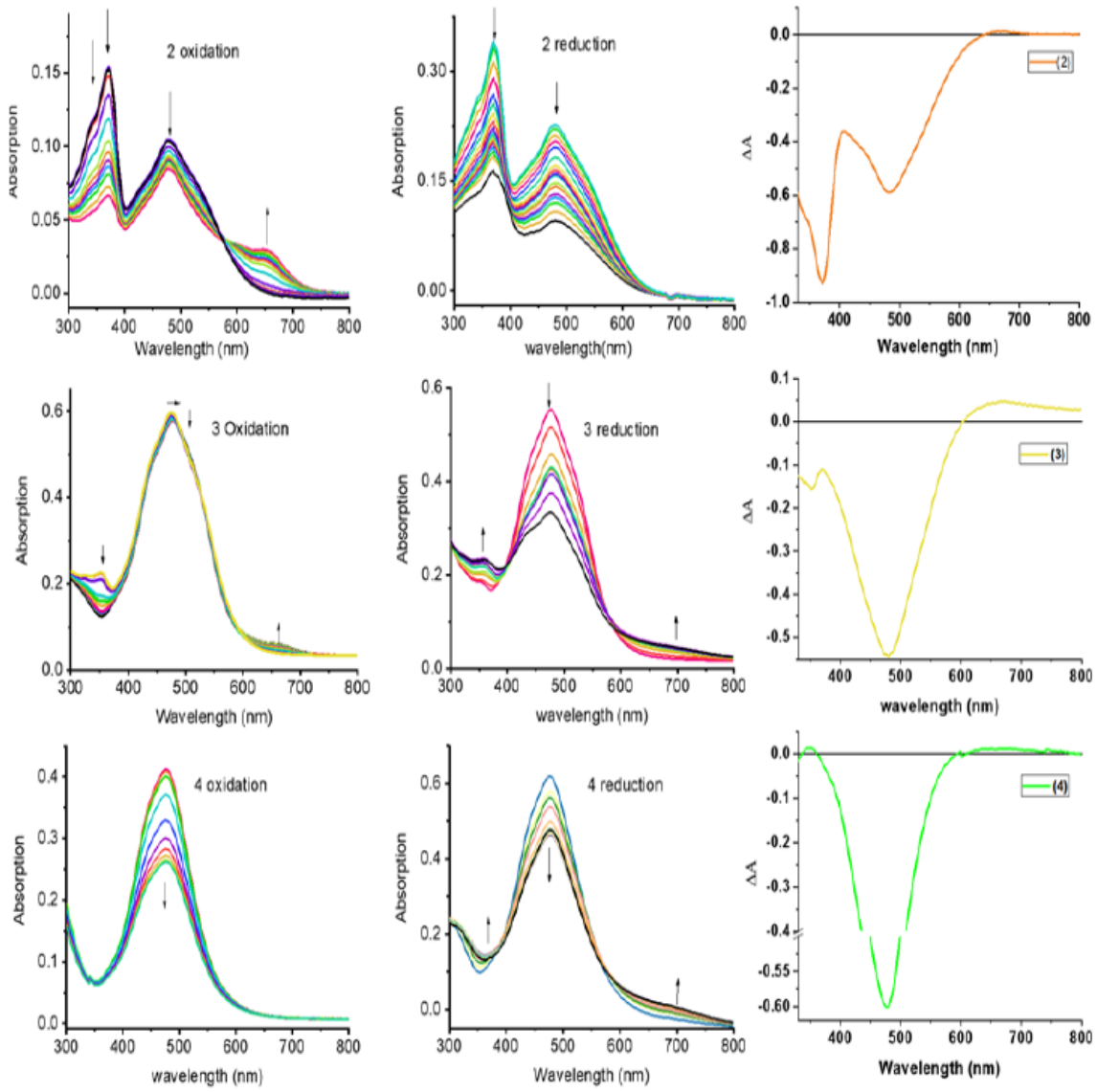

Figure 4.7: Spectral changes observed during (a) first oxidation and (b) first reduction of indicated compounds in DCB containing 0.2 M (TBA)ClO_4. Spectrum deduced for the charge transfer state using spectroelectrochemical data (see text for details) is show on the right-hand panel for each compound.

An energy diagram was established to visualize the energetics of charge transfer and charge separation states in these conjugates, as shown in Figure 4.6d. Energy of different states were established from free-energy calculations,[58-59] as listed in Table 4.1. From such a diagram, it was clear that excitation of the conjugates, 2-4 either that the locally excited (near-UV) or charge transfer (visible) peak positions would produce the respective excited states. The excited state

species, $(NND\text{-}TCBD)_{1\text{-}3}$-$^{1}TPA^{*}$ formed from the locally excited state would readily produce initial charge transfer state, $(NND\text{-}TCBD)_{1\text{-}3}^{\delta-}$-$TPA^{\delta+}$ involving one of the NND-TCBD entities (free NND is not abbreviated for simplicity). Such a state can also be produced by direct excitation of the visible charge transfer band. The charge transfer state thus generated could further undergo electron transfer to generate the $(NND\text{-}TCBD_{1\text{-}3})^{\bullet-}$-$TPA^{\bullet+}$ charge separated species. Although initial charge separation state would involve only one of the NND-TCBD entities, due to electron exchange, the anion radical could spread over other NND-TCBD entities, as suggested by the earlier discussed frontier LUMOs. Finally, the charge separated species could relax back to the ground state.

In order to probe the anticipated photochemical events and to seek the effect of multiple NND-TCBD entities in prolonging lifetime of charge separated states via the earlier discussed electron exchange mechanism, femtosecond transient absorption studies (fs-TA) were performed. Three solvents of varying polarity were used as the solvent polarity would influence lifetime of charge separated states, and samples were excited at both locally excited (350 nm) and charge transfer (500 nm) peak positions.

As shown in Figure 4.8a(i), singlet excited state of compound 1 ($^{1}TPA^{*}$) in benzonitrile was formed instantaneously upon 350 nm laser excitation featuring excited state absorption (ESA) maxima at 533, 601 and 1382 nm (see spectrum at 2.22 ps) as well as ground state bleach in 400-450 nm range. To gather insight into the deactivation, global target analysis [60-61] was performed. A kinetic model including three species was satisfactory. The species associated spectra (SAS) and population kinetics of the three species is shown in Figure 4.8a, ii and iii, respectively. The first species with a lifetime of ~200 fs was within the temporal resolution of our instrument that decayed to develop the second component with singlet excited state features with a lifetime of 49

ps. The third component which could be attributed to the decaying singlet to triplet state had a time constant of about 2.30 ns. Due to lack of any TCBD entities in 1, no electron transfer could be detected.

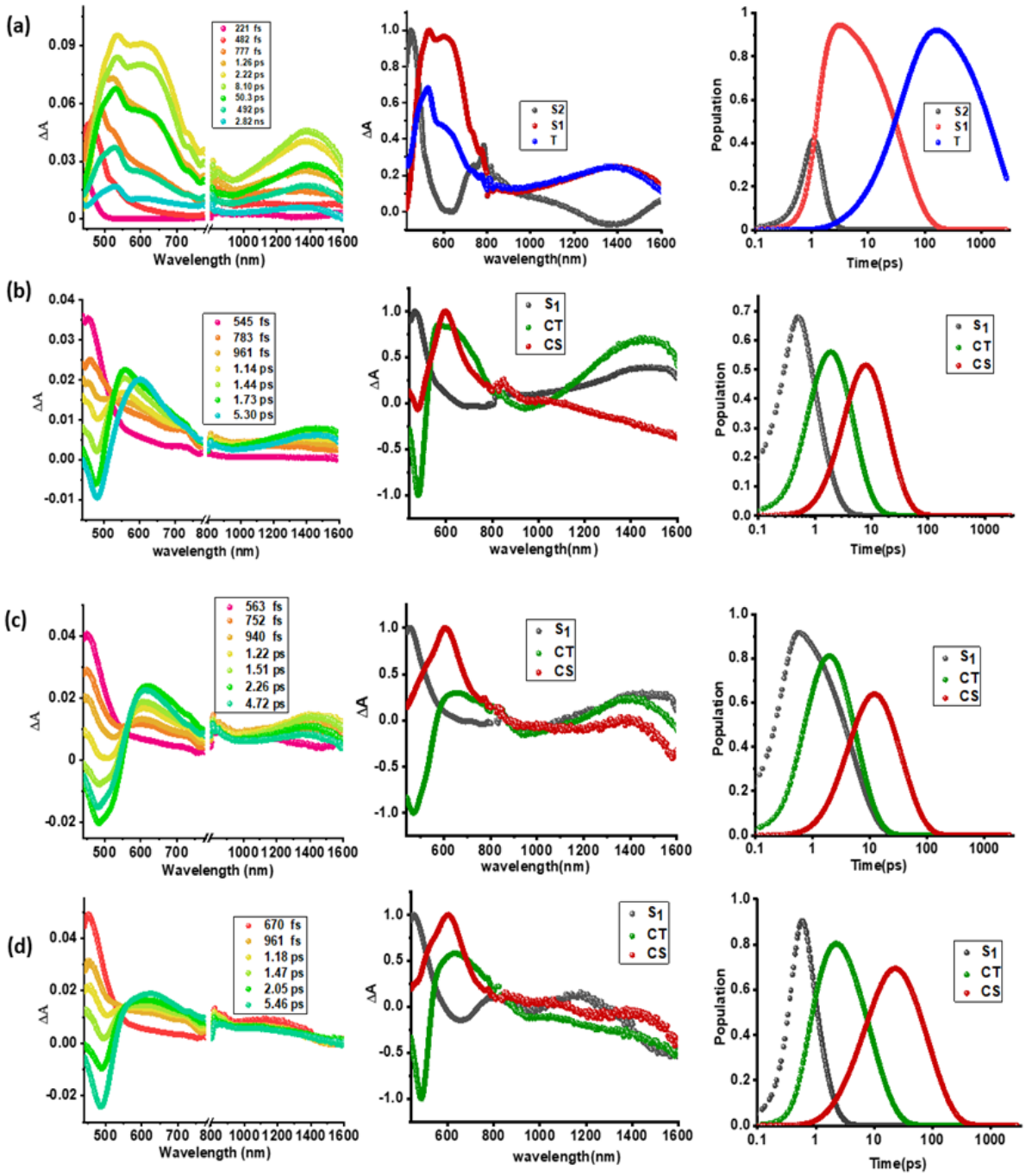

Figure 4.8: Fs-TA spectra at the indicated delay times, (a-d, panel i), species associated spectra (a-d, panel ii), and population kinetics (a-d, panel iii) of compounds 1-4 (a through d) in benzonitrile. The samples were excited at 350 nm corresponding to locally excited state.

In contrast to the spectral features of compound 1, the donor-acceptor conjugates 2-4 revealed the anticipated ultrafast charge transfer and charge separation processes. In the case of 2, where only one NND-TCBD entity is present, occurrence of relatively simple photoinduced charge transfer could be envisioned. However, in the case of 3 and 4 featuring two and three entities of NND-TCBD attached to TPA, a symmetry breaking charge transfer could be envisioned due to presence of multiple numbers of equally positioned acceptor entities. Presence of higher number of acceptors could improve the charge transfer by the respective statistical factor or even more by quantum coherence effects.[62] The first panel in Figure 4.8 (b-d) show transient spectra at the indicated delay times for compounds 2-4. The ESA peak of the singlet excited state located in the 450-500 nm range revealed rapid decay with new peaks in the 610-620 nm range and near-IR range. These spectra were subjected to target analysis that required three components for satisfactory fit. These SAS are shown in Figure 4.8 (b-d), middle panel. In all these, the first spectrum with characteristic features of the singlet excited state had a time constant of less than 1 ps, and as predicted, the magnitude of these time constants further decreased with increase in the number of NND-TCBD entities (statistical factor of quenching). The second SAS with time constants of 3.48-5.64 ps has been attributed to the charge transfer state. Here, the depleted peak intensity in the near-IR region has been tentatively assigned to stimulated emission of CT state. With the decay of the second component, the third component was evolved that has been attributed to the charge separated species as this spectrum resembled largely that derived for charge separation product from the earlier discussed spectroelectrochemical studies (see Fig. 4.6c). It may be mentioned here that the SAS of third component is distinctly different from the triplet state SAS shown in Figure 4.8a, panel ii. The time constants for the charge separated state were found to be 14.9, 32.68 and 75.1 ps, respectively, for compounds 2, 3, and 4. These results reveal persistence

of the charge separated state in compounds 3 and 4 compared to that in 2**.**

Intrigued with these findings, next, we changed the solvent to less polar DCB and nonpolar toluene. In both of these solvents the spectral trends were almost the same (see Figs. 4.9 and 4.10). Further, target analysis was performed to evaluate the kinetic factors as listed in Table 4.2. Such data confirmed persistence of charge separated states in both solvents. Changing the excitation wavelength to 500 nm corresponding to the charge transfer also revealed excited state charge separation (Figs. 4.11, 4.12 and 4.13). In this case, the data could be satisfactorily fitted to two components, one to the excited state charge transfer with time constants of few ps and the second one for the charge separated state. It may be mentioned here that irrespective of the excitation wavelengths (LE or CT), the SAS generated for charge transfer and charge separation states revealed close resemblance.

Table 4.2: **Time constants evaluated from GloTarAn target analysis of fs-TA spectral data in solvents of varying polarity and at different excitation wavelengths for the investigated central triphenylamine derived, dimethylamine-tetracyanobutadiene conjugates.**

Compound	Solvent	λ_{ex}, nm	S_1, ps	CT, ps	CS, ps
1	Toluene	350	842	--	--
2			2.36	4.17	17.02
3			1.56	10.01	39.32
4			0.54	25.37	93.20
2		500	--	3.59	14.92
3			--	7.29	24.10
4			--	16.8	56.30
1	DCB	350	111	--	--
2			1.99	3.87	16.40
3			1.14	8.12	37.59
4			0.35	13.6	87.70
2		500	--	2.49	13.93
3			--	5.78	20.45
4			--	8.76	60.41
1	PhCN	350	49	--	--

Compound	Solvent	λ_{ex}, nm	S_1, ps	CT, ps	CS, ps
2			0.89	3.48	14.9
3			0.80	4.99	32.68
4			0.67	5.64	75.10
2		500	--	1.38	10.23
3			--	3.69	24.65
4			--	4.98	43.29

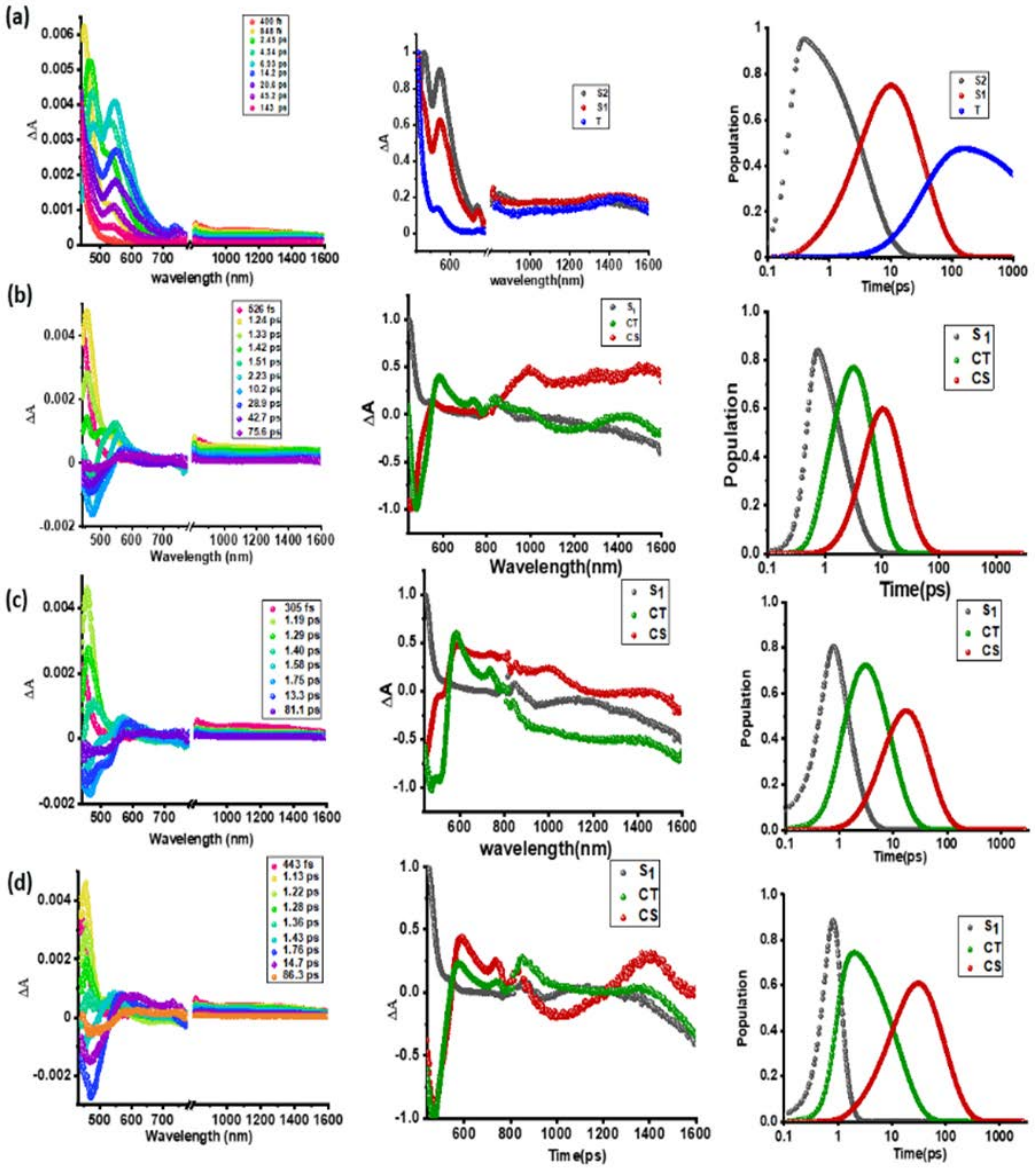

Figure 4.9: Fs-TA spectra at the indicated delay times of compounds 1-4 in DCB. The samples were excited at 350 nm corresponding to local excited state. The SAS and population kinetic plots are shown in the middle and right panels.

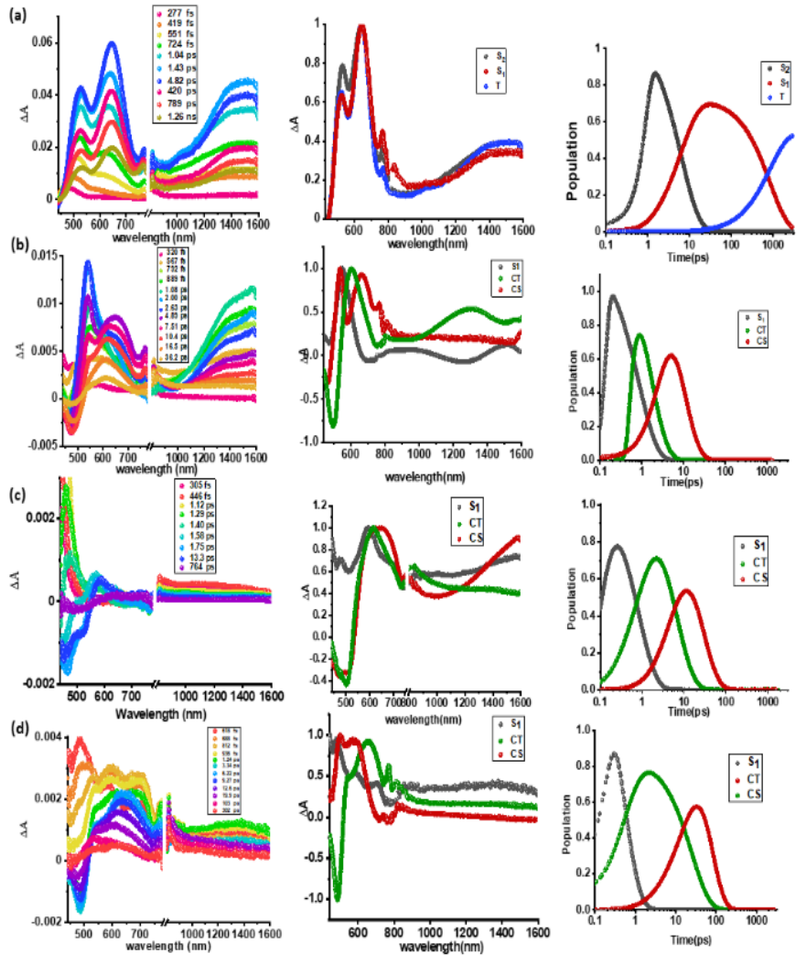

Figure 4.10: Fs-TA spectra at the indicated delay times of compounds 1-4 in toluene. The samples were excited at 350 nm corresponding to local excited state. The SAS and population kinetic plots are shown in the middle and right panels.

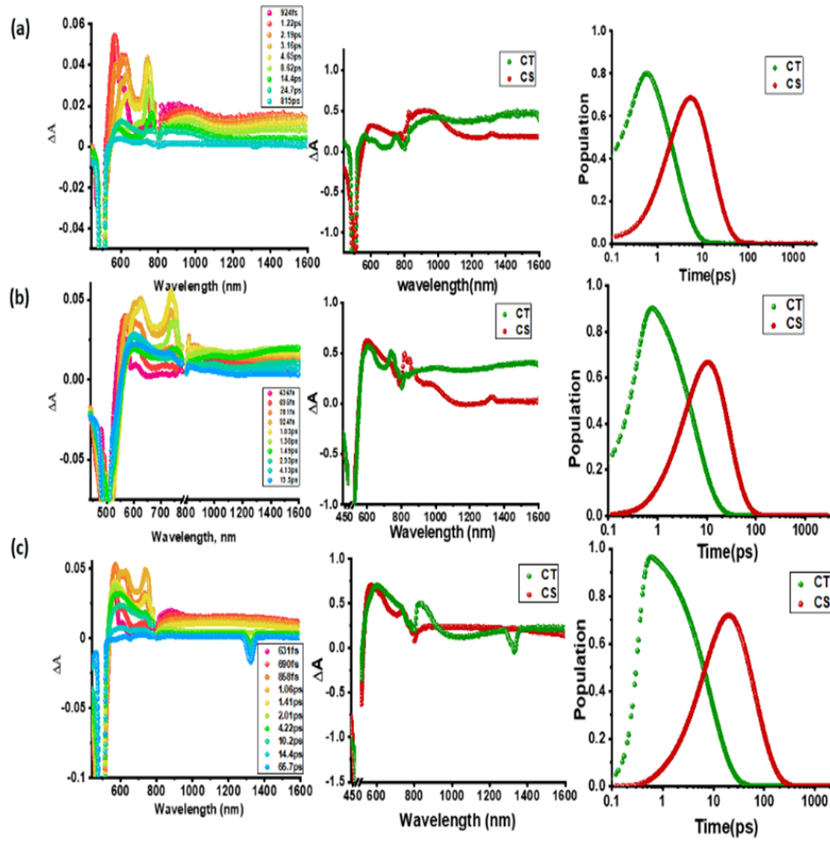

Figure 4.11: Fs-TA spectra at the indicated delay times of compounds 2-4 in DCB. The samples were excited at 500 nm corresponding to charge transfer band. Right hand panel shows the population kinetics. The dip at 500 nm is due to excitation laser.

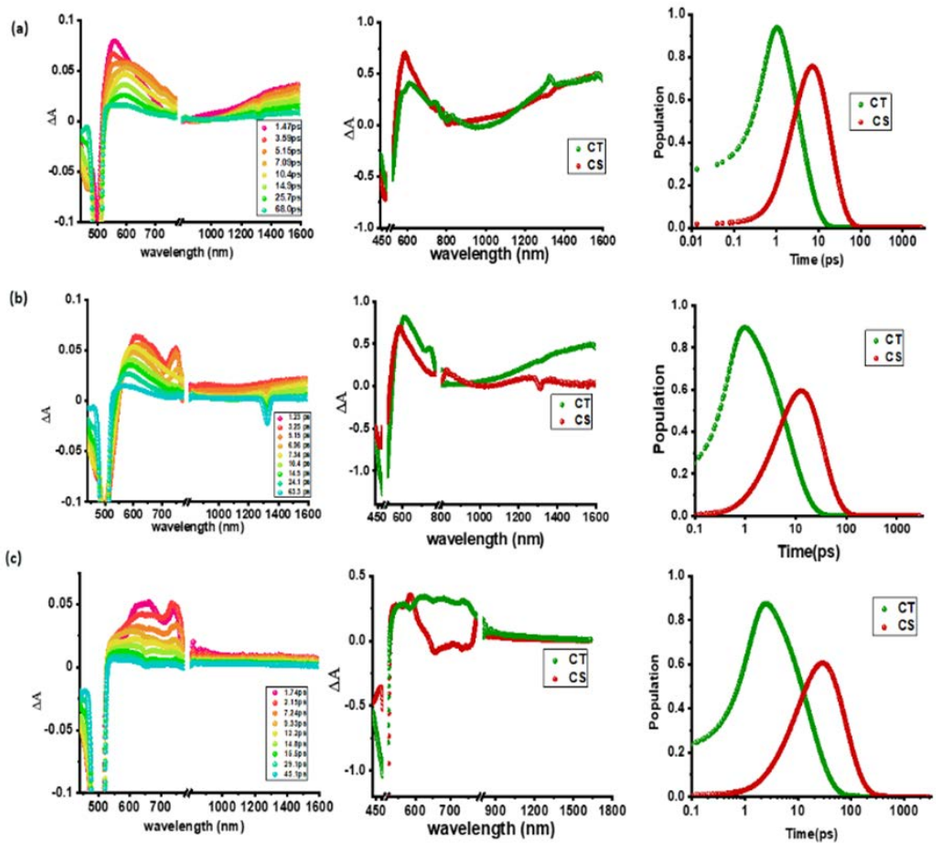

Figure 4.12: Fs-TA spectra at the indicated delay times of compounds 2-4 in toluene. The samples were excited at 500 nm corresponding to charge transfer band. Right hand panel shows the population kinetics. The dip at 500 nm is due to excitation laser.

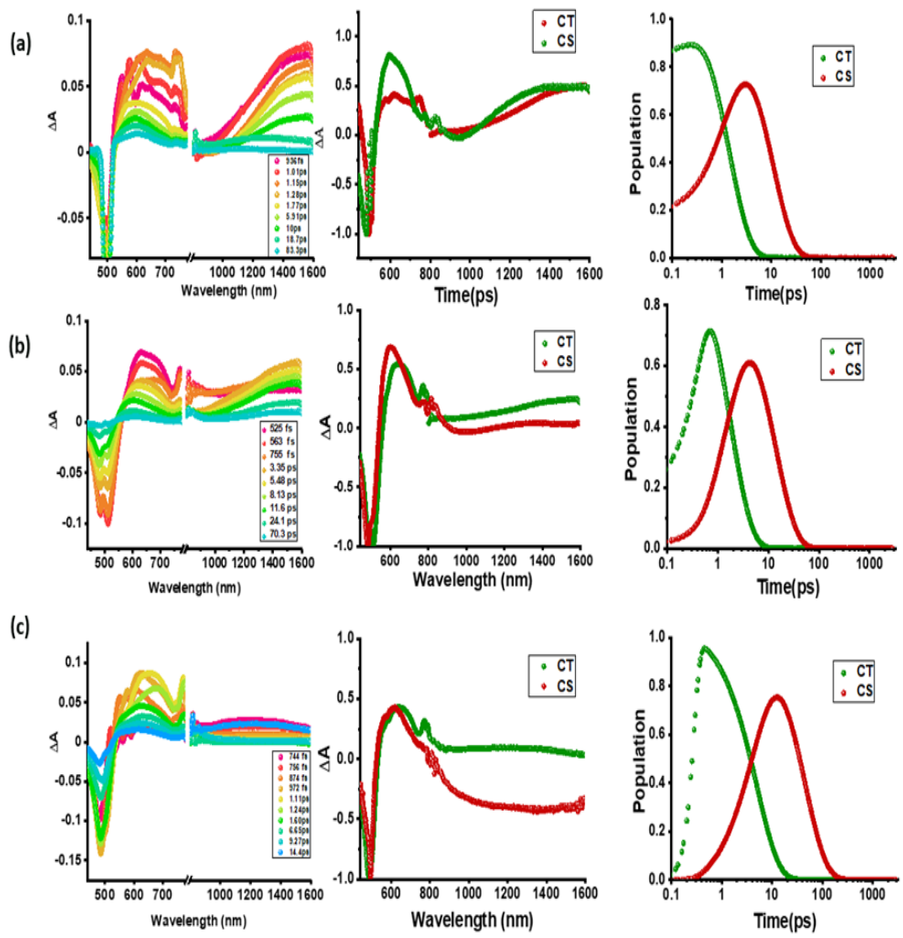

Figure 4.13: Fs-TA spectra at the indicated delay times of compounds 2-4 in benzonitrile. The samples were excited at 500 nm corresponding to charge transfer band. Right hand panel shows the population kinetics. The dip at 500 nm is due to excitation laser.

As pointed out earlier, in synthetic multimodular donor-acceptor systems, charge stabilization is often achieved by following the mechanism of natural photosynthesis where electron migration occurs across the system distantly separating the positive and negative ions thus minimizing their electrostatic attraction.[20-22] Electron/hole delocalization in multiple donor or accepting bearing systems, and utilization of high-energy triplet sensitizers to promote electron transfer from the long-lived triplet excited states are also some of the known mechanisms to extend the lifetime of the charge separated species. The present multi-modular systems, 3 and 4, differ in their design wherein the same acceptor unit, NND-TCBD is covalently linked to the central TPA. Electron exchange has been witnessed upon first reduction of these compounds unlike that in 2 bearing a single NND-TCBD entity. It appears that such electron exchange is responsible for extending the lifetime of the charge separated states in these novel donor-acceptor conjugates.

4.1.4 Conclusions

In summary, we have developed exceptional molecular donor-acceptor systems consisting of C_3 symmetric central triphenylamine derived, dimethylamine-tetracyanobutadiene conjugates. In these systems, the NND-TCBD promoted charge transfer extending the absorption covering the visible region. Electrochemical studies revealed electron exchange in compounds 3 and 4 carrying multiple numbers of NND-TCBD entities. Frontier LUMO energy levels and orbital coefficients helped us in rationalizing such electron exchange. The spectrum of the charge transfer state was possible to deduce from manipulation of spectroelectrochemical data. Finally, we have been able to demonstrate the effect of electron exchange in prolonging the lifetime of charge separated states in compounds 3 and 4 from fs-TA spectral studies in solvents of varying polarity. To our knowledge, this is the first report where such a charge stabilizing mechanism involving electron exchange has been proposed and demonstrated experimentally. The present findings are very

important to further our understanding on the fundamentals of electron transfer in multi-modular systems; strengthen our knowledge on the early events of natural photosynthesis and seek novel applications in optoelectronics. In this context, it may be pointed out here that in bacterial photosynthesis, the primary electron donor is an electronically interacting bacteriochlorophyll dimer, $[BChl]_2$.[63] The initial electron transfer species, $[BChl]_2^{\bullet+}$ could slow down the charge recombination via a similar electron exchange mechanism and could be a reason for natural choice of a bacteriochlorophyll dimer instead of a monomer.

4.1.5 Notes and References

1. N. Armaroli and V. Balzani, *Angewandte Chemie International Edition,* 2007, **46**, 52-66.
2. P. M. Beaujuge and J. M. J. Fréchet, *J. Am. Chem. Soc.,* 2011, **133**, 20009-20029.
3. F. D'Souza and O. Ito, *Chem. Soc. Rev.,* 2012, **41**, 86-96.
4. M. E. El-Khouly, S. Fukuzumi and F. D'Souza, *Chemphyschem,* 2014, **15**, 30-47.
5. Bottari and T. Torres, *"Organic Nanomaterials: Synthesis, Characterization, and Device Applications", Eds: T. Torres and G. Bottari, John Wiley & Sons, Inc., Hoboken, NJ, 2013.*
6. H. Imahori, T. Umeyama and S. Ito, *Acc. Chem. Res.,* 2009, **42**, 1809-1818.
7. D. Gust, T. A. Moore and A. L. Moore, *Faraday Discuss.,* 2012, **155**, 9-26.
8. N. Martín, L. Sánchez, M. Á Herranz, B. Illescas and D. M. Guldi, *Acc. Chem. Res.,* 2007, **40**, 1015-1024
9. G. Bottari, G. de la Torre, D. M. Guldi and T. Torres, *Chem. Rev.*, 2010, **110**, 6768-6816.
10. N. Zarrabi, S. Seetharaman, S. Chaudhuri, N. Holzer, V. S. Batista, A. van der Est, F. D'Souza and P. K. Poddutoori, *J. Am. Chem. Soc.,* 2020, **142**, 10008-10024.
11. L. Hammarström, *Acc. Chem. Res.,* 2015, **48**, 840-850.
12. A. Arrigo, A. Santoro, F. Puntoriero, P. P. Laine and S. Campagna, *Coord. Chem. Rev.,* 2015, **304**, 109-116.
13. S. Fukuzumi, K. Ohkubo and T. Suenobu, *Acc. Chem. Res.,* 2014, **47**, 1455-1464.
14. D. Gust, T. A. Moore and A. L. Moore, *Acc. Chem. Res.,* 2009, **42**, 1890-1898.

15. F. D'Souza and O. Ito, *Chem. Soc. Rev.*, 2012, **41**, 86-96.

16. M. Barrejón, L. M. Arellano, F. D'Souza and F. Langa, *Nanoscale*, 2019, **11**, 14978-14992.

17. C. B. KC and F. D'Souza, *Coord. Chem. Rev.*, 2016, **322**, 104-141.

18. D. Kim, *Multiporphyrin arrays: Fundamentals and applications*, 2012.

19. R. Canton-Vitoria, H. B. Gobeze, V. M. Blas-Ferrando, J. Ortiz, Y. Jang, F. Fernández-Lázaro, Á Sastre-Santos, Y. Nakanishi, H. Shinohara, F. D'Souza and N. Tagmatarchis, *Angew. Chem. Int. Ed. Engl.*, 2019, **58**, 5712-5717.

20. R. Cogdell and C. Mullineaux, *Photosynthesis Res.*, 2008, **95**, 117.

21. R. C. Leegood, *Annals of Botany*, 2006, **97**, 152-153.

22. B. Green and W. W. Parson, *Light-Harvesting Antennas in Photosynthesis*, Springer Netherlands, 2003.

23. T. Hasobe, P. V. Kamat, V. Troiani, N. Solladié, T. K. Ahn, S. K. Kim, D. Kim, A. Kongkanand, S. Kuwabata and S. Fukuzumi, *J Phys Chem B*, 2005, **109**, 19-23.

24. T. Hasobe, K. Saito, P. V. Kamat, V. Troiani, H. Qiu, N. Solladié, K. S. Kim, J. K. Park, D. Kim, F. D'Souza and S. Fukuzumi, *J. Mater. Chem.*, 2007, **17**, 4160-4170.

25. C. Obondi O., G. N. Lim, B. Churchill, P. K. Poddutoori, A. van der Est and F. D'Souza, *Nanoscale*, 2016, **8**, 8333-8344.

26. D. R. Subedi, H. B. Gobeze, Y. E. Kandrashkin, P. K. Poddutoori, A. van der Est and F. D'Souza, *Chem. Commun.*, 2020, **56**, 6058-6061.

27. S. Gangala and R. Misra, *J. Mater. Chem. A*, 2018, **6**, 18750-18765.

28. A. Hagfeldt, G. Boschloo, L. Sun, L. Kloo and H. Pettersson, *Chem. Rev.*, 2010, **110**, 6595-6663.

29. L. Sun, F. Bai, Z. Zhao and H. Zhang, *Solar Energy Mater. Solar Cells*, 2011, **95**, 1800-1810.

30. Y. Patil and R. Misra, *Chem. Asian J.*, 2018, **13**, 220-229.

31. Y. Wu and W. Zhu, *Chem. Soc. Rev.*, 2013, **42**, 2039-2058.

32. M. Y. Berezin and S. Achilefu, *Chem. Rev.*, 2010, **110**, 2641-2684.

33. J. Min, Y. N. Luponosov, D. Baran, S. N. Chvalun, M. A. Shcherbina, A. V. Bakirov, P. V. Dmitryakov, S. M. Peregudova, N. Kausch-Busies, S. A. Ponomarenko, T. Ameri and C. J. Brabec, *J. Mater. Chem. A*, 2014, **2**, 16135-16147.

34. F. Bures, W. B. Schweizer, J. C. May, C. Boudon, J. Gisselbrecht, M. Gross, I. Biaggio and F. Diederich, *Chemistry*, 2007, **13**, 5378-5387.

35. J. Wang, Q. Xiao and J. Pei, *Org. Lett.*, 2010, **12**, 4164-4167.

36. M. Poddar and R. Misra, *Chem. Asian J.*, 2017, **12**, 2908-2915.

37. Y. Patil, R. Misra, F. C. Chen, M. L. Keshtov and G. D. Sharma, *RSC Adv.*, 2016, **6**, 99685-99694.

38. T. Ishi-i, K. Ikeda, M. Ogawa and Y. Kusakaki, *RSC Adv.*, 2015, **5**, 89171-89187.

39. Y. Li, S. Gao, N. Zhang, X. Huang, J. Tian, F. Xu, Z. Sun, S. Yin, X. Wu and W. Chu, *J. Mater. Chem. C*, 2019, **7**, 2686-2698.

40. A. Kundu, S. Karthikeyan, D. Moon and S. P. Anthony, *CrystEngComm*, 2017, **19**, 6979-6985.

41. M. Kivala, C. Boudon, J. Gisselbrecht, P. Seiler, M. Gross and F. Diederich, *Angew. Chem. Int. Ed.*, 2007, **46**, 6357-6360.

42. A. Gopinath, N. Manivannan, S. Mandal, N. Mathivanan and A. S. Nasar, *J. Mater. Chem. B*, 2019, **7**, 6010-6023.

43. T. Michinobu, C. Boudon, J. Gisselbrecht, P. Seiler, B. Frank, N. N. P. Moonen, M. Gross and F. Diederich, *Chemistry – A European Journal*, 2006, **12**, 1889-1905.

44. M. Kivala, C. Boudon, J. Gisselbrecht, P. Seiler, M. Gross and F. Diederich, *Angew. Chem. Int. Ed.*, 2007, **46**, 6357-6360.

45. T. Michinobu, *Chem. Soc. Rev.*, 2011, **40**, 2306-2316.

46. T. Shoji, S. Ito, K. Toyota, T. Iwamoto, M. Yasunami and N. Morita, *Eur. J. Org. Chem.*, 2009, **2009**, 4307-4315.

47. P. Gautam, R. Sharma, R. Misra, M. L. Keshtov, S. A. Kuklin and G. D. Sharma, *Chem. Sci.*, 2017, **8**, 2017-2024.

48. Y. Patil, R. Misra, R. Singhal and G. D. Sharma, *J. Mater. Chem. A*, 2017, **5**, 13625-13633.

49. M. Sekita, B. Ballesteros, F. Diederich, D. M. Guldi, G. Bottari and T. Torres, *Angew. Chem. Int. Ed.*, 2016, **55**, 5560-5564.

50. K. A. Winterfeld, G. Lavarda, J. Guilleme, M. Sekita, D. M. Guldi, T. Torres and G. Bottari, *J. Am. Chem. Soc.*, 2017, **139**, 5520-5529.

51. K. A. Winterfeld, G. Lavarda, J. Guilleme, D. M. Guldi, T. Torres and G. Bottari, *Chem. Sci.*, 2019, **10**, 10997-11005.

52. H. Gotfredsen, T. Neumann, F. E. Storm, A. V. Muñoz, M. Jevric, O. Hammerich, K. V. Mikkelsen, M. Freitag, G. Boschloo and M. B. Nielsen, *ChemPhotoChem*, 2018, **2**, 976-985.

53. P. Gautam, R. Misra, M. B. Thomas and F. D'Souza, *Chem. Eur. J.*, 2017, **23**, 9192-9200.

54. R. Sharma, M. B. Thomas, R. Misra and F. D'Souza, *Angew. Chem. Int. Ed.*, 2019, **58**, 4350-4355.

55. Y. Rout, Y. Jang, H. B. Gobeze, R. Misra and F. D'Souza, *J. Phys. Chem. C*, 2019, **123**, 23382-23389.

56. M. Poddar, Y. Jang, R. Misra and F. D'Souza, *Chem. Eur. J.*, 2020, **26**, 6869-6878.

57. *Gaussian 09*, Revision C.01, M. J. Frisch, G. W. Trucks, H. B. Schlegel, G. E. Scuseria, M. A. Robb, J. R. Cheeseman, G. Scalmani, V. Barone, B. Mennucci, G. A. Petersson, H. Nakatsuji, M. Caricato, X. Li, H. P. Hratchian, A. F. Izmaylov, J. Bloino, G. Zheng, J. L. Sonnenberg, M. Hada, M. Ehara, K. Toyota, R. Fukuda, J. Hasegawa, M. Ishida, T. Nakajima, Y. Honda, O. Kitao, H. Nakai, T. Vreven, J. A. , Jr. , Montgomery, J. E. Peralta, F. Ogliaro, M. Bearpark, J. J. Heyd, E. Brothers, K. N. Kudin, V. N. Staroverov, R. Kobayashi, J. Normand, K. Raghavachari, A. Rendell, J. C. Burant, S. S. Iyengar, J. Tomasi, M. Cossi, N. Rega, J. M. Millam, M. Klene, J. E. Knox, J. B. Cross, V. Bakken, C. Adamo, J. Jaramillo, R. Gomperts, R. E. Stratmann, O. Yazyev, A. J. Austin, R. Cammi, C. Pomelli, J. W. Ochterski, R. L. Martin, K. Morokuma, V. G. Zakrzewski, G. A. Voth, P. Salvador, J. J. Dannenberg, S. Dapprich, A. D. Daniels, Ö. Farkas, J. B. Foresman, J. V. Ortiz, J. Cioslowski, D. J. Fox, Gaussian, Inc., Wallingford, CT, USA, **2009**.

58. D. Rehm and A. Weller, *Isr. J. Chem.*, 1970, **8**, 259-271.

59. Gibbs free-energy change associated for excited state charge separation (CS) and dark charge recombination (CR) were estimated according to equations i-iii

$$-\Delta G_{CR} = E_{ox} - E_{red} + \Delta G_S \quad \text{(i)}$$

$$-\Delta G_{CS} = \Delta E_{00} - (-\Delta G_{CR}) \quad \text{(ii)}$$

where ΔE_{00} corresponds to the singlet state energy of 1. The term ΔG_S refers to electrostatic energy calculated according to dielectric continuum model (see equation iii). The E_{ox} and E_{red} represent the oxidation potential and the first reduction potential, respectively.

$$\Delta G_S = e^2/4\,\pi\,\varepsilon_o\,[\,-\,1/R_{cc}\,\varepsilon_R) \quad \text{(iii)}$$

The symbols ε_0 and ε_R represent vacuum permittivity and dielectric constant of DCB used for photochemical and electrochemical studies (= 9.93). R_{CC} are the center-to-center distance between donor and acceptor entities from the computed structures. Energy of charge transfer was calculated from peak maxima of charge transfer peak.

60. J. Snellenburg, S. Laptenok, R. Seger, K. Mullen,and I. van Stokkum, *J. of Stat. Software,* 2012, **49** 1-22.

61. http://glotaran.org/

62. S. Rafiq and G. D. Scholes, *J. Am. Chem. Soc.,* 2019, **141**, 708-722.

63. J. Deisenhofer, O. Epp, K. Miki, R. Huber and H. Michel, *J. Mol. Biol.*, 1984, **180**, 385-398.

4.2 Star-Shaped Triphenylamine-Tetracyanobutadiene-Phenothiazine Push-Pull Systems: Role of Terminal Phenothiazine in Improving Charge Transfer*

4.2.1 Introduction

Over the years, organic π-conjugated chromophores have been the subject of intense research due to their wide-ranging applications in materials science, optoelectronics, and biomedicine.[1-19] Among these, the π-conjugated, spatially close, donor-acceptor (D–π–A) push-pull compounds have become one of the successful strategies in the design and synthesis of optoelectronic materials. The strongly interacting D-π-A type push-pull systems can lower the optical band gap and extend the absorption spectrum towards longer wavelengths.[20-21] Advantageously, the energy levels and band gaps of such push-pull systems can be tuned effectively by the selection of acceptor and donor entities, and π-bridge and spacer.[20-21]

The triphenylamine (TPA) core is one of the widely used electron-donating units for the construction of C_3 star-shaped molecules due to the sp^3 hybridized orbital of the nitrogen atom. TPA generally shows good electron-donating and high charge-transporting properties.[22-28] Similarly, another electron donor, phenothiazine (PTZ), is an important class of heterocyclic compound with a slightly non-planar geometry due to the presence of electron-rich nitrogen and

* Section 4.2 is reproduced from Yadav, Indresh Singh, Ajyal Z Alsaleh, Blake Martin, Rajneesh Misra, and Francis D'Souza. "Star-Shaped Triphenylamine–Tetracyanobutadiene–Phenothiazine Push–Pull Systems: Role of Terminal Phenothiazine in Improving Charge Transfer," The Journal of Physical Chemistry C 126, no. 31 (2022): 13300-10. With permission from the American Chemical Society.

sulfur heteroatoms.[29-30] PTZs have been extensively used for chemical sensors, photovoltaic devices, and organic light-emitting diodes (OLEDs).[30-33] Phenothiazine as such is a colorless compound with an absorption maxima around 316 nm. The structure of phenothiazine possesses some unique features different from that of a typical triarylamine. The two phenyl groups of phenothiazine are nearly coplanar, allowing the extension of the π-delocalization over the entire molecule. The electron-rich nature of a phenothiazine provides a good relay for the electron migration in multi-modular donor-acceptor systems.

Tetracyanoethylene (TCNE) is a powerful electron acceptor and its reaction with π-conjugated electron-rich alkynes by a [2 + 2] cycloaddition−retroelectrocyclization reaction, according to Diederich's procedure,[34-36] results in push-pull systems carrying electron-deficient, tetracyanobutadiene (TCBD) electroactive unit. The strong push-pull effects result in electron polarization (also often termed as ground state charge transfer) resulting in a new low-energy optical transition extending the optical coverage. Making use of the facile reaction and optical properties they have extensively explored building TCBD-substituted push-pull systems,[37-40] and polymers as promising materials for photovoltaic applications.[41-50] Our groups have explored a wide variety of donor-functionalized TCBD-based molecular systems exhibiting novel optical and excited-state properties including ultrafast charge transfer and intervalence charge transfer properties.[51-61]

In the present investigation, making use of the novel electronic and structural properties of TPA, PTZ and TCBD, we have designed, symmetric and asymmetric, multi-modular push-pull systems, 1–4 wherein the TCBD is positioned between the terminal PTZ and central TPA entities (Fig. 4.14). The number of TCBD entities has been varied to probe their effect on both ground and excited-state properties. Further, the second series of compounds lacking the terminal PTZ, C1–

C4, have also been synthesized to investigate the role of terminal PTZ in 1–4 in governing the excited-state charge transfer events. Key findings are summarized in the following paragraphs.

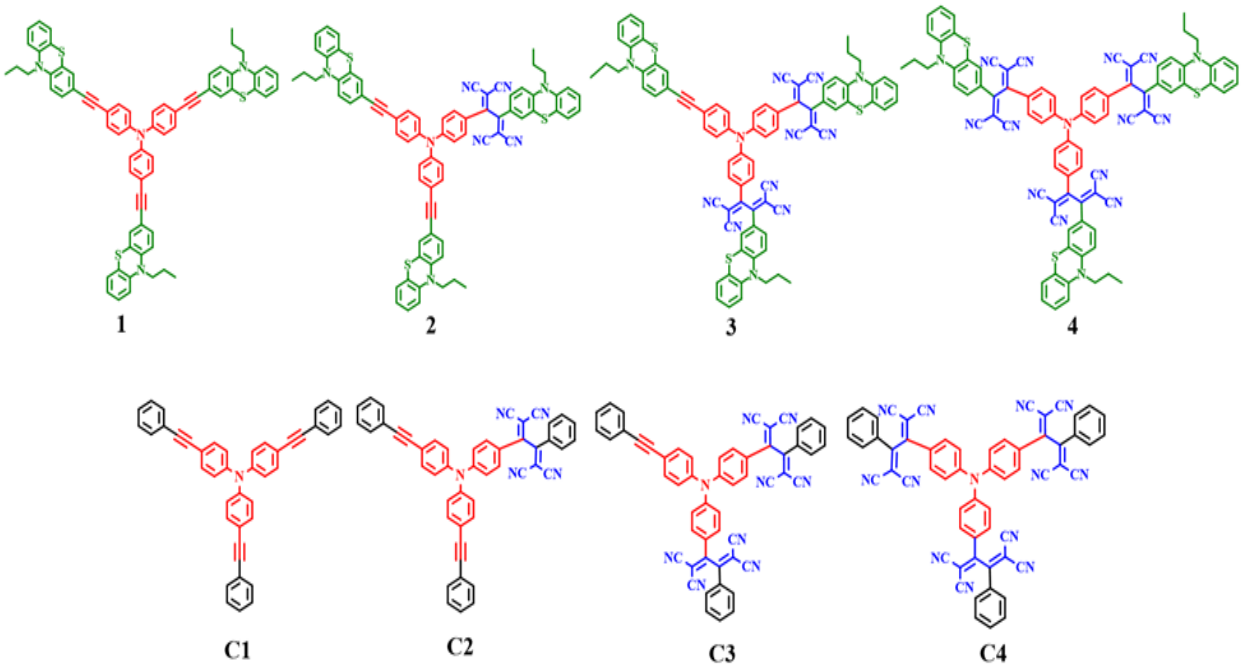

Figure 4.14: Structure and abbreviation of star-shaped, central triphenylamine derived, phenothiazine-tetracyanobutadiene conjugates, 1–4 (abbreviated as (PTZ-TCBD)$_{0\text{-}3}$-TPA-(PTZ)$_{0\text{-}3}$; (PTZ-TCBD)$_0$-TPA-(PTZ)$_3$ = 1; (PTZ-TCBD)$_1$-TPA-(PTZ)$_2$ = 2, (PTZ-TCBD)$_2$-TPA-(PTZ)$_1$ = 3, and (PTZ-TCBD)$_3$-TPA-(PTZ)$_0$ = 4 and the control compounds, C1–C4 (abbreviated as (Ph-TCBD)$_{0\text{-}3}$-TPA; (Ph-TCBD)$_0$-TPA = C1; (Ph-TCBD)$_1$-TPA = C2, (Ph-TCBD)$_2$-TPA = C3 and (Ph-TCBD)$_3$-TPA = C4) synthesized to probe excited-state charge transfer events.

4.2.2 Synthesis

Scheme 4.2 shows the developed synthetic scheme for compounds 1–4 while details are presented in the experimental section. Briefly, the symmetrical compound 1 was synthesized by the Pd-catalyzed Sonogashira cross-coupling of tris-(4-iodophenyl)-amine (1a) and corresponding 3-ethynyl-10-propyl-10*H*-phenothiazine (1b) in the presence of $Pd(PPh_3)_4$ and CuI in degassed THF: TEA (1:1) under argon atmosphere at 65 °C for 16 h which resulted in 1 at 66% yield. The TCBD functionalized symmetrical and unsymmetrical compounds 2–4 were synthesized via [2+2] cycloaddition-retro-electrocyclization reaction with the strong electron acceptor TCNE.[28] The

reaction of symmetrical 1 with one equivalent of TCNE in DCM at room temperature for 4 h resulted in an exclusive mono- TCBD substituted unsymmetrical compound 2 in 62% yield. Similarly, the reaction of symmetrical 1 with two equivalents of TCNE in DCM solvent at 40 °C for 12 h resulted in di-TCBD substituted unsymmetrical 3 in 65% yield, whereas increasing the reaction temperature to 60 °C for 24 h using four equivalents of TCNE with symmetrical 1 in DCE solvent resulted in tri-TCBD substituted symmetrical 4 in 68% yield.

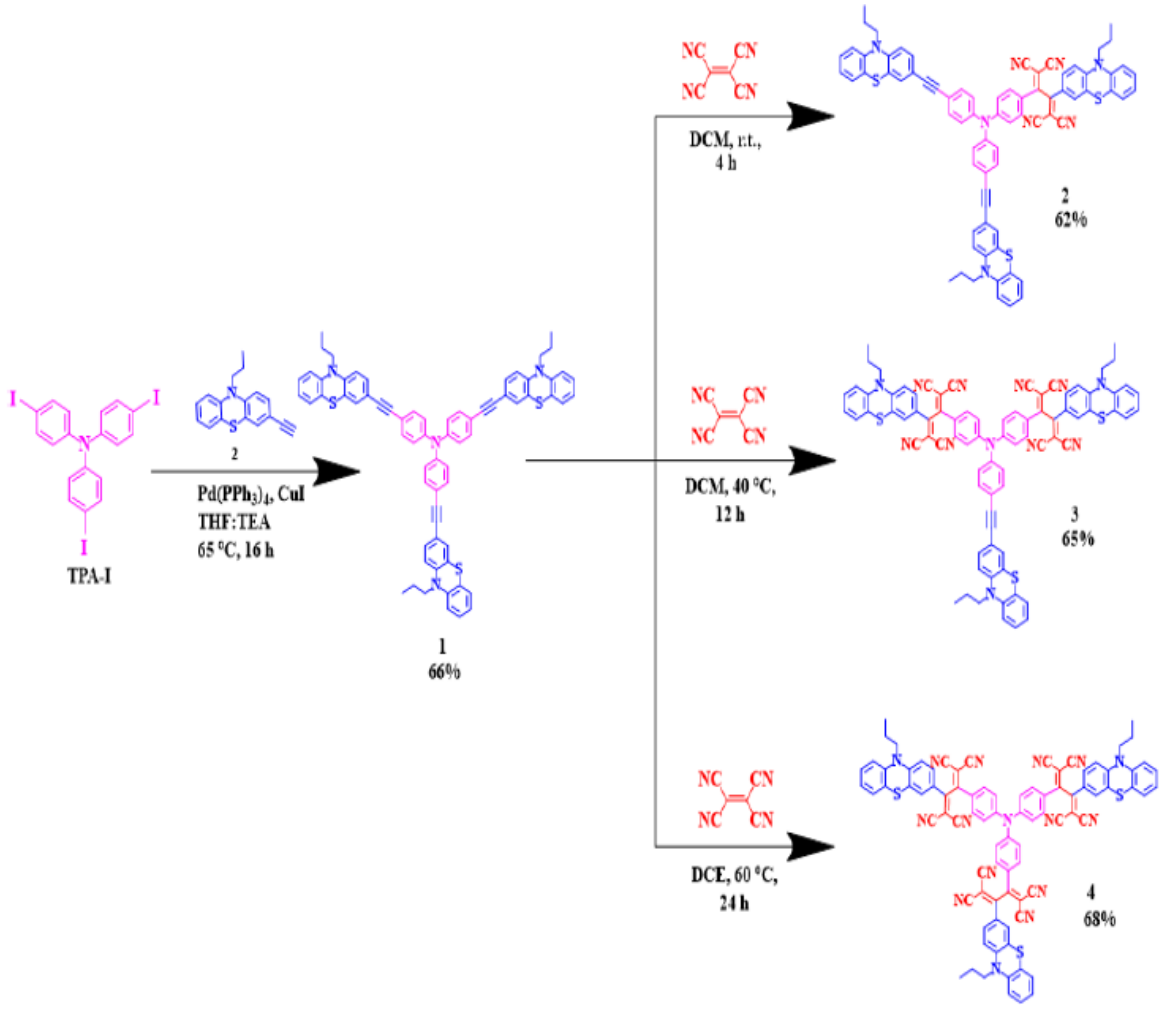

Scheme 4.2: Synthetic scheme of compounds 1–4.

The control compounds, C1–C4 were synthesized according to the earlier reported procedure.[62] All of the reported compounds were purified through silica gel (100-200 mesh) column chromatography using Hexane: DCM solvent.

4.2.3 Results and Discussion

Absorption and emission properties of compounds C1–C4 and 1–4 were subsequently investigated to evaluate the effect of TCBD in these compounds and the role of the second electron donor, PTZ in 1–4. Compound C1 revealed a single absorption band located at 372 nm (see Table 4.3 for spectral data). The introduction of TCBD resulted in two peaks, the first one in the 300–340 nm range and the second one in the 450-650 nm range (see Fig. 4.15a). The first one was attributed to the normal $\pi-\pi^*$ transition while the second one was for the ground state charge transfer (or charge polarization, $TCBD^{\delta-}$-$TPA^{\delta+}$). Importantly, as the number of TCBD entities increased, a systematic blue-shift of both peak maxima was witnessed. Interestingly, the introduction of the second electron donor, PTZ revealed better optical coverage in 2–4 extending the absorption well into the near-IR region (Fig. 4.15b). The spectrum of 1 revealed two peaks, the first one as a shoulder-type peak at 330 nm while the second one at 394 nm. Introducing the TBCD revealed a total of three absorption bands, two in the 300–420 nm region attributable to the $\pi-\pi^*$ transitions of the PTZ and TPA entities and a broader peak in the 420–750 nm range due to charge polarization. Similar to C2–C4, with the increase in TCBD entities in 2–4, a systematic blue shift was observed for both types of peaks suggesting that the PTZ is involved in the charge polarization, that is, the formation of $PTZ^{\delta-}$-$TCBD^{\delta-}$-TPA type species (with some contributions from TPA, *vide supra*).

Table 4.3: Absorption and luminescence spectral details of the investigated compounds in DCB.

Compound	Absorption, nm	Fluorescence, nm	Phosphorescence, nm
C1	373	417	698
C2	343 431 512	___	___
C3	314 395 520	___	___
C4	303 497 517	___	___
1	323 393	470	701

Compound	Absorption, nm	Fluorescence, nm	Phosphorescence, nm
2	322 365 520	___	___
3	318 390 525	___	___
4	315 385 504	___	___

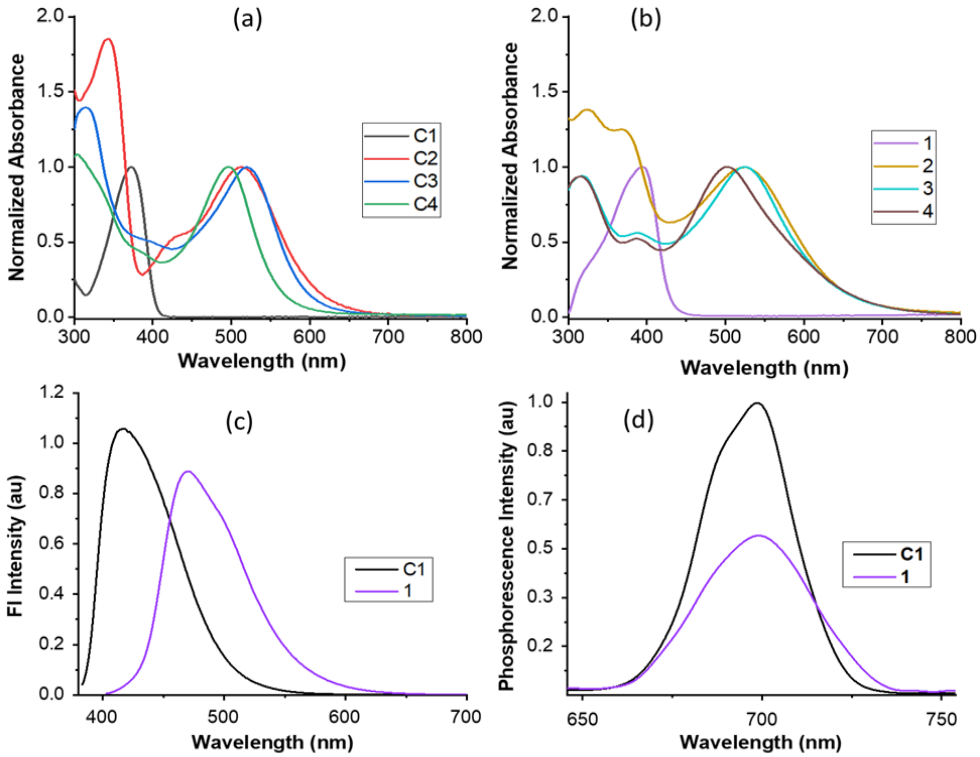

Figure 4.15: Absorption (a and b), fluorescence (c), and phosphorescence (d) spectra of the indicated compounds in DCB. Phosphorescence was recorded at 77K. The samples were excited at peak maxima located in the 300-400 nm region of the corresponding compound (see Table 4.3).

Among the investigated compounds only C1 and 1 were found to be luminescent upon excitation of the samples corresponding to the π–π^* peak maxima (Fig. 4.15c). The fluorescence maxima of C1 were located at 416 nm while that of 1 was located at 470 nm. Direct excitation of the charge transfer peaks in the visible region and extending the monitoring window did not show new peaks corresponding to charge transfer emission. It is likely that the intensities of such peaks are low. Lifetimes of C1 and 1 determined from the time-correlated single counting technique were found to be 2.89 ns for C1 and 2.59 ns for 1 (see Fig. 4.16 for delay plot). Phosphorescence of both C1 and 1 was also recorded at liquid nitrogen temperature (Fig. 4.15d). Peak maxima of C1 were

located at 698 nm while that of 1 was at 701 nm.

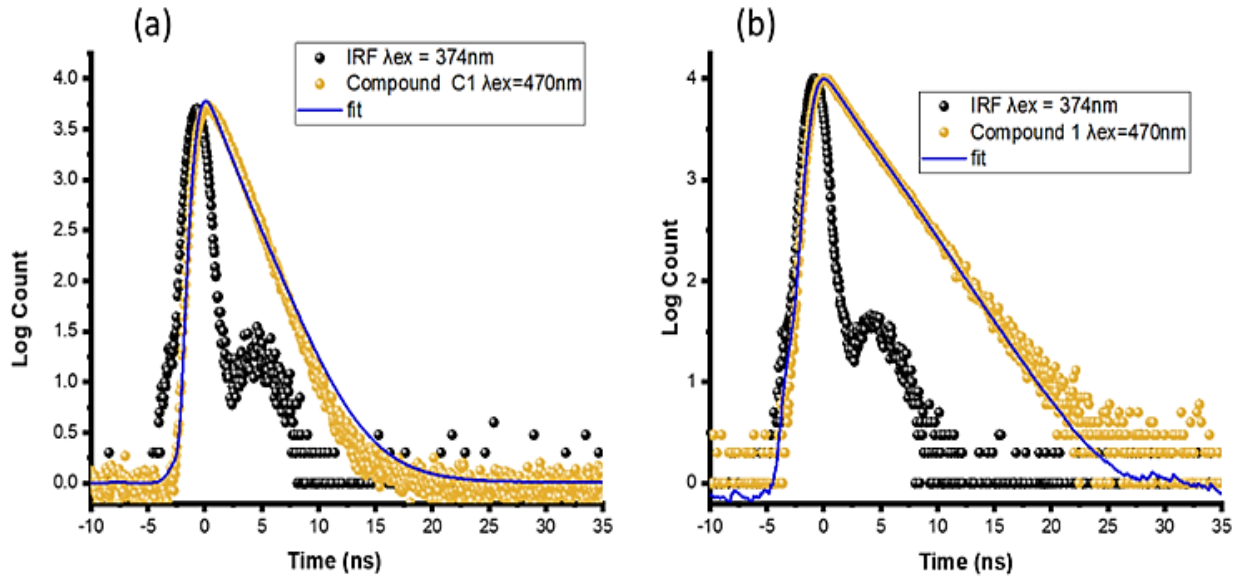

Figure 4.16: Fluorescence decay profiles of (a) C1 and (b) 1 in DCB.

Next, electrochemical studies using both cyclic (CV, to check reversibility) and differential pulse voltammetry (DPV, for peak potential measurement) were performed in DCB containing 0.1 M (TBA)ClO_4. CVs and DPVs are shown in Figures 4.17 and 4.18, respectively, while the data are summarized in Table 4.4. The first oxidation of C1 bearing only TPA was located at 1.12 V vs. Ag/AgCl while for 1 having both PTZ and TPA, oxidation at 0.94 and 1.19 V was observed, and by comparison, the first oxidation to the PTZ entity and the second one to TPA entity was possible to arrive. The electron-deficient TCBD is known to reveal two one-electron reductions, this seems to be the case in the C2–C4 and 2–4 series. In the case of C2–C4, the first reduction of TCBD was located at -0.19, -0.14, and -0.11 V, that is, TCBD reduction progressively became easier. Importantly, in the case of C3 and C4, the first reduction was a split peak, suggesting electron exchange between the TCBD entities.[56] On the oxidation side, the first oxidation of C2–C4 was located at 1.35, 1.46, and 1.67 V. This was also the trend for subsequent oxidations. That is, increasing the TCBD entities made the oxidation process gradually harder.

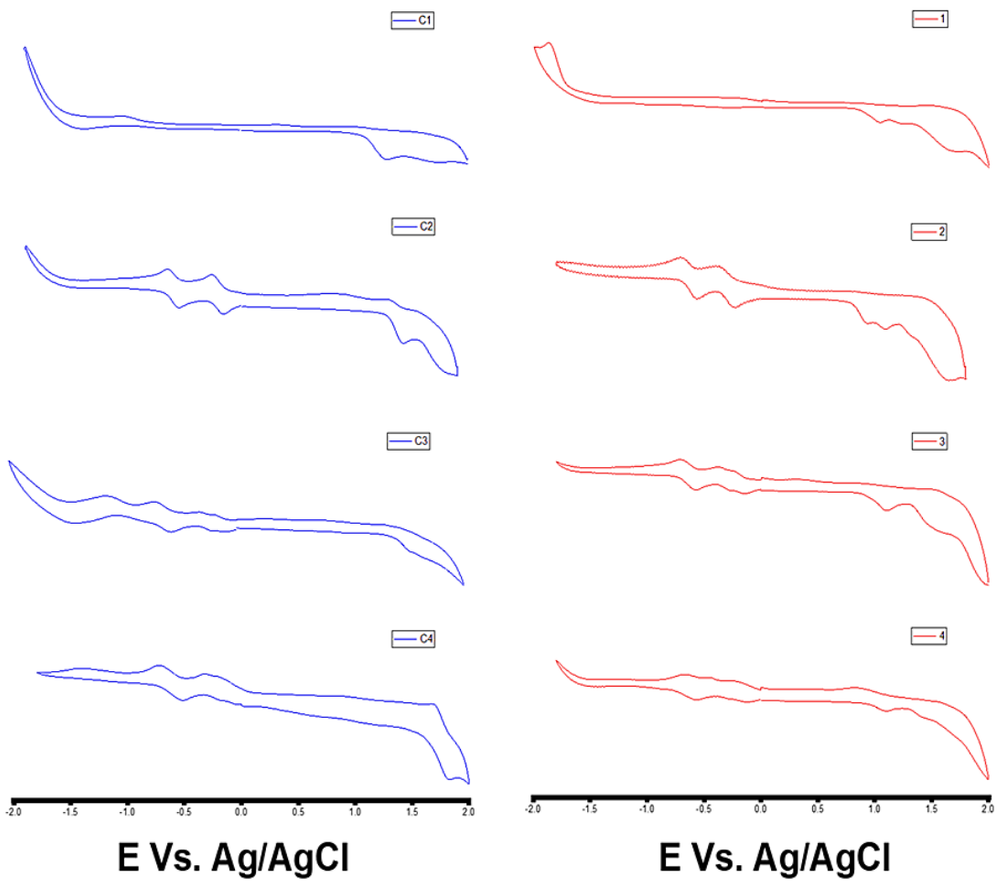

Figure 4.17: Cyclic voltammograms of the indicated compounds in DCB containing 0.1 M (TBA)ClO_4.

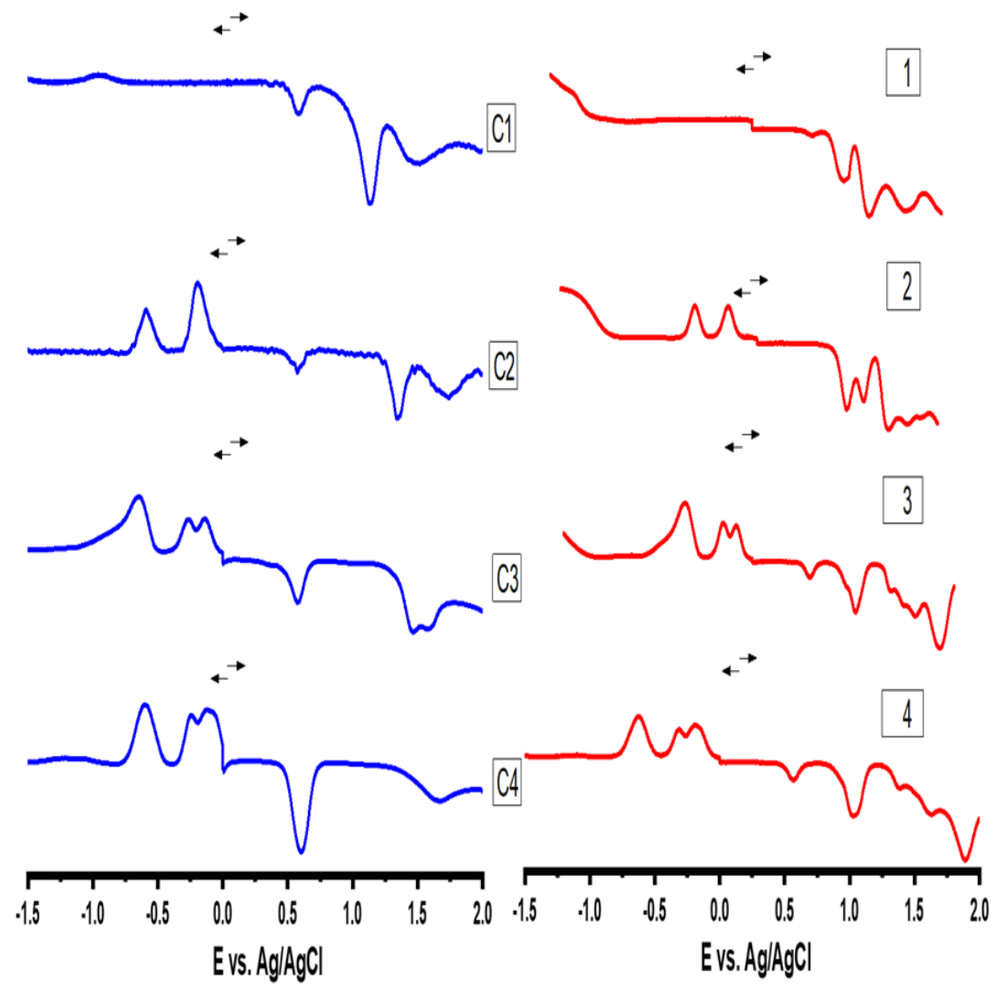

Figure 4.18: Differential pulse voltammograms of the indicated compounds in DCB containing 0.1 M (TBA)ClO_4.

Table 4.4: **Electrochemical redox potentials of the investigated compounds in DCB containing 0.1 M (TBA)ClO_4.**

Compound	Potential E vs. Ag/AgCl							$\Delta E_{1/2}$, V
	E_{ox}				E_{red}			
C1	1.12	1.62						> 3.0
1	0.94	1.19	1.51					> 3.0
C2	1.35	1.67			-0.19	-0.59		1.54
2	0.87	1.03	1.27	1.44	-0.28	-0.60		1.15
C3	1.46	1.44	1.56		-0.14	-0.26	-0.65	1.60
3	1.03	1.38	1.64	1.83	-0.16	-0.29	-0.67	1.19
C4	1.67				-0.11	-0.24	-0.60	1.78
4	1.03	1.38	1.63	1.89	-0.19	-0.31	-0.62	1.22

The electrochemical redox gap ($\Delta E_{1/2}$), that is, the potential difference between the first oxidation and first reduction was 1.54 V for C2, 1.60 V for C3, and 1.78 V for C4. This trend was consistent with the blue shift observed along with the series in the optical absorption spectral studies. Such a trend was also observed for compounds 2–4, however, due to facile reduction of PTZ over TPA, the measured $\Delta E_{1/2}$ were even smaller. $\Delta E_{1/2}$ values of 1.15 V for 2, 1.19 V for 3, and 1.22 V for 4 were observed, a trend that was also consistent with red-shift optical coverage of 2–4 compared to C2–C4, and comparatively shrinking of the gap along with series due to increased number of TCBD entities.[56] It is of significance to note reduced $\Delta E_{1/2}$ with the addition of the second electron donor in the investigated series of compounds, 2–4.

Geometry optimization followed by generating frontier orbitals to visualize donor-acceptor push-pull sites within the studied molecules was performed. For this, the structures were optimized on the B3LYP/6-31G* basis set, and functional,[63] and frontier HOMO and LUMO were generated, as shown in Figure 4.19. As expected, the HOMO of both C1 and 1 were spread all over the molecules. In the case of C2 and 2, HOMO spreading on the TPA and PTZ-TPA arms away from the TCBD entity and LUMO on TCBD was obvious. This trend was also observed for C3 and 3,

where HOMO on TPA and PTZ-TPA arms lacking TCBD was witnessed (more on the PTZ site). The LUMOs were on both TCBD entities. In the case of C4 and 4, HOMO on the central TPA and PTZ-TCBD arm, and LUMO on two of the TCBD entities were witnessed. These results reveal charge transfer type interactions in C2–C4 and 2–4 involving neighboring TPA/PTZ electron donor and TCBD electron acceptor. Importantly, in cases 2 and 3, the presence of HOMO on free PTZ and LUMO on TCBD with a center-to-center distance of 16.4 Å was possible to arrive. In this instance, selective excitation of the free-PTZ entity could result in charge separation.

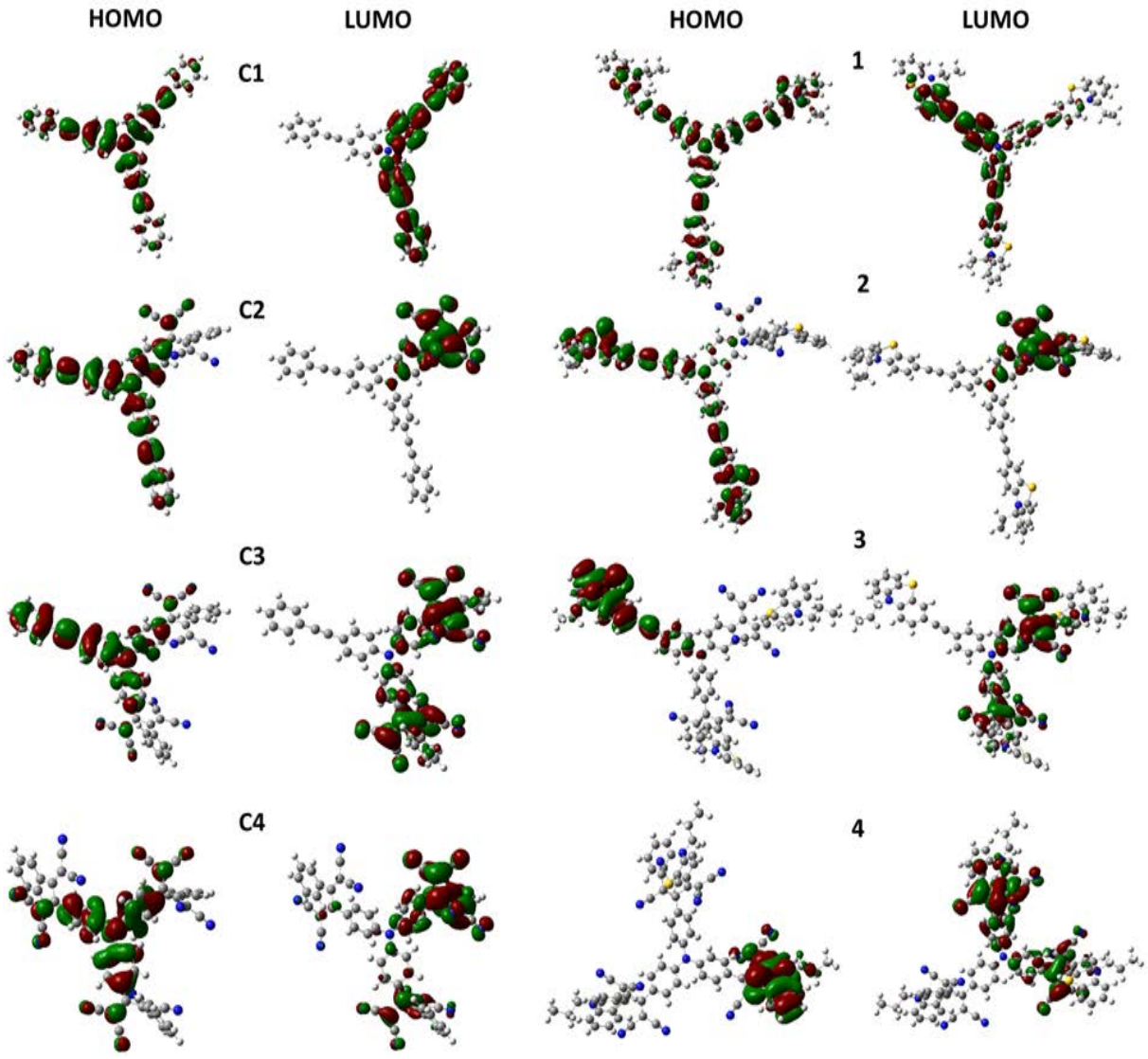

Figure 4.19: Frontier HOMO and LUMO on B3LYP/6-31G* optimized structure of the investigated compounds.

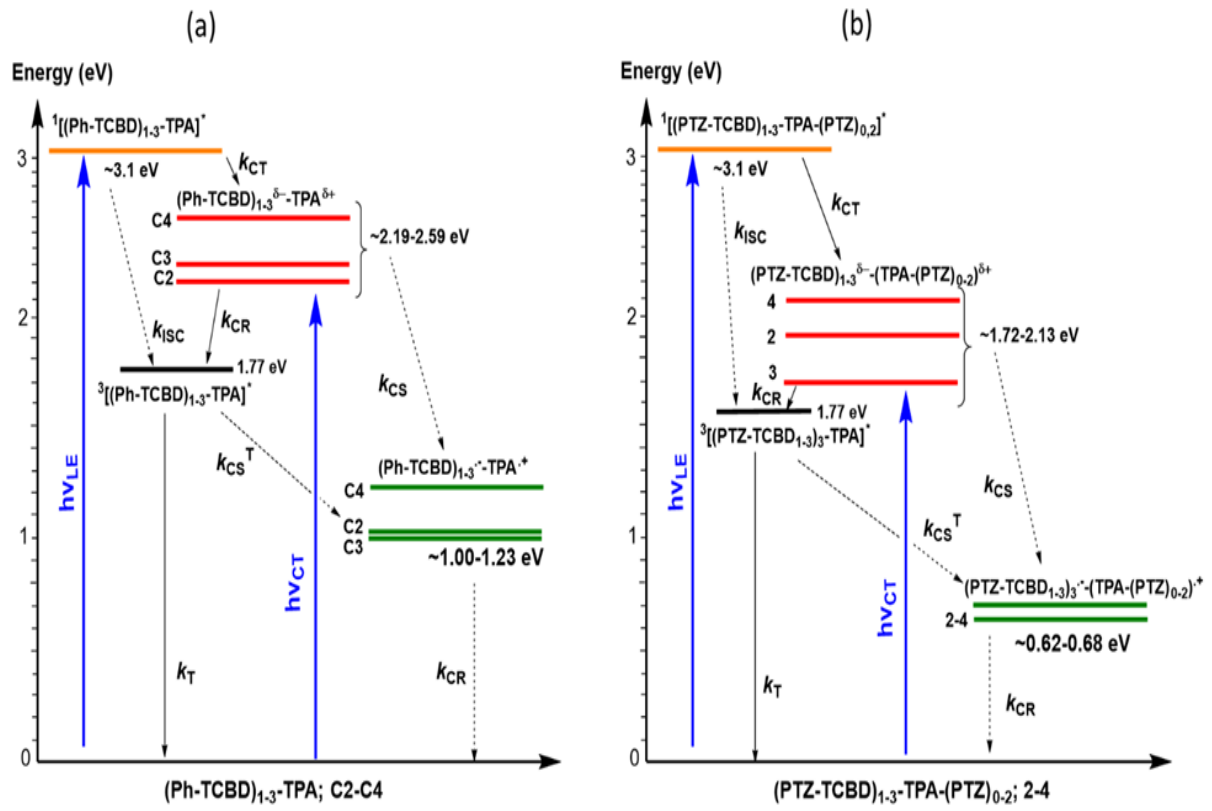

Figure 4.20: Energy level diagram demonstrating excited charge transfer and charge separation events upon photoexcitation of C2–C4 and 2–4 push-pull systems. The energy of the charge transfer states, (Ph-TCBD)$_{1\text{-}3}^{\delta-}$-TPA$^{\delta+}$ in the case of C2–C4, and (PTZ-TCBD)$_{1\text{-}3}^{\delta-}$-TPA-(PTZ)$_{0\text{-}2}^{\delta+}$ in the case of 2–4 are the energy difference between the respective HOMO and LUMO levels arrived from the DFT calculations. Under the conditions of λ_{CT} excitation, the excited state species is the excited singlet charge transfer complex, 1[(Ph-TCBD)$_{1\text{-}3}^{\delta-}$-TPA$^{\delta+}$)]* in the case of C2–C4 and 1[(PTZ-TCBD)$_{1\text{-}3}^{\delta-}$-TPA-(PTZ)$_{0\text{-}2}^{\delta+}$]* in the case of 2–4; not shown in the diagram for brevity. The energy of the charge-separated states was calculated according to the Rehm-Weller approach in DCB.

From the spectral, luminescence, computational, and electrochemistry data, energy level diagrams were established to visualize different photochemical events in the studied push-pull systems (Fig. 4.20). The HOMO–LUMO energy gap from the computational studies was used as the energy of the CT state, E_{CT} in the energy diagram. The energy of the charge-separated state in benzonitrile was calculated according to the Rehm-Weller approach [64] using optical and electrochemical data according to the following equations.

$$-\Delta G_{CR} = E_{ox} - E_{red} + \Delta G_S \quad \text{(Eq 4.1)}$$

$$-\Delta G_{CS} = \Delta E_{0\text{-}0}\text{-}(-\Delta G_{CR}) \quad \text{(Eq 4.2)}$$

$$\Delta G_S = e^2/4\,\pi\varepsilon_o\,[\,-\,1/R_{cc}\,\varepsilon_R] \qquad \text{(Eq 4.3)}$$

where ΔE_{00} corresponds to the singlet state energy of 1. The term ΔG_S refers to electrostatic energy calculated according to the dielectric continuum model (see Eq. 4.3). The E_{ox} and E_{red} represent the oxidation potential and the first reduction potential, respectively. The symbols ε_0 and ε_R represent the vacuum permittivity and dielectric constant of DCB used for photochemical and electrochemical studies (= 9.93). R_{CC} is the center-to-center distance between donor and acceptor entities from the computed structures. The energy of charge transfer was calculated from the peak maxima of the charge transfer peak.

In the case of compounds C2–C4 (see Fig. 4.20a), excitation of TPA corresponding to its π–π (locally excited, LE) peak maxima, would populate the singlet excited state ^{1}[(Ph-TCBD)$_{1\text{-}3}$-TPA]* having enough energy to promote the charge transfer event to yield (Ph-TCBD)$_{1\text{-}3}^{\delta-}$-TPA$^{\delta+}$). Direct excitation of the CT band would produce the singlet excited state of the charge transfer state, ^{1}[(Ph-TCBD)$_{1\text{-}3}$ $^{\delta-}$-TPA $^{\delta+}$)] *. In a polar solvent such as benzonitrile, the CT state could undergo the charge-separated (CS) state producing radical ion-pairs, (Ph-TCBD)$_{1\text{-}3}$ $^{\delta-}$-TPA $^{\delta+}$) in competition with populating the low-lying triplet excited state, ^{3}[(Ph-TCBD)$_{1\text{-}3}$-TPA]*. A relatively complex situation arises in compounds 2–4 due to the presence of PTZ with and without connected TCBD entity(ies) (Fig. 4.20b). In this instance, the ^{1}[(PTZ-TCBD)$_{1\text{-}3}$-TPA-(PTZ)$_{0\text{-}2}$]* state produced by LE excitation would promote the CT state to produce (PTZ-TCBD)$_{1\text{-}3}$ $^{\delta-}$-TPA-(PTZ)$_{0\text{-}2}$ $^{\delta+}$. Direct excitation corresponding to CT peak maxima, could also populate the ^{1}[(PTZ-TCBD)$_{1\text{-}3}$-TPA-(PTZ)$_{0\text{-}2}$]* state. From the location of the frontier orbitals, formation of ^{1}[(PTZ-TCBD) $^{\delta-}$-TPA-(PTZ)$_2$ $^{\delta+}$]* in the case of 2, formation of ^{1}[(PTZ-TCBD)$_2$ $^{\delta-}$-TPA-(PTZ) $^{\delta+}$]* in the case of 3, and formation of ^{1}[(PTZ-TCBD)$_3$ $^{\delta-}$-TPA $^{\delta+}$]* in the case of 4 could be envisioned. Since the energy of these CT states is higher than CS state, the resulting CT state could populate the

triplet state or end up producing charge separates states, viz., [(PTZ-TCBD)$^{\bullet-}$-TPA-(PTZ)$_2$$^{\bullet+}$ in the case of 2, (PTZ-TCBD)$_2$$^{\bullet-}$-TPA-(PTZ)$^{\bullet+}$ in the case of 3, and (PTZ-TCBD)$_3$$^{\bullet-}$-TPA$^{\bullet+}$]* in the case of 4. A charge-separated state may be preferred in cases 2 and 3 due to the distal positioning of the free PTZ and PTZ-TCBD, donor, and acceptor entities.

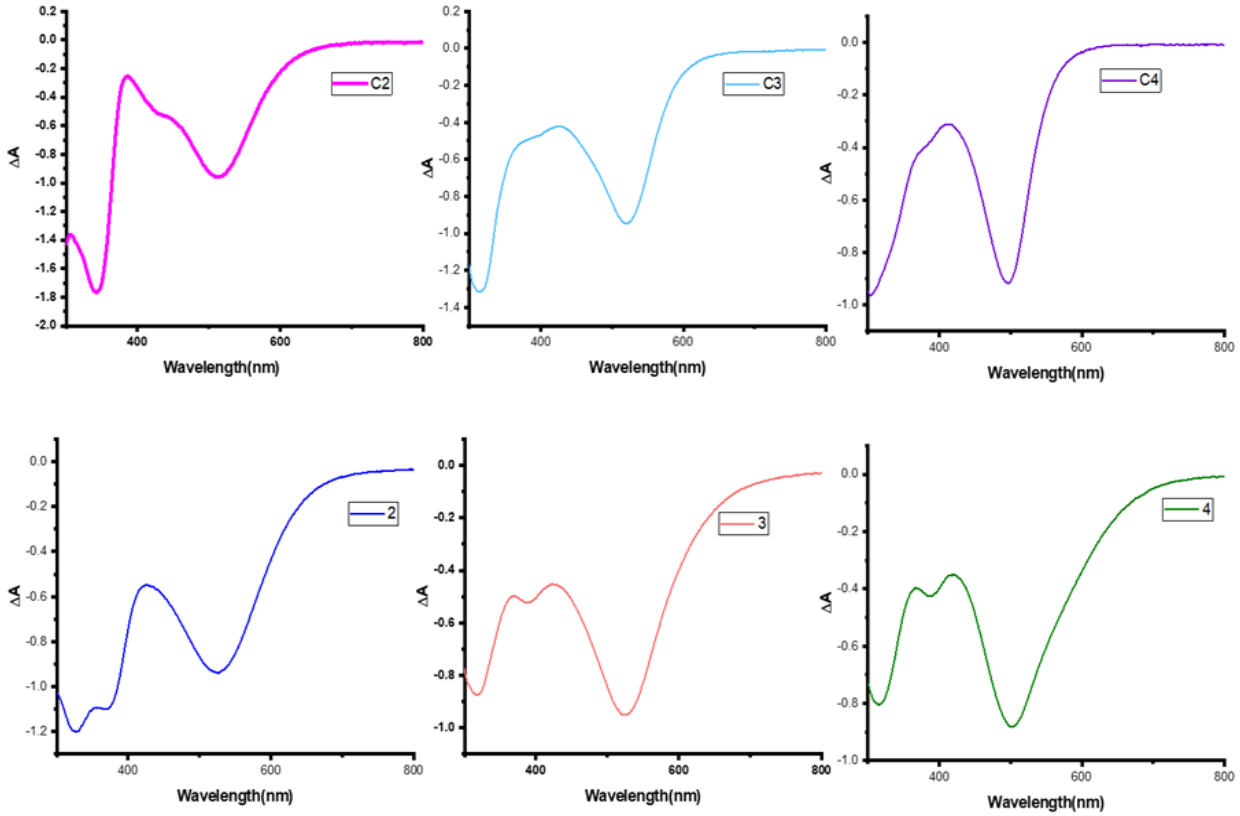

Figure 4.21: Spectrum deduced for the charge separated states from spectroelectrochemical studies of the indicated compounds in DCB.

In an effort to arrive at the spectrum of the charge transfer/separation species, spectroelectrochemical studies on both series of compounds, viz., C2–C4, and 2–4 were performed. For this, spectral data during the process of first oxidation and first reduction for each compound was recorded by applying appropriate potentials (100 mV past the redox peak potentials). The final spectrum of the cation and anion were digitally added and subtracted with the neutral species to generate the differential absorption spectrum corresponding to the charge

transfer/separation species. Figure 4.21 shows the spectrum for each push-pull system generated in this fashion. The main features involved depleted peaks in the 300-340 nm range and 500-515 nm range. For compounds 2–4, another depleted peak in the 380–390 nm range was also observed. Should there is excited-state charge transfer/separation in these push-pull systems, the spectrum of the transient species corresponding to the CT state should match closely with that of the spectrum arrived from spectroelectrochemical studies.

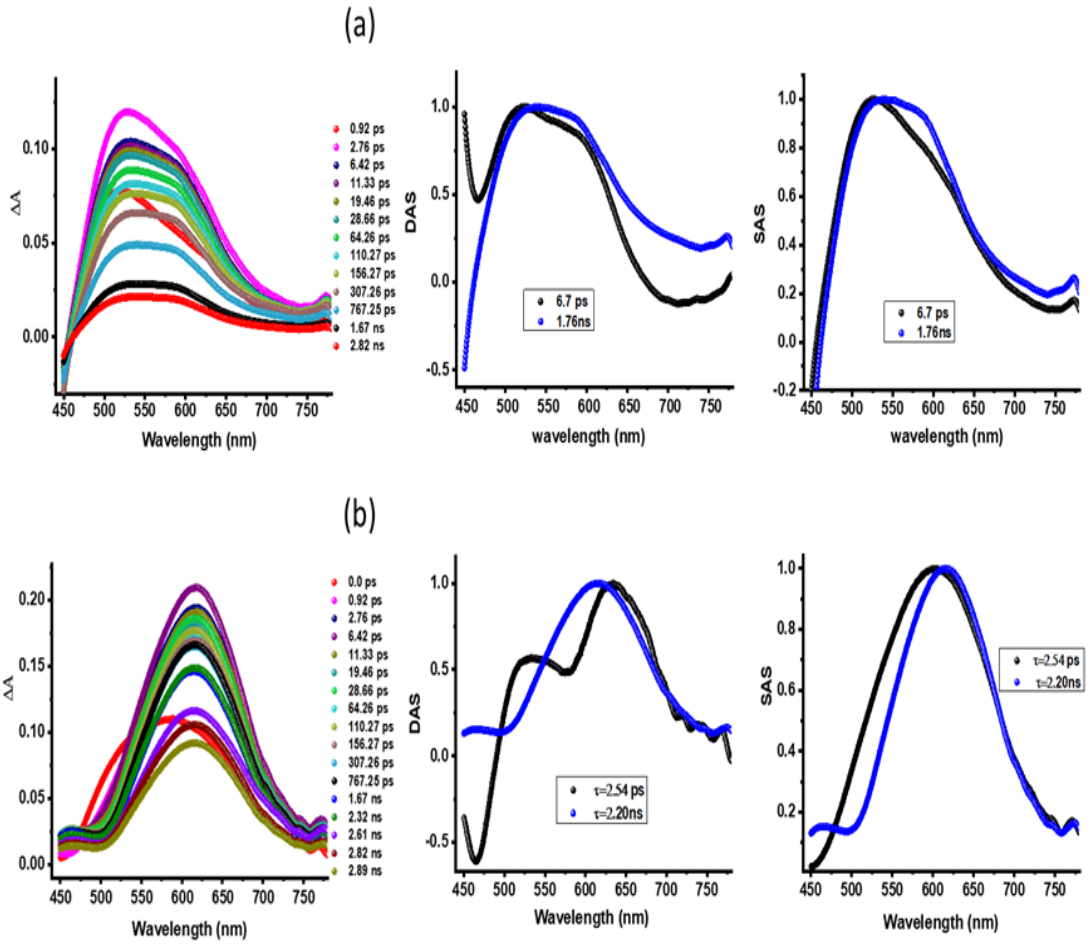

Figure 4.22: Fs-TA spectra at the indicated delay times of (a) C1 and (b) 1 in benzonitrile. DAS and SAS spectra are shown on the right-hand side of each spectrum.

Having detailed the possible photochemical events in the studied push–pull systems as summarized above, next, transient pump-probe spectral studies were performed using both LE and CT excitation wavelengths. Figures 4.22 (a and b) show the femtosecond transient absorption (fs-

TA) spectra of C1 and 1 (having no TCBD) in benzonitrile, respectively, along with the decay-associated spectra (DAS) and species associated spectra (SAS) from Glotaran analysis[65-66] of the transient data. In the case of C1, the singlet excited state (S_1) species obtained within the first 6–7 ps revealed a broad excited state absorption (ESA) peak at 527 nm. The decay of this peak was associated with another less intense broad peak with maxima at 540 nm. A two-component fit was representing the initial S_1 and a triplet excited state, T_1 formed from the process of intersystem crossing (ISC) was satisfactory whose DAS and SAS spectra are shown on the right-hand side of Figure 4.22a. The lifetime of the T_1 state was 1.76 ns suggesting the formation of a short-lived triplet excited state. In the case of 1, the S_1 state formed within the first 2–3 ps, revealed ESA peaks at 623 nm. With time, a blue shift accompanied decay and a new peak at 412 nm was witnessed. A two-component fit was representing the initial S_1 and the T_1 state was satisfactory whose DAS and SAS spectra are shown on the right-hand side of Figure 4.22b. The lifetime of the T_1 state was found to be 2.20 ns, not significantly different from that of C1.

Next, photophysical properties of the relatively simpler version of push-pull systems, C2–C4 were performed in polar benzonitrile as the charge separation process is favored in polar solvents (Fig. 4.23). The samples were excited at 350 nm corresponding to the LE excitation. In all three systems, the S_1 species formed within the first 1-3 ps, revealed two main ESA peaks, the first one in the 490 nm region and the second one in the 630 nm range. There was a systematic blue shift of the first peak with the increase in the TCBD entities, that is, peak locations at 498 nm for C1, 481 nm for C2, and 478 nm for C3 were witnessed. The decay of this peak was associated with an initial negative signal in the 500 nm range, and the recovery of this signal was associated with a new peak in the 550 nm range. The DAS and SAS spectra for each compound are shown on the right-hand side. A three-component fit representing $S_1 \rightarrow CT \rightarrow T_1$ was satisfactory.

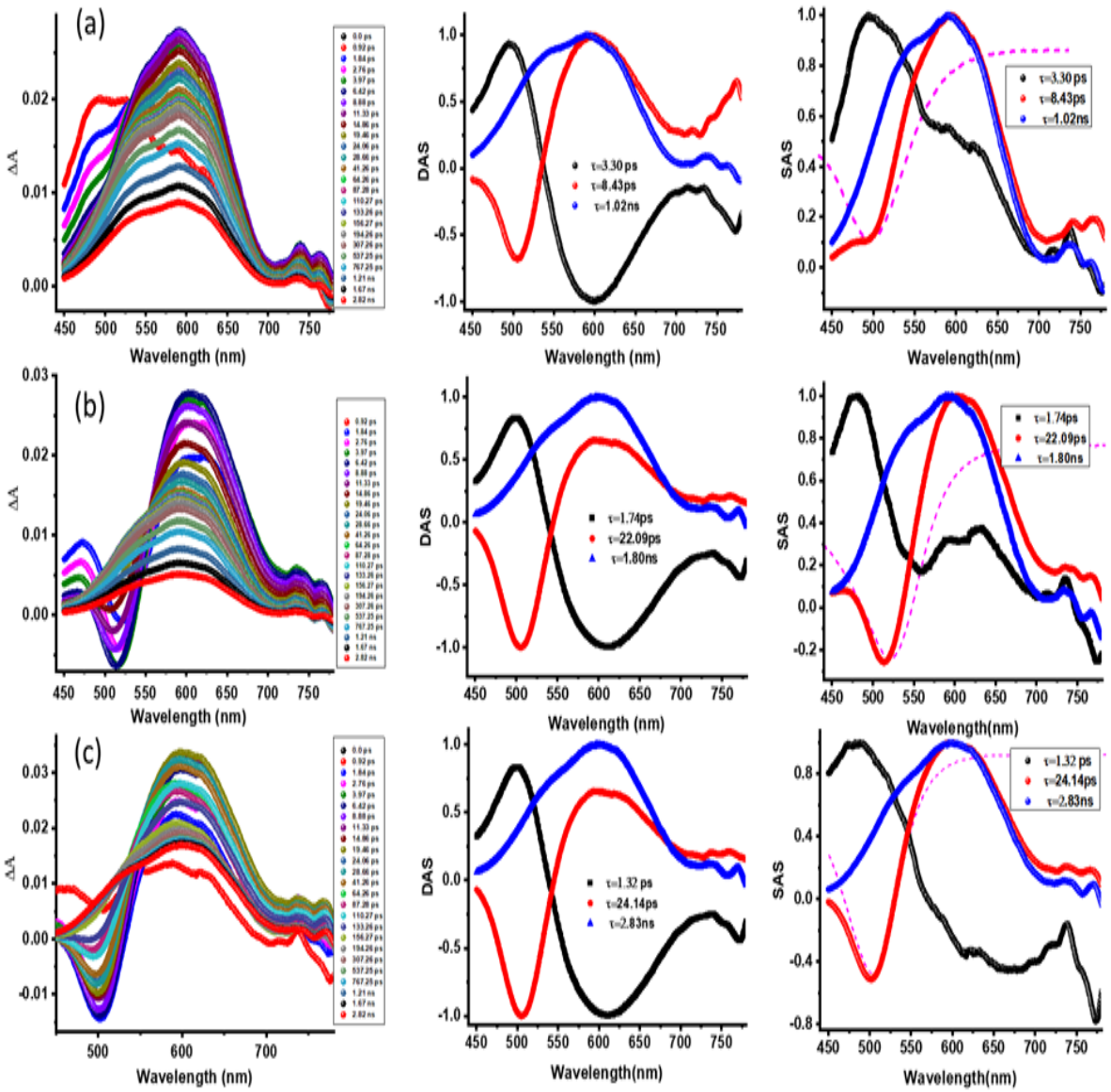

Figure 4.23: Fs-TA spectra at the indicated delay times of compounds C2–C4 in benzonitrile (λ_{ex} = 350 nm). Decay and species-associated spectra from Glotaran analysis are shown on the right-hand side. The dashed line in the SAS panel corresponds to the spectrum deduced for the CT state from spectroelectrochemical studies.

The DAS spectra in the middle panel nicely demonstrate the sequential occurrence of these events while the SAS spectrum attributed to the CT state (red trace) agreed well with the spectrum deduced for the CT state from spectroelectrochemical studies (dashed magenta line). These results unequivocally prove the occurrence of CT in C2–C4 in DCB. In all these systems, the spectrum attributed to the T_1 state (blue line) was almost similar and agreed with that observed for C1 in

Figure 4.22. The time constants of the CT states (average lifetime of the state) were 8.43, 22.09, and 24.14 ps, respectively for C2, C3, and C4, that is, with an increase in the number of TCBD entities, improved lifetimes for the CT states to some extent were witnessed. Lifetimes of the T_1 state were in the range of 1-3 ns. Compounds **C2–C4** were also excited at 500 nm corresponding to the charge transfer band (see Fig. 4.24).

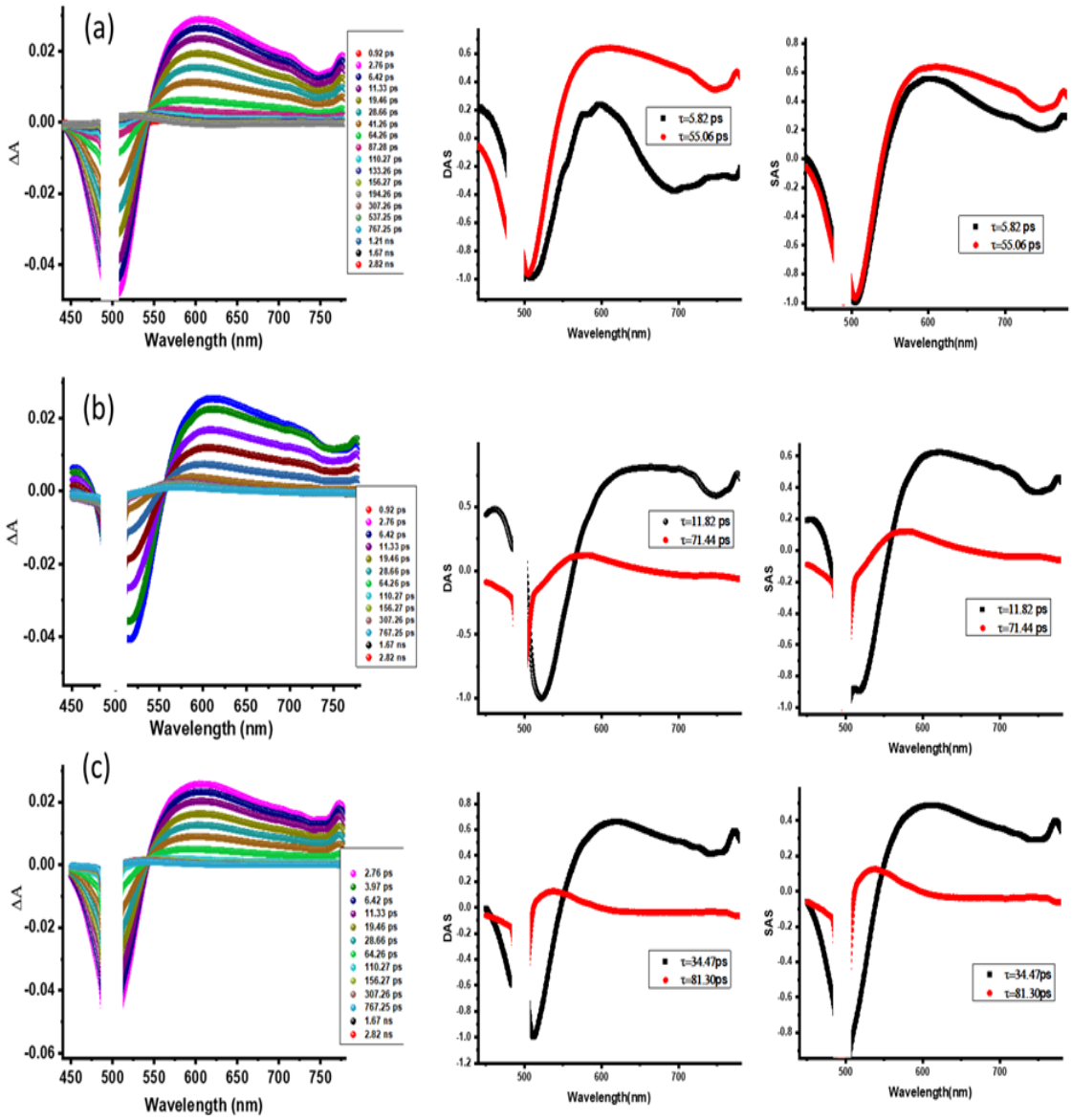

Figure 4.24: Fs-TA spectra at the indicated delay times of compounds C2-C4 in benzonitrile (λ_{ex} = 500 nm). Decay and species associated spectra from Glotaran analysis are shown on the right-hand side. The spectrum is blocked in the 500 nm range to avoid scatted excitation light.

The instantaneously formed $^{1}[(\text{Ph-TCBD})_{1\text{-}3}^{\delta-}\text{-TPA}^{\delta+})]^{*}$ was characterized by an ESA peak in the 602-606 nm range, and a negative peak in the 510-520 nm range, expected for the CT state from the earlier discussed spectroelectrochemical data. A two-component fit was satisfactory in the Glotaran analysis whose DAS and SAS are shown in Figure 4.24 on the right-hand side of the corresponding transient spectra. The first state, the singlet excited CT state revealed lifetimes of 5.82, 11.82, and 34.47 ps, respectively, for C2, C3, and C4, lightly lower than those observed for the CT state time constants for the samples excited at 350 nm corresponding to LE state. The spectral features of the second component were that of the T1 state, however, the time constants were much smaller in the range of 55-81 ps. The data were also subjected to a three-component fit to seek any long-lived component representing the charge-separated state. However, no strong evidence of charge-separated product could be obtained.

Next, transient spectra of compounds 2–4 were recorded in benzonitrile, excited at 393 nm corresponding to the LE state. Figure 4.25 shows the spectral data along with the DAS and SAS from Glotaran analysis. The $^{1}[(\text{PTZ-TCBD})_{1\text{-}3}\text{-TPA-}(\text{PTZ})_{0\text{-}2}]^{*}$ formed within the first few ps was characterized by an ESA peak at 620-640 nm range along with a negative peak in the 500 nm range. The decay of the ESA peak was accompanied by a blue shift along with a shoulder peak in the 540 nm range. A three-component fit in Glotaran representing $S_1 \rightarrow CT \rightarrow T_1$ was satisfactory whose spectra are shown on the respective right-hand side. As observed for compounds C2–C4, the SAS spectrum obtained for the T_1 state was in agreement with what was observed for compound 1. Importantly, the SAS spectrum corresponding to the CT state matched well with that arrived from spectroelectrochemical results. Time constants of the CT state were 24.94, 43.10, and 57.89 ps, respectively, for 2, 3, and 4. Importantly, these values were much higher than that observed for C2–C4 lacking the terminal electron donor, PTZ. The T_1 state had time constant

values ranging between 880-910 ps. The data was also subjected to four-component fits, both sequential and simultaneous modes to seek any long-lived CS states. However, no such events could be observed suggesting that the CT state transforms into the corresponding triplet state, as shown in the energy diagram in Figure 4.20.

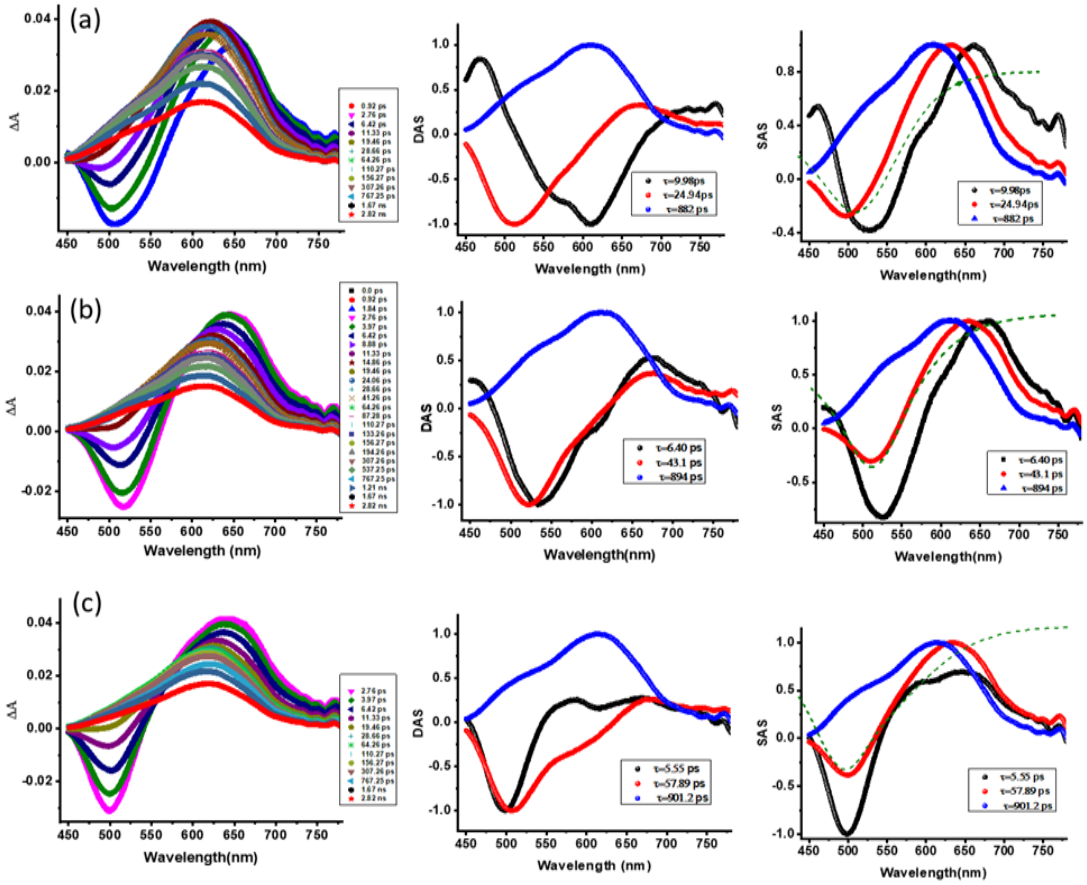

Figure 4.25: Fs-TA spectra at the indicated delay times of compounds 2–4 in benzonitrile (λ_{ex} = 393 nm). Decay and species-associated spectra from Glotaran analysis are shown on the right-hand side. The dashed line in the SAS panel corresponds to the spectrum deduced for the CT state from spectroelectrochemical studies.

Finally, compounds 2–4 were also excited at 500 nm corresponding to the CT state, as shown in Figure 4.26. The $^{1}[(PTZ\text{-}TCBD)_{1\text{-}3}{}^{\delta-}\text{-}TPA\text{-}(PTZ)_{0\text{-}2}{}^{\delta+}]^{*}$ formed revealed an ESA peak in the 650 nm region and a negative peak in the 500 nm range. Decay/recovery of these peaks was associated with a new peak in the 600 nm region suggesting that the $^{1}CT^{*}$ transforms into a T_1 state

prior to returning to the ground state. A two-component analysis representing $^{1}CT^{*}$ → T_1 was satisfactory in these systems, as shown by DAS and SAS spectra on the right-hand panels. Time constants for the $^{1}CT^{*}$ states were found to be 5.74, 7.09, and 8.32 ps, much smaller than when the samples were excited at their respective LE states. Importantly, with an increase of TCBD entities, time constants for CT state improved. The time constants for the T_1 state also followed such a trend with the highest time constants of about 600 ps in the case of 4.

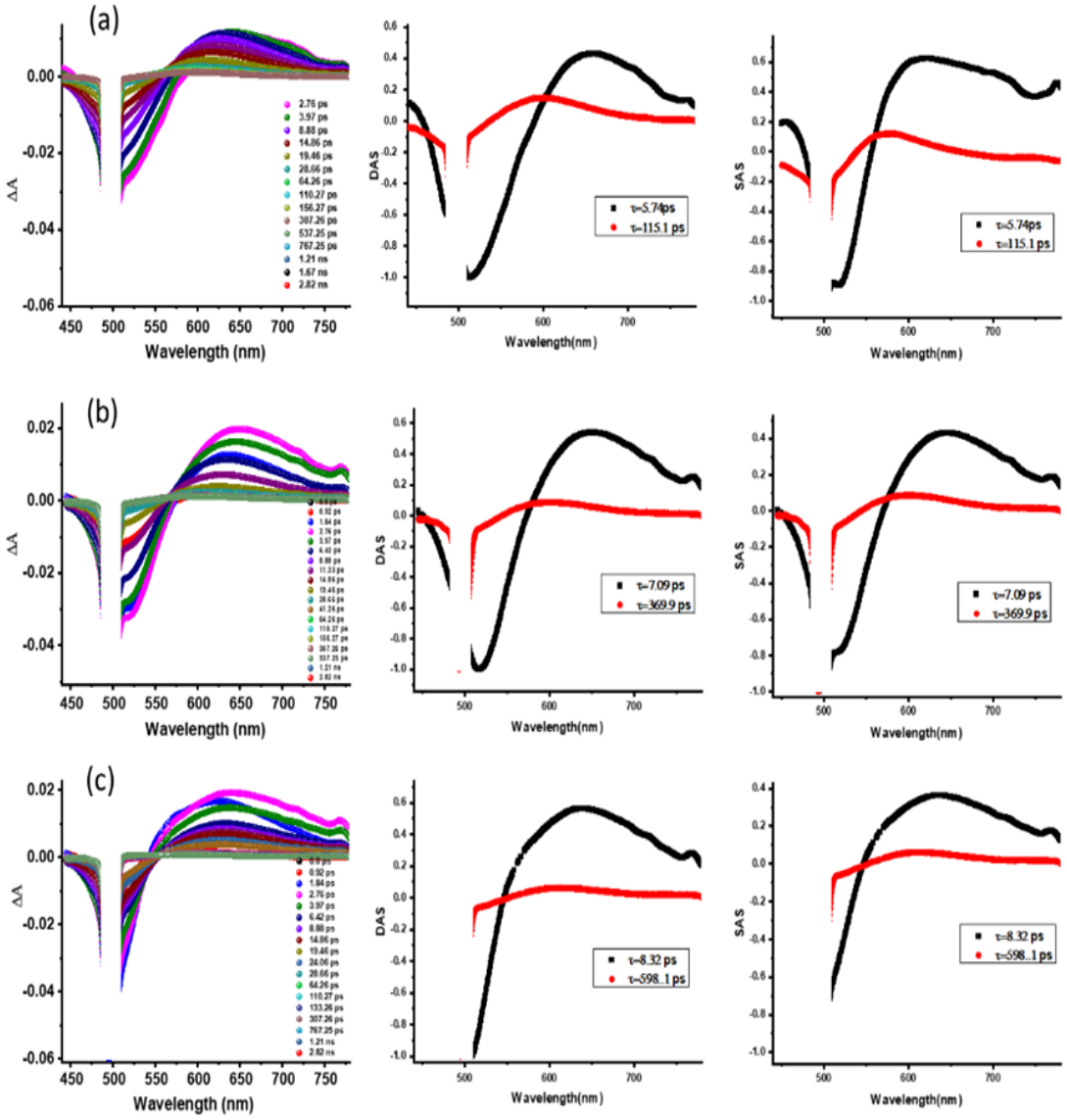

Figure 4.26: Fs-TA spectra at the indicated delay times of compounds 2-4 in benzonitrile (λ_{ex} = 500 nm). Decay and species associated spectra from Glotaran analysis are shown on the right-hand side. The spectrum is blocked in the 500 nm range to avoid scatted excitation light.

4.2.4 Conclusions

In summary, a novel series of push-pull systems by introducing a powerful electron acceptor, TCBD between the donor entities of a C3 symmetric TPA-$(PTZ)_3$ molecular scaffold has been synthesized *via* Pd-catalyzed Sonogashira cross-coupling reaction, followed by [2+2] cycloaddition-retroelectrocyclization reaction. As a control, a TPA scaffold lacking PTZ was also synthesized. The number of TCBD entities was varied between 1 and 3 in these push-pull systems to evaluate the effect of TCBD entities in promoting charge polarization in the ground state and excited state charge transfer, and the role of PTZ in stabilizing the charge transfer states. The strong push-pull effects promoted charge polarization resulting in the extension of the absorption covering the 300**–**800 nm range. Electrochemical studies revealed electron exchange resulting in the splitting of the first reduction wave of TCBD in compounds C3, C4, 3**,** and 4 carrying two or three TCBD or PTZ-TCBD entities. Frontier orbitals on energy-optimized structures helped in arriving at different charge-transfer states. The spectrum of the charge transfer state was possible to arrive from spectroelectrochemical data. Finally, using pump-probe spectroscopy followed by Global target analysis, it has been possible to demonstrate the occurrence of excited charge transfer in these compounds, when the samples were excited both at the locally excited and charge polarized absorption peak maxima. The significance of the additional electron donor in these multi-modular systems in prolonging the lifetime of the charge transfer is borne out from the present study.

4.2.5 References and Notes

1. Armaroli, N.; Balzani, V. The Future of Energy Supply: Challenges and Opportunities. *Angew. Chem. Int. Ed*. 2007, **46** (1–2), 52–66.
2. Beaujuge, P. M.; Fréchet, J. M. J. Molecular Design and Ordering Effects in π-Functional Materials for Transistor and Solar Cell Applications. *J. Am. Chem. Soc*. 2011, **133** (50), 20009–20029.

3. D'Souza, F.; Ito, O. Photosensitized Electron Transfer Processes of Nanocarbons Applicable to Solar Cells. *Chem. Soc. Rev.* 2011, **41** (1), 86–96.

4. El-Khouly, M. E.; Fukuzumi, S.; D'Souza, F. Photosynthetic Antenna–Reaction Center Mimicry by Using Boron Dipyrromethene Sensitizers. *ChemPhysChem* 2014, **15** (1), 30–47.

5. Bottari, G.; Torres, T. Organic Nanomaterials: *Synthesis, Characterization, and Device Applications*, Eds: Torres, T.; Bottari, G. John Wiley & Sons, Inc., Hoboken, NJ, 2013.

6. Imahori, H.; Umeyama, T.; Ito, S. Large π-Aromatic Molecules as Potential Sensitizers for Highly Efficient Dye-Sensitized Solar Cells. *Acc. Chem. Res*. 2009, 42 (11), 1809–1818.

7. Gust, D.; Moore, T. A.; Moore, A. L. Realizing Artificial Photosynthesis. *Faraday Discuss.* 2012, **155** (0), 9–26.

8. Martín, N.; Sánchez, L.; Herranz, M. Á.; Illescas, B.; Guldi, D. M. Electronic Communication in Tetrathiafulvalene (TTF)/C60 Systems: Toward Molecular Solar Energy Conversion Materials? *Acc. Chem. Res*. 2007, **40** (10), 1015–1024.

9. Bottari, G.; de la Torre, G.; Guldi, D. M.; Torres, T. Covalent and Noncovalent Phthalocyanine−Carbon Nanostructure Systems: Synthesis, Photoinduced Electron Transfer, and Application to Molecular Photovoltaics. *Chem. Rev*. 2010, **110** (11), 6768–6816.

10. Zarrabi, N.; Seetharaman, S.; Chaudhuri, S.; Holzer, N.; Batista, V. S.; van der Est, A.; D'Souza, F.; Poddutoori, P. K. Decelerating Charge Recombination Using Fluorinated Porphyrins in N,N -Bis(3,4,5-Trimethoxyphenyl)Aniline—Aluminum(III) Porphyrin—Fullerene Reaction Center Models. *J. Am. Chem. Soc*. 2020, **142** (22), 10008–10024.

11. Hammarström, L. Accumulative Charge Separation for Solar Fuels Production: Coupling Light-Induced Single Electron Transfer to Multielectron Catalysis. *Acc. Chem. Res*. 2015, **48** (3), 840–850.

12. Arrigo, A.; Santoro, A.; Puntoriero, F.; Lainé, P. P.; Campagna, S. Photoinduced Electron Transfer in Donor–Bridge–Acceptor Assemblies: The Case of Os(II)-Bis(Terpyridine)-(Bi)Pyridinium Dyads. *Coord. Chem. Rev*. 2015, **304–305**, 109–116.

13. Fukuzumi, S.; Ohkubo, K.; Suenobu, T. Long-Lived Charge Separation and Applications in Artificial Photosynthesis. *Acc. Chem. Res*. 2014, **47** (5), 1455–1464.

14. Gust, D.; Moore, T. A.; Moore, A. L. Solar Fuels via Artificial Photosynthesis. *Acc. Chem. Res*. 2009, **42** (12), 1890–1898.

15. D'Souza, F.; Ito, O. Photosensitized Electron Transfer Processes of Nanocarbons Applicable to Solar Cells. *Chem. Soc. Rev.* 2011, **41** (1), 86–96.

16. Barrejón, M.; Arellano, L. M.; D'Souza, F.; Langa, F. Bidirectional Charge-Transfer Behavior in Carbon-Based Hybrid Nanomaterials. *Nanoscale* 2019, **11** (32), 14978–14992.

17. KC, C. B.; D'Souza, F. Design and Photochemical Study of Supramolecular Donor–Acceptor Systems Assembled via Metal–Ligand Axial Coordination. *Coord. Chem. Rev*. 2016, **322**, 104–141.

18. D. Kim, *Multiporphyrin arrays: Fundamentals and applications*, 2012.

19. Canton-Vitoria, R.; Gobeze, H. B.; Blas-Ferrando, V. M.; Ortiz, J.; Jang, Y.; Fernández-Lázaro, F.; Sastre-Santos, Á.; Nakanishi, Y.; Shinohara, H.; D'Souza, F.; Tagmatarchis, N. Excited-State Charge Transfer in Covalently Functionalized MoS2 with a Zinc Phthalocyanine Donor–Acceptor Hybrid. *Angew. Chem. Int. Ed*. 2019, **58** (17), 5712–5717.

20. Misra, R.; Bhattacharyya, S. P. Nonlinear Optical Response of ICT Molecules. Intramolecular Charge Transfer: *Theory and Applications* 2018.

21. May, V.; Kühn, O. *Charge and energy transfer dynamics in molecular systems*, John Wiley & Sons 2008.

22. Gangala, S.; Misra, R. Spiro-Linked Organic Small Molecules as Hole-Transport Materials for Perovskite Solar Cells. *J. Mater. Chem. A* 2018, **6** (39), 18750–18765.

23. Hagfeldt, A.; Boschloo, G.; Sun, L.; Kloo, L.; Pettersson, H. Dye-Sensitized Solar Cells. *Chem. Rev.* 2010, **110** (11), 6595–6663.

24. Sun, L.; Bai, F.-Q.; Zhao, Z.-X.; Zhang, H.-X. Design of New Benzothiadiazole-Based Linear and Star Molecules with Different Functional Groups as Solar Cells Materials: A Theoretical Approach. Solar Energy Materials and Solar Cells 2011, **95** (7), 1800–1810.

25. Rout, Y.; Gautam, P.; Misra, R. Unsymmetrical and Symmetrical Push–Pull Phenothiazines. *J. Org. Chem*. 2017, **82** (13), 6840–6845.

26. Wu, Y.; Zhu, W. Organic Sensitizers from D–π–A to D–A–π–A: Effect of the Internal Electron-Withdrawing Units on Molecular Absorption, Energy Levels and Photovoltaic Performances. *Chem. Soc. Rev*. 2013, **42** (5), 2039–2058.

27. Berezin, M. Y.; Achilefu, S. Fluorescence Lifetime Measurements and Biological Imaging. *Chem. Rev.* 2010, **110** (5), 2641–2684.

28. Kivala, M.; Boudon, C.; Gisselbrecht, J.-P.; Seiler, P.; Gross, M.; Diederich, F. Charge-Transfer Chromophores by Cycloaddition–Retro-Electrocyclization: Multivalent Systems and Cascade Reactions. *Angew. Chem. Int.* Ed. 2007, **46** (33), 6357–6360.

29. Bureš, F. Fundamental Aspects of Property Tuning in Push–Pull Molecules. *RSC Adv.* 2014, **4** (102), 58826–58851.

30. Sailer, M.; Gropeanu, R.-A.; Müller, T. J. J. Practical Synthesis of Iodo Phenothiazines. A Facile Access to Electrophore Building Blocks. *J. Org. Chem.* 2003, **68** (19), 7509–7512.

31. Franz, A. W.; Rominger, F.; Müller, T. J. J. Synthesis and Electronic Properties of Sterically Demanding N-Arylphenothiazines and Unexpected Buchwald−Hartwig Aminations. *J. Org. Chem.* 2008, **73** (5), 1795–1802.

32. Peterson, B. M.; Ren, D.; Shen, L.; Wu, Y.-C. M.; Ulgut, B.; Coates, G. W.; Abruña, H. D.; Fors, B. P. Phenothiazine-Based Polymer Cathode Materials with Ultrahigh Power Densities for Lithium Ion Batteries. *ACS Appl. Energy Mater.* 2018, **1** (8), 3560–3564.

33. Hart, A. S.; K. C., C. B.; Subbaiyan, N. K.; Karr, P. A.; D'Souza, F. Phenothiazine-Sensitized Organic Solar Cells: Effect of Dye Anchor Group Positioning on the Cell Performance. *ACS Appl. Mater. Interfaces* 2012, **4** (11), 5813–5820.

34. Tancini, F.; Monti, F.; Howes, K.; Belbakra, A.; Listorti, A.; Schweizer, W. B.; Reutenauer, P.; Alonso-Gómez, J.-L.; Chiorboli, C.; Urner, L. M.; Gisselbrecht, J.-P.; Boudon, C.; Armaroli, N.; Diederich, F. Cyanobuta-1,3-Dienes as Novel Electron Acceptors for Photoactive Multicomponent Systems. *Chem. Eur. J.* 2014, **20** (1), 202–216.

35. Gotfredsen, H.; Neumann, T.; Storm, F. E.; Muñoz, A. V.; Jevric, M.; Hammerich, O.; Mikkelsen, K. V.; Freitag, M.; Boschloo, G.; Nielsen, M. B. Donor−Acceptor-Functionalized Subphthalocyanines for Dye-Sensitized Solar Cells. *ChemPhotoChem* 2018, **2** (11), 976–985.

36. Michinobu, T.; Diederich, F. The [2+2] Cycloaddition-Retroelectrocyclization (CA-RE) Click Reaction: Facile Access to Molecular and Polymeric Push-Pull Chromophores. *Angew. Chem. Int. Ed*. 2018, **57** (14), 3552–3577.

37. Philippe, C.; Bui, A. T.; Beau, M.; Bloux, H.; Riobé, F.; Mongin, O.; Roisnel, T.; Cordier, M.; Paul, F.; Lemiègre, L.; Trolez, Y. Synthesis and Photophysical Properties of 1,1,4,4-Tetracyanobutadienes Derived from Ynamides Bearing Fluorophores. *Chem. Eur. J*. 2022, **28** (23), e202200025.

38. Philippe, C.; Coste, M.; Bretonnière, Y.; Lemiègre, L.; Ulrich, S.; Trolez, Y. Quadruple Functionalization of a Tetraphenylethylene Aromatic Scaffold with Ynamides or Tetracyanobutadienes: Synthesis and Optical Properties. *Eur. J. Org. Chem*. 2022, e202200049.

39. Bui, A. T.; Philippe, C.; Beau, M.; Richy, N.; Cordier, M.; Roisnel, T.; Lemiègre, L.; Mongin, O.; Paul, F.; Trolez, Y. Synthesis, Characterization and Unusual near-Infrared Luminescence of 1,1,4,4-Tetracyanobutadiene Derivatives. *Chem. Commun*. 2020, **56** (24), 3571–3574.

40. Pokladek, Z.; Ripoche, N.; Betou, M.; Trolez, Y.; Mongin, O.; Olesiak-Banska, J.; Matczyszyn, K.; Samoc, M.; Humphrey, M. G.; Blanchard-Desce, M.; Paul, F. Linear Optical and Third-Order Nonlinear Optical Properties of Some Fluorenyl- and Triarylamine-Containing Tetracyanobutadiene Derivatives. *Chem. Eur. J.* 2016, **22** (29), 10155–10167.

41. Gopinath, A.; Manivannan, N.; Mandal, S.; Mathivanan, N.; Nasar, A. S. Substituent Enhanced Fluorescence Properties of Star α-Cyanostilbenes and Their Application in Bioimaging. *J. Mater. Chem. B* 2019, **7** (39), 6010–6023.

42. Kivala, M.; Boudon, C.; Gisselbrecht, J.-P.; Seiler, P.; Gross, M.; Diederich, F. Charge-Transfer Chromophores by Cycloaddition–Retro-Electrocyclization: Multivalent Systems and Cascade Reactions. *Angew. Chem. Int. Ed.* 2007, **46** (33), 6357–6360.

43. Sekita, M.; Ballesteros, B.; Diederich, F.; Guldi, D. M.; Bottari, G.; Torres, T. Intense Ground-State Charge-Transfer Interactions in Low-Bandgap, Panchromatic Phthalocyanine–Tetracyanobuta-1,3-Diene Conjugates. *Angew. Chem.* 2016, **128** (18), 5650–5654.

44. Shoji, T.; Ito, S. Azulene-Based Donor–Acceptor Systems: Synthesis, Optical, and Electrochemical Properties. *Chem. Eur. J.* 2017, **23** (66), 16696–16709.

45. Simón Marqués, P.; Castán, J. M. A.; Raul, B. A. L.; Londi, G.; Ramirez, I.; Pshenichnikov, M. S.; Beljonne, D.; Walzer, K.; Blais, M.; Allain, M.; Cabanetos, C.; Blanchard, P. Triphenylamine/Tetracyanobutadiene-Based π-Conjugated Push–Pull Molecules End-Capped with Arene Platforms: Synthesis, Photophysics, and Photovoltaic Response. *Chem. Eur. J.* 2020, **26** (69), 16422–16433.

46. Winterfeld, K. A.; Lavarda, G.; Guilleme, J.; Sekita, M.; Guldi, D. M.; Torres, T.; Bottari, G. Subphthalocyanines Axially Substituted with a Tetracyanobuta-1,3-Diene–Aniline Moiety: Synthesis, Structure, and Physicochemical Properties. *J. Am. Chem. Soc.* 2017, **139** (15), 5520–5529.

47. Winterfeld, K. A.; Lavarda, G.; Guilleme, J.; Guldi, D. M.; Torres, T.; Bottari, G. Subphthalocyanine–Tetracyanobuta-1,3-Diene–Aniline Conjugates: Stereoisomerism and Photophysical Properties. *Chem. Sci.* 2019, **10** (48), 10997–11005.

48. Bui, A. T.; Philippe, C.; Beau, M.; Richy, N.; Roisnel, T.; Lemiègre, L.; Mongin, O.; Paul, F.; Trolez, Y. Synthesis, Characterization and Unusual near-Infrared Luminescence of 1,1,4,4-Tetracyanobutadiene Derivatives. *Chem. Commun.* 2020, **56** (24), 3571–3574.

49. Gotfredsen, H.; Neumann, T.; Storm, F. E.; Muñoz, A. V.; Jevric, M.; Hammerich, O.; Mikkelsen, K. V.; Freitag, M.; Boschloo, G.; Nielsen, M. B. Donor−Acceptor-Functionalized Subphthalocyanines for Dye-Sensitized Solar Cells. *ChemPhotoChem* 2018, **2** (11), 976–985.

50. Gotfredsen, H.; Neumann, T.; Storm, F. E.; Muñoz, A. V.; Jevric, M.; Hammerich, O.; Mikkelsen, K. V.; Freitag, M.; Boschloo, G.; Nielsen, M. B. Donor−Acceptor-Functionalized Subphthalocyanines for Dye-Sensitized Solar Cells. *ChemPhotoChem* 2018, **2** (11), 976–985.

51. Gautam, P.; Misra, R.; Thomas, M. B.; D'Souza, F. Ultrafast Charge-Separation in Triphenylamine-BODIPY-Derived Triads Carrying Centrally Positioned, Highly Electron-Deficient, Dicyanoquinodimethane or Tetracyanobutadiene Electron-Acceptors. *Chem. Eur. J.* 2017, 23 (38), 9192–9200.

52. Sharma, R.; Thomas, M. B.; Misra, R.; D'Souza, F. Strong Ground- and Excited-State Charge Transfer in C3-Symmetric Truxene-Derived Phenothiazine-Tetracyanobutadine and Expanded Conjugates. *Angew. Chem.* 2019, **131** (13), 4394–4399.

53. Rout, Y.; Jang, Y.; Gobeze, H. B.; Misra, R.; D'Souza, F. Conversion of Large-Bandgap Triphenylamine–Benzothiadiazole to Low-Bandgap, Wide-Band Capturing Donor–Acceptor Systems by Tetracyanobutadiene and/or Dicyanoquinodimethane Insertion for Ultrafast Charge Separation. *J. Phys. Chem. C* 2019, **123** (38), 23382–23389.

54. Poddar, M.; Jang, Y.; Misra, R.; D'Souza, F. Excited-State Electron Transfer in 1,1,4,4-Tetracyanobuta-1,3-Diene (TCBD)- and Cyclohexa-2,5-Diene-1,4-Diylidene-Expanded TCBD-Substituted BODIPY-Phenothiazine Donor–Acceptor Conjugates. *Chem. Eur. J.* 2020, **26** (30), 6869–6878.

55. Pinjari, D.; Alsaleh, A. Z.; Patil, Y.; Misra, R.; D'Souza, F. Interfacing High-Energy Charge-Transfer States to a Near-IR Sensitizer for Efficient Electron Transfer upon Near-IR Irradiation. *Angew. Chem. Int. Ed.* 2020, **59** (52), 23697–23705.

56. Yadav, I. S.; Alsaleh, A. Z.; Misra, R.; D'Souza, F. Charge Stabilization via Electron Exchange: Excited Charge Separation in Symmetric, Central Triphenylamine Derived, Dimethylaminophenyl–Tetracyanobutadiene Donor–Acceptor Conjugates. *Chem. Sci.* 2021, **12** (3), 1109–1120.

57. Jang, Y.; Rout, Y.; Misra, R.; D'Souza, F. Symmetric and Asymmetric Push–Pull Conjugates: Significance of Pull Group Strength on Charge Transfer and Separation. *J. Phys. Chem. B* 2021, **125** (16), 4067–4075.

58. Khan, F.; Jang, Y.; Patil, Y.; Misra, R.; D'Souza, F. Photoinduced Charge Separation Prompted Intervalence Charge Transfer in a Bis(Thienyl)Diketopyrrolopyrrole Bridged Donor-TCBD Push-Pull System. *Angew. Chem. Int. Ed*. 2021, **60** (37), 20518–20527.

59. Shinde, J.; Thomas, M. B.; Poddar, M.; Misra, R.; D'Souza, F. Does Location of BF2-Chelated Dipyrromethene (BODIPY) Ring Functionalization Affect Spectral and Electron Transfer Properties? Studies on α-, β-, and Meso-Functionalized BODIPY-Derived Donor–Acceptor Dyads and Triads. *J. Phys. Chem. C* 2021, **125** (43), 23911–23921.

60. Sekaran, B.; Dawson, A.; Jang, Y.; MohanSingh, K. V.; Misra, R.; D'Souza, F. Charge-Transfer in Panchromatic Porphyrin-Tetracyanobuta-1,3-Diene-Donor Conjugates: Switching the Role of Porphyrin in the Charge Separation Process. *Chem. Eur. J.* 2021, **27** (57), 14335–14344.

61. Yadav, I. S.; Jang, Y.; Rout, Y.; Thomas, M. B.; Misra, R.; D'Souza, F. Near-IR Intramolecular Charge Transfer in Strongly Interacting Diphenothiazene-TCBD and Diphenothiazene-DCNQ Push-Pull Triads. *Chem. Eur. J.* 2022, **28** (25), e202200348.

62. Misra, R.; Maragani, R.; Gautam, P.; Mobin, S. M. Tetracyanoethylene Substituted Triphenylamine Analogues. *Tet. Letts.* 2014, **55** (51), 7102–7105.

63. Frisch, M. J.; Trucks, G. W.; Schlegel, H. B.; Scuseria, G. E.; Robb, M. A.; Cheeseman, J. R.; Scalmani, G.; Barone, V.; Mennucci, B.; Petersson, G. A.; Nakatsuji, H.; Caricato, M.; Li, X.; Hratchian, H. P.; Izmaylov, A. F.; Bloino, J.; Zheng, G.; Sonnenberg, J. L.; Hada, M.; Ehara, M.; Toyota, K.; Fukuda, R.; Hasegawa, J.; Ishida, M.; Nakajima, T.; Honda, Y.; Kitao, O.; Nakai, H.; Vreven, T.; Montgomery, J. A., Jr.; Peralta, J. E.; Ogliaro, F.; Bearpark, M.; Heyd, J. J.; Brothers, E.; Kudin, K. N.; Staroverov, V. N.; Kobayashi, R.; Normand, J.; Raghavachari, K.; Rendell, A.; Burant, J. C.; Iyengar, S. S.; Tomasi, J.; Cossi, M.; Rega, N.; Millam, N. J.; Klene, M.; Knox, J. E.; Cross, J. B.; Bakken, V.; Adamo, C., Jaramillo, J.; Gomperts, R.; Stratmann, R. E.; Yazyev, O.; Austin, A. J.; Cammi, R.; Pomelli, C.; Ochterski, J. W.; Martin, R. L.; Morokuma, K.; Zakrzewski, V. G.; Voth, G. A.; Salvador, P.; Dannenberg, J. J.; Dapprich, S.; Daniels, A. D.; Farkas, O.; Foresman, J. B.; Ortiz, J. V.; Cioslowski, J.; Fox, D. J. Gaussian 09, Revision A.02; Gaussian, Inc., Wallingford, CT, 2009.

64. Rehm, D.; Weller, A. Kinetics of Fluorescence Quenching by Electron and H-Atom Transfer. *Isr. J. Chem*. 1970, **8** (2), 259–271.

65. Snellenburg, J. J.; Laptenok, S.; Seger, R.; Mullen; K. M.; van Stokkum, I. H. Glotaran: A Java-based graphical user interface for the R package TIMP. *J. Stat. Softw*. 2012, **49**, 1-22.

66. http://glotaran.org/

CHAPTER 5

EXCITATION WAVELENGTH-DEPENDENT CHARGE STABILIZATION IN HIGHLY INTERACTING PHENOTHIAZINE SULFONE-DERIVED DONOR-ACCEPTOR CONSTRUCTS*

5.1 Introduction

Following the early events occurring in natural photosynthesis,[1] the study of artificial photosynthetic multi-modular DA constructs[2-9] has played a prominent role in the production of π-conjugated systems useful for a range of applications in energy harvesting, organic electronics, and photonics.[9-18] In this context, close proximity and high exergonicity of DA constructs can be utilized to facilitate intramolecular charge transfer (ICT) and fine-tuning of the optical and excited-state properties,[19-20] however, excited state CS and charge recombination (CR) processes in such systems occur rapidly, making them less appealing in light energy harvesting applications. In synthetic artificial photosynthetic systems, long-lived CSS is often achieved by optimal positioning of the donor and acceptor systems and by following a multi-step sequential electron transfer mechanism.[21-26] In a few instances, heavy atom-bearing triplet sensitizers have also been used,[27-28] however, such strategy in the directly connected highly interacting DA constructs has been nonexistent.

The TCBD and exTCBD-based directly connected DA push-pull systems[29-30] show strong ICT covering absorption in the visible and near IR regions, that is, exhibiting optical properties of black absorbers. Photosensitizers such as porphyrins, phthalocyanines, subphthalocyanines,

* This chapter is reproduced from Sheokand, Manju, Ajyal Z Alsaleh, Francis D'Souza, and Rajneesh Misra. "Excitation Wavelength-Dependent Charge Stabilization in Highly Interacting Phenothiazine Sulfone-Derived Donor–Acceptor Constructs," The Journal of Physical Chemistry B 127, no. 12 (2023): 2761-73, with permission from the American Chemical Society.

BODIPYs, azaBODIPYs, triphenylamine, phenothiazine, and diketopyrrolopyrroles have been used in these constructions to extend the optical coverage into the visible and near-IR region.[31-49]

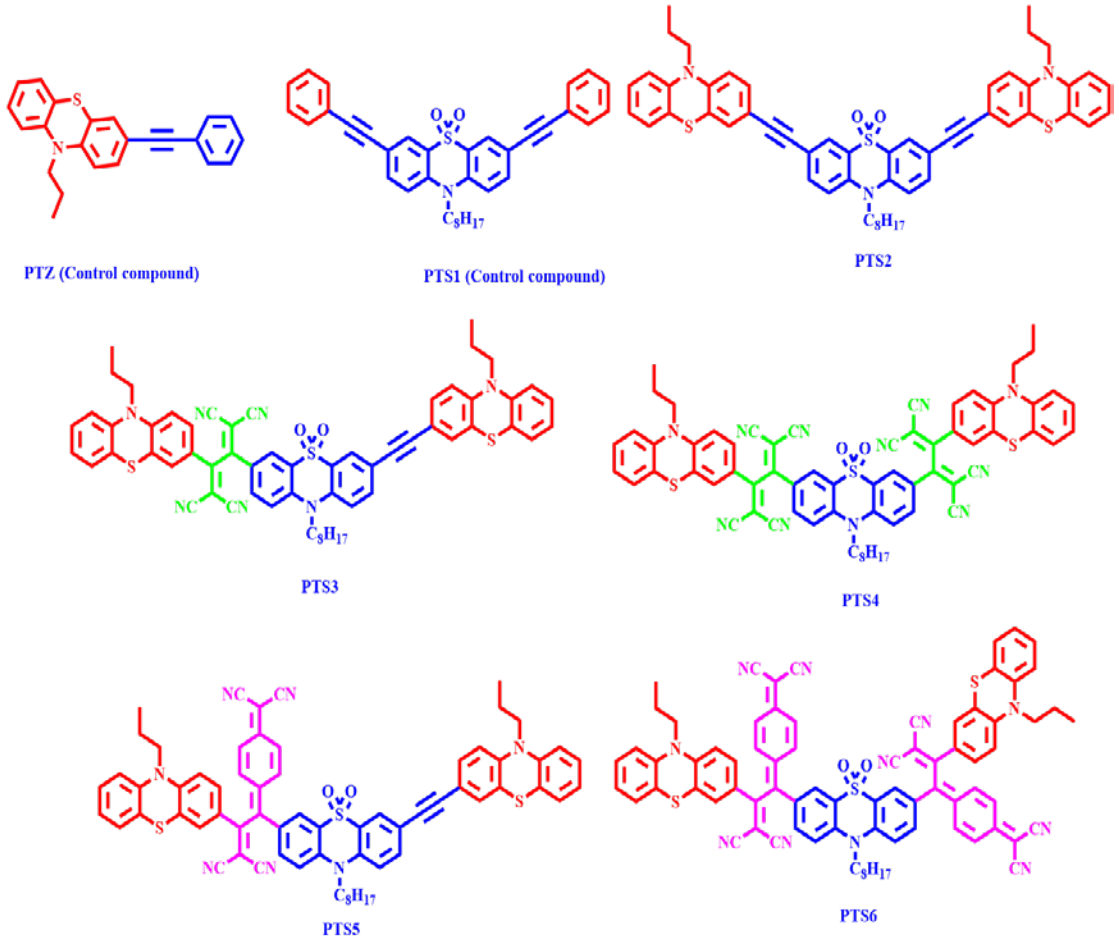

Figure 5.1: The molecular structures of phenothiazine sulfone-based push-pull constructs.

Sadly, owing to close proximity and high exergonicity, the excited state CS and CR in these systems occurred within a few picoseconds.[31-50] Extending the lifetime of the CSS in these systems thus far has been a challenge. In the present study, we have overcome this issue by designing multi-modular DA systems derived from a bis-phenothiazine-phenothiazine sulfone (PTZ-PTZSO$_2$-PTZ, PTS2 in Fig. 5.1) scaffold. Introducing TCBD and exTCBD into PTS2 (PTS3–PTS6 in Fig. 5.1) modulates the energy levels of the DA constructs in such a way that the charge transfer process can be initiated from the ^{3}PTZ* state[50] when they are excited at wavelengths corresponding to the

locally excited (LE) states. Owing to the spin-forbidden CR process, long-lived CSSs are observed. Interestingly, when the molecules are excited at the ICT peak positions, the CSS of the singlet character reveals ultrafast CR (spin allowed process) without prolonging its lifetime. This study has provided us with an opportunity to modulate the kinetics of electron transfer to secure the much-desired long-lived CSSs as a function of excitation wavelength in highly interacting DA constructs.

5.2 Synthesis

PTS2 bearing two terminal PTZ units and a central $PTZSO_2$ was synthesized as the starting material for introducing TCBD and exTCBD entities. The synthesis of PTS2 was carried out *via* the Pd-catalyzed Sonogashira cross-coupling reaction of dibromo-substituted phenothiazine sulfone 1 with 2.2 equivalent of ethynyl phenothiazine 2 in THF/TEA (1:1) solvent at 70 ºC for 12 h. Following purification by column chromatography, PTS2 was obtained with 76% yield (Scheme 5.1). The starting compounds, bromo-substituted $PTZSO_2$, 1 and ethynyl phenothiazine, 2 were synthesized using reported procedures.[51] A control compound, PTZ-control, with phenyl rings as the end-capping unit has also been synthesized.

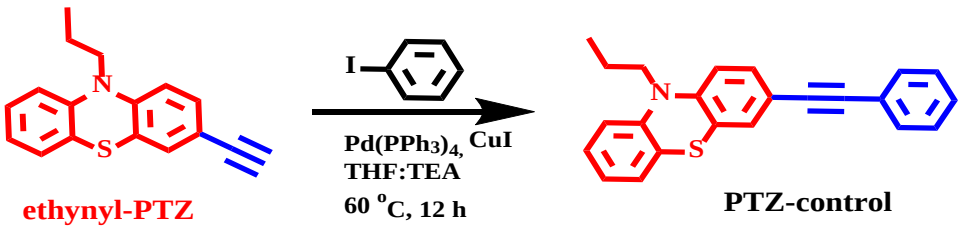

Scheme 5.1: Synthetic scheme of PTZ-control compound.

The TCBD and exTCBD featured phenothiazine sulfone DA constructs, PTS3–PTS6, were synthesized *via* the Pd-catalyzed Sonogashira cross-coupling reaction and [2+2] cycloaddition−retroelectrocyclization reaction. Here, we have varied the acceptor from mono-TCBD to bis-TCBD in PTS3–PTS4, and additionally exploited the exTCBD unit from mono-

exTCBD to bis-exTCBD in PTS5–PTS6. The [2 + 2] cycloaddition−retroelectrocyclization reaction[29-30] of chromophore PTS2 with 1.1 equivalent of TCNE in dichloromethane solvent for 24 h at room temperature resulted in unsymmetrical chromophore PTS3 in 56% yield, whereas the reaction of PTS2 with 2.2 equivalent of TCNE resulted in symmetrical chromophore PTS4 in 70% yield. The expanded TCBD functionalized unsymmetrical chromophore PTS5 was synthesized *via* [2 + 2] cycloaddition−retroelectrocyclization reaction of PTS2 with 1.1 equivalent of TCNQ in DCE solvent for 48 h at 120 °C in 48% yield. The reaction of PTS2 with 2.2 equivalent of TCNQ resulted in the expanded TCBD functionalized symmetrical chromophore PTS6 in 56% yield (Scheme 5.2). The synthetic procedure for control compound PTS1 is given in Scheme 5.3.

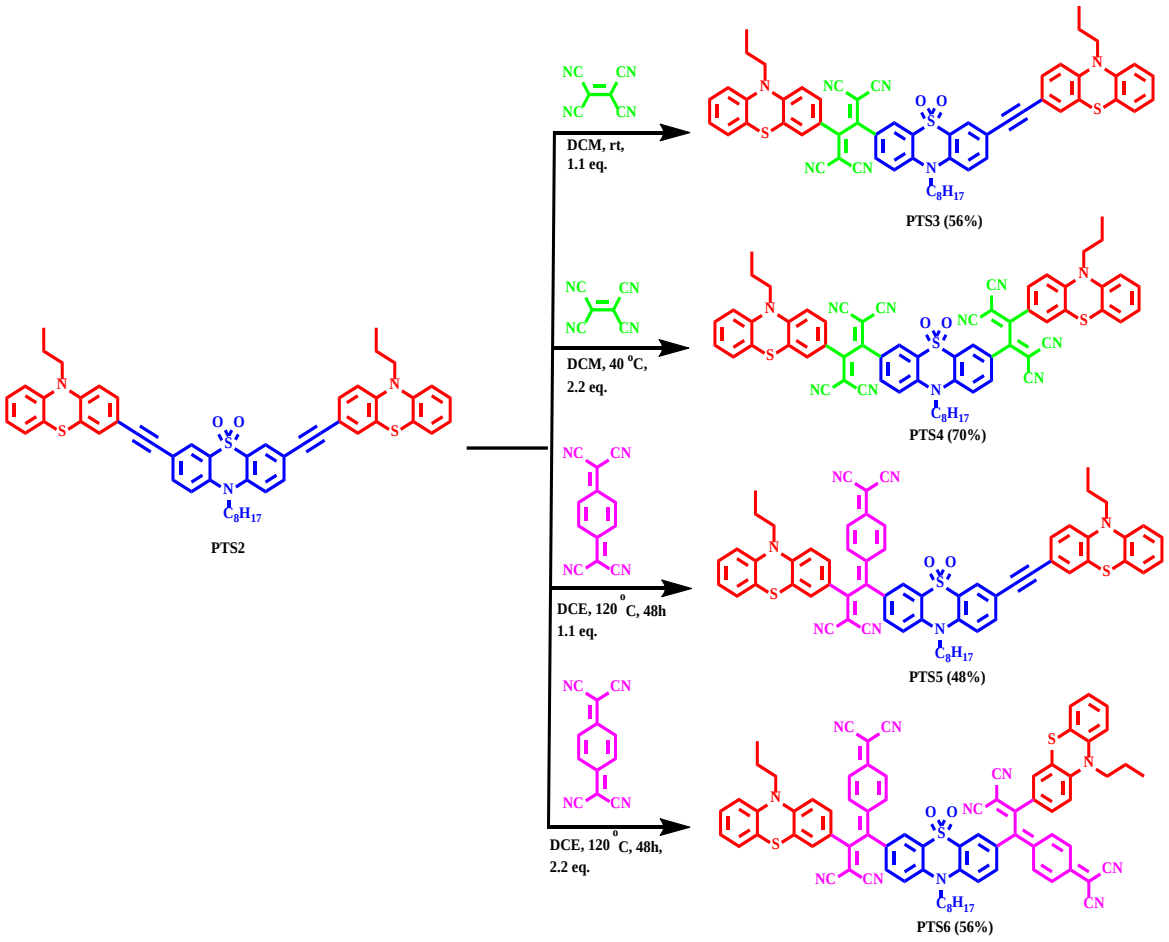

Scheme 5.2: Synthetic route of symmetrical and unsymmetrical PTZSO$_2$-based push-pull PTS3–PTS6.

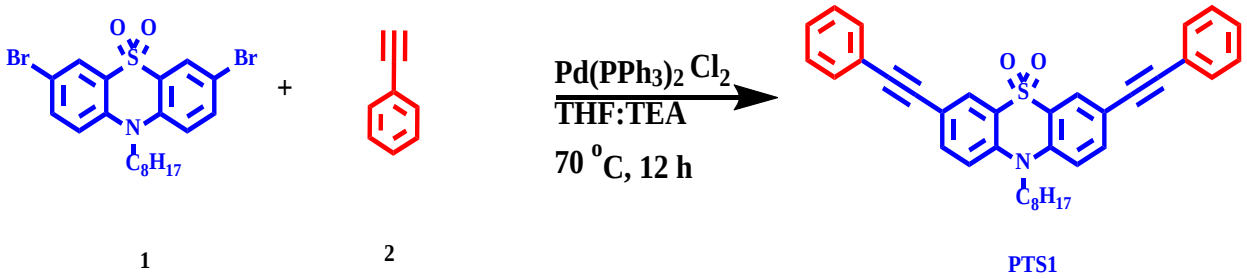

1 2 PTS1

Scheme 5.3: Synthetic route of PTS1.

5.3 Results and Discussion

5.3.1 Absorption Spectra

The optical properties of the PTS1–PTS6 constructs were recorded in dichloromethane as shown in Figure 5.2 and the data are listed in Table 5.1. The absorption spectrum of symmetrical PTS2 shows an absorption band at 389 nm, which is attributed to the π–π* transition. The absorption spectra of TCBD functionalized unsymmetrical and symmetrical chromophores, PTS3 and PTS4 exhibited multiple absorption bands (300−460 nm) in the lower wavelength region attributed to the π–π* electronic transitions. The broad absorption band for PTS3 and PTS4 at the longer wavelength of 570 nm and 546 nm, respectively, is ascribed to the ICT transitions (also known as intramolecular charge polarization) due to the strong D-A push-pull interactions. The symmetrical chromophore PTS4 showed a comparatively broad ICT band compared to the unsymmetrical PTS3 owing to the incorporation of an additional TCBD unit. The chromophores PTS5 and PTS6 incorporated with exTCBD acceptor showed a broad absorption in the longer wavelength region of 550−1000 nm which could be attributed to the ICT transitions and the absorption band around 400 nm in the lower wavelength region to the π–π* electronic transitions. The ICT band of PTS5 and PTS6 was red-shifted by 90–120 nm due to the incorporation of stronger acceptor exTCBD units than the chromophores PTS3 and PTS4 having comparatively weaker TCBD (*vide supra*).

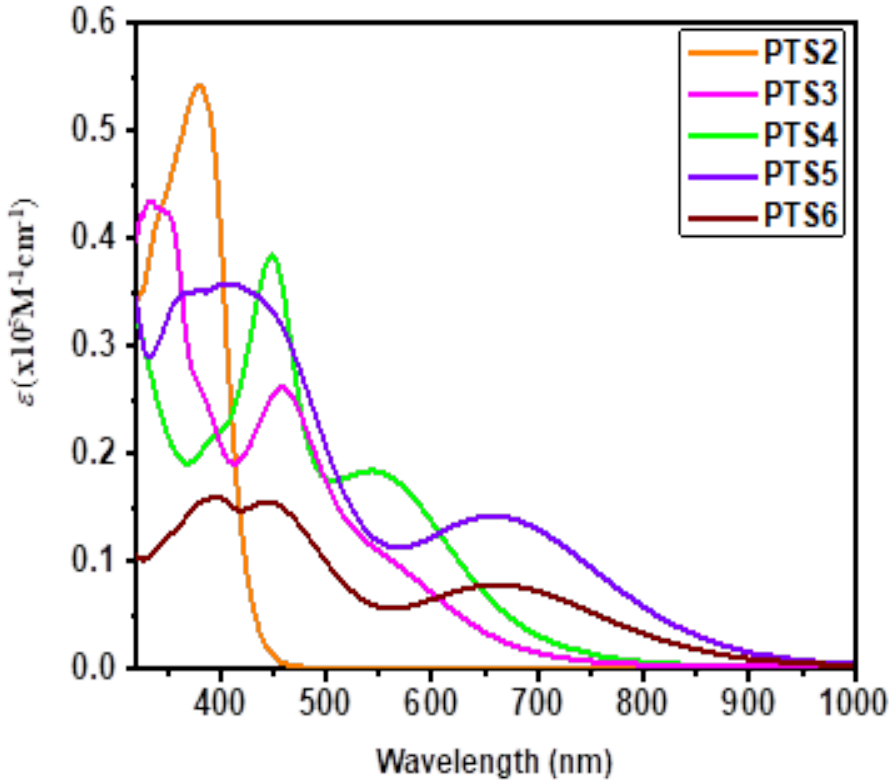

Figure 5.2: Electronic absorption spectra of PTS2–PTS6 donor-acceptor constructs in dichloromethane.

Table 5.1: Photophysical and electrochemical data of chromophores PTS1–PTS6.

Compound	λ_{abs} [nm] $\varepsilon/10^5(M^{-1}cm^{-1})$	HOMO (eV)[a]	LUMO (eV)[a]	ΔE^a	ΔE_g (HOMO–LUMO gap)[b]
PTS2	381 (54140)	−5.06	−2.60	1.81	3.40
PTS3	456 (26140), 570 (10160)	−5.34	−4.15	1.04	2.09
PTS4	450 (38390), 546 (18410)	−5.59	−4.25	1.21	2.05
PTS5	406 (35410), 660 (14240)	−5.31	−4.21	0.98	1.46
PTS6	448 (15570), 663 (7850)	−5.42	−4.23	0.96	1.62

(a) HOMO-LUMO energy gap from electrochemical studies by using cyclic voltammetry. (b) Theoretical energy gap calculated from density functional theory.

5.3.2 Solvatochromism

The effect of solvents of different polarities on the ICT transition of PTS2 was investigated through absorption and emission spectroscopy (Fig. 5.3). The ICT transition is expected to enhance

the dipole moment of the molecule in the excited state resulting in a polarized excited state.[19-20] The reorganization of polar solvent molecules around the polarized excited state results in the stabilization of the excited state which is observed *via* the redshift in the emission spectrum of PTS2 on varying the solvent polarity from non-polar (cyclohexane, toluene) to polar solvent (1,4-dioxane, THF, chloroform, dichloromethane (DCM)). In contrast to the absorption spectra (see Fig. 5.4), the emission spectra of PTS2 exhibit noticeable change due to the formation of a more polarized excited state than the electronic ground states. In the non-polar solvent, *i.e.* cyclohexane, a blue color emission was recorded at 453 nm with a shoulder peak at 479 nm owing to the localized excited (LE) emission. On increasing the solvent polarity from toluene to DCM, the peak corresponding to LE emission was merged into CT emission, and a broad spectrum with emission maxima was recorded at 473 nm (toluene), 475 nm (1,4-dioxane), 483 nm (chloroform), 488 nm (THF), and 497 nm (DCM), respectively. The chromophores PTS3–PTS6 were non-emissive in the solvents of varying polarities as emission gets quenched by the incorporation of TCBD and exTCBD electron acceptor units.

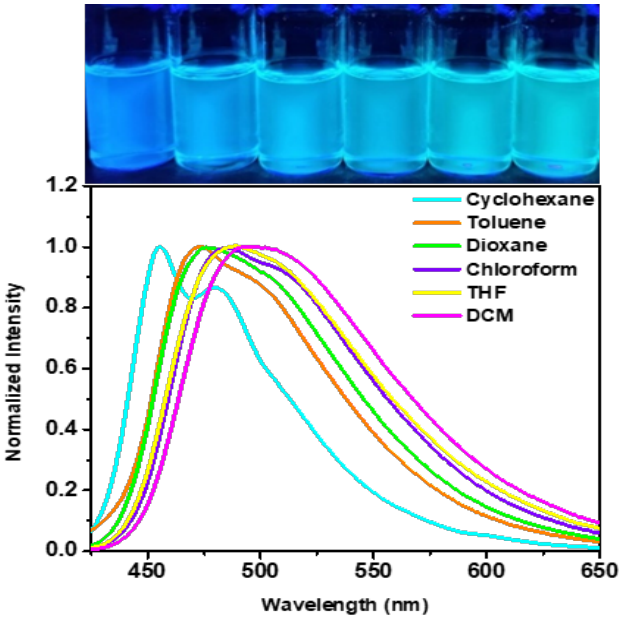

Figure 5.3: The normalized emission spectrum of PTS2 in solvents of varying polarities.

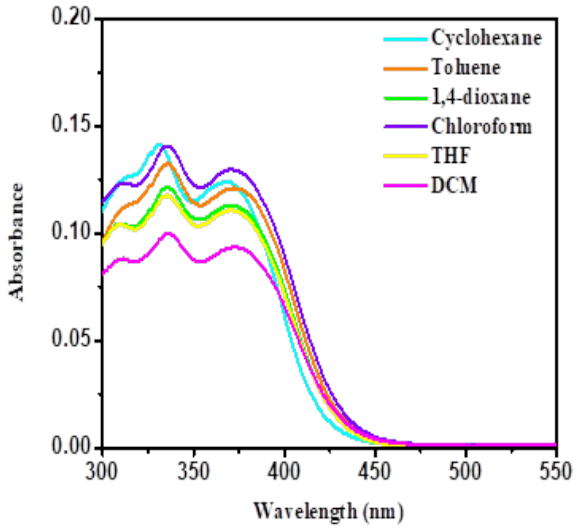

Figure 5.4: Absorption spectrum of PTS2 in solvents of different polarities.

5.3.3 Aggregation-Induced Emission (AIE)

The PTS2 is supposed to exhibit aggregation-induced emission owing to the AIE active butterfly-shaped phenothiazine unit, which shows strong yellow color emission in the solid-state.[52] The PTS2 is readily soluble in DMF and the gradual increase of water fraction in DMF results in the formation of nano-aggregates. The PTS2 exhibits a light yellow color emission at 524 nm in pure DMF. The addition of water up to 30% results in a gradual decrease in the intensity of emission spectra which is attributed to the stabilization of the CT state in the solvent of high polarity. At a 40% water fraction, a new emission peak appeared at 563 nm, which showed a redshift of 39 nm. The enhanced emission at 40% water fraction could be assigned to the formation of nano-aggregates, and the intensity of AIE gradually increases up to 70% water fraction. At high water concentrations, a slight decrease in the emission intensity was observed, which is attributed to the formation of large-sized nano-aggregates, which are less exposed to radiation as compared to smaller aggregates. The AIE behavior was also studied using absorption spectroscopy (Fig. 5.5). The absorption spectra for chromophore PTS2 revealed no significant change up to 60% water

fraction, above which there was a scattering of light or the Mie effect[57] observed due to the formation of nanoaggregates. The AIE behavior of PTS2 is shown in Figure 5.6 under UV illumination. The chromophores PTS3–PTS6 incorporated with TCBD and exTCBD units are not fluorescent in the solid state and were not susceptible to exhibiting AIE behavior.

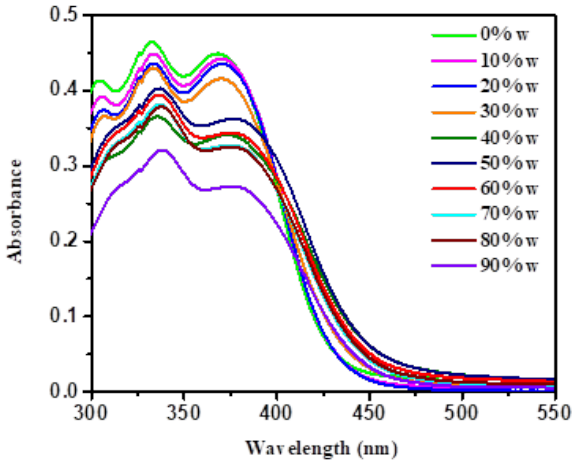

Figure 5.5: Electronic absorption spectra of PTS2 in DMF-water mixtures (0% to 90% water).

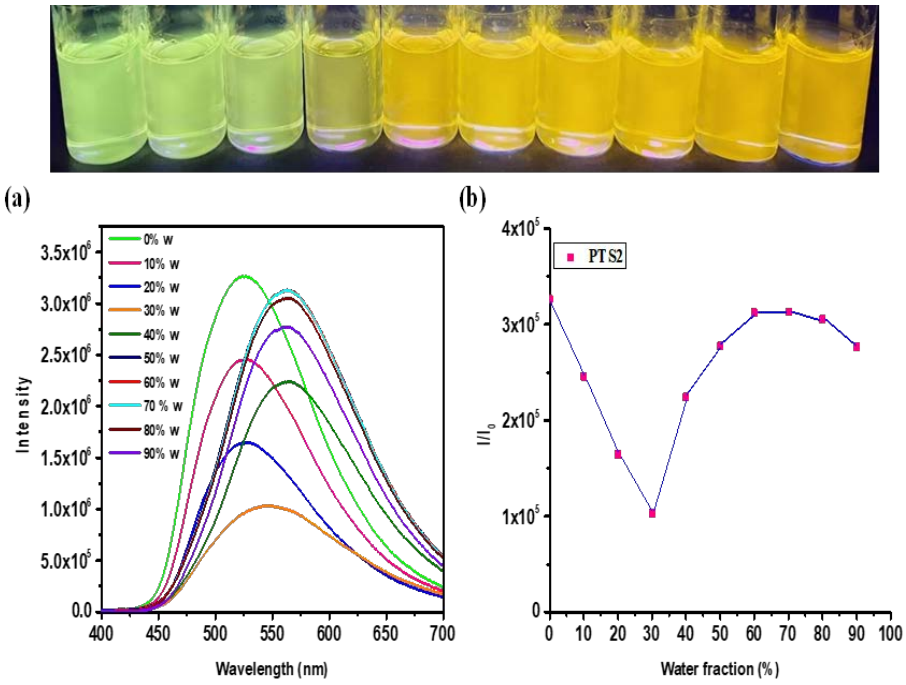

Figure 5.6: (a) Emission spectrum of PTS2 in DMF–water mixtures (0–90% water), and (b) plot of fluorescence intensity vs. % of water fraction (f_w) (PTS2 concentration = 10 µM; intensity was calculated at λ_{max}). The top panel shows a picture of the PTS2 solution in DMF on increasing the addition of water under UV-light illumination.

5.3.4 Mechanochromism

Compound PTS2 was predicted to exhibit mechano-responsive behavior owing to the conformationally flexible butterfly-shaped phenothiazine moiety in the molecular framework.[52-53] The attachment of phenothiazine units *via* triple bond at 3 and 7 positions could enhance the flexibility of donor phenothiazine unit around the central phenothiazine sulfone moiety and promote physical structural change owing to a twisted structure on applying the mechanical stimuli. The pristine form of PTS2 is light orange in color and emits at 568 nm. The application of mechanical grinding of PTS2 resulted in bright yellow emission at 540 nm (Fig. 5.7). The powder X-ray diffraction (PXRD) of PTS2 in the pristine and ground state, shown in Figure 5.8, revealed the amorphous nature of PTS2 in both states and there is no major structural change upon grinding the material.

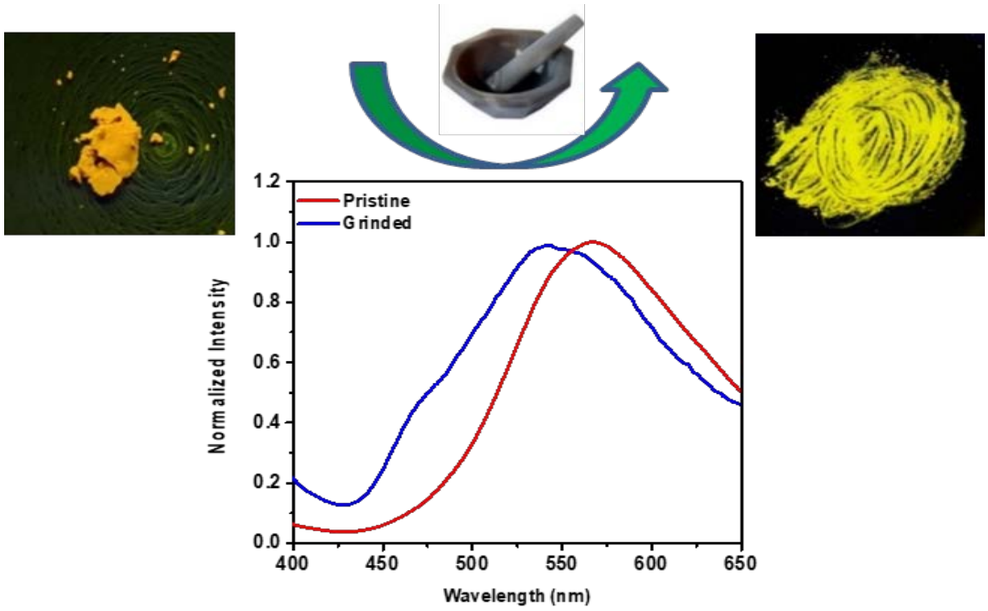

Figure 5.7: Solid state emission of PTS2 in the pristine and milled form.

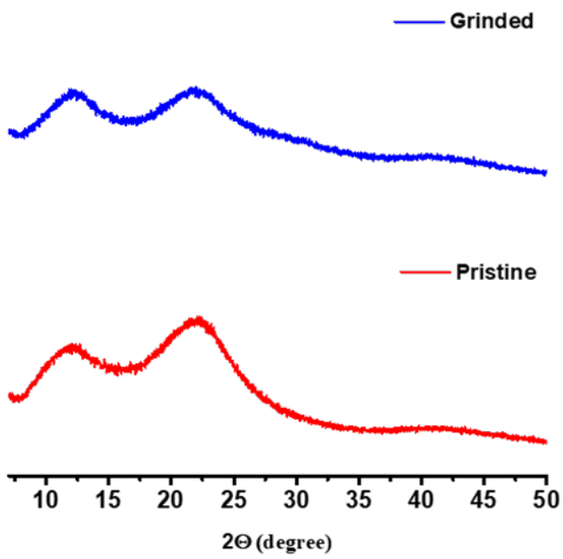

Figure 5.8: PXRD graph of PTS2 in the pristine and grounded state.

5.3.5 Theoretical Studies

The density functional theory (DFT) calculations on PTS2–PTS6 were performed to optimize the molecular geometry and electronic properties using the B3LYP/6-31G** basis set.[54] In order to reduce the computation time, the propyl substituent was used instead of the octyl substituent at the central $PTZSO_2$. The TCBD and exTCBD substituted chromophores PTS3–PTS6 exhibited a non-planar framework owing to the presence of a butterfly-shaped $PTZSO_2$ unit as the central core and additional acceptor TCBD units (Fig. 5.9). The frontier orbitals of PTS2–PTS6 are shown in Figure 5.9. The HOMO energy level in PTS2 is distributed throughout the molecule but the LUMO is concentrated mostly on the $PTZSO_2$ unit with some contributions to the terminal phenothiazine entities. In the unsymmetrical chromophores PTS3 and PTS5, the electron density of the HOMO is mainly concentrated on the terminal PTZ unit with some coefficients on the phenyl ring of the central $PTZSO_2$. In these molecules, the LUMO is predominantly concentrated on the acceptor TCBD unit and extended toward the central $PTZSO_2$ unit. In the case of TCBD functionalized symmetrical chromophores PTS4 and PTS6, the electron density of the HOMO energy levels was mainly concentrated on the terminal donor PTZ unit. The incorporation of additional TCBD or exTCBD in PTS4 and PTS6 tends to increase the acceptor character and the LUMO energy levels were localized on the TCBD unit. The outcomes of the theoretical calculations show excellent intramolecular electronic communication. The electron-withdrawing character of the TCBD/exTCBD acceptor units caused a significant decrease in the HOMO–LUMO energy gap in PTS2–PTS6. The theoretically calculated HOMO–LUMO gaps for PTS2–PTS6 are 3.44, 1.94, 2.19, 1.49, and 1.69 eV, respectively. These values are in good agreement with experimental data calculated from electrochemical studies (*vide supra*). The HOMO–LUMO gap in PTS2–PTS6 follows the order PTS2 > PTS4 > PTS3 > PTS6 > PTS5, which is reflected in

their electronic absorption. The chromophore PTS2 with a high HOMO–LUMO gap has exhibited absorption in the lower wavelength region, whereas the TCBD/exTCBD functionalized PTS3–PTS6 showed red-shifted absorption in the NIR region due to the tuned HOMO–LUMO gap.

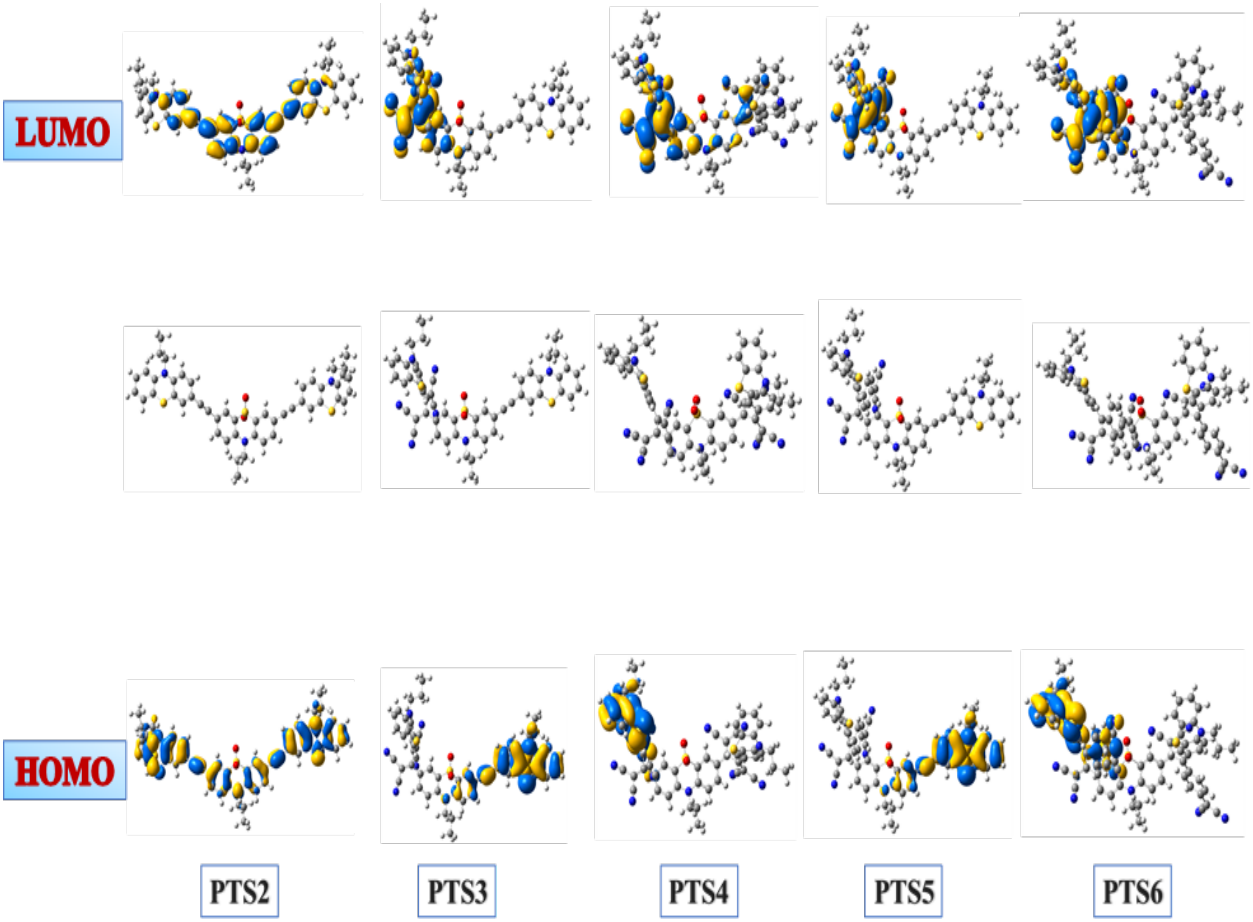

Figure 5.9: Optimized structure, frontier HOMO and LUMO orbitals of PTS2–PTS6.

5.3.6 Electrochemical Studies

The redox properties of chromophores PTS1–PTS6 were evaluated by the means of cyclic voltammetry (CV) in o-dichlorobenzene (DCB) containing 0.1 M $TBA(ClO)_4$ as a supporting electrolyte. The voltammograms are shown in Figure 5.10 and the peak potentials are listed in Table 5.2 while the calculated energy gap (difference between the first oxidation and first reduction) is given in Table 5.2.

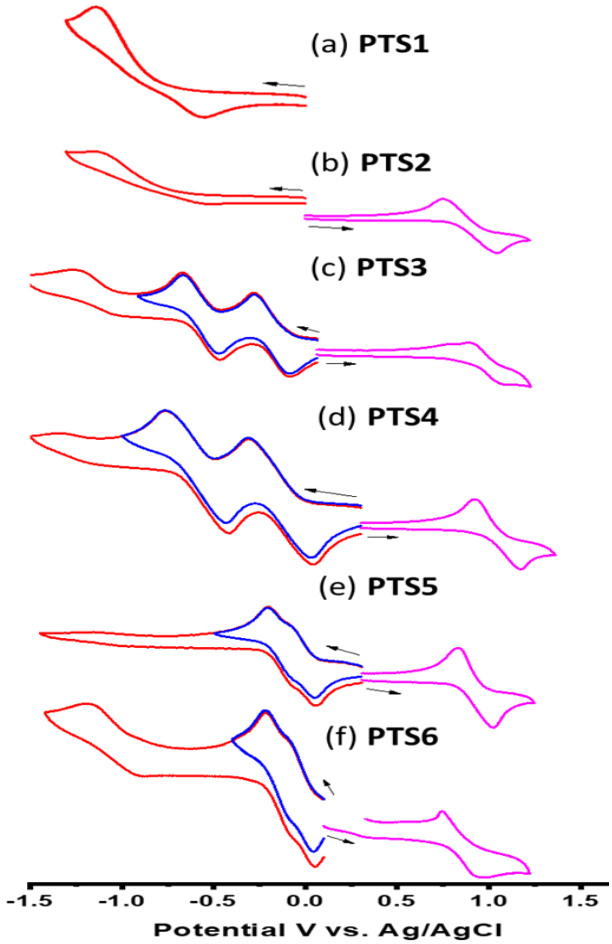

Figure 5.10: Cyclic voltammograms of PTS1–PTS6 recorded in 0-dichlorobenzene, 0.1 M (TBA)ClO_4 at scan rate of 0.1 V s^{-1}.

Table 5.2: Electrochemical peak potentials, measured from differential pulse voltammetry of the investigated compounds in DCB containing 0.1 M (TBA)Cl_4.

Compound	Potential V vs. Ag/AgCl							
	$E_{oxidation}$				$E_{reduction}$			
PTS1				1.63			-0.95	-1.72
PTS2	0.86		1.36	1.80			-0.95	-1.72
PTS3	0.88	1.06	1.47	1.90	-0.16	-0.54	-1.03	-1.75
PTS4		1.07		1.87	-0.14	-0.57	-1.13	-1.72
PTS5	0.95		1.50		-0.03	-0.13	-1.02	-1.72
PTS6	0.95	1.28	0.27		-0.01	-0.13	-1.03	-1.72

PTZ-control with only a PTZ entity revealed oxidation at 0.81 V vs. Ag/AgCl

corresponding to $PTZ^{0/\bullet+}$ process. PTS1 with only a $PTZSO_2$ group revealed a quasi-reversible reduction at -0.95 V vs. Ag/AgCl suggesting it is fairly electron-deficient due to the sulfone group. Irreversible oxidation at E_{pa} = 1.63 V was also observed. The oxidations of PTZ entities in PTS2 were located at 0.86 and 1.36 V while the reduction corresponding to the central $PTZSO_2$ was at -0.95 V. The electron donor role of PTZ and acceptor role of $PTZSO_2$ in PTS2 is thus born out. In the cases of PTS3 and PTS4, with one and two entities of TCBDs, additional cathodic processes corresponding to TCBD reductions were observed. In PTS3, two reductions at -0.16 and -0.54 V corresponding to $TCBD^{0/\cdot-}$ and $TCBD^{\cdot-/2-}$ were witnessed while the PTZ oxidation was slightly anodically shifted and appeared at 0.88 and 1.06 V. The first oxidation was due to the PTZ entity far from TCBD and the second peak was due to PTZ close to TCBD. An anodic shift of about 180 mV in the latter process is due to the electronic effect induced by the neighboring TCBD entity. In the case of PTS4, although the TCBD reductions appeared to have almost the same potential, the PTZ oxidation appeared as a single peak at 1.07 V as both PTZ entities were close to TCBD. In the case of PTS5 and PTS6, having one and two entities of exTCBDs, reductions corresponding to the exTCBD occurred at much lower potentials compared to that observed for TCBD in PTS3 and PTS4. The first two reductions of exTCBD in PTS5 were located at -0.03 and -0.13 V and oxidation at 0.95 V corresponding to PTZ entities (overlap of two anodic waves) were observed. A similar trend was also observed for PTS6. In this case, exTCBD reductions were at -0.01 and -0.13 V, and the first oxidation corresponding to phenothiazine was at 0.90 V. The electrochemical redox gap, ΔE, followed the order: PTS6 < PTS5 < PTS3 < PTS4 < PTS2. This trend agrees well with the optical coverage of these compounds displayed in Figure 5.2.

5.3.7 Energy Consideration for Excited-State Electron Transfer

In benzonitrile (solvent used in photochemical studies), PTS2, absorption, and

fluorescence peak maxima were located at 370 and 500 nm, respectively, not significantly different from that observed in DCB, from which an $E_{0,0}$ value of 2.90 eV was calculated. The phosphorescence spectrum of PTS1 is shown in Figure 5.11. Triplet emission at 520 nm was observed from which energy of the triplet state, E_T = 2.38 eV was obtained. The singlet lifetime of PTS2, from the time-correlated single-photon counting (TCSPC) technique, was found to be 4.6 ns which was smaller than that of PTS1 being 5.8 ns (both monoexponential decays), suggesting the occurrence of excited state events in PTS2 (see Fig. 5.12 for decay curves).

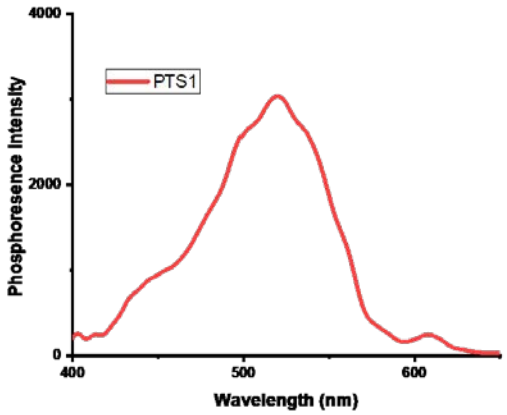

Figure 5.11: **The phosphorescence spectrum of PTS1 at liquid nitrogen temperature in O_2-free toluene.**

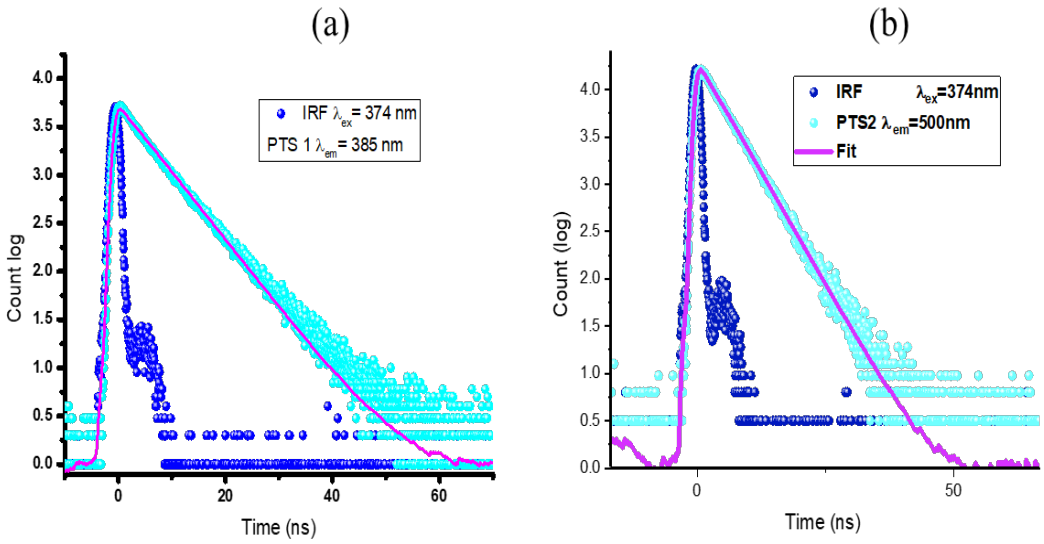

Figure 5.12: Fluorescence decay curves of (a) PTS1 and (b) PTS2.

The absorption and emission spectra of PTZ-control are shown in Figure 5.13. Absorption peak maxima at 349 nm, fluorescence peak maxima at 460 nm, and phosphorescence (at liquid nitrogen temperature) at 532 nm was observed. The singlet lifetime of PTZ-control from the TCSPC technique revealed a monoexponential decay with a lifetime of 5.09 ns. From the phosphorescence peak maxima, triplet energy for $^{3}PTZ^{*}$ was calculated to be 2.32 eV. In order to visualize the possibility of excited-state charge transfer, using the optical, computational, and redox data, energy level diagrams were established. Free-energy of charge separation and charge recombination was estimated using the Rehm-Weller approach.[55] Figure 5.14 (a and b), respectively show the energy level diagrams of PTS2, and TCBD-derived systems (PTS3 and PTS4), while Figure 5.15 shows exTCBD-derived systems (PTS5 and PTS6).

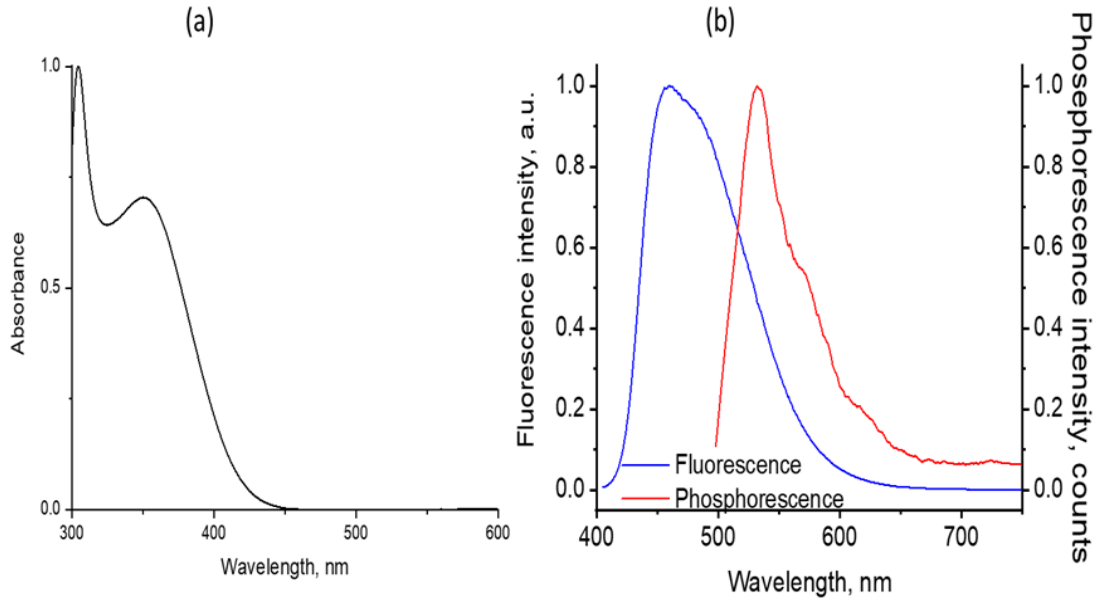

Figure 5.13: (a) Absorption and (b) emission spectra (λ_{ex} = 349 nm) of PTZ-control in benzonitrile. The phosphorescence was recorded at liquid nitrogen temperature in O_2-free toluene.

As shown in Figure 5.14a, in the case of the quadrupolar PTS2 system comprised of two PTZ electron donors and one $PTZSO_2$ electron acceptor, photoinduced electron transfer (PET) from both singlet and triplet excited states yielding $PTZ^{\bullet+}$- $PTZSO_2^{\bullet-}$-PTZ charge-separated state

in benzonitrile is thermodynamically possible. The relatively high energy of $^{3}PTZ^{*}$ (2.32 eV) or $^{3}PTZSO_2^{*}$ (2.38 eV) formed from the intersystem crossing of the respective singlet excited states was realized to be an important contributor. If electron transfer indeed originates from the $^{3}PTZ^{*}$ or $^{3}PTZSO_2^{*}$ then the charge-separated state would also be a triplet state. Under such circumstances, charge recombination would be a slow process as this is a spin-forbidden process. Relatively long-lived charge-separated states could be anticipated from such a process.

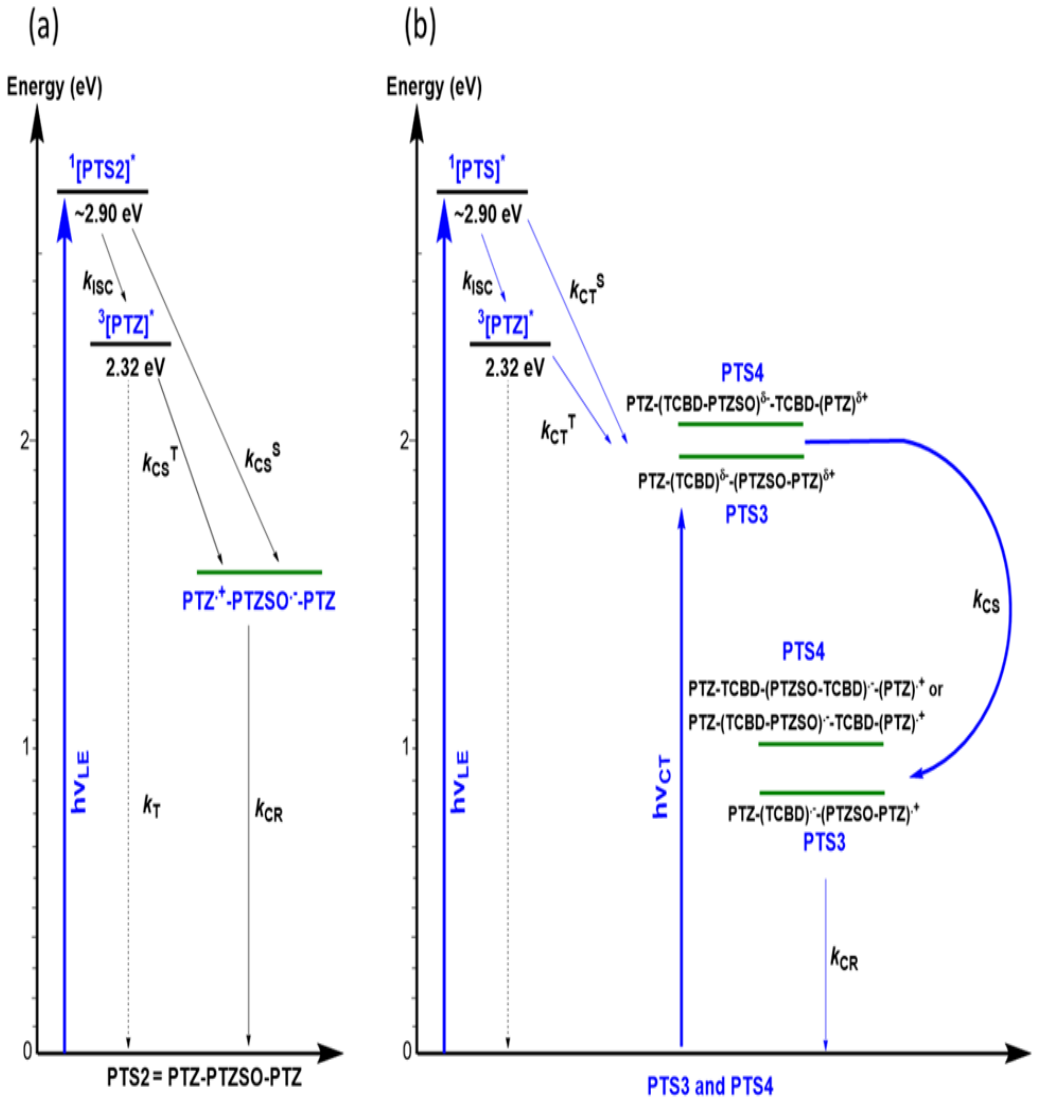

Figure 5.14: Energy level diagrams showing different photochemical events in (a) PTS2 triad and (b) TCBD bearing systems under local excitation (LE) and charge transfer (CT) peak positions (see text for details). Note - Excitation of PTS3 and PTS4 corresponding to their CT would produce their singlet excited states, not shown for brevity.

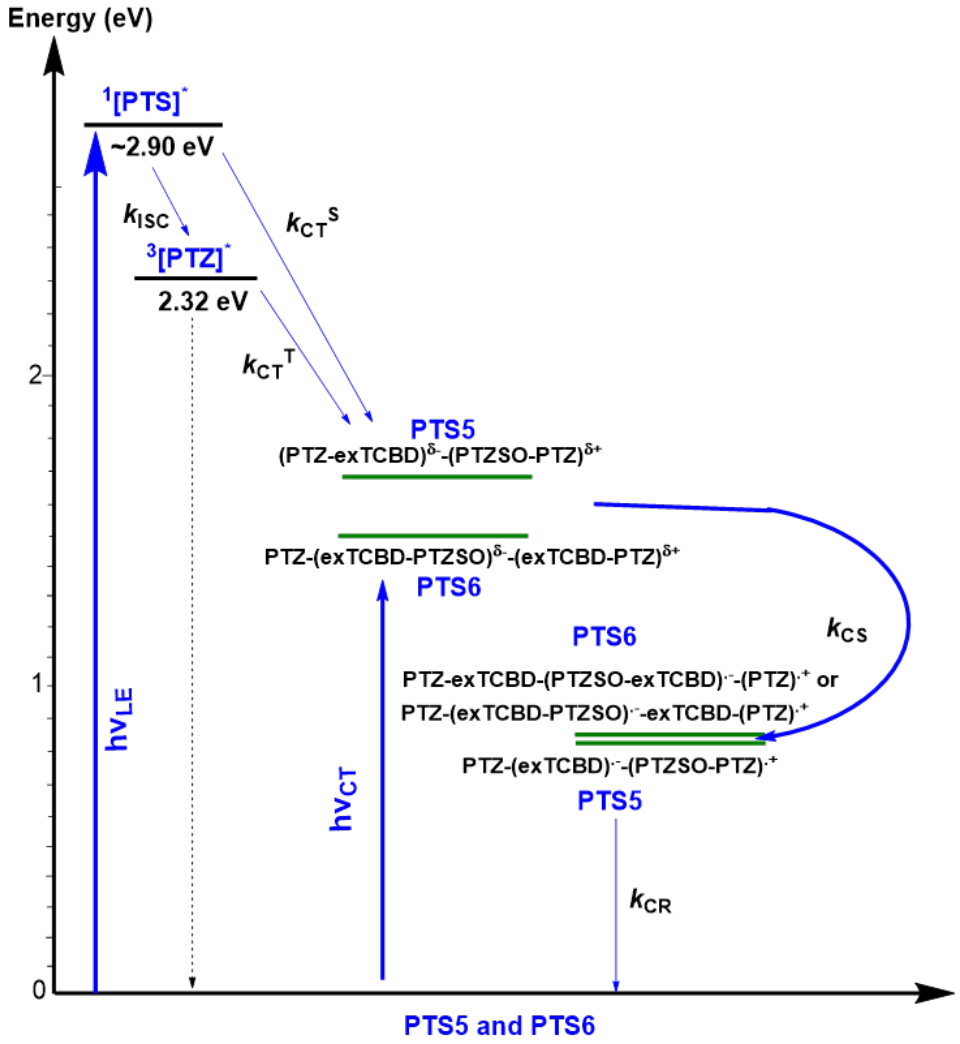

Figure 5.15: Energy level diagram showing different photochemical events in PTS5 and PTS6 upon excitation corresponding to LE and CT peak positions. Excitation of PTS5 and PTS6 corresponding to their CT would produce their singlet excited states, not shown for brevity.

The energy diagrams for systems showing strong charge transfer events are shown in Figures 5.14b and 5.15. From the earlier discussed optical data, two types of excitation processes, viz., local excitation (LE) and charge transfer (CT), are possible in both TCBD and exTCBD possessing systems. The energy of the CT state evaluated from computational results (energy difference between HOMO and LUMO levels) and CS state from the traditional Rehm-Weller approach (including the energy of solvation from the Dielectric continuum model)[49] are utilized in the construction of these diagrams. It is important to note that both E_{CT} and E_{CS} are well-below

those of both E_S and E_T energies under the conditions of LE excitation. Under such circumstances, $^3PTZ^*$ formed upon intersystem crossing (ISC) of $^1PTZ^*$ can be involved in the CT and CS processes resulting in the radical ion-pair formation of triplet character. However, when these systems are excited at longer wavelengths corresponding to CT peak maxima, the E_{CT} would be much lower than either E_{CT} or E_{CS} states. If ET occurs, the resulting CS product will be of singlet character, and under such circumstances, faster CR to the ground state could be expected due to the singlet nature of the product, lowering the overall lifetime of the CSS. Importantly, due to the high exergonicity of the CS events, much faster electron transfer events could also be anticipated. It may be mentioned here that in a recently reported study by us featuring PTZ monomer and dimer carrying TCBD and exTCBD, the E_T and E_{CT} were almost the same, especially in the case of TCBD systems, creating a ping-pong effect between triplet and charge-transfer states.[49] The present study with a central $PTZSO_2$ seems to lower the E_{CT} energy facilitating CT and CS originating from the triplet state.

Pump-probe spectroscopic studies using 100 fs laser pulses of selected wavelengths are subsequently performed to witness the charge transfer/separation and kinetics as a function of excitation wavelengths involving the LE and CT peak positions. In order to help interpret the transient spectral results, the oxidized and reduced species of the investigated compounds were generated as shown in Figure 5.16. The oxidized species of PTZ2 exhibited a low-intensity new peak at 470-550 nm, however, no new peaks were observed during the reduction of PTZ2. The oxidized species of PTS3 and PTS4 revealed a new peak in the 600 nm region while the reduced species revealed a broad peak spanning the 500–800 nm range. Similarly, a new peak in the 980 nm region for the oxidized species of PTS5 and PTS6, new peaks at 645, and a broad peak spanning 880–1400 nm with peak maxima at 1142 nm for the reduced species were observed.

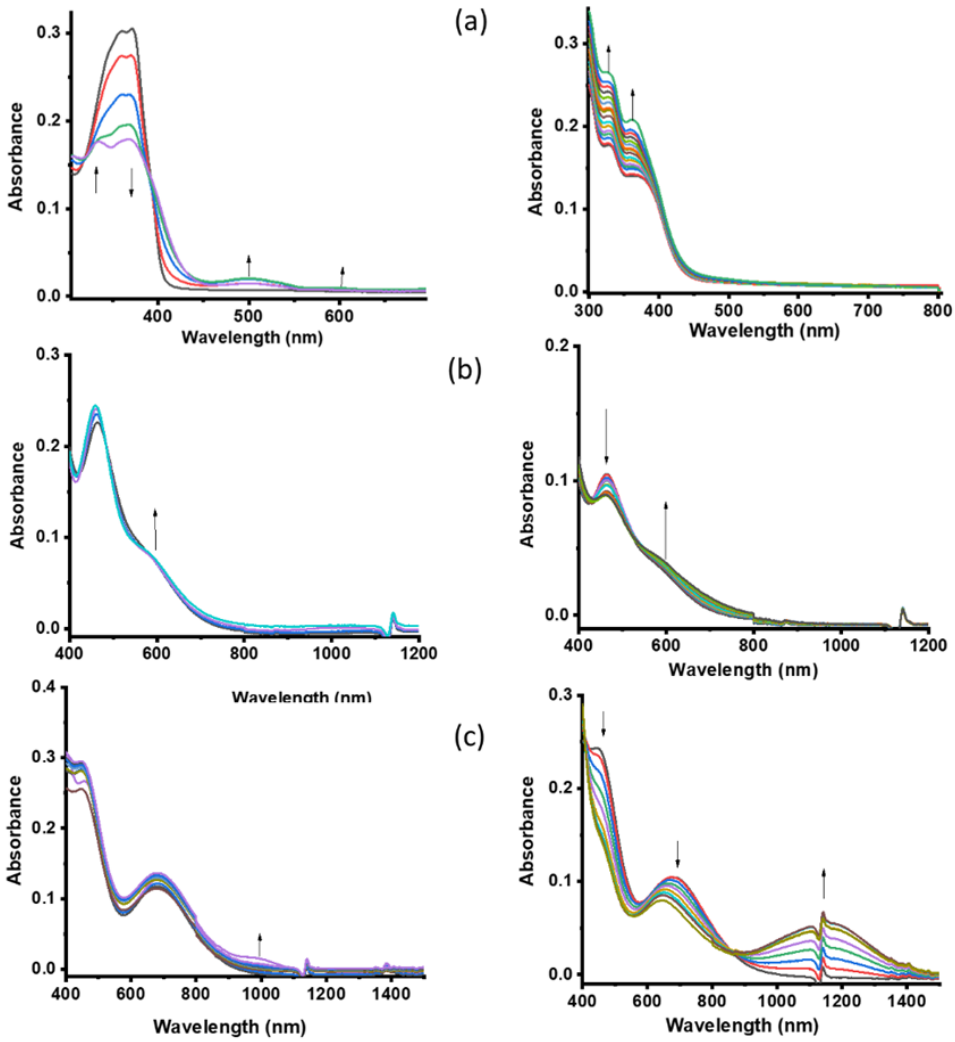

Figure 5.16: Spectral changes associated with chemical oxidation and reduction of (a) PTZ-control oxidation from spectroelectrochemistry (left) PTS1 oxidation (right). Oxidation (left) and reduction (right of (b) PTS3 and (c) PTS5 in DCB. Nitrosonium tetrafluoroborate was used as an oxidizing agent and bis(cyclopentadienyl) cobalt was used as a reducing agent.

Figure 5.17a shows the femtosecond transient absorption (fs-TA) spectra at the indicated delay times for PTZ-control in benzonitrile at the excitation wavelength of 395 nm. The $^{1}PTZ^{*}$ formed was characterized by a broad negative signal covering the 480–500 nm range, and from the earlier discussed spectral data, this has been attributed to the process of stimulated emission (SE). Recovery of this signal was slow consistent with its long singlet lifetime of 5.09 ns. The recovery was associated with the slow growth of a new signal in the 580–600 nm which could be attributed to the $^{3}PTZ^{*}$. In the case of PTS1 having only a $PTZSO_2$, the fs-TA spectral features

were different (see Fig. 5.17b). A strong excited state absorption peak (ESA) spanning the 500–600 nm region was observed with a negative peak in the 490 nm range due to SE. Decay/recovery of the positive and negative signals was accompanied by new peaks at 520, 600, 734, and 761 nm attributable to the triplet excited state.

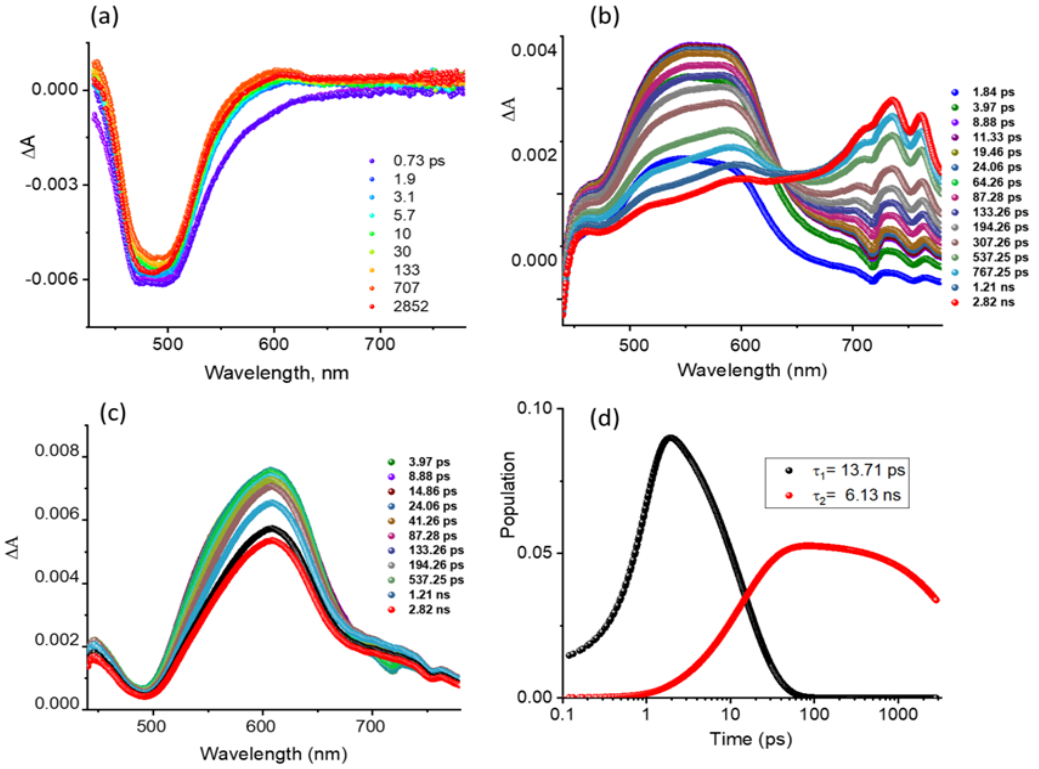

Figure 5.17: Fs-TA spectra at the indicated delay times of (a) PTZ-control (excitation = 395 nm), (b) PTS1 (excitation = 366 nm) and (c) PTS2 (excitation = 366 nm) in PhCN. (d) shows the population kinetics of different photo-events of PTS2.

The fs-TA spectra of the triad PTS2 having two PTZ and a central $PTZSO_2$ are shown in Figure 5.17c. It may be mentioned here that at the excitation wavelength of 366 nm both chromophores are likely to get excited resulting in oxidative (from excited PTZ) and reductive (from excited $PTZSO_2$) electron transfer events. From Figure 5.14a, charge separation from both the singlet and the triplet excited states was expected although the latter would be the primary contributor. The transient spectra revealed a strong peak at 606 nm with small spectral shifts during the course of the experiment. Since both $^3PTZ^*$ and $PTZ^{\bullet+}$ signals are expected in this region, from

the spectral trends, the presence of both $^3PTZ^*$ and $PTZ^{\bullet+}$ at the earlier delay times and only $PTZ^{\bullet+}$ at the latter time was obvious. That is, $^3PTZ^*$ and $^3PTZSO_2{}^*$ involvement in CS and not their singlet excited states was obvious. Expectedly, $^3PTZSO_2{}^*$ peaks, expected in the 520, 600, 734, and 761 nm range (see Fig. 5.17b), were absent further confirming its involvement in the charge separation process. The majority of the signal persisted beyond the 3 ns, the delay time of our instrument setup, further supporting the CS process to originate from the triplet excited state. The data was further subjected to global target analysis[56-57] wherein both two-component fit (representing $T_1 \rightarrow$ CS) and three-component fit (representing $S_1 \rightarrow T_1 \rightarrow$ CS) was applied. The lifetime of the long-lived component, attributable to the CS state was 6.13 ns, however, this could be considered the lower limit as much of the signal was still present.

Next, the push-pull systems derived from TCBD, PTS3**,** and PTS4, were investigated by exciting the sample at 400 nm corresponding to the LE state. As shown in Figure 5.17b, at this excitation wavelength, the $^1PTZ^*$ is expected to undergo ISC to produce $^3PTZ^*$ that would eventually promote CT and CS states of triplet character. This seems to be the case in the data shown in Figure 5.18. In the case of PTS3, the $^1PTS3^*$ formed within about 2 ps revealed ESA peaks at 535, 734, 758, and 898 nm (see Fig.5.18a). A negative peak at 456 nm representing SE was also observed. decay/recovery of the ESA/SE peaks resulted in a spectrum with a peak maxima at 637 nm attributable to $^3PTS3^*$ state (see spectrum at 3.97 ps). The decay of this peak was associated with a blue shift with a peak maxima at 601 nm. From the earlier discussed spectroelectrochemical results on PTZ3, this could be attributed to the charge-separated state (both oxidized and reduced PTZ3 had positive absorbance in this region as shown in Figure 5.18b. Glotaran analysis was subsequently performed for a three-component fit representing $S_1 \rightarrow T_1 \rightarrow$ CS processes. The species-associated spectra (SAS) for each species are shown in Figure 5.18a

middle panel while population kinetics are shown right the right-hand panel. The SAS spectra closely resembled that expected for the given species. From population kinetics data, the average lifetimes for T_1 and CS were found to be 11.55 and 3.10 ns. Lifetime for the CS state was generally higher than that reported for other donor-TCBD systems by us and others[30-50] wherein singlet excited state species were involved in promoting CS events. A similar trend representing $S_1 \rightarrow T_1 \rightarrow$ CS processes was observed in the case of PTS4 (see Fig. 5.18b) wherein the SAS spectra closely resembled that expected for the given species. From population kinetics data, the average lifetimes for T_1 and CS were found to be 9.52 ps and 5.22 ns. We also analyzed the data by a four-component fit representing $S_1 \rightarrow T_1 \rightarrow$ CT $\rightarrow$ CS processes. However, both CT and CS were very close suggesting these two processes occur almost simultaneously.

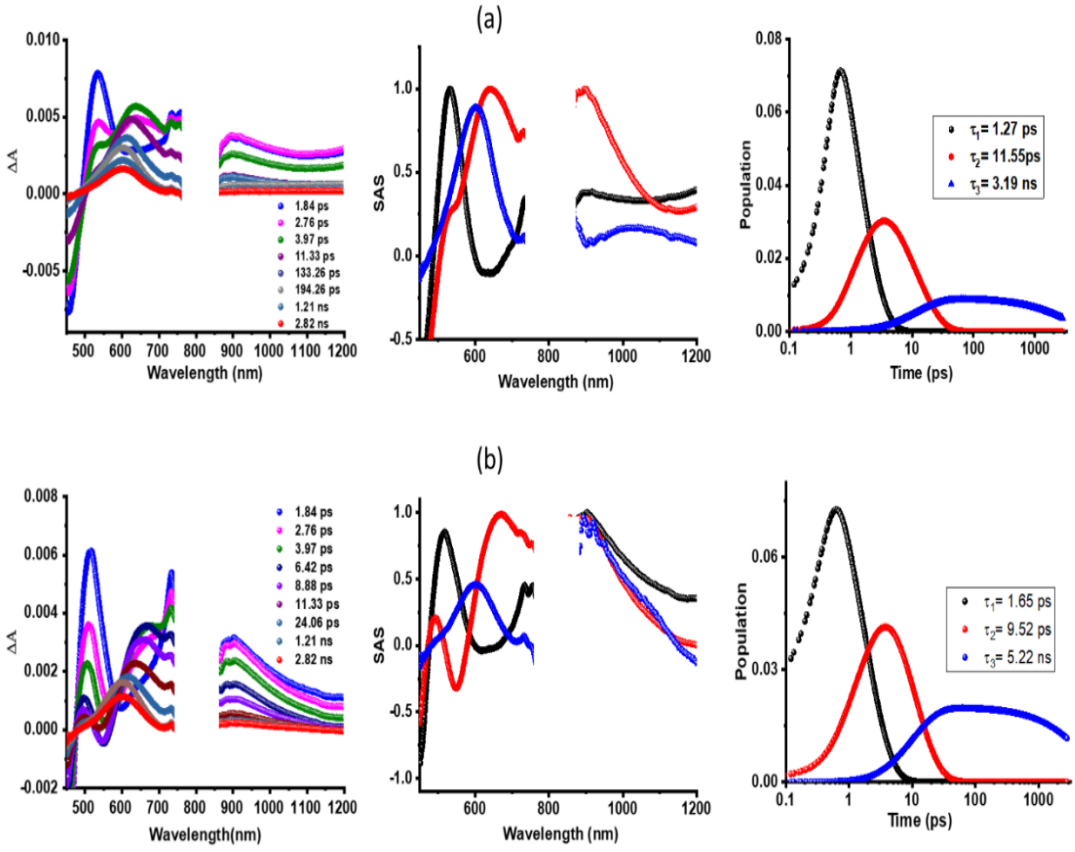

Figure 5.18: Fs-TA spectra at the indicated delay times of (a) PTS3 and (b) PTS 4 at the excitation wavelength of 400 nm. The middle and right-hand panels show, respectively, SAS and population kinetics of different species.

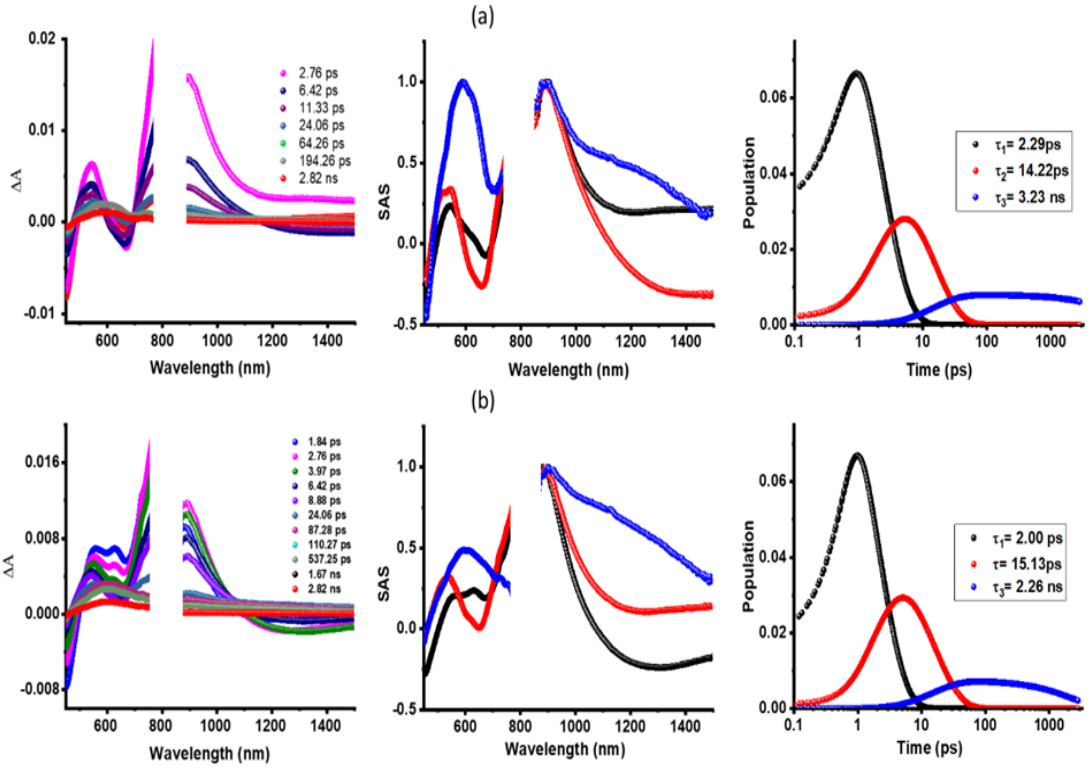

Figure 5.19: Fs-TA spectra at the indicated delay times of (a) PTS5 and (b) PTS6 at the excitation wavelength of 400 nm. The middle and right-hand panels show, respectively, SAS and population kinetics of different species.

Next, fs-TA studies on PTS5 and PTS6 carrying a much stronger electron acceptor exTCBD were performed by exciting the samples at 400 nm representing LE excitation. The energy diagram (Fig. 5.15) also predicted the possibility of CT and CS processes originating from the $^3PTZ^*$ and $^3PTZSO_2^*$ thus enhancing the lifetime of the CS products. Figure 5.19 shows the fs-TA spectra at the indicated delay times, SAS, and population kinetics representing the $S_1 \rightarrow T_1 \rightarrow$ CS processes of these two compounds. Spectral appearance in the 800–1000 nm range suggests the strong spectral overlap of different states including the CT state. Thus, the SAS attributed to the T_1 state could have contributions from the CT state also. Our attempts to separate these two events were not fully successful. Importantly, the SAS representing the CS state clearly revealed the expected near-IR peak of $PTZ5^{\bullet-}$ in the 1000–1400 nm range confirming its presence. The lifetimes of the T_1 and CS from population kinetics were found to be 14.22 ps and 3.23 ns for

PTS5 and 15.13 ps and 2.26 ns in the case of PTS6. Due to the higher exergonicity of exTCBD systems, faster CS events in PTS5 and PTS6 compared to PTS3 and PTS4 have been witnessed.

As discussed earlier, excitation of the PTS3–PTS6 corresponding to their CT state peak position is expected to generate their corresponding $^1CT^*$ states, viz., ^{1}[PTZ-(TCBD- PTZSO$_2$)$^{\delta-}$-TCBD-(PTZ)$^{\delta+}$]* in the case of PTS3, ^{1}[PTZ-(TCBD)$^{\delta-}$-(PTZSO$_2$-PTZ)$^{\delta+}$]* in the case of PTS4, ^{1}[PTZ-(exTCBD-PTZSO$_2$)$^{\delta-}$-(exTCBD-PTZ)$^{\delta+}$]* in the case of PTS5, and ^{1}[(PTZ-exTCBD)$^{\delta-}$-(PTZSO$_2$-PTZ)$^{\delta+}$]* in the case of PTS6, respectively (derived based on the location of the frontier orbitals in Fig. 5.9). The $^1CT^*$ states thus produced could undergo CS, especially in polar benzonitrile utilized here, or relax to the ground state directly. If it undergoes the former process, due to the singlet origin of the charge-separated product, the lifetime of such species would be much shorter than that discussed earlier for the triplet state-originated charge separation. In order to confirm this, fs-TA spectral studies on PTS3–PTS6, excited at their CT peak maxima, were performed. Figure 5.20 shows data corresponding to PTS3 and PTS4 while Figure 5.21 shows that of PTS5 and PTS6.

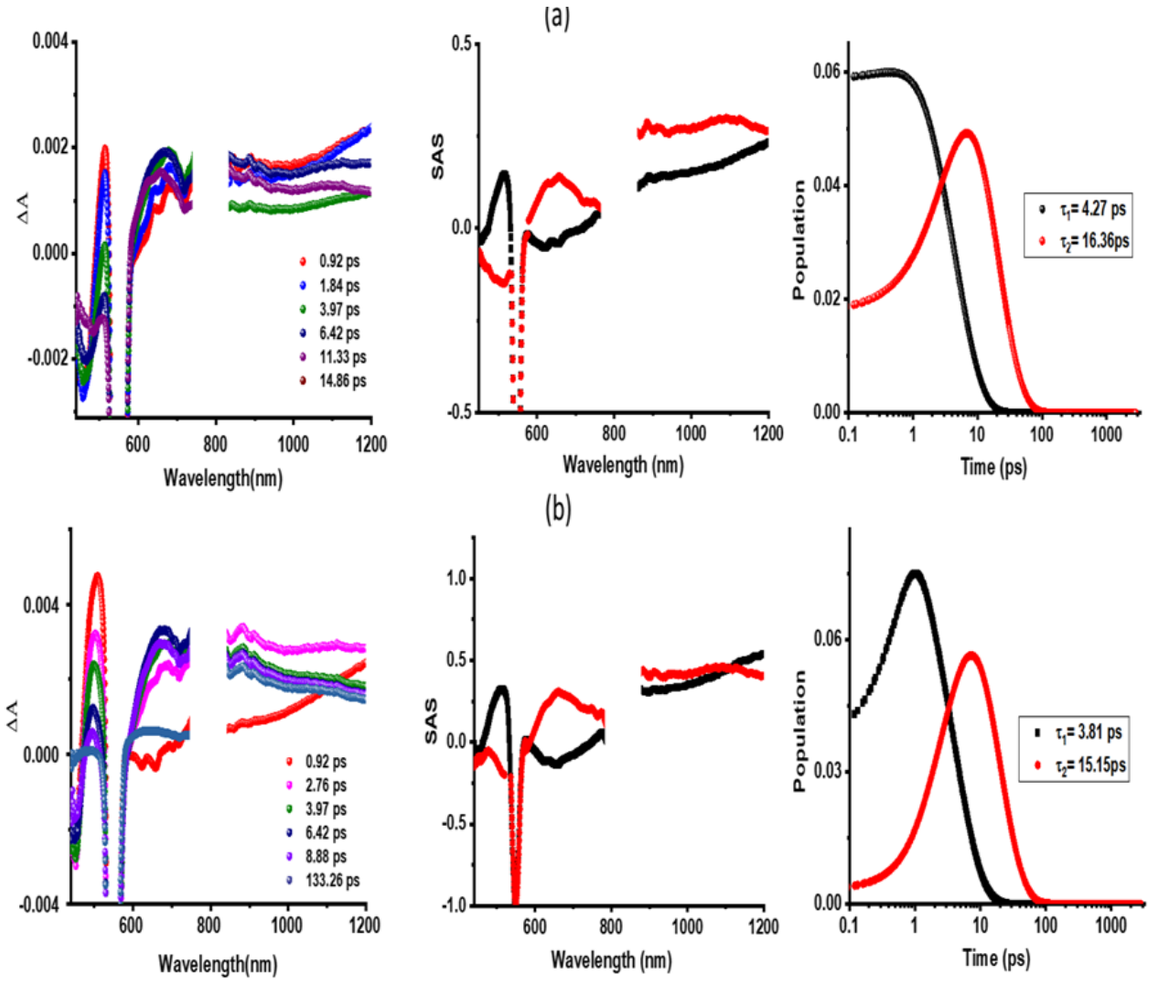

Figure 5.20: Fs-TA spectra at the indicated delay times of PTS3 and PTS 4 at the excitation wavelength of 555 nm corresponding to the CT state. The middle and right-hand panels show, respectively, SAS and population kinetics of different species.

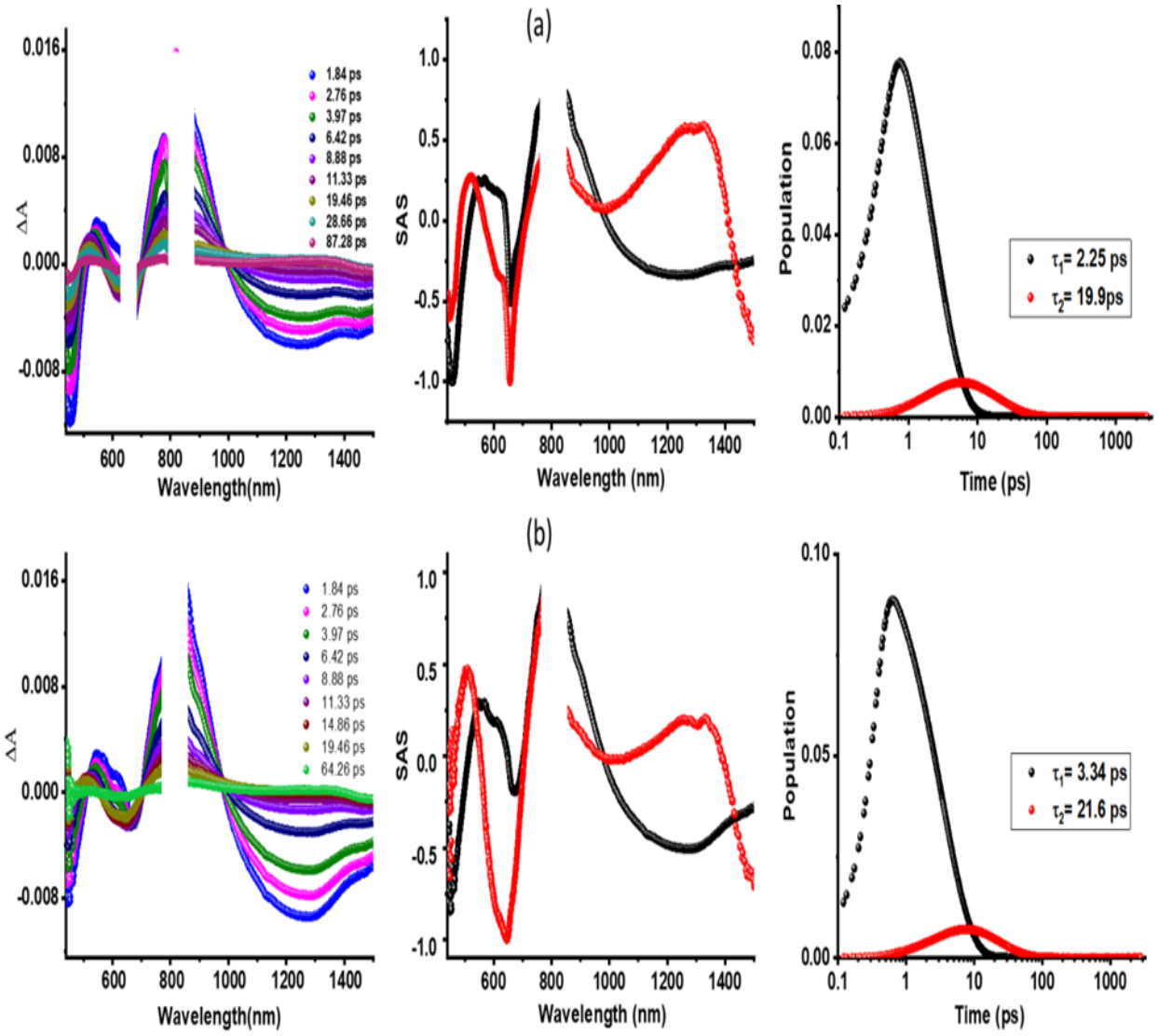

Figure 5.21: Fs-TA spectra at the indicated delay times of (a) PTS5 and (b) PTS6 at the excitation wavelength of 680 nm. The middle and right-hand panels show, respectively, SAS and population kinetics of different photo events.

As can be seen from the presented data, all of the photochemical events were completed within about 80 ps for both TCBD or exTCBD bearing push-pull compounds, a good sign that these are $^{1}CT^{*}$ → CS originated species. The SAS spectra attributed to the CS state matched closely to the earlier discussed results when LE excitation was used, including the near-IR peak in the case of PTS5 and PTS6 (see Fig. 5.21). The lifetime of the charge-separated states of singlet character from the analysis of population kinetics was found to be 16.36 ps for PTS3, 15.15 ps for PTS4,

19.9 ps for PTS5**,** and 21.6 ps for PTS6. It may be mentioned here that the spectra associated with the charge-separated state appear slightly different due to different excited state species produced at different wavelengths. These lifetime values are comparable to the lifetime of other Donor-TCBD and Donor-exTCBD systems (Donor = electron-rich photosensitizer), reported earlier,[30-50] all originating from their respective singlet excited states.

5.4 Conclusions

Extension of the lifetime of charge-separated states in strongly interacting push-pull systems by making use of the triplet excited states formed with the choice of excitation wavelengths has been successfully demonstrated. To accomplish this task, electron-rich phenothiazine and electron-deficient phenothiazine sulfone were used to form the initial triad. Several interesting properties, including mechanochromism, solvatochromism, and aggregation-induced emission were observed in this triad. The introduction of stronger electron acceptors, TCBD and exTCBD resulted in intramolecular charge transfer both in the ground and excited states. The formation of high-energy triplet states (2.32–2.38 eV) of both phenothiazine and phenothiazine sulfone was established from phosphorescence studies suggesting that they can promote electron transfer resulting in long-lasting, charge-separated states of triplet character irrespective of the nature of electron acceptors, $PZSO_2$ or TCBD/exTCBD due to thermodynamic feasibility of such reactions. This phenomenon was possible to demonstrate using femtosecond transient absorption spectral studies where excitation of the studied push-pull systems corresponding to the locally excited state resulted in the formation of the triplet excited states of the probes by intersystem crossing and due to their high energy, they were able to promote charge separation. The lifetime of the charge-separated states was much higher than what would be expected from their singlet excited state. Alternatively, excitation of the push-pull systems

corresponding to their charge-transfer state also promoted charge separation but due to the singlet character of the products, fast charge recombination was witnessed. The present study brings out the significance of high-energy triplet states and excitation wavelength selection, the two key parameters, in promoting and stabilizing charge separation in highly interacting push-pull systems.

5.5 References and Notes

1. Deisenhofer, J.; Norris, J. R. *Photosynthetic Reaction Center*; Academic Press: San Diego, CA, 2013; Vol. 2.

2. Wasielewski, M. R. Self-Assembly Strategies for Integrating Light Harvesting and Charge Separation in Artificial Photosynthetic Systems. *Acc. Chem. Res.* 2009, **42**, 1910−1921.

3. Straight, S. D.; Kodis, G.; Terazono, Y.; Hambourger, M.; Moore, T. A.; Moore, A. L.; Gust, D. Energy Conversion in Natural and Artificial Photosynthesis. *Nat. Nanotechnol.* 2008, **3**, 280−283.

4. Bottari, G.; de la Torre, G.; Guldi, D. M.; Torres, T. Covalent and Noncovalent Phthalocyanine-Carbon Nanostructure Systems: Synthesis, Photoinduced Electron Transfer, and Application to Molecular Photovoltaics. *Chem. Rev.* 2010, **110**, 6768−6816.

5. Guldi, D. M.; Sgobba, V. Carbon Nanostructures for Solar Energy Conversion Schemes. *Chem. Commun.* 2011, **47**, 606−610.

6. D'Souza, F.; Ito, O. Photosensitized Electron Transfer Processes of Nanocarbons Applicable to Solar Cells. *Chem. Soc. Rev.* 2012, **41**, 86−96.

7. D'Souza, F.; Ito, O. In Multiporphyrin Array: Fundamentals and Applications; Kim, D., Ed.; Pan Stanford Publishing: Singapore, 2012; Chapter 8, pp 389−437.

8. Imahori, H.; Umeyama, T.; Ito, S. Large π-Aromatic Molecules as Potential Sensitizers for Highly Efficient Dye-Sensitized Solar Cells. *Acc. Chem. Res.* 2009, **42** (11), 1809–1818.

9. KC, C. B.; D'Souza, F. Design and Photochemical Study of Supramolecular Donor−Acceptor Systems Assembled via Metal−Ligand Axial Coordination. *Coord. Chem. Rev.* 2016, **322**, 104−141.

10. Zhang, J., Xu, W., Sheng, P., Zhao, G. and Zhu, D., Organic donor–acceptor complexes as novel organic semiconductors. *Acc. Chem. Res.*, 2017, **50**, 1654-1662.

11. Sommer, M., Huettner, S. and Thelakkat, M., Donor–Acceptor Block Copolymers for Photovoltaic Applications. *J. Mater. Chem.*, 2010, **20**, 10788–10797.

12. Deibel, C., Strobel, T. and Dyakonov, V., Role of the Charge Transfer State in Organic Donor–Acceptor Solar Cells. *Adv. Mater.*, 2010**, 22**, 4097–4111.

13. Balzani, V.; Credi, A.; Venturi, M. Photochemical Conversion of Solar Energy. *ChemSusChem* 2008, 1, 26−58.

14. Armaroli, N.; Balzani, V. The Future of Energy Supply: Challenges and Opportunities. *Angew. Chem., Int. Ed.* 2007, **46**, 52–66.

15. Beaujuge, P. M.; Fréchet, J. M. J. Molecular Design and Ordering Effects in π-Functional Materials for Transistor and Solar Cell Applications. *J. Am. Chem. Soc.* 2011, **133**, 20009–20029.

16. Hammarström, L. Accumulative Charge Separation for Solar Fuels Production: Coupling Light-Induced Single Electron Transfer to Multielectron Catalysis. *Acc. Chem. Res.* 2015, ***48***, 840–850.

17. Bottari, G.; Torres, T. *Organic Nanomaterials: Synthesis, Characterization, and Device Applications,* Eds: Torres, T.; Bottari, G. John Wiley & Sons, Inc., Hoboken, NJ, 2013.

18. Wu, Y.; Zhu, W. Organic Sensitizers from D–π–A to D–A–π–A: Effect of the Internal Electron-Withdrawing Units on Molecular Absorption, Energy Levels and Photovoltaic Performances. *Chem. Soc. Rev.* 2013, **42**, 2039–2058.

19. Misra, R.; Bhattacharyya, S. P. Nonlinear Optical Response of ICT Molecules. *Intramolecular Charge Transfer: Theory and Applications* 2018.

20. May, V.; Kühn, O. *Charge and Energy Transfer Dynamics in Molecular Systems*, John Wiley & Sons 2008.

21. Fukuzumi, S.; Ohkubo, K.; Suenobu, T. Long-Lived Charge Separation and Applications in Artificial Photosynthesis. *Acc. Chem. Res.* 2014, **47**, 1455–1464.

22. Barrejón, M.; Arellano, L. M.; D'Souza, F.; Langa, F. Bidirectional Charge-Transfer Behavior in Carbon-Based Hybrid Nanomaterials. *Nanoscale* 2019, **11**, 14978–14992.

23. D. Kim, *Multiporphyrin arrays: Fundamentals and applications*, 2012.

24. Higashino, T.; Yamada, T.; Yamamoto, M.; Furube, A.; Tkachenko, N. V.; Miura, T.; Kobori, Y.; Jono, R.; Yamashita, K.; Imahori, H. Remarkable Dependence of the Final Charge Separation Efficiency on the Donor-Acceptor Interaction in Photoinduced Electron Transfer. *Angew. Chem., Int. Ed.* 2016, **55**, 629−633.

25. Zarrabi, N.; Seetharaman, S.; Chaudhuri, S.; Holzer, N.; Batista, V. S.; van der Est, A.; D'Souza, F.; Poddutoori, P. K. Decelerating Charge Recombination Using Fluorinated Porphyrins in *N,N* -Bis(3,4,5-Trimethoxyphenyl)Aniline—Aluminum(III) Porphyrin—Fullerene Reaction Center Models. *J. Am. Chem. Soc.* 2020, **142**, 10008–10024.

26. Canton-Vitoria, R.; Gobeze, H. B.; Blas-Ferrando, V. M.; Ortiz, J.; Jang, Y.; Fernández-Lázaro, F.; Sastre-Santos, Á.; Nakanishi, Y.; Shinohara, H.; D'Souza, F.; Tagmatarchis, N. Excited-State Charge Transfer in Covalently Functionalized MoS2 with a Zinc Phthalocyanine Donor–Acceptor Hybrid. *Angew. Chem., Int. Ed.* 2019, **58**, 5712–5717.

27. van Dijk, S. I.; Groen, C. P.; Hartl, F.; Brouwer, A. M.; Verhoeven, J. W. Long-Lived Triplet State Charge Separation in Novel Piperidine-Bridged Donor−Acceptor Systems. *J. Am. Chem. Soc*. 1996, **118**, 8425−8432.

28. Obondi, C. O.; Lim, G. N.; Churchill, B.; Poddutoori, P. K.; van der Est, A.; D'Souza, F. Modulating the Generation of Long-Lived Charge Separated States Exclusively from the Triplet Excited States in Palladium Porphyrin−Fullerene Conjugates. *Nanoscale* 2016, **8**, 8333−8344.

29. Kivala, M.; Boudon, C.; Gisselbrecht, J.-P.; Seiler, P.; Gross, M.; Diederich, F. Charge-Transfer Chromophores by Cycloaddition–Retro-Electrocyclization: Multivalent Systems and Cascade Reactions. *Angew. Chem., Int. Ed.* 2007, **46**, 6357–6360.

30. Michinobu, T.; Diederich, F. The [2+2] Cycloaddition-Retroelectrocyclization (CA-RE) Click Reaction: Facile Access to Molecular and Polymeric Push-Pull Chromophores. *Angew. Chem., Int. Ed.* 2018, **57**, 3552–3577.

31. Sekita, M.; Ballesteros, B.; Diederich, F.; Guldi, D. M.; Bottari, G.; Torres, T. Intense Ground-State Charge-Transfer Interactions in Low-Bandgap, Panchromatic Phthalocyanine-Tetracyanobuta-1,3-diene Conjugates. *Angew. Chem., Int. Ed.* 2016, **55**, 5560−5564.

32. Winterfeld, K. A.; Lavarda, G.; Guilleme, J.; Sekita, M.; Guldi, D. M.; Torres, T.; Bottari, G. Subphthalocyanines Axially Substituted with a Tetracyanobuta-1,3-diene−Aniline Moiety: Synthesis, Structure, and Physicochemical Properties. *J. Am. Chem. Soc*. 2017, **139**, 5520−5529.

33. Leliege, A., Blanchard, P., Rousseau, T. and Roncali, J., Triphenylamine/tetracyanobutadiene-based DAD π-conjugated systems as molecular donors for organic solar cells. *J. Org. Lett.* 2011, **13**, 3098−3101.

34. Shoji, T.; Ito, S. Azulene-Based Donor–Acceptor Systems: Synthesis, Optical, and Electrochemical Properties. *Chem. Eur. J.* 2017, **23**, 16696–16709.

35. Simón Marqués, P.; Castán, J. M. A.; Raul, B. A. L.; Londi, G.; Ramirez, I.; Pshenichnikov, M. S.; Beljonne, D.; Walzer, K.; Blais, M.; Allain, M.; Cabanetos, C.; Blanchard, P. Triphenylamine/Tetracyanobutadiene-Based π-Conjugated Push–Pull Molecules End-Capped with Arene Platforms: Synthesis, Photophysics, and Photovoltaic Response. *Chem. Eur. J.* 2020, **26**, 16422–16433.

36. Winterfeld, K. A.; Lavarda, G.; Guilleme, J.; Guldi, D. M.; Torres, T.; Bottari, G. Subphthalocyanine–Tetracyanobuta-1,3-Diene–Aniline Conjugates: Stereoisomerism and Photophysical Properties. *Chem. Sci.* 2019, **10**, 10997–11005.

37. Bui, A. T.; Philippe, C.; Beau, M.; Richy, N.; Cordier, M.; Roisnel, T.; Lemiègre, L.; Mongin, O.; Paul, F.; Trolez, Y. Synthesis, Characterization and Unusual near-Infrared Luminescence of 1,1,4,4-Tetracyanobutadiene Derivatives. *Chem. Commun.* 2020, **56**, 3571–3574.

38. Gotfredsen, H.; Neumann, T.; Storm, F. E.; Muñoz, A. V.; Jevric, M.; Hammerich, O.; Mikkelsen, K. V.; Freitag, M.; Boschloo, G.; Nielsen, M. B. Donor−Acceptor-Functionalized Subphthalocyanines for Dye-Sensitized Solar Cells. *ChemPhotoChem* 2018, **2**, 976–985.

39. Gautam, P.; Misra, R.; Thomas, M. B.; D'Souza, F. Ultrafast Charge-Separation in Triphenylamine-BODIPY-Derived Triads Carrying Centrally Positioned, Highly Electron-Deficient, Dicyanoquinodimethane or Tetracyanobutadiene Electron-Acceptors. *Chem. Eur. J.* 2017, **23**, 9192−9200.

40. Sharma, R.; Thomas, M. B.; Misra, R.; D'Souza, F. Strong Ground- and Excited-State Charge Transfer in C3-Symmetric Truxene-Derived Phenothiazine-Tetracyanobutadine and Expanded Conjugates. *Angew. Chem. Int. Ed.* 2019, **131**, 4394−4399.

41. Rout, Y.; Jang, Y.; Gobeze, H. B.; Misra, R.; D'Souza, F. Conversion of Large-Bandgap Triphenylamine–Benzothiadiazole to Low-Bandgap, Wide-Band Capturing Donor–Acceptor Systems by Tetracyanobutadiene and/or Dicyanoquinodimethane Insertion for Ultrafast Charge Separation. *J. Phys. Chem. C* 2019, **123**, 23382–23389.

42. Poddar, M.; Jang, Y.; Misra, R.; D'Souza, F. Excited-State Electron Transfer in 1,1,4,4-Tetracyanobuta-1,3-Diene (TCBD)- and Cyclohexa-2,5-Diene-1,4-Diylidene-Expanded TCBD-Substituted BODIPY-Phenothiazine Donor–Acceptor Conjugates. *Chem. Eur. J.* 2020, **26**, 6869–6878.

43. Pinjari, D.; Alsaleh, A. Z.; Patil, Y.; Misra, R.; D'Souza, F. Interfacing High-Energy Charge-Transfer States to a Near-IR Sensitizer for Efficient Electron Transfer upon Near-IR Irradiation. *Angew. Chem., Int. Ed.* 2020, **59**, 23697–23705.

44. Yadav, I. S.; Alsaleh, A. Z.; Misra, R.; D'Souza, F. Charge Stabilization via Electron Exchange: Excited Charge Separation in Symmetric, Central Triphenylamine Derived, Dimethylaminophenyl–Tetracyanobutadiene Donor–Acceptor Conjugates. *Chem. Sci.* 2021, **12** (3), 1109–1120.

45. Jang, Y.; Rout, Y.; Misra, R.; D'Souza, F. Symmetric and Asymmetric Push–Pull Conjugates: Significance of Pull Group Strength on Charge Transfer and Separation. *J. Phys. Chem. B* **2021**, *125*, 4067–4075.

46. Khan, F.; Jang, Y.; Patil, Y.; Misra, R.; D'Souza, F. Photoinduced Charge Separation Prompted Intervalence Charge Transfer in a Bis(Thienyl)Diketopyrrolopyrrole Bridged Donor-TCBD Push-Pull System. *Angew. Chem., Int. Ed.* 2021, **60**, 20518–20527.

47. Shinde, J.; Thomas, M. B.; Poddar, M.; Misra, R.; D'Souza, F. Does Location of BF2-Chelated Dipyrromethene (BODIPY) Ring Functionalization Affect Spectral and Electron

Transfer Properties? Studies on α-, β-, and Meso-Functionalized BODIPY-Derived Donor–Acceptor Dyads and Triads. *J. Phys. Chem. C* 2021, **125**, 23911–23921.

48. Sekaran, B.; Dawson, A.; Jang, Y.; MohanSingh, K. V.; Misra, R.; D'Souza, F. Charge-Transfer in Panchromatic Porphyrin-Tetracyanobuta-1,3-Diene-Donor Conjugates: Switching the Role of Porphyrin in the Charge Separation Process. *Chem. Eur. J.* 2021, **27**, 14335–14344.

49. Yadav, I. S.; Jang, Y.; Rout, Y.; Thomas, M. B.; Misra, R.; D'Souza, F. Near-IR Intramolecular Charge Transfer in Strongly Interacting Diphenothiazene-TCBD and Diphenothiazene-DCNQ Push-Pull Triads. *Chem. Eur. J.* 2022, **28**, e202200348.

50. Rout, Y.; Motanari, C.; Pasciucco, E.; Misra, R.; Carlotti, B. Tuning the Fluorescence and the Intramolecular Charge Transfer of Phenothiazine Dipolar and Quadrupolar Derivatives by Oxygen Functionalization, *J. Am. Chem. Soc*. 2021, **143**, 9933-9943.

51. Rout, Y.; Gautam, P.; Misra, R. Unsymmetrical and Symmetrical Push–Pull Phenothiazines. *J. Org. Chem.* 2017, **82**, 6840–6845.

52. Ekbote, A., Mobin, S.M. and Misra, R., Stimuli-responsive phenothiazine-based donor–acceptor isomers: AIE, mechanochromism and polymorphism. *J. Mater. Chem. C*, 2020**, 8**, 3589−3602.

53. Tu, L.; Xie, Y.; Li, Z. Advances in Pure Organic Mechanoluminescence Materials, *J. Phys. Chem. Lett*. 2022, **13**, 5605-5617.

54. Frisch, M. J.; Trucks, G. W.; Schlegel, H. B.; Scuseria, G. E.; Robb, M. A.; Cheeseman, J. R.; Scalmani, G.; Barone, V.; Mennucci, B.; Petersson, G. A.; Nakatsuji, H.; Caricato, M.; Li, X.; Hratchian, H. P.; Izmaylov, A. F.; Bloino, J.; Zheng, G.; Sonnenberg, J. L.; Hada, M.; Ehara, M.; Toyota, K.; Fukuda, R.; Hasegawa, J.; Ishida, M.; Nakajima, T.; Honda, Y.; Kitao, O.; Nakai, H.; Vreven, T.; Montgomery, J. A., Jr.; Peralta, J. E.; Ogliaro, F.; Bearpark, M.; Heyd, J. J.; Brothers, E.; Kudin, K. N.; Staroverov, V. N.; Kobayashi, R.; Normand, J.; Raghavachari, K.; Rendell, A.; Burant, J. C.; Iyengar, S. S.; Tomasi, J.; Cossi, M.; Rega, N.; Millam, N. J.; Klene, M.; Knox, J. E.; Cross, J. B.; Bakken, V.; Adamo, C., Jaramillo, J.; Gomperts, R.; Stratmann, R. E.; Yazyev, O.; Austin, A. J.; Cammi, R.; Pomelli, C.; Ochterski, J. W.; Martin, R. L.; Morokuma, K.; Zakrzewski, V. G.; Voth, G. A.; Salvador, P.; Dannenberg, J. J.; Dapprich, S.; Daniels, A. D.; Farkas, O.; Foresman, J. B.; Ortiz, J. V.; Cioslowski, J.; Fox, D. J. Gaussian 09, Revision A.02; Gaussian, Inc., Wallingford, CT, 2009.

55. Rehm, D.; Weller, A. Kinetics of Fluorescence Quenching by Electron and H-Atom Transfer. *Isr. J. Chem.* 1970, **8**, 259–271.

56. Snellenburg, J. J.; Laptenok, S.; Seger, R.; Mullen; K. M.; van Stokkum, I. H. Glotaran: A Java-based graphical user interface for the R package TIMP. *J. Stat. Softw.* 2012, **49**, 1–22.

57. Ekbote, A., Han, S.H., Jadhav, T., Mobin, S.M., Lee, J.Y. and Misra, R., Stimuli responsive AIE active positional isomers of phenanthroimidazole as non-doped emitters in OLEDs. *J. Mater. Chem. C*, 2018, ***6*(8)**, 2077–2087.

CHAPTER 6

SUMMARY AND FUTURE PERSPECTIVE DIRECTION

6.1 Summary

The escalating global energy demand and environmental impacts resulting from nonrenewable fossil fuel usage have spurred the search for sustainable energy solutions. Artificial photosynthesis, which efficiently harnesses solar energy, emerges as a promising strategy to address rising energy needs and environmental concerns. The primary goal of artificial photosynthesis is to develop innovative technologies that convert solar energy into electric current or storable fuel energy, inspired by natural photosynthesis mechanisms. By understanding the efficient light energy harvesting and charge separation processes in natural photosynthesis, artificial photosynthesis aims to design molecular and nanohybrid systems to achieve clean, affordable, and sustainable energy production. Investing in renewable energy infrastructure further supports this endeavor, promising a future free from dependency on finite fossil fuels and a more sustainable planet for humanity.

The dissertation focuses on exploring innovative molecular and supramolecular donor-acceptor architectures, aiming to replicate the early stages of natural photosynthesis involving charge and electron transfer events. Through ultrafast transient absorption spectroscopy, various donor-acceptor systems were extensively analyzed to investigate their photochemical events. The data analysis provided valuable insights into the subtle differences among donor-acceptor systems, crucial for understanding natural photosynthesis and enhancing solar energy harvesting efficiency. The work involves designing, synthesizing, and studying artificial photosynthesis systems to harness light energy, with a key goal being the achievement of long-lived charge-separated states through covalent interactions and multi-modular donor-acceptor systems with electron transfer

processes. These advancements hold promise for developing renewable energy technologies like photoelectrochemical devices, solar fuels, and solar catalysts.

Chapter 3 of the dissertation explores innovative donor-acceptor push-pull constructs with a focus on a far-red absorbing sensitizer, azaBODIPY, as the electron acceptor. These push-pull systems consist of different nitrogenous electron donors (N,N-dimethylaniline, triphenylamine, and phenothiazine) connected through an acetylene linker. The investigation utilizes spectroscopic, electrochemical, and computational methods to study the structural integrity and photochemical events of these systems. Charge separation is confirmed through spectroelectrochemical studies in polar solvents, indicating the presence of (azaBODIPY$^{\bullet-}$) peaks in the visible and near-IR regions. The synthesized push-pull systems exhibit panchromatic absorption, resulting from intramolecular charge transfer and near-IR absorption from azaBODIPY. Excited state electron transfer properties are explored using different techniques, revealing efficient charge separation in various solvents. The charge-separated states show lifetimes of 50–200 ps, depending on the donor's nature. The successful combination of high-energy charge transfer states with near-IR sensitizers holds promise for optoelectronic applications, opening up possibilities for novel multi-modular systems in energy and optoelectronic research.

Continuing with the focus on novel push-pull systems, the subsequent part of this chapter investigates combinations of triphenylamine-tetracyanobutadiene (TPA-TCBD) and azaBODIPY to achieve efficient excited state charge separation for potential optoelectronic applications across a wide optical range. These systems exhibit panchromatic light absorption by combining intramolecular charge transfer with near-IR absorption. Electrochemical and computational studies are used to visualize excited state events and determine energy levels. Femtosecond transient

absorption (fs-TA) studies monitor charge transfer events, revealing the impact of solvent polarity, linked CT entities, and excitation wavelength on the CS state lifetime. Remarkably, in compound 3, electron exchange between symmetrically attached TPA-TCBD entities extends the CS state lifetime. The combination of TPA-TCBD with azaBODIPY creates a panchromatic light-absorbing system. Spectroelectrochemical studies confirm the presence of different charge transfer and charge separation states, allowing deduction of the charge-separated species' spectrum upon one-electron reduction. The research demonstrates efficient charge separation upon near-IR or CT excitation, suggesting potential applications in energy and optoelectronic systems.

Chapter 4 presents a series of push-pull systems (1–4) composed of triphenylamine (TPA) and phenothiazine (PTZ) as donor molecules, along with a central electron acceptor, TCBD. Control compounds (C1-C4) were synthesized to investigate the influence of terminal PTZ on charge transfer events. These systems exhibited a broad intramolecular charge transfer band in the visible-near IR region, resulting from strong push-pull interactions. Electrochemical studies revealed multiple redox processes, while spectroelectrochemical analyses provided insights into the spectral features of charge transfer species. Computational methods (DFT) were utilized to visualize the charge transfer within different donor and acceptor entities. Excited charge transfer was demonstrated through femtosecond transient absorption spectral studies. Notably, the application of pump-probe spectroscopy followed by Global target analysis confirmed excited charge transfer in the presence of PTZ, which effectively stabilized the charge transfer state. The integration of computational methods and spectroscopic techniques contributed valuable insights into the charge transfer processes, offering potential implications for advancements in light energy conversion and optoelectronic devices.

The latter part of this chapter focuses on π-conjugated donor-acceptor chromophores and

their properties, along with their applications in organic photovoltaics, molecular electronics, and bioimaging. Star-shaped π-conjugated molecular systems are preferred due to their improved solubility and reduced aggregation. The design flexibility of these systems allows for the adjustment of electronic and photonic properties by modifying donor, acceptor, and π-spacer units. Commonly used components in these systems are Triphenylamine and Tetracyanoethylene (TCNE). This study addresses the challenge of achieving charge stabilization in donor-TCBD systems. It presents the development of molecular donor-acceptor systems containing C3 symmetric central triphenylamine-derived dimethylamine-tetracyanobutadiene conjugates, which promote charge transfer and extend absorption into the visible spectrum. The investigation involves electrochemical analysis and manipulation of spectroelectrochemical data to determine the charge transfer state's spectrum. The results demonstrate how electron exchange prolongs the lifetime of charge-separated states, indicating a proposed and demonstrated charge-stabilizing mechanism. The significance of these findings lies in enhancing our understanding of electron transfer in multi-modular systems, which could have potential applications in optoelectronics. An analogy is drawn to bacterial photosynthesis, where a similar electron exchange mechanism might explain the preference for a bacteriochlorophyll dimer over a monomer as the primary electron donor.

The main objective of Chapter 5 was to enhance the stability of donor-acceptor (DA) structures, critical for developing advanced light energy conversion devices in artificial photosynthesis, by increasing the lifetime of charge-separated (CS) states. This is especially crucial when DA structures are closely spaced and strongly interacting. Dr. Rajneesh Misra and his student designed new push-pull systems (PTS2–PTS6) based on a π-conjugated phenothiazine sulfone ($PTZSO_2$) framework and incorporated potent electron acceptors (TCBD and exTCBD) to

modify their spectral and photophysical properties. The PTS2 system exhibited intriguing characteristics such as solvatochromism, aggregation-induced emission, and mechanochromic behaviors. Excitation wavelength played a significant role in charge stabilization, with LE peak positions demonstrating notable effects compared to CT transitions. The bis-phenothiazine-phenothiazine sulfone scaffold (PTZ-PTZSO_2-PTZ) was designed to tackle rapid charge recombination in multi-modular donor-acceptor (D-A) systems. To enhance charge transfer from the triplet excited state of the electron donor ($^3PTZ^*$) during the LE (locally excited) state excitation, the scaffold incorporated TCBD (tetracyanobuta-1,3-diene) and exTCBD (extended tetracyanobuta-1,3-diene) moieties. Phosphorescence studies revealed the formation of high-energy triplet states at (2.32–2.38 eV) in both phenothiazine and phenothiazine sulfone, enabling efficient electron transfer and resulting in long-lasting charge-separated states with triplet character, independent of the electron acceptors used, due to thermodynamic feasibility. Femtosecond transient absorption spectral studies demonstrated the formation of triplet excited states via intersystem crossing, enabling effective charge separation and leading to significantly longer lifetimes of charge-separated states than those from singlet excited states. However, charge separation from singlet excited states exhibited rapid charge recombination. In conclusion, this study underscored the importance of high-energy triplet states and excitation wavelength selection as critical factors for promoting and stabilizing charge separation in highly interacting push-pull systems.

This work's findings provide a valuable understanding of photochemical processes in diverse donor-acceptor systems, facilitating informed design and synthesis of solar energy harvesting devices, ultimately paving the way for a solar-powered future. The study highlights the rapid charge transfer and light absorption properties of most push-pull systems across the visible

and near-IR spectrum, indicating their potential application in optoelectronic devices, such as bulk heterojunction solar cells, for enhanced light energy conversion.

6.2 Future Perspective Direction

The research presented in this dissertation paves the way for exciting future directions in the field of optoelectronics and energy research. Building on the success of the donor-acceptor push-pull systems investigated here, there are several promising avenues for further exploration. First, the fine-tuning of these push-pull systems with a focus on achieving even longer charge separation lifetimes could significantly enhance their efficiency for energy harvesting applications. The research in Chapter 3, for instance, has already demonstrated efficient charge separation, but the lifetimes of these separated charges vary depending on the donor molecule used. Future work should aim to precisely control and increase these lifetimes, possibly by exploring different donor molecules or modifying existing ones. Longer charge separation lifetimes are desirable because they provide more time to capture and utilize the separated charges in various energy applications.

Furthermore, exploring the scalability and compatibility of these multi-modular systems for real-world applications, such as solar cells or light-emitting diodes (LEDs), represents an important next step. Integration with existing materials and technologies, as well as developing novel device architectures, will be essential for translating these findings from the lab to practical use. In addition, the potential for these systems to operate in diverse environmental conditions, including different solvents and excitation wavelengths, should be thoroughly investigated. This research could lead to the development of adaptable optoelectronic materials capable of efficient charge separation under various circumstances.

Moreover, the environmental impact of materials and processes used in constructing light-harvesting devices and LEDs are another vital aspect of future research. As concerns about

sustainability and eco-friendliness continue to grow, rising the ecological footprint of artificial photosynthesis technologies becomes increasingly important. Researchers should focus on developing environmentally responsible approaches that minimize the environmental burden associated with the production and operation of these devices, thereby aligning light energy harvesting with the principles of green and sustainable technology.

Lastly, a promising avenue for improving energy conversion efficiency is offered by the exploration of multi-exciton generation within donor-acceptor push-pull systems. The potential for generating multiple electron-hole pairs from a single photon is being investigated, and profound implications for enhancing the performance of energy conversion devices are witnessed. By harnessing the phenomenon of multi-exciton generation, the quantum yield of these systems can be significantly enhanced, making them more efficient in converting light energy into electricity. Great potential for advancing the state of the art in light energy harvesting is held by this area of research, and it should be pursued diligently in the future.

In conclusion, as the field of optoelectronics continues to evolve, interdisciplinary collaboration between chemists, physicists, and engineers will be instrumental in harnessing the full potential of these push-pull systems. Overall, the future of this research lies in expanding its application scope, improving its efficiency, and addressing practical challenges to enable innovative solutions in the realms of energy and optoelectronics.

APPENDIX

LIST OF PUBLICATIONS

C. Cooper, R. Paul, A. Alsaleh, S. Washburn, W. Rackers, S. Kumar, V. N. Nesterov, F. D'Souza, S. A. Vinogradov and H. Wang, *Chemistry–A European Journal*, 2023, e202302013.

M. Sheokand, A. Z. Alsaleh, F. D'Souza and R. Misra, *The Journal of Physical Chemistry B*, 2023, **127**, 2761-2773.

T. P. Pandurang, J. Cacaccio, F. A. Durrani, M. Dukh, A. Z. Alsaleh, M. Sajjad, F. D'Souza, D. Kumar and R. K. Pandey, *Molecules*, 2023, **28**, 3782.

A. Ganesan, S. Alhowity, A. Z. Alsaleh, M. Guragain, O. Omolere, T. R. Cundari, J. Kelber and F. D'Souza, *Journal of The Electrochemical Society*, 2023, **170**, 056501.

I. S. Yadav, A. Z. Alsaleh, B. Martin, R. Misra and F. D'Souza, *The Journal of Physical Chemistry C*, 2022, **126**, 13300-13310.

E. Nikoloudakis, A. Z. Alsaleh, G. Charalambidis, A. G. Coutsolelos and F. D'Souza, *Chemical Communications*, 2022, **58**, 12078-12081.

R. Canton-Vitoria, A. Z. Alsaleh, G. Rotas, Y. Nakanishi, H. Shinohara, D. Francis and N. Tagmatarchis, *Nanoscale*, 2022, **14**, 15060-15072.

I. S. Yadav, A. Z. Alsaleh, R. Misra and F. D'Souza, *Chemical science*, 2021, **12**, 1109-1120.

Y. Hu, A. Alsaleh, O. Trinh, F. D'Souza and H. Wang, *Journal of Materials Chemistry A*, 2021, **9**, 27692-27700.

M. K. Chahal, A. Liyanage, A. Z. Alsaleh, P. A. Karr, J. P. Hill and F. D'Souza, *Chemical science*, 2021, **12**, 4925-4930.

D. Pinjari, A. Z. Alsaleh, Y. Patil, R. Misra and F. D'Souza, *Angewandte Chemie International Edition*, 2020, **59**, 23697-23705.

K. Prakash, A. Z. Alsaleh, Neeraj, P. Rathi, A. Sharma, M. Sankar and F. D'Souza, *ChemPhysChem*, 2019, **20**, 2627-2634.

G. Argade, S. Sanders, G. Mohandass, A. Alsaleh, F. D'Souza, T. Golden and R. Mishra, *Journal of Materials Engineering and Performance*, 2019, **28**, 852-862.